

**FABRICATION OF POROUS CARBON
STRUCTURES FOR BIOLOGICAL FUEL CELLS**

Negar Amini

A thesis submitted for the degree of Doctor of Philosophy
in the Faculty of Engineering of the University of London

**School of Engineering and Materials Science
Queen Mary, University of London**

2010

Acknowledgments

I would like to express my sincere gratitude to my supervisor, Prof. Z. X. Guo, who gave me the opportunity to work in his group and on this project. I am also grateful of his guidance, support and advice. Besides, I would like to express my deep appreciation to Dr. K. F. Aguey-Zinsou for all the helpful discussions, assistance and encouragement throughout the project.

Many thanks go to the academic and technical staff in the Department of Materials, Queen Mary, in particular, Dr. Monisha Philips, Dr. Zofia Luklinska, Mr. Mick Willis and Mr. John Caulfield for their technical support, Dr. Haixue Yan for helping me to use the SPS and Mr. Giuseppe Viola for the assistance in the mechanical tests of my samples. I would also like to thank technical and research staff in the Department of Chemistry, University College London, especially, Dr. Steve Firth, Mr. Martin Vickers and Mr. Dave Knapp for their technical assistance and Dr. Suela Kellici for helping me to measure the surface area and pore size distribution of my samples by the BET technique. In the meantime, I would like to acknowledge all my colleagues in the group and my friends who helped me through difficult times and made my life in London more enjoyable.

I would like to express my deepest gratitude to my parents for their endless support and all the sacrifices they made to get me to this point. Thank you mum for giving me the opportunities you never had. My special thanks to my husband, Reza, for all the patience, support and encouragement during my PhD study. I am also grateful of my sister, Nana, and her husband, as well as my brother, Pouya, and his wife for their care and always being there for me.

Abstract

Biofuel cells demand three-dimensional, “high” surface area electrodes with “high” electrical conductivity and structural integrity. The aim of this project is to design and fabricate porous carbon structures as electrodes for enzyme and microbe immobilisation in biofuel cells. These electrodes should have homogeneous pore size distributions, “high” electrical conductivity, “good” mechanical strength and a suitable surface for enzyme and microbe immobilisation.

Various routes have been introduced to produce porous carbon electrodes with different ranges of pore sizes. In the case of microbial fuel cells where the pore sizes need to be in the micrometric ranges, a foaming method was adopted. To develop porous carbon electrodes with pore sizes in the nanometre ranges, a templating method was used. Highly ordered hierarchical mesoporous and macroporous carbon structures were obtained using the templating method. Ultimately, a polymer blend technique was developed to produce porous carbon electrodes in large-scales. Porous carbons prepared by this method composed of pores in the micrometric ranges and nanometre pores on the walls of the electrodes’ structures.

Various methods to improve mechanical strength and electrical conductivity of the fabricated electrodes were examined. Successive impregnations of the samples in a resin improved the strength and the conductivity of the samples. Moreover, to increase the electrical conductivity of the electrodes, catalytic graphitisation was tested and different graphitic components were produced. The graphitised carbons exhibited electrical conductivities of up to fifty times larger than those obtained from the non-graphitised samples. Electrochemical behaviour of the amorphous and the graphitic carbon electrodes was investigated and it was found that the fabricated electrodes were electrochemically active.

Table of Contents

Abstract	3
List of Tables	9
List of Figures	10
Introduction	19
Chapter 1: Literature Survey	22
1.1 Introduction	22
1.2 Why Using Carbon Structures?	23
1.2.1 Physical Properties of Carbon.....	23
1.2.2 Surface Chemistry of Carbon.....	25
1.3 Preparation of Carbon Structures	26
1.3.1 Carbon from Aromatic Hydrocarbons	28
1.3.1.1 Pitches	28
1.3.1.2 Coals.....	30
1.3.1.3 Properties of Carbons Derived from Aromatic Hydrocarbons	31
1.3.2 Carbon from Polymers	31
1.3.2.1 Phenolics	33
1.3.2.2 Polyfurfuryl Alcohol	35
1.3.2.3 Properties of Carbons Derived from Polymers	37
1.3.3 Summary	40
1.4 Formation of Porous Carbons	40
1.4.1 Foaming Method	42
1.4.2 Templating Method.....	44
1.4.3 Physical Properties of Porous Carbons	49
1.4.3.1 Relative Density	49
1.4.3.2 Electrical Conductivity.....	50
1.4.3.3 Mechanical Strength.....	51
1.4.4 Summary	52

1.5 Porous Carbon as an Electrode	52
1.5.1 Basics of Electrochemistry.....	53
1.5.2 Electrochemical Properties of Carbon	58
1.5.3 Summary	59
1.6 How to Reach the Ideal Properties?	59
1.6.1 Mechanical Strength.....	60
1.6.2 Electrical Conductivity.....	61
1.6.3 Surface Chemistry	64
1.7 Objectives.....	67
1.8 Summary	70
Chapter 2: Carbon Preparation from Polyfurfuryl Alcohol.....	73
2.1 Introduction	73
2.2 Synthesis of PFA.....	73
2.3 Confirmation of the PFA Synthesis	74
2.3.1 Chemical Structure.....	74
2.3.2 Thermal Behaviour.....	75
2.4 Properties of the Pyrolysed PFA.....	77
2.4.1 Structure	77
2.4.2 Density	79
2.4.3 Mechanical Strength.....	79
2.4.4 Electrical Conductivity.....	80
2.5 Summary	81
Chapter 3: Macroporous Carbon Materials Derived from Foaming Method	82
3.1 Introduction	82

3.2 Fabrication of Carbon Foams and Their Properties	82
3.2.1 Method-1: Sintering	83
3.2.2 Method-2: Impregnation with PFA.....	85
3.2.2.1 Morphology and Porosity.....	86
3.2.2.2 Shrinkage.....	89
3.2.2.3 Structure	90
3.2.2.4 Density and Mechanical Strength	91
3.2.2.5 Electrical Conductivity.....	93
3.2.3 Method-3: Foaming with No Powder	94
3.2.3.1 Morphology and Porosity.....	95
3.2.3.2 Shrinkage.....	96
3.2.3.3 Structure	97
3.2.3.4 Density and Mechanical Strength	97
3.2.3.5 Electrical Conductivity.....	99
3.2.4 Summary	99
3.3 Improving Electrical Conductivity of the Foams	100
3.3.1 Materials Preparation	100
3.3.2 Characterisation and Properties.....	101
3.3.2.1 Structure and Morphology	101
3.3.2.2 Degree of Graphitisation.....	106
3.3.2.3 Electrical Conductivity.....	108
3.3.3 Summary	109
3.4 Electrochemical Behaviour of the Fabricated Foams.....	109
3.5 Summary	115
Chapter 4: Ordered Porous Carbon Materials Derived from Templating Method	116
4.1 Introduction	116
4.2 Preparation of Porous Carbon Monoliths and the Properties.....	117
4.2.1 Using Polystyrene Template	117
4.2.1.1 Synthesis of Polystyrene Spheres and the Properties.....	117
4.2.1.2 Fabrication of Porous Carbon Monoliths and Their Properties	120
4.2.2 Using Silica Template	123
4.2.2.1 Fabrication of Porous Carbon Monoliths.....	124
4.2.2.2 Properties of the Fabricated Carbon Monoliths	126

4.2.3 Summary	134
4.3 Electrochemical Behaviour of the Porous Carbons Fabricated	134
4.4 Summary	137
Chapter 5: Carbon Electrodes in Large-Scales.....	138
5.1 Introduction	138
5.2 Preparation of Porous Carbon Electrodes.....	139
5.3 Properties of the Fabricated Carbon Electrodes.....	141
5.3.1 Morphology and Porosity.....	141
5.3.2 Structure	144
5.3.3 Shrinkage and Density	145
5.3.4 Mechanical Strength.....	146
5.3.5 Electrical Conductivity.....	148
5.3.6 Electrochemical Behaviour	149
5.4 Summary	155
Chapter 6: General Discussion	156
Chapter 7: Conclusions and Future Work	161
7.1 Conclusions	161
7.2 Future Work	162
References	164
Appendix A: Biofuel Cells	185
Appendix B: Techniques for Characterising Structure and Properties of Carbon Materials	192
B.1 X-Ray Diffraction.....	192
B.2 Transmission Electron Microscopy	193

B.3 Raman Spectroscopy	194
B.4 Pycnometry.....	194
B.5 Four- Point Probe Method for Electrical Resistivity	196
B.6 Compression Test for Mechanical Strength	198
Appendix C: Techniques for Characterising Porous Carbons	200
C.1 Scanning Electron Microscopy.....	200
C.2 Mercury Intrusion Porosimetry	201
C.3 Brunauer-Emmett-Teller (BET) Surface Area Analyser.....	202
C.3.a Classification of Gas Adsorption Isotherms	204
C.3.b Classification of Adsorption-Desorption Hysteresis Loops	205
Appendix D: Analysis of Surface Functional Groups.....	208
D.1 Titration.....	208
D.2 Fourier Transform Infrared (FTIR) Spectroscopy	208
D.3 X-ray Photoelectron Spectroscopy (XPS).....	210
D.4 Temperature Programmed Desorption (TPD).....	211
Appendix E: Other Instruments and Materials Used in this Project.....	213
Appendix F: Supplementary Results.....	218
Appendix G: Presentations and Publications	221

List of Tables

Table 1-1: Carbon yields of various precursor materials [32].	27
Table 1-2: Physical and mechanical properties of vitreous carbon and other carbon materials at 25 °C [63].	39
Table 1-3: Properties of a vitreous carbon foam with 97% pore volume [63].	43
Table 1-4: Pore size of some mesoporous silica structures [13].	46
Table 2-1: Preparation of PFA with different viscosities.	74
Table 3-1: Summary of the physical properties of the carbon foams prepared by Method-2.	94
Table 3-2: Different structures of the produced carbon foams and their structural properties.	108
Table 3-3: Calculated parameters of 1 mM ferricyanide/0.1 M NaCl and capacitance values at produced carbon electrodes from the CV curves.	115
Table 4-1: Structural parameters of the silica templates and the carbon monoliths produced by Method-II.	130
Table 4-2: Capacitance values of the mesoporous and macroporous carbons at various scan rates.	136
Table 5-1: Capacitance of porous carbon electrodes after polymer burn out at various scan rates.	151
Table 5-2: Calculated parameters of 1 mM ferricyanide/0.1 M NaCl at the carbon electrodes after polymer burn out and after impregnation with PFA from the CV curves at various scan rates.	154
Table D-1: Infrared spectra assignments of functional groups on carbon surfaces [6].	209
Table D-2: Functional groups determined by XPS from the O1s peaks [9].	210
Table D-3: Evolved gases, obtained by TPD technique, from functional groups present on carbon surfaces [9, 10].	211

List of Figures

Fig. 1-1: Crystal structure of graphite [20].	24
Fig. 1-2: Carbon phase diagram [21].	25
Fig. 1-3: Structures of oxygen functional groups on carbon surfaces [29].	26
Fig. 1-4: The Franklin models of carbon structure (a) graphitisable and (b) non-graphitisable carbons [34].	28
Fig. 1-5: Schematic diagram of pitch pyrolysis [40].	30
Fig. 1-6: Chemical structure of polyvinylchloride [35].	32
Fig. 1-7: Chemical structure of (a) phenol and (b) formaldehyde [51, 52].	34
Fig. 1-8: Chemical structure of (a) novolac [50] and (b) resol resins [53].	34
Fig. 1-9: Furfuryl alcohol [57].	35
Fig. 1-10: Acid-catalysed condensation of FA which results in (a) methylene and (b) dimethyleneoxide [58].	36
Fig. 1-11: Molecular structure of cured PFA [59].	36
Fig. 1-12: Intermediate products formed during thermal decomposition of polyfurfuryl alcohol [60].	37
Fig. 1-13: Schematic model of the ribbon structure of glassy carbon [64].	38
Fig. 1-14: Schematic pore classification according to their access to surrounding [71].	41
Fig. 1-15: SEM micrographs of (a) 100 and (b) 30 ppi, nominal pores per linear inch, RVC [78].	42
Fig. 1-16: Schematic of the overall template synthetic procedure for microporous carbons using a zeolite Y template [13].	44
Fig. 1-17: Schematic representation of the formation of an ordered mesoporous carbon using a mesoporous silica template [95].	45
Fig. 1-18: A) SEM of a porous SiO ₂ opal. B) SEM of a fracture surface of a graphitic carbon inverse	47
Fig. 1-19: Schematic of the synthetic of porous carbons using surfactant templates [107].	48
Fig. 1-20: Electrical conductivity of porous glassy carbons annealed at 2700 °C versus density [116].	51

Fig. 1-21: A typical cyclic voltammogram [118], where “pc” is the cathodic peak (reduction peak) and “pa” is the anodic peak (oxidation peak).	53
Fig. 1-22: Schematic model of the double-layer region. 0 is electrode-electrolyte interface, 1 is IHP (inner Helmholtz plane), 2 is OHP (outer Helmholtz plane) and 3 is the diffusive layer [121, 122].....	55
Fig. 1-23: Schematic of electron transfer at an electrode surface [128].	57
Fig. 1-24: Structure of turbostratic carbon [150].	62
Fig. 1-25: Theoretical values of crushing strength of porous glassy carbon against relative density.	68
Fig. 1-26: Theoretical values of electrical conductivity of porous glassy carbon against relative density.	70
Fig. 2-1: Furfuryl alcohol, picture at the left hand side, and Polyfurfuryl alcohol, at the right.	73
Fig. 2-2: Infrared spectrum of PFA as synthesised.	75
Fig. 2-3: TGA (-) and DTA (--) profiles of pyrolysis of PFA in argon at 10 °C min ⁻¹	76
Fig. 2-4: Gas evolution profiles of pyrolysis of PFA in argon at 10 °C min ⁻¹	77
Fig. 2-5: XRD pattern of the carbonised PFA.....	78
Fig. 2-6: Raman spectrum of the carbonised PFA.	79
Fig. 2-7: Compressive stress (MPa) vs. time (s) graphs obtained from the compression tests for two samples of PFA that have been cured in air and nitrogen, respectively and carbonised at the same conditions.	80
Fig. 3-1: Schematic diagram of foaming process [213].	83
Fig. 3-2: Schematic diagram of debinding procedure.	84
Fig. 3-3: SEM image of a carbon foam after polymer burn out.....	85
Fig. 3-4: SEM images of sintered carbon foams (prepared with Method-1 and using SPS process) at 2175 °C for (A) 5 min and (B) 15 min.	85
Fig. 3-5: Pictures of the carbon foams fabricated (a) before polymer burn out, (b) after polymer burn out and (c) after impregnation with PFA and carbonisation (Method-2).	86

Fig. 3-6: Field emission scanning electron microscopy images of the carbonised foams prepared with Method-2 after (A) first, (B) second and (C) third impregnation with PFA.	87
Fig. 3-7: Pore size distribution curves of two samples of carbon foam prepared by Method-2 and impregnated with PFA once (porous carbon 1) and three samples of carbon foams prepared by Method-2 and impregnated with PFA twice (porous carbon 2) and three samples of carbon foams prepared by Method-2 and impregnated with PFA three times (porous carbon 3).....	88
Fig. 3-8: Log differential intrusion (mL g^{-1}) vs. average pore size diameter (μm) of carbon foams prepared by Method-2 and impregnated with PFA once (porous carbon 1), twice (porous carbon 2) and three times (porous carbon 3).	89
Fig. 3-9: Shrinkage of the carbon foams, prepared by Method-2, after polymer burn out vs. different amounts of graphite powder (vol.%) added.	90
Fig. 3-10: Structure of the carbon foams prepared by Method-2 and impregnated with PFA once.	91
Fig. 3-11: Compressive stress (MPa) vs. time (s) obtained from the compression test of carbon foam prepared by Method-2 after second impregnation with PFA.	92
Fig. 3-12: Theoretical values of compressive strength (MPa) of glassy carbon vs. relative density (—) and compressive strength vs. relative density of the carbon foams impregnated with PFA once (porous carbon 1), twice (porous carbon 2) and three times (porous carbon 3).....	93
Fig. 3-13: Schematic diagram of heating cycle for debinding and carbonisation of the foams prepared by Method-3.	95
Fig. 3-14: Field emission scanning electron microscopy image of a carbonised foam prepared by Method-3 after second impregnation with PFA.	95
Fig. 3-15: Log differential intrusion (mL g^{-1}) vs. pore size diameter (μm) for carbon foam prepared by Method-3 and after first impregnation with PFA.	96
Fig. 3-16: (a) XRD pattern and (b) Raman spectrum of carbon foam prepared by Method-3 and impregnated with PFA once.	97
Fig. 3-17: Compressive stress (MPa) vs. time (s) graph obtained from the compression test for carbon foam prepared by Method-3 after polymer burn out.....	98

Fig. 3-18: XRD pattern of carbon foam prepared by Method-2 but using amorphous carbon powder instead of graphite powder.	102
Fig. 3-19: XRD pattern of carbonised PFA+Ni(NO ₃) ₂	102
Fig. 3-20: XRD patterns of carbon foams before any nickel treatments (amorphous carbon) and after addition of 0.01 and 0.05 mol L ⁻¹ nickel salts by Method-A, produced T-component and G-component, respectively.	103
Fig. 3-21: TEM image of a graphitised carbon T-component obtained by addition of 0.004 mol L ⁻¹ nickel nitrate and using Method-B for catalyst addition. (a) amorphous carbon and (b) graphitic carbon.....	104
Fig. 3-22: TEM image of the produced graphitic carbon G-component obtained by addition of 0.22 mol L ⁻¹ nickel by Method-A.	105
Fig. 3-23: Raman spectra of the amorphous carbon foam and the graphitic carbons of T-component and G-component produced by Method-A and by addition of 0.01 and 0.05 mol L ⁻¹ nickel nitrate, respectively.....	107
Fig. 3-24: Three electrode cell used for investigating the electrochemical behaviour of the produced carbon foams.	110
Fig. 3-25: CV curves of carbon foams produced by (a) carbon powder and (b) graphite powder, at a 100 mV s ⁻¹ scan rate in an aqueous 0.1 M NaCl solution. ...	111
Fig. 3-26: CV curves of graphitised carbon foams produced by carbon powder and with different structures of (a) T-component and (b) G-component, at 100 mV s ⁻¹ scan rate in an aqueous 0.1 M NaCl solution.	112
Fig. 3-27: Cyclic voltammetric behaviour of (a) carbon foam at different scan rates and (b) carbon foam/G-component at 100 mV s ⁻¹ (c) graphite foam-T-component at different scan rates (d) graphite foam heat treated at 540 °C for 10 h, at different scan rates and all in 1 mM ferricyanide/0.1 M NaCl.	113
Fig. 3-28: ΔE _p as a function of scan rate in 1 mM ferricyanide/0.1 M NaCl for different produced electrodes.	114
Fig. 4-1: TEM images of PS spheres synthesised using a stirring speed of 247 rpm and at (a) 8K and (b) 12K magnifications.	118
Fig. 4-2: TEM image of PS spheres synthesised using a stirring speed of 650 rpm.	119

Fig. 4-3: Particle size distributions of the PS spheres prepared at a stirring speed of 247 and 650 rpm, respectively.	119
Fig. 4-4: TGA (--) and DTA (-) curves of PS spheres heated from RT to 600 °C at 2 °C min ⁻¹ in nitrogen.....	120
Fig. 4-5: Schematic diagram of synthesising porous carbon from PS template.	120
Fig. 4-6: SEM images of PS spheres after centrifugation at 950 rpm for 15 h.....	121
Fig. 4-7: Carbonisation cycle of PFA resin + PS template.	122
Fig. 4-8: Porous carbon resulted from PS template of an initial PS sphere size of 610 nm.....	123
Fig. 4-9: Transmission electron micrographs of the colloidal silica as received (a) Snowtex-ZL with particle sizes of 70-100 nm and (b) Ludox AS-40 with an average particle size of 22 nm.....	123
Fig. 4-10: Differential thermal analysis (DTA) and thermal gravimetric (TG) analysis of silica dry gel. The transition of the silica particles is highlighted in the illustration [227].....	124
Fig. 4-11: A silica template and resulted macroporous carbon from the template produced by Method-I.....	125
Fig. 4-12: Picture of (a) mesoporous silica template, (b) silica template after impregnation with OxA and FA and in situ polymerisation, (c) mesoporous carbon resulted from carbonisation and silica removal, all were produced by Method-II.	126
Fig. 4-13: Ordered macroporous carbon prepared from silica template using Method-I.	127
Fig. 4-14: Highly ordered mesoporous carbon prepared from silica template using Method-II.	128
Fig. 4-15: Nitrogen sorption isotherms and pore size distribution (inset) of the mesoporous silica template and the carbon monoliths prepared by Method-II.	129
Fig. 4-16: Nitrogen sorption isotherms and pore size distribution (inset) of the macroporous silica template and the carbon monoliths prepared by Method-II.	130

Fig. 4-17: Compressive stress (MPa) vs. time (s) obtained from the compression tests of (a) mesoporous and (b) macroporous carbon materials prepared from silica templates by Method-II.....	131
Fig. 4-18: Theoretical values of compressive strength (MPa) of glassy carbon vs. relative density (—) and compressive strength vs. relative density of (1) the macroporous and (2) the mesoporous carbon materials prepared from silica templates by Method-II.	132
Fig. 4-19: Theoretical values of electrical conductivity ($S\ cm^{-1}$) for glassy carbon vs. relative density (—) and conductivity vs. relative density of (1) the macroporous and (2) the mesoporous carbon materials prepared from silica templates by Method-II.	133
Fig. 4-20: Cyclic voltammograms of mesoporous carbon monoliths prepared by silica templates in 0.1 M NaCl solution at various scan rates (0.5, 10 and 100 $mV\ s^{-1}$).....	135
Fig. 4-21: Cyclic voltammograms of macroporous carbon monoliths prepared by silica templates in 0.1 M NaCl solution at various scan rates (0.5, 10 and 100 $mV\ s^{-1}$).....	135
Fig. 4-22: Cyclic voltammetric behaviour of the macroporous carbons prepared from silica templates in 1 mM ferricyanide/ 0.1 M NaCl at various scan rates (2, 10 and 100 $mV\ s^{-1}$).....	137
Fig. 5-1: Schematic diagram of the polymer blend technique used for preparation of large porous carbon electrodes.....	139
Fig. 5-2: A picture of porous carbon material (bended) prepared by the polymer blend technique and carbonised under a nitrogen flow of 1500 $mL\ min^{-1}$	140
Fig. 5-3: A schematic diagram of curing and carbonisation cycle of the samples prepared by the polymer blend technique.	140
Fig. 5-4: Picture of porous carbon materials prepared in different shapes and sizes by the polymer blend technique. In every set of samples the larger sample is before the carbonisation and the smaller one is after the carbonisation. ..	141
Fig. 5-5: Field emission scanning electron microscopy images of porous carbon electrode prepared with the polymer blend technique after impregnation with PFA at different magnifications.	142

Fig. 5-6: Field emission scanning electron microscopy images of the polyethylene particles at different magnifications.....	142
Fig. 5-7: Pore size diameter (μm) vs. Log differential intrusion (mL g^{-1}) for porous carbons prepared by the polymer blend technique after polymer burn out (---) and after impregnation with PFA (—).....	143
Fig. 5-8: Pore size distributions (mesopore) of porous carbons prepared by the polymer blend technique, after polymer burn out (---) and after impregnation with PFA (—).	144
Fig. 5-9: (a) XRD pattern and (b) Raman spectrum of the porous carbons prepared by the polymer blend technique and impregnated with PFA.....	145
Fig. 5-10: Compressive stress (MPa) vs. time (s) obtained from the compression tests of the carbon materials (sample a) prepared by the polymer blend technique (a) after polymer burn out and (b) after impregnation with PFA.....	147
Fig. 5-11: Compressive strength (MPa) vs. sample diameter (mm) obtained for the porous carbons prepared by the polymer blend technique with different diameters (a: 11, b: 20 and c: 37.7 mm) after polymer burn out and after impregnation with PFA (a: 10, b: 18.5 and c: 35.5 mm).	147
Fig. 5-12: Theoretical values of compressive strength (MPa) of glassy carbon vs. relative density (—) and compressive strength vs. relative density of porous carbons with different diameters (samples a, b and c) after polymer burn out (\blacktriangle) and after impregnation with PFA (\bullet).....	148
Fig. 5-13: Theoretical values of electrical conductivity (S cm^{-1}) for glassy carbon vs. relative density (—) and conductivity vs. relative density of the porous carbons with different diameters (samples a, b and c) prepared by the polymer blend technique after polymer burn out (\blacktriangle) and after impregnation with PFA (\bullet).....	149
Fig. 5-14: Cyclic voltammograms of porous carbon electrodes after polymer burn out in 0.1 M NaCl solution at various scan rates.	150
Fig. 5-15: Cyclic voltammetric behaviour of the porous carbons after polymer burn out in 1 mM ferricyanide/ 0.1 M NaCl at various scan rates.	152
Fig. 5-16: Cyclic voltammetric behaviour of the porous carbons after impregnation with PFA in 1 mM ferricyanide/ 0.1 M NaCl at various scan rates.....	152

Fig. 5-17: ΔE_p as a function of scan rate (v) in 1 mM ferricyanide/0.1 M NaCl for the porous carbons after polymer burn out (\blacktriangle) and after impregnation with PFA (\bullet).	153
Fig. 5-18: Cathodic peak current as a function of (scan rate) ^{1/2} in 1 mM ferricyanide/0.1 M NaCl for the porous carbons after polymer burn out and after impregnation with PFA.	155
Fig. A-1: Schematic diagram of half-biofuel cell [8].	186
Fig. A-2: Schematic of enzyme-based biofuel cells [9].	187
Fig. A-3: Different methods of enzyme immobilisation; (a) adsorption, (b) covalent attachment [9].	188
Fig. A-4: Various ways of mediators' attachment to the microorganisms: a, mediator and microorganisms are present in the solution; b, microorganisms are covalently linked to the electrode surface; c, mediators are covalently attached to the outer membrane of microorganisms [15].	189
Fig. B-1: Schematic of transmission electron microscope [6].	193
Fig. B-2: Simplified diagram of the pycnometer [8].	195
Fig. B-3: Micromeritics AccuPyc 1330 Pycnometer [9].	196
Fig. B-4: Schematic of the linear four-point resistivity probe [11].	197
Fig. B-5: Jandel four point probing system. Multi height probe with RM3-AR test unit [13].	198
Fig. C-1: Schematic drawing of a scanning electron microscope. CRT=cathode ray tube display [2].	201
Fig. C-2: Micromeritics Mercury Intrusion Autopore IV [5].	202
Fig. C-3: Classification of gas adsorption isotherms [8, 10].	204
Fig. C-4: Classification of adsorption-desorption hysteresis loops [10].	205
Fig. C-5: Micromeritics ASAP 2420 surface area and porosimetry system [13].	206
Fig. D-1: Functional groups determined with XPS showing the relevant oxygen atoms at their corresponding binding energies in Table D-2 [9].	210

Fig. E-1: Lenton vacuum tube furnace.....	213
Fig. E-2: Schematic of spark plasma sintering (SPS) process [1].....	214
Fig. E-3: Schematic drawing of Viscometer Model B [3].	215
Fig. E-4: 15 ton manual hydraulic press (Specac) [6].....	216
Fig. F-1: XRD patterns of the carbon foams after addition of 0.01, 0.05 and 0.22 mol L ⁻¹ nickel salt by Method 1 that produced graphitic carbons T- and G-components.	218
Fig. F-2: XRD patterns of the carbon foams after addition of 0.004 and 0.11 mol L ⁻¹ nickel salt by Method 2 that produced graphitic carbons T- and G-components, respectively.	218
Fig. F-3: Raman spectra of graphitised carbon T-component produced by Method 2.	219
Fig. F-4: Raman spectra of graphitised carbon G-component produced by Method 2.	219
Fig. F-5: Pictures of the machined porous carbon electrode produced by the polymer blend technique [provided by Dr. G. C. Premier from Department of Engineering, University of Glamorgan].....	220

Introduction

The aim of this project is to fabricate electrodes to be used in biological fuel cells for hosting enzymes and microbes. Electrodes play an important role in the efficiency of biofuel cells. For instance, high enzyme loading is vital for high output current density of the biofuel cells [1, 2] and electrodes with large surface areas ($> 1 \text{ m}^2 \text{ g}^{-1}$) lead to high enzyme loading and higher diffusion of reactants and products and therefore higher efficiency. It is important that the pore sizes of the porous electrodes match the sizes of enzymes and microbes. For instance, even though activated carbons possess a large surface area (over $1000 \text{ m}^2 \text{ g}^{-1}$ [3]), these are not suitable for hosting enzymes or microbes as their micropores are inaccessible. On the other hand, relatively large pore sizes of porous electrodes lead to quick leach out of adsorbed enzymes or microbes [4]. Therefore, there is a need to produce porous carbons with pores in the nanometric ranges for enzyme immobilisation and in the case of hosting microbes, porous carbons with pores in the micrometric ranges are desirable.

Electrodes to be used in biofuel cells demand “high” electrical conductivity for effective electron transport. Moreover, electrodes need to be inert toward reactants, products and electrolyte. A suitable electrode surface chemistry for enzyme/microbe immobilisation is also critical. Carbon has been reported as an attractive electrode material for biofuel cells as it is abundant, renewable, cheap and can be chemically modified by different means [5]. In this work, carbon was the material of choice for electrodes, as porous carbon electrodes offer high surface area, relatively high electrical conductivity (dependant on the form of carbon) and adjustable surface properties for enzyme/microbe immobilisation.

It has been shown that the use of three-dimensional electrodes in biofuel cells has resulted in an increase of power output compared to two-dimensional or flat electrodes [6]. For instance, reticulated vitreous carbon (RVC) has been used in microbial fuel cell as anode and cathode electrodes for its high surface area (51 and $114 \text{ m}^2 \text{ m}^{-3}$, respectively), to increase the power output of the biofuel cell [7].

Moreover, microbial fuel cells usually require large electrodes with mechanically robust structures to withstand handling and fluid flow.

Producing mechanically stable carbon materials with “high” surface area and “high” electrical conductivity is very difficult. This is because introducing porosity in a material reduces its relative density and as a result decreases its mechanical strength and electrical conductivity [8, 9]. Therefore, a balance between these properties has to be achieved. Furthermore, various methods for producing mesoporous and macroporous carbon materials have been reported in the literature but the porous carbon materials produced with these methods are either not in monolithic forms (they are in powder forms) or not mechanically stable. In this thesis these problems have been tackled.

Chapter 1 of this thesis reviews the literature on the preparation methods and properties of the porous carbon materials as electrodes for biofuel cells. Various types of carbon precursors and their properties are summarised in this chapter and a suitable precursor is selected, considering the required properties of the carbon material as an electrode. Moreover, methods for fabrication of porous carbon electrodes are reviewed in this chapter, and appropriate methods of producing mesoporous and macroporous carbons are chosen. Methods for improving different properties (mechanical, electrical and electrochemical) of porous carbon electrodes are also discussed in this chapter.

Chapter 2 presents the synthesis method of the carbon precursor of choice, polyfurfuryl alcohol, and the properties of the carbon derive from this precursor. This resin is used as a carbon precursor in all the fabrication methods of porous carbon electrodes in this project.

Chapter 3 presents a foaming method for fabrication of carbon foams with pores in the micrometric ranges. This method is modified to improve the mechanical property of the carbon foams. Different properties of the carbon foams produced by this method and the modified methods are reported in this chapter. Catalytic graphitisation for improvement of electrical conductivity of the carbon foams is tested and reported.

Finally, the electrochemical behaviour of the amorphous and the graphitised carbon foams is demonstrated in this chapter.

Chapter 4 summarises the templating routes for production of mesoporous and macroporous carbon monoliths with homogenous pores in the nanometric ranges. Two types of hard and soft templates are used and the properties of the carbon obtained from these templates, as well as the production methods are compared. A preliminary study of electrochemical behaviour of the carbon materials fabricated by this method is presented in this chapter.

In Chapter 5, a method for producing porous carbon electrodes in large-scales is developed. In this method two types of polymers are blended; one is the carbon precursor and the other is a thermally decomposed polymer. With this method it is possible to prepare stable porous carbon electrodes in different shapes and sizes. The electrochemical behaviour of the porous carbon electrodes produced by this method is examined and presented in this chapter.

A general discussion is presented in Chapter 6, and Chapter 7 presents conclusions and future work.

Chapter 1: Literature Survey

1.1 Introduction

The aim of this chapter is to review the knowledge to date on the preparation and use of porous carbon materials as electrodes for biological fuel cells. Porous carbon materials have received a great deal of interest due to their various applications. They can be used for gas separation, water purification, catalyst support and electrodes for electrochemical double layer capacitors and fuel cells [10-13]. In electrochemical applications where inertness, low cost and “good” electrical conduction of the electrodes are required, carbon is a material of choice as it offers corrosion resistance (in mild conditions) and reasonable electronic conductivity at the same time [14]. In particular, for biological fuel cell application, carbon could be a material of choice as porous carbon electrodes offer high surface area, high electronic conduction for fast electron transfer and tailorable surface properties for enzyme/microbe immobilisation.

Practically, porous carbon electrodes need to meet a range of requirements to be used for enzyme and microbe immobilisation in biofuel cells: (a) suitable pore sizes matching the sizes of enzymes and microbes; (b) mechanical strength to withstand handling and machining; (c) high electrical conductivity for a fast electron transfer; (d) suitable surface chemistry to facilitate the immobilisation of enzymes and to ensure fast electron transfer. Producing a material with high surface area ($> 1 \text{ m}^2 \text{ g}^{-1}$) and at the same time “high” mechanical strength or “high” conductivity is a challenge. Creating porosity decreases the mechanical strength while increases the electrical resistivity. Therefore, these properties need to be balanced.

Various types of carbon precursors can be used for fabrication of carbon electrodes. These precursors are summarised in this chapter and a suitable precursor has been selected according to the required properties of the carbon material as an electrode. Furthermore, different methods of preparing porous carbon materials are reviewed in the current chapter and suitable methods for producing macro- and mesoporous carbon structures have been chosen. In this chapter methods for improving

mechanical, electrical and electrochemical properties of porous carbon electrodes are also discussed.

1.2 Why Using Carbon Structures?

An electrode material for biological fuel cell needs to show “high” electrical conductivity, “high” surface area and “good” inertness, while facilitating electron transfer. Metals can be good candidates but are relatively poor in terms of corrosion resistance and also attaching an enzyme to a metal surface usually leads to enzyme denaturation and loss of enzyme catalytic activity [15]. Another option could be transition metals such as platinum and gold that are resistant to corrosion, however, they are expensive and rare. Among the non-metallic materials, carbon is a suitable electrode material. Carbon has a relatively high electrical conductivity (about 200 S cm^{-1} at $25 \text{ }^\circ\text{C}$ [16]) and corrosion resistant in mild conditions (room temperature and neutral PH). In theory, its surface chemistry is adjustable for enzyme or microbe immobilisation. Furthermore, carbon can be prepared in various forms and different levels of porosity. Examples of common porous carbons with industrial applications are: activated carbons (in the forms of fibres, cloth or felt), carbon nanotubes and reticulated vitreous carbon [17].

1.2.1 Physical Properties of Carbon

Physical properties of carbon depend on its atomic structure. Various types of atomic structures are possible for carbon. This is due to the quite unique position of the carbon in the periodic table. The carbon atom with an atomic number of six has four outer electrons capable of multi-bonding as tetrahedral sp^3 -hybrid, trigonal planar sp^2 and linear sp [18]. These different hybrid configurations form different allotropes of carbon that can be classified into three major categories: (i) The sp^2 structures which include graphite, the graphitic materials and amorphous carbon; (ii) The sp^3 structures which include diamond and Lonsdaleite; (iii) The Fullerenes that combines both sp^2 and sp^3 bonds. Different allotropes of carbons possess different physical, mechanical and chemical properties. Among all the carbon allotropes, graphite and diamond are the two common crystalline forms.

Electrical conductivity of carbon can be explained by movement of electrons in its atomic structure. For example, in the structure of graphite, electrical resistivity is low in the basal planes as the atoms are held together in two-dimensional hexagonal networks by strong sp^2 -hybrid σ -bonds. Whereas, between the graphene layers the bonding is delocalised π bonds and the spacing between the planes is relatively large (see Fig. 1-1). Therefore, the movement of the electrons is more difficult in this direction and the electrical resistivity is high. The electric conductivity values for graphite are often cited as 3.3 S cm^{-1} in the c direction (normal to the basal plane) and $2000\text{-}4000 \text{ S cm}^{-1}$ along the basal plane [19]. Graphite can be considered as a semi-metal, in terms of electrical conductivity, and diamond as an insulator. Other carbon materials have electrical conductivity between these two forms of carbon, *e.g.* 200 S cm^{-1} for vitreous carbon.

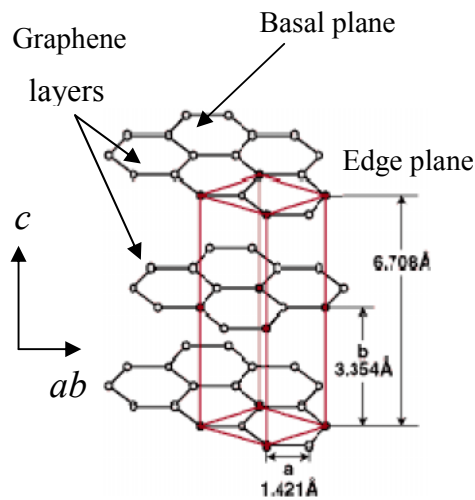


Fig. 1-1: Crystal structure of graphite [20].

Mechanical strength of carbon materials depend on various factors such as the crystallite orientation, porosity and structural defects. In graphite, the strength in the basal plane is higher than the interplanar strength. This is due to the strong bond between atoms in the basal planes than the bonds between the planes. Fig. 1-2 shows that graphite is the most stable allotrope of carbon at ambient conditions and diamond is the most stable allotrope of carbon at high pressures [20]. In terms of hardness, graphite is one of the softest materials and diamond is one of the hardest materials known.

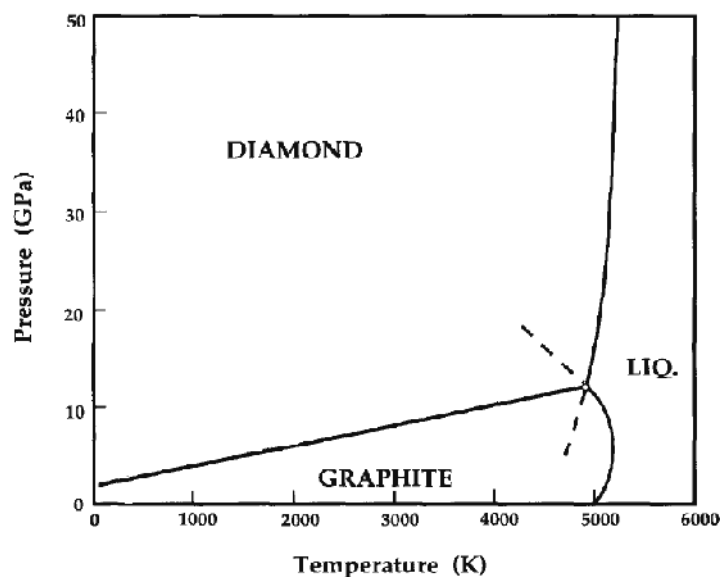


Fig. 1-2: Carbon phase diagram [21].

1.2.2 Surface Chemistry of Carbon

Surface chemistry of carbon electrodes plays an important role in the efficiency of biofuel cells. Ideally, enzymes/microbes should be immobilised on the surface of the electrode without denaturation and decay of the catalytic activity. Generally, the surface chemistry of carbon materials is due to a range of oxygen functional groups. For instance, the wettability [22] and adsorptive behaviour of a carbon [23, 24], as well as its catalytic [25], and its electrical properties [26] are influenced by the nature and extent of the surface oxygen groups. For example, creating acidic oxygen functional groups (carboxyl, phenolic and lactonic) on the carbon surfaces hinders alkane adsorption [27]. Kong *et al.* [28] have also shown that by exposing a single-walled carbon nanotube (SWNT) to gaseous molecules such as NO_2 or NH_3 the electrical conductivity of the SWNT increases or decreases dramatically. This is because exposure to NH_3 shifts the valence band of the nanotubes away from the Fermi level, whereas exposure to NO_2 results in the Fermi level shifting closer to the valence band.

Fig. 1-3 summarises examples of oxygen functional groups that can be found on carbon surfaces. The most common oxygen groups on carbon surfaces are carboxyl, lactone, phenol and carbonyl groups.

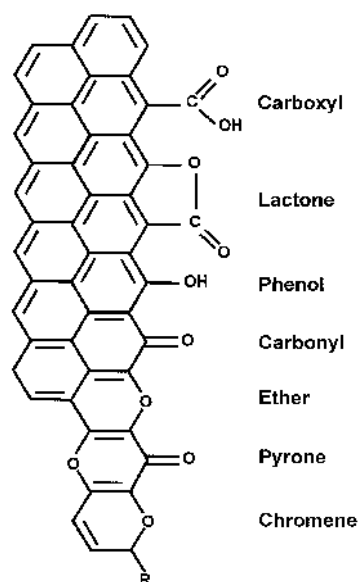


Fig. 1-3: Structures of oxygen functional groups on carbon surfaces [29].

The chemisorption of oxygen is greatly dependent on the crystalline nature of the carbon. Under the same conditions, well-ordered carbons containing small concentration of edge sites will chemisorb less oxygen than more amorphous carbons such as activated carbons [30]. On the other hand, chemisorption of oxygen also depends on the degree of porosity. Porosity increases surface area and hence the reactivity of the material. For instance, activated carbons with high surface areas are prompt to have a high density of oxygen functional groups than pore free or closed pore glassy carbons [31]. Temperature also affects the chemisorption of oxygen. For example, above 450 °C graphite oxidises with water, oxygen and many other oxidants such as acids.

1.3 Preparation of Carbon Structures

In order to obtain a suitable porous structure, it is advantageous to directly prepare the porous carbon electrode from the starting materials. Carbon materials always result from the carbonisation of organic materials, *i.e.* carbon precursors. In carbonisation, the organic material transforms to carbon by thermolysis under an oxygen-free atmosphere to avoid oxidation. Various types of carbon precursors can be used to prepare carbon materials. These precursors will lead to different carbon yields and types (graphitisable and non-graphitisable) after carbonisation.

Carbon yield is defined as the ratio of the weight of the carbon residue after carbonisation to the weight of the starting material. Typical carbon yields of common precursor materials are shown in Table 1-1. The carbon yields of the materials mentioned in the table are not fixed and depend on experimental conditions, *i.e.* heating rate, the composition of the atmosphere and the pressure [32, 33].

Table 1-1: Carbon yields of various precursor materials [32].

Precursor	Carbon Yield (%)	Type of Carbon*
<u>Aromatic hydrocarbons</u>		
Coal-tar pitches	40-60	Coke
Petroleum fractions	50-60	Coke
Naphtalene, C ₁₀ H ₈		Coke
Biphenyl, C ₁₂ H ₁₀		Char
<u>Polymers</u>		
Polyvinyl chloride, (CH ₂ CHCl) _n	42	Coke
Polyimide (Kapton), (C ₂₂ H ₁₀ O ₅ N ₂) _n	60	Coke
Polyvinylidene chloride, (CH ₂ CCl ₂) _n	25	Char
Polyfurfuryl alcohol, (C ₅ O ₂ H ₆) _n	50-56	Char
Phenolic resins, (C ₁₅ O ₂ H ₂₀) _n	50-55	Char
Polyacrylonitrile (PAN), (CH ₂ CHCN) _n	46-50	Char
Cellulose, (C ₁₂ O ₁₀ H ₁₈) _n	20	Char

* Coke is a graphitisable and char is a non graphitisable carbon.

As it can be seen from Table 1-1, carbonisation of different types of precursors result in either coke or char. Coke is a graphitisable carbon and char is a non-graphitisable carbon. Graphitisable carbons are carbons that become graphitic on heating beyond 2000 °C, and non-graphitisable carbons cannot become graphitic even above 2000 °C. The terms graphitisable and non-graphitisable carbons were first introduced by Rosalind Elsie Franklin (1950, 1951). The different types of carbons are illustrated in Fig. 1-4. It can be seen that graphitic carbons show a linear structure with alignment of graphitic planes, while the structure of non-graphitic carbons show more disorders.

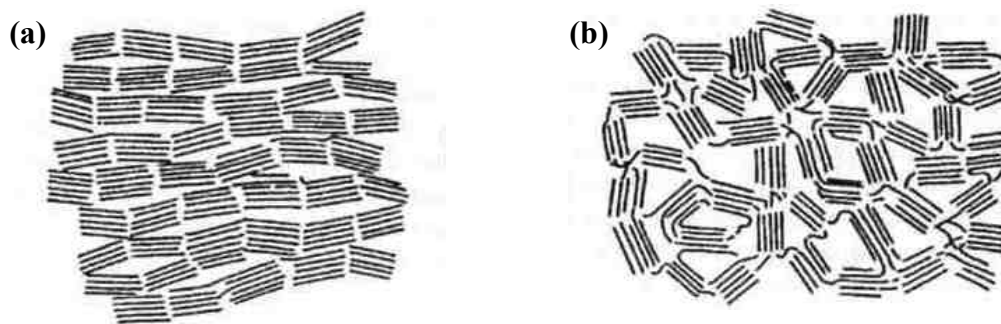


Fig. 1-4: The Franklin models of carbon structure (a) graphitisable and (b) non-graphitisable carbons [34].

Generally, carbon precursors can be classified in two main groups: derivatives from hydrocarbons and from polymers. This classification will be used in this thesis for further discussions.

1.3.1 Carbon from Aromatic Hydrocarbons

Aromatic hydrocarbons are interesting materials for the fabrication of carbon as they contain a high amount of carbon atoms and they have a “graphite-like structure”, *i.e.* they contain benzene rings and their small aromatic structure can reach the three-dimensional order of graphite by heat treatment. The general carbonisation mechanism of polyaromatic hydrocarbons involves rupturing the carbon-hydrogen bonds and removal of hydrogen [35]. Some of the hydrocarbons go through a mesophase stage during carbonisation process. This stage usually occurs at temperatures above 400 °C, and during this stage large polyaromatic molecules are formed. These molecules gradually increase in size and start to align themselves and form pre-cokes or green cokes [36]. Two commonly used hydrocarbons as carbon precursors are pitches and coals which are described in the two following sections.

1.3.1.1 Pitches

Pitches have high carbon yield and they tend to form graphitic carbon structures at high temperatures (> 2300 °C). The obtainable carbon yield from pitch depends on the composition of the precursor pitch and the conditions of pyrolysis. Restricting the evolution of volatile molecules present in the pitch can increase its carbon yield. This

can be done by decreasing the heating rate, applying pressure or using chemical additives, such as sulphur and iodine, prior to the thermal decomposition of the pitch. For example, it was reported that the iodine addition to coal tar pitch increased its carbon yield from 40 to 70% [37]. This was due to the acceleration of dehydrogenation reactions at temperatures between 200 and 400 °C. It has been found that the carbon yields of pitches at atmospheric pressure are about 50% by weight and carbonisation under high pressure (~100 MPa) can result in yields in excess of 90% for some pitches [38]. This is due to the participation of volatile species in the aromatic growth and polymerisation processes when carbonisation is carried out under pressure.

Pitches are derived from organic precursors using variety of processes such as solvent extraction and thermal treatments. Pitches usually have complex physical and chemical properties due to their broad range of molecular weight constituents. The two most common pitches that are used in the moulded graphite industry are coal-tar pitch and petroleum pitch [39]. Coal-tar pitch is the solid residue remaining after the distillation of coal-tar and its composition varies depending on the nature of the coal-tar. Petroleum pitch is the residue from the distillation of petroleum fractions. Like coal-tar pitch it is solid at room temperature, has a broad softening range and no well-defined melting point.

In order to be able to use pitches for the preparation of porous carbons, the thermal plastic properties of the pitch needs to be adjusted to meet the foaming requirements. This can be done by thermal treatment to control the viscosity and softening temperature of the pitch by removing the volatiles. As a result, the degree of polymerisation and condensation of the pitch changes through de-hydrogenation of polyaromatic molecules of the pitch precursors. Fig. 1-5 shows a schematic representation of the carbonisation process of a pitch which involves aromatic growth and polymerisation [40]. In this process first carbon-hydrogen bonds and carbon-carbon bonds break to form reactive radicals, then the molecules rearrange and thermal polymerisation happens. After polymerisation, aromatic condensation and elimination of side chains and hydrogen occur.

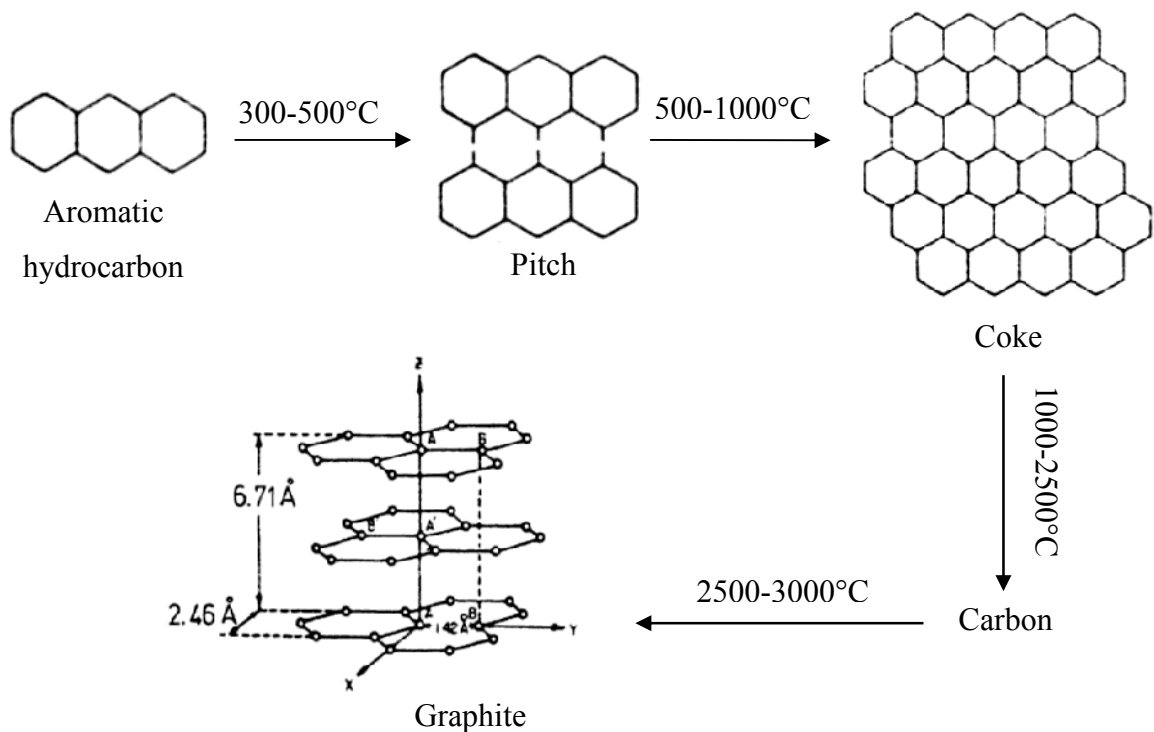


Fig. 1-5: Schematic diagram of pitch pyrolysis [40].

1.3.1.2 Coals

Coals have a wide range of carbon content (50 to over 95%) and they show a broad variation in properties depending on their source. Coals result from peat precursors by gradual transformation at temperatures around 200-250 °C and high pressures [41]. The structure changes from a peat through lignite, the lowest rank of coal, to anthracite which is the highest rank of coal. Sub-bituminous and bituminous coals are also intermediate structures. The coal rank defines by the carbon to hydrogen ratio of the material. The carbon content of bituminous coals is 60-80% and the rest is composed of water, air, hydrogen and sulphur whereas, the carbon content of anthracite is between 92 and 98%.

Foaming behaviour of the coal precursors depend on their plastic properties. For example, precursors with high fluidity lead to low-density carbon foams. Fluidity of the coals can be adjusted by de-volatilisation and solvent extraction [42]. In these processes light fractions, that are rich in transferable hydrogen, are removed and therefore larger condensed aromatic molecules are formed and fluidity is decreased [43].

1.3.1.3 Properties of Carbons Derived from Aromatic Hydrocarbons

Carbonisation of most aromatic hydrocarbons results in formation of coke (Table 1-1) which easily converts into a well-ordered graphitic structure. However, some aromatic compounds, such as phenanthrene and biphenyl, form char instead of coke. The structure of these compounds is branched aromatic rather than linear aromatic and therefore they do not pass through a liquid stage during their carbonisation and orientation process, which is a key factor in graphitisation, cannot take place for these precursors [44, 45].

In terms of mechanical and electrical properties of the carbon foams derived from aromatic compounds, it has been observed that precursors which are isotropic in nature (after carbonisation) yield high-strength structural carbon foams, whereas, anisotropic precursors result in carbon foams with high electrical conductivities [46]. For example, pitch-based carbon foams that develop large anisotropic domain result in highly graphitisable carbon, while pitches that develop small anisotropic domains are less graphitisable but are mechanically stronger. Therefore, pitch precursors can produce either mechanically strong or high conductivity carbon foams. Whereas, raw coals and coal solvent extracts generate strong (3 to 10 MPa in compressive strength depending on the density) and isotropic carbon foams which are good candidates for structural and energy absorption applications.

1.3.2 Carbon from Polymers

Polymers generally have lower carbon yields than aromatic hydrocarbons because they contain elements such as chlorine, oxygen or nitrogen in addition to hydrogen and carbon. However, they are easier to process as they do not need any modification and pretreatment before use. Polymer precursors that go through a liquid or mesophase stage above a certain temperature are called thermoplastic precursors and those that degrade by heating without going through a liquid stage are called thermoset precursors [47]. Thermoset precursors cure irreversibly to a stronger form that means they cannot melt or re-shape after they cure and therefore, they cannot align themselves and are non-graphitisable. The existence of highly cross-linked

aromatic structures either in the original polymer or during degradation prevents graphitisation of the thermoset precursor. Examples of thermoset precursors include polyfurfuryl alcohol and phenol formaldehyde. However, polycyclic aromatic structures not cross-linked can reorient if they pass through a liquid stage. For instance, polyvinyl chloride and polyvinyl acetate show this kind of behaviour and are thermoplastic precursors. The major polymers in the production of synthetic graphite are listed in Table 1-1 and the general mechanism of carbonisation is described below.

In carbonisation of polymers the following three possibilities can occur depending on the type of polymer [35]:

1) The chains degrade into small molecules and the products are evolved as gases leaving little or no carbon behind such as polyethylene or polystyrene. These materials have a low carbon yield and cannot be considered as suitable precursors. Polyethylene and polystyrene break down completely into gaseous products at 450-480 °C and 370-420 °C, respectively.

2) Other type of polymer, thermoplastic, goes through a mesophase stage during carbonisation and the result is a crystalline anisotropic coke which on heating to 2700 °C transforms to graphitic material. An example of this behaviour is polyvinyl chloride (PVC). The structure of this polymer is shown in Fig. 1-6. PVC contains a chain of sp^3 carbon atoms with a chlorine atom attached to alternate carbon atoms. It is formed by polymerisation of the vinyl chloride monomer.

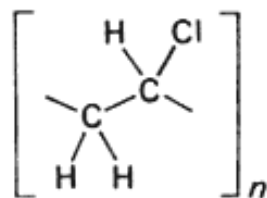
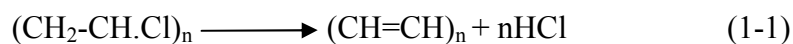


Fig. 1-6: Chemical structure of polyvinylchloride [35].

When PVC is heated under an inert atmosphere, above 200 °C HCl is evolved according to the reaction below:



PVC darkens to a new polymer $(\text{CH=CH})_n$ which becomes very fluid on heating to 380 °C due to thermal degradation. By further heating, the material solidifies and carbonises to form a coke. The carbonisation behaviour of this material is similar to pitch. The polymer chain breaks down and the constituent parts cyclise to form small aromatic products which fuse together to form larger aromatic sheets. These sheets stack above each other to form a “liquid crystal” and the liquid crystals combine to form large grains which become solid and make the grain boundaries in the final graphitised coke. It should be mentioned that contrary to these polymeric systems, the coking process in hydrocarbons is very slow and can take few days to complete due to slow aromatising process.

3) In the third type of polymers, thermosetting, the chains remain intact and the material does not pass through a plastic state during carbonisation and is not graphitisable even when heated to 3000 °C. Examples of such polymers are phenolics and polyfurfuryl alcohol which have relatively high carbon yields of 50 to 56%. The use of such thermosetting polymers facilitates the formation of porous carbons with controlled pore size distribution through template methods. Several examples can be found in the literature, *e.g.* Fuertes *et al.* [48] used furfuryl alcohol and phenolic resins to prepare mesoporous carbon structures and concluded that the type of carbon precursors affect the size of the mesopores derived from the template. Moreover, high surface area carbon monoliths with hierarchical structures were fabricated using furfuryl alcohol as carbon precursor [49]. The carbonisation process of thermosetting polymers will be discussed in more details in the following sections.

1.3.2.1 Phenolics

Phenolics $(\text{C}_{15}\text{O}_2\text{H}_{20})_n$ are a class of polymers obtained by a condensation polymerisation between, for example, phenol ($\text{C}_6\text{H}_5\text{OH}$) and formaldehyde (H_2CO) with elimination of water. The chemical structures of phenol and formaldehyde are shown in Fig. 1-7. The polymerisation process includes addition of formaldehyde to

phenol, chain growth or prepolymer formation, and finally, cross-linking or curing reactions [50].

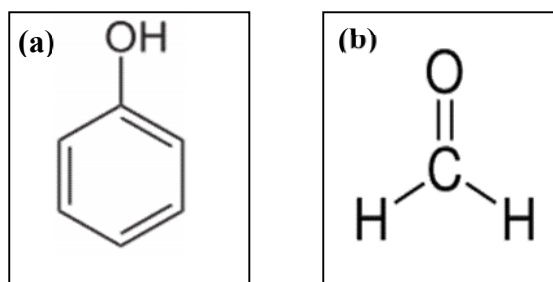


Fig. 1-7: Chemical structure of (a) phenol and (b) formaldehyde [51, 52].

Depending on the pH two types of prepolymer can be obtained: novolacs and resols. Novolacs are formed under highly acidic conditions and with a molar formaldehyde to phenol (FP) ratio of less than one. These consist of phenol rings connected solely by methylene bridges (Fig. 1-8 (a)). In resols, the FP ratios are greater than one and they are formed under basic conditions. Resols consist of phenol rings connected by dimethylene ether bridges and methylol groups in addition to methylene bridges (Fig. 1-8 (b)). Novolacs are cured by addition of a hardener, while resols cross-link by heating and without addition of a cross-linking agent. The curing process of both polymers includes cross-linking of linear chains by forming a gel at some intermediate stage of the process.

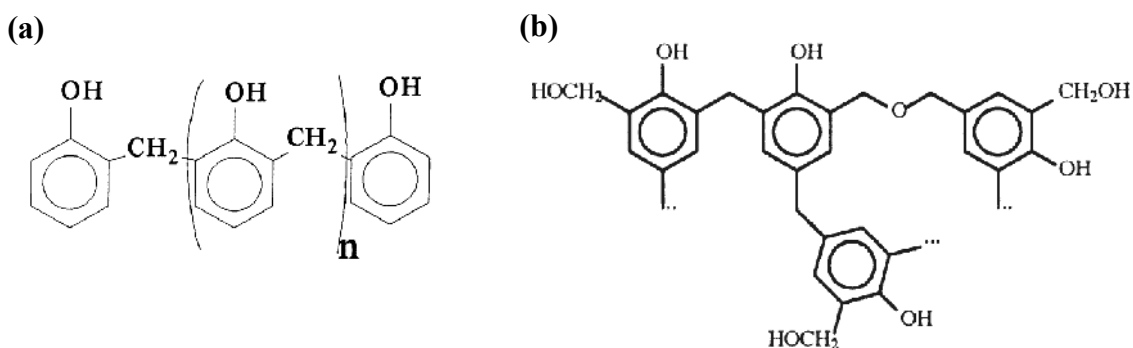


Fig. 1-8: Chemical structure of (a) novolac [50] and (b) resol resins [53].

Ordered mesoporous carbon materials can be synthesised using functionalised phenolic resins as the organic precursor through a templating route. These precursors contain a high density of hydroxyl groups that can form strong hydrogen bond with block copolymers as templates [54].

The behaviour of a phenolic resin during carbonisation depends on the degree of cross-linking. When a weakly cross-linked material is heated slowly, low molecular weight compounds such as unreacted phenol, short chain polymers and water are evolved between 100 and 350 °C. If the material is highly cross-linked water is not evolved until above 400 °C and the amount of low molecular weight polymer volatiles is decreased [55]. Basically, the pyrolysis gas products are CH₄, H₂, CO and CO₂, with H₂ and CH₄ releasing mainly above 450 °C [56]. The structure rearranges to an unsaturated aromatic residue at temperatures around 500 °C and ultimately a cross-linked aromatic network forms.

1.3.2.2 Polyfurfuryl Alcohol

Polyfurfuryl alcohol (PFA) is a thermosetting resin with high carbon yield. PFA is made from furfuryl alcohol. Furfuryl alcohol (C₅H₆O₂) is a furanic compound (C₄H₄O) which is used to produce various types of resins. Its chemical structure is shown in Fig. 1-9.

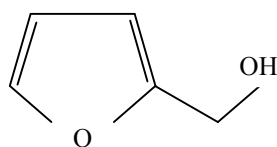


Fig. 1-9: Furfuryl alcohol [57].

The polymerisation process of furfuryl alcohol (FA) is acid catalysed and always leads ultimately to a black crosslinked product. The first phase of this process consists of condensation reactions between the OH group and either a hydrogen atom of a furan ring (head-to-tail structure, as shown in Fig. 1-10 (a)), or another OH group (head-to-head structure, Fig. 1-10 (b)).

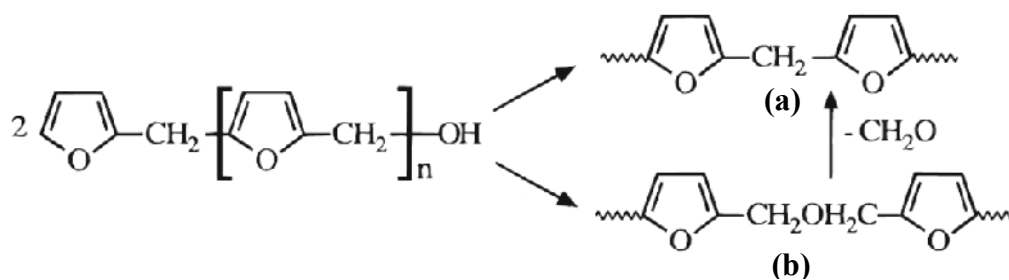


Fig. 1-10: Acid-catalysed condensation of FA which results in (a) methylene and (b) dimethyleneoxide [58].

This series of acid-catalysed condensations produces linear oligomers which can contain both methylene and dimethyleneoxide ($-\text{CH}_2\text{-O-CH}_2\text{-}$) molecules. Under strongly acidic conditions, dimethyleneoxide has a tendency to lose formaldehyde (CH_2O) and revert to methylene (Fig. 1-10). This phenomenon as well as the higher kinetic tendency for head-to-tail condensation, results in macromolecular structures in which methylene bridges are more common [57]. These two reactions are followed by further crosslinking. Fig. 1-11 illustrates the molecular structure of the cross-linked PFA.

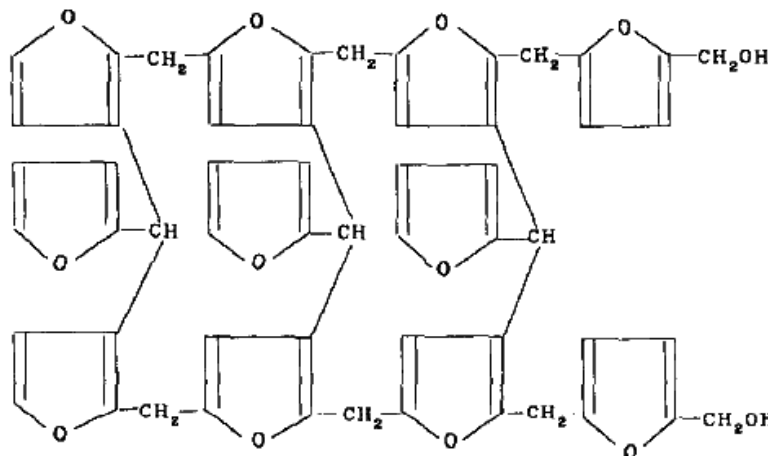


Fig. 1-11: Molecular structure of cured PFA [59].

Fitzer *et al.* [60] have studied the thermal degradation of PFA thoroughly. They showed that the furan rings break up and disappear at temperatures below $450\text{ }^\circ\text{C}$. This is accompanied by loss of H_2O , CH_4 , CO and CO_2 (Fig. 1-12). The methylene bridges are dehydrogenated at temperatures above $450\text{ }^\circ\text{C}$ and adjacent carbon-carbon chains with conjugated double bonds are formed. The pyrolysis gases during the

thermal decomposition of polyfurfuryl alcohol resin mainly consist of water and carbon monoxide. Carbon dioxide, methane and hydrogen are formed in smaller amounts [61]. The carbonisation of the PFA reached completion at around 900 °C [62].

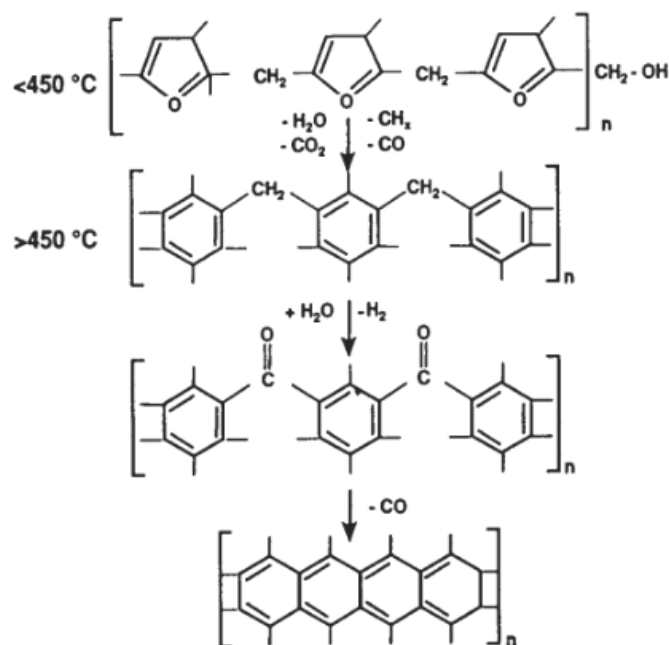


Fig. 1-12: Intermediate products formed during thermal decomposition of polyfurfuryl alcohol [60].

1.3.2.3 Properties of Carbons Derived from Polymers

Carbonisation of polymeric precursors results in a vitreous or glassy carbon. A material is considered vitreous when it has no crystalline long-range order. During a typical carbonisation process, the polymer is heated slowly in a reducing or inert atmosphere ($1\text{-}5\text{ }^\circ\text{C min}^{-1}$ to about $800\text{ }^\circ\text{C}$ and $5\text{-}10\text{ }^\circ\text{C min}^{-1}$ from $800\text{-}1000\text{ }^\circ\text{C}$ [63]). The heating rate to be chosen depends on the rate of diffusion of the volatile by-product of pyrolysis. This diffusion rate must be slow enough to avoid disruption and rupture of the carbon structure.

Vitreous carbon is made up of condensed aromatic ribbon molecules which are randomly oriented and are cross-linked by carbon-carbon covalent bonds. This random structure is believed to have the form of an extensive network of graphitic ribbons as is shown in Fig. 1-13. From the high resistance of the glassy carbon to

graphitisation, it can be concluded that the configuration of these ribbons is very stable [64]. In vitreous carbon the crystalline size (L_c) are small (up to ~ 4 nm) and within each crystallite, the interatomic distances vary by more than 5% from those of the ideal graphite in both the basal plane and between planes.

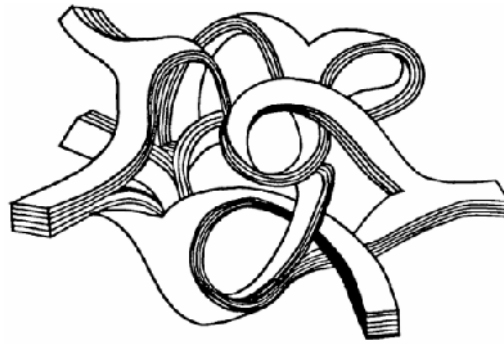


Fig. 1-13: Schematic model of the ribbon structure of glassy carbon [64].

It has been suggested that the structure of vitreous carbon includes some sp^3 (tetragonal) bonds in addition to the graphitic sp^2 (trigonal) bonds. The sp^3 bonds are characteristic of diamond bonding and this can be the reason of the isotropy, high strength and the hardness of the vitreous carbon [35]. Furthermore, the ribbon network and sp^3 bonds in glassy carbon are the two factors preventing ordering of the structure regardless of the graphitisation temperature.

Vitreous carbon has a low density of 1.54 g cm^{-3} compared with 2.2 g cm^{-3} in single crystal graphite and a uniform structure which is normally free of defects. The low density of vitreous carbon is a result of existence of micropores in the network structure due to the inefficient packing in an isotropic assembly of ribbons [65]. Its hardness, specific strength and modulus are high due to the covalent bond. Some properties of solid vitreous carbon as carbonised and after heat treatment to $3000 \text{ }^\circ\text{C}$ are shown in Table 1-2 [63]. The table includes the properties of a typical moulded graphite and pyrolytic graphite for comparison. Moulded graphite is derived from precursors that graphitise at high temperatures, such as petroleum cokes and coal-tar pitch, and pyrolytic graphite is produced from gaseous precursors, such as methane and other gaseous hydrocarbons, by chemical vapour deposition (CVD) technique.

It can be seen from the Table1-2 that the mechanical properties of vitreous carbon are usually higher and the thermal conductivity lower than those of other forms of carbon. Electrical conductivity of these carbons depends on the type of precursors, the process and the degree of graphitisation. Electrical conductivities of vitreous carbon and moulded graphite are reported around 200 S cm^{-1} and electrical conductivity of pyrolytic graphite is close to the conductivity of the ideal graphite crystal ($2000\text{-}4000 \text{ S cm}^{-1}$ in the *ab* directions) [16].

Table1-2: Physical and mechanical properties of vitreous carbon and other carbon materials at $25 \text{ }^\circ\text{C}$ [63].

Properties	Vitreous Carbon		Moulded Graphite	Pyrolytic Graphite*
	As Is	Heat Treated At $3000 \text{ }^\circ\text{C}$		
Density (g cm^{-3})	1.54	1.42	1.72-1.90	2.10-2.24
Flexural strength (MPa)	210	260	10-100	80-170 (c)
Compressive strength (MPa)	580	480	65-89	
Young's modulus of elasticity (GPa)	35	35	5-10	28-31
Hardness (HV)	340	230	40-100	240-370
Coef. of thermal expansion $20 - 200 \text{ }^\circ\text{C}$, $\text{m m}^{-1} \text{ K}^{-1} \times 10^{-6}$	3.5	2.6	3.2-5.7	0 (ab) 15-25 (c)
Thermal conductivity ($\text{W m}^{-1} \text{ K}^{-1}$)	4.6	6.3	31-159	1-3 (c) 190-390 (ab)

* These graphites have a high degree of crystallite alignment and their properties tend to be anisotropic.

The chemical properties of vitreous carbons are usually similar to those of the graphite crystal. Its resistance to chemical attack is normally very good and is one of its outstanding characteristics. This is attributed to its low permeability, negligible porosity and a low specific surface [66]. Vitreous carbon does not react with nitric, sulphuric, hydrofluoric and chromic acids, and it is not attacked by halogens such as bromine even at high temperatures. As an example, the chemical inertness and good

electrical conductivity of vitreous carbon makes it a suitable material for acid-battery electrodes [67, 68].

1.3.3 Summary

In conclusion, considering the carbon precursors with high yield, polymers are better precursors in terms of processing. Processing high carbon yield hydrocarbons such as pitches and coals are time consuming and their carbonisation requires pressure to achieve a high carbon yield. Moreover, these precursors usually need some modifications before carbonisation. Among polymers, thermosetting polymers usually are used for preparation of porous carbon monoliths as they don't go through a liquid phase during the carbonisation and can keep the shape. Polyfurfuryl alcohol and phenolic polymers are the two most common used precursors in production of carbon monoliths. This is due to their fairly high carbon yield. Polyfurfuryl alcohol loses less volatile during curing and carbonisation compare to phenolic resins. This induce a more dense final carbonised material and thus with higher mechanical strength and lower electrical resistivity than the one obtained from phenolic resins [69]. However, more functionalised phenolic resins may often be the possibility of making carbons with better properties (mechanical, electrical, *etc.*), but designing of a suitable raw monomer is time consuming and expensive. Carbonisation of polymeric precursors results in a non-graphitisable carbon. Hence, some strategies need to be developed to facilitate graphitisation.

1.4 Formation of Porous Carbons

In order to achieve high current yield in a biofuel cell, its electrode needs to have a high surface area as well as high electrical conductivity. Electrodes with large surface areas lead to high enzyme loading and high diffusion of reactants and products and therefore high efficiency. Thus, synthesis of stable monolithic carbons with high surface area and adjustable structure and properties are of great interest. Porous carbons can be made by several methods, *e.g.* foaming and templating methods. These methods produce porous structures with different pore size ranges and each has its pros and cons. For example, templating method produce porous carbons with more

homogeneous pore sizes compared to the foaming method. However, the templating method can be more difficult to apply for production of carbons in large-scales.

It is usually hard to give a consistent classification of porous structure in solid materials. They can be classified based on pore origin, structure, size and accessibility to surroundings [70]. Fig. 1-14 shows a schematic of pore classification regarding their accessibility to surroundings. The pores that have access to the external surface are named open pores, like the (b), (c), (d), (e) and (f) pores shown in Fig. 1-14. They are accessible for molecules or ions in the surroundings. Some may be open only at one end such as (b) and (f); they are described as blind pores. Others may be open at two ends like (e).

Closed pores (a) are caused by insufficient evolution of gaseous substances. They do not affect the adsorption and permeability of molecules, but they influence the mechanical properties of solid materials [71].

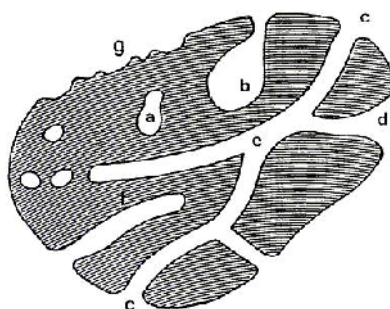


Fig. 1-14: Schematic pore classification according to their access to surrounding [71].

Another classification of pores in porous solids is with respect to their pore sizes. The pore size is a major property in practical applications of porous materials. According to the International Union of Pure and Applied Chemistry (IUPAC), porous carbon materials can be classified into three categories based on their pore sizes [72, 73]: microporous < 2 nm; mesoporous 2 nm $<$ 50 nm; and macroporous > 50 nm.

Regarding methods to produce porous carbons, foaming or template methods can be used. These methods are further discussed below.

1.4.1 Foaming Method

Carbon foams can be produced from different precursors of polymers and pitches. Carbon foams from polymer precursors can be prepared by polymerisation of a resin combined with foaming agents followed by carbonisation [74-76]. Classically, polyurethane and phenolic resins have been used as foaming agents. The resulting carbon foam is a reticulated vitreous carbon (RVC). The structure of RVC is shown in Fig. 1-15.

Important process variables in carbonisation of a resin include the concentration of the resin, the type of solvent, the solution viscosity and the carbonisation temperature and rate. The foam is typically carbonised at 700–1100 °C, however, it has been shown that the minimum electrical resistivity is achieved at carbonisation temperatures of 900 °C and above [69]. This is correlated to the fact that at lower carbonisation temperatures the energy for elimination of carbon-carbon bonds and oxygen functional groups are insufficient. During the production of RVC, a linear shrinkage of approximately 30% occurs [77].

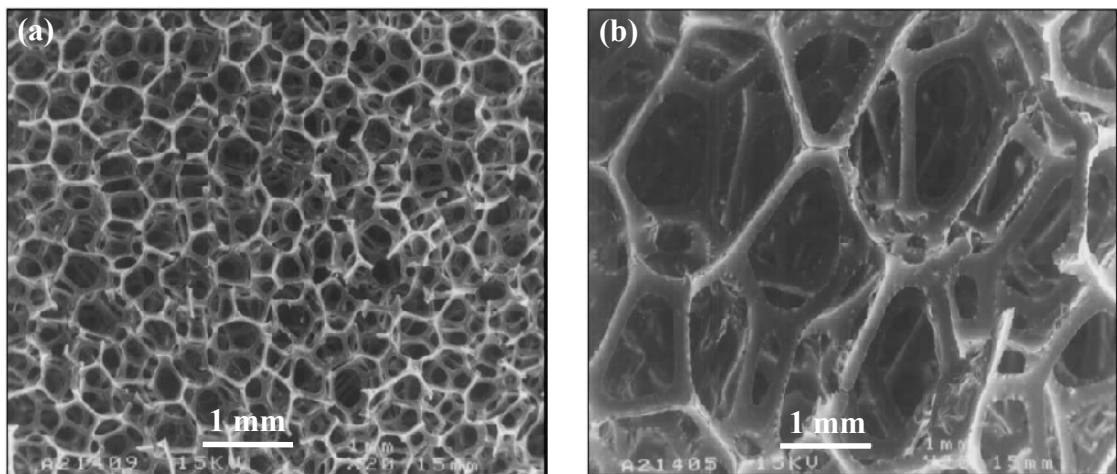


Fig. 1-15: SEM micrographs of (a) 100 and (b) 30 ppi, nominal pores per linear inch, RVC [78].

Vitreous carbon foams are produced in several pore sizes. Table 1-3 shows properties of vitreous carbon foam with 97% pore volume. These foams have low density with relatively even pore distribution and moderate mechanical strength of 0.07-3.4 MPa. The electrical conductivity of the strut is 200 S cm⁻¹ [63].

Table 1-3: Properties of a vitreous carbon foam with 97% pore volume [63].

Bulk void volume (%)	97
Bulk density (g cm ⁻³)	0.05
Strut density (g cm ⁻³)	1.49
Strut resistivity (10 ⁻⁴ Ω cm)	50
Crushing strength (MPa) (Function of pore size)	0.07-3.4
Surface area (m ² g ⁻¹)	1.62

Vitreous carbon foams are chemically inert with a wide range of usable potentials (1.2 to -1.0 V vs. SCE¹). Therefore, they can be used as electrodes for lithium-ion and other types of batteries as well as for general electrochemistry [78, 79].

Carbon foams have also been produced using synthetic pitch, such as Mitsubishi AR mesophase pitch [80-84]. The foaming process involves controlled heating of the precursors under pressure in an inert atmosphere. During heating, the evolving gases act as bubble agents to create pores in the precursor material while the volume of foaming precursor increases. The resultant foam can attain a high degree of graphitisation and accordingly has very good thermal and electrical conductivities, which is a good candidate for electrodes and thermal management. The properties of carbon foam derived from pitch precursors can be controlled by adjusting the thermoplastic behaviour of precursors and the foaming conditions. The resultant carbon foam could be either a strong structural material or a highly thermal/electrical conductive material. Moreover, either open or close cell structures are possible.

Comparing the foaming methods from polymer and pitch precursors, it can be concluded that in the foaming method using pitch precursors no foaming agent or stabilisation step is required. This simplifies the foaming process. However, the foaming process requires pressure to control the evolving gases which makes the process more complicated compared with the method from polymer precursors.

¹ SCE or the Saturated Calomel Electrode is a reference electrode based on the reaction between mercury metal and mercury (I) chloride (Hg₂Cl₂, “calomel”).

1.4.2 Templating Method

Templating method is a practical approach for preparation of well structured porous carbons with pore sizes ranging from micropores (< 2 nm) [85], to mesopores (2-50 nm) [86] and macropores (> 50 nm) [87]. This method involves synthesis of a template and impregnation of the template with a carbon precursor followed by carbonisation of the precursor and ultimately, leaching of the template [88]. According to the required pore size, different inorganic templates have been used for making porous carbon materials. Some of these templates and the processing methods for producing micro-, meso- and macro-porous carbons are summarised in this section.

In order to make high surface area microporous carbon materials, zeolites can be used as inorganic templates [88-92]. Zeolites are crystalline aluminosilicates having ordered and uniform micropores. Their pore sizes are in the range of 0.3-1.0 nm, depending on the type of zeolite and its preparation method [93]. As the walls of zeolites have a uniform thickness of < 1 nm, zeolites are used as templates for the preparation of microporous carbons with uniform pore sizes. Fig. 1-16 shows the overall template method for producing microporous carbons using a zeolite Y template. A carbon precursor is impregnated into the pores and channels of the zeolite and then is carbonised. After removal of the zeolite template, a microporous carbon structure is produced. In order to avoid collapse of the carbon framework during the template removal and obtaining microporous carbons with structural regularity of the zeolite, the pores in the zeolite templates should be sufficiently large, *i.e.* > 0.6 - 0.7 nm [85], as well as the channels and pores of the zeolite templates should be completely filled with the precursor, for example by a two-step carbonisation method [94].

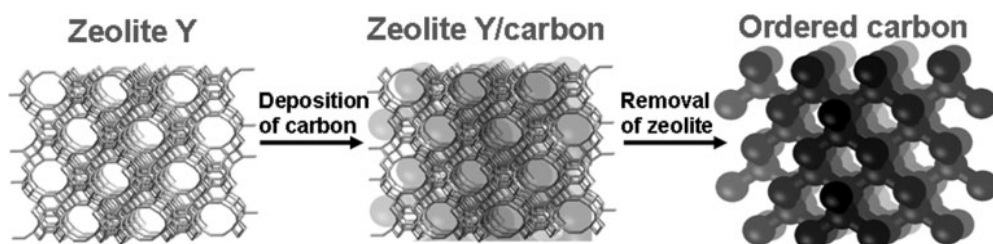


Fig. 1-16: Schematic of the overall template synthetic procedure for microporous carbons using a zeolite Y template [13].

Ordered mesoporous carbon materials have been synthesised using mesostructured silica templates. For example, Ryoo *et al.* [95] report the synthesis of ordered carbon molecular sieves by carbonisation of sucrose inside the mesopores of a MCM-48² aluminosilicate template. Fig. 1-17 shows the general template strategy used for the synthesis of ordered mesoporous carbon materials by means of mesoporous silica templates. The carbonisation of phenolic resin inside the pores of a MCM-48 template, followed by the dissolution of the aluminosilicate template, produce an ordered mesoporous carbon of 2 nm sized pores separated by 2 nm thick carbon walls [95, 96].

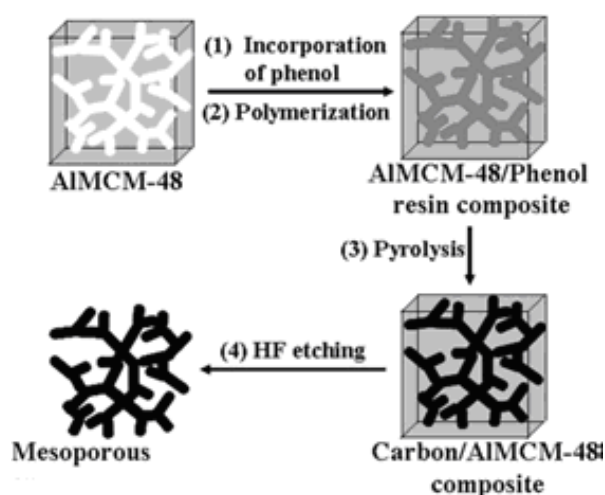


Fig. 1-17: Schematic representation of the formation of an ordered mesoporous carbon using a mesoporous silica template [95].

Another example of synthesising ordered mesoporous carbon is the use of ordered mesoporous silica molecular sieve SBA-15 as templates [97-99]. The SBA-15 silica is made of a hexagonal array of nanotubes, with a uniform diameter, connected through micropores inside the walls of the main channel. The resulting mesoporous carbon from the SBA-15 template, contains cylindrical pores of 5.9 nm diameters and pores between the adjacent cylinders of 4.2 nm [100].

In the group of mesostructured silica templates, MCM-41 silica with a hexagonally ordered structure is found to be unsuitable for synthesis of ordered mesoporous carbon as its application results in a disordered high surface area microporous carbon

² MCM-48 is a silicate framework with a unique cubic arrangement of three-dimensional interconnected mesopores.

[101, 102]. For applications such as enzyme immobilisation MCM-type materials are successful in hosting only small enzymes due to their small pore sizes (see Table 1-4). The developments of SBA-15 and mesocellular foams (MCF) have solved this problem with MCM-type materials [99], and have made these mesoporous materials more suitable for enzyme immobilisation. However, using mesoporous silica as a template has some drawbacks. The process is expensive, time consuming, unsuitable for large-scale production and industrial applications.

Table 1-4: Pore size of some mesoporous silica structures [13].

Mesoporous Silica	Pore Size
MCM-41 & MCM-48	2-4 nm
SBA-15	5-13 nm
MCF	15-40 nm

Another type of templates for preparation of porous carbons is colloidal crystals. These can be assembled from a variety of colloidal particles, including silica spheres and polymer latex spheres in the size range of tens of nanometers to micrometers. To produce porous carbons from these templates, monodispersity of the spheres is required to form ordered close-packed arrays. Moreover, they must be compatible with all processing conditions and should be wettable by the precursors for the framework and eventually they must be removable under conditions that do not destroy the carbon framework. For these reasons, silica and polymer spheres have, so far, been used to template periodic porous carbons [103].

Colloidal silica spheres have been extensively used as templates to synthesise porous carbons. In a typical process, a carbon precursor is impregnated into the interstitial space of the colloidal silica aggregates and carbonised. Before the infiltration of the carbon precursor, the silica particles may be “sintered” to create necks between the particles. This leads to interconnections between the spherical pores in the resulting carbons. For example, spherical submicrometer-sized silica particles have been used as templates for the synthesis of macroporous carbon materials, see Fig. 1-18. The

pore size of the resulting macroporous carbons can be controlled by varying the particle size of the silica spheres.

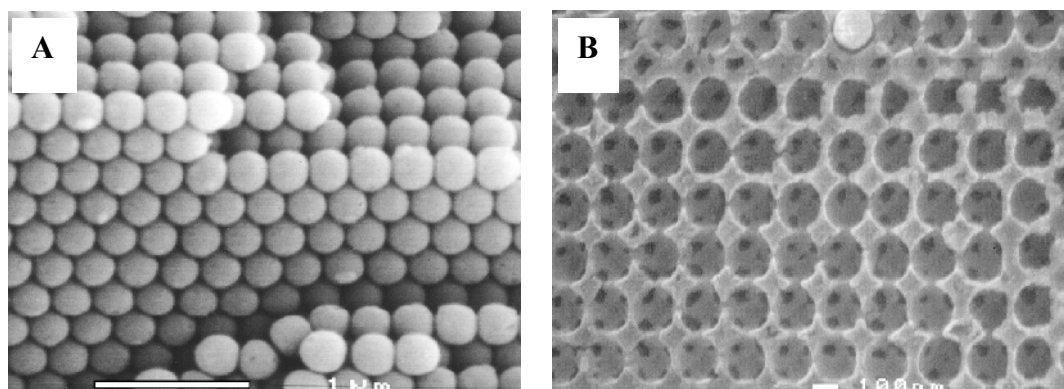


Fig. 1-18: A) SEM of a porous SiO₂ opal. B) SEM of a fracture surface of a graphitic carbon inverse opal based on 200 nm hollow spheres [87].

The colloidal silica templates can be prepared inexpensively on large-scales (scales of hundreds of grams). Therefore, this is a practicable route for production of bulk porous carbon materials [104]. However, removal of the silica templates requires treatment with a strong and toxic acid such as HF, which is a drawback of using this material as a template [13].

In order to facilitate the removal of the template, polymer spheres can be used instead of silica. When polymer beads are used as template, they can be easily burnt out during the carbonisation process and this obviously simplify the preparation of porous carbons with ordered pore size distribution. In order to infiltrate a precursor into the template without destroying its structure it is necessary to make a stable colloidal crystal structure. To achieve this, the colloidal crystal aggregates can be annealed at a temperature slightly higher than the glass transition temperature (T_g) of the polymer [105]. Removal of the latex is carried out by calcination (> 350 °C, depending on the wall composition) or by extraction with a suitable solvent (tetrahydrofuran (THF)/acetone or toluene) [103]. Therefore, the removal of the template is easier with latex spheres than silica spheres. However, the shrinkage of structure by removing a polymer template is much higher than removing a silica template.

Surfactant templates can also be used for fabrication of mesoporous carbons. Pore sizes of porous carbons produced from the surfactant templating method varies from

0.5 to > 60 nm [106, 107]. Fig. 1-19 shows the synthetic procedure of porous carbons using a surfactant template, cetyltrimethylammonium bromide (CTAB). The assembly of ionic surfactants, such as cationic quaternary ammonium, and polymer precursors through the electrostatic interaction mainly results in disordered mesostructures. This is due to the uncontrolled polymerisation of organic precursors and the weak interaction between the organic polymer frameworks and amphiphilic cationic surfactants [108]. The charge density of the ionic surfactants is not large enough to attract the carbon precursor, such as phenolic resins, and this result in the reduction of miscibility between organic frameworks and surfactants after polymerisation and therefore macroscopic phase separation.

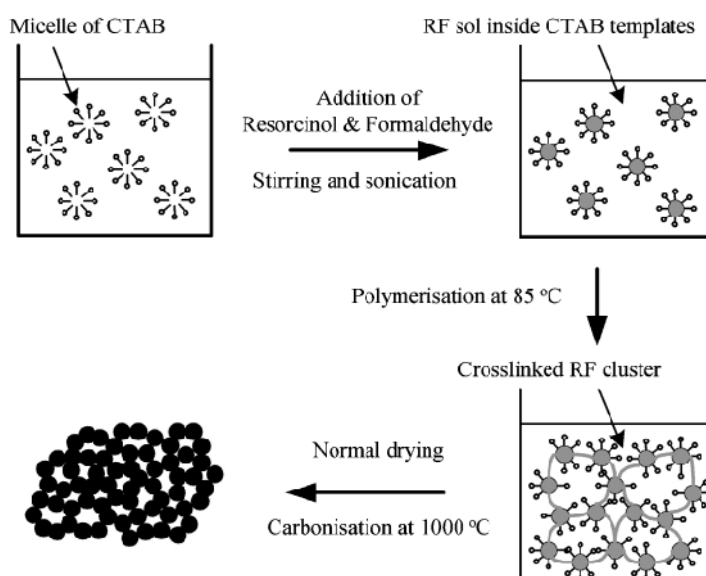


Fig. 1-19: Schematic of the synthetic of porous carbons using surfactant templates [107].

Another effective route to prepare mesoporous carbons can be the block copolymer templating method, using hydrogen-bonding interactions between the template and the precursor [99, 109]. For instance, highly ordered mesoporous carbons, with pore sizes in the range of 3.9-7 nm, have been synthesised in a system of phenolic resols as precursors and PEO-containing block copolymers as templates [110, 111]. The precursors have lots of hydroxyl and benzyl groups that can form strong hydrogen-bonding interactions with amphiphilic block copolymers. Self-assembly of block copolymers produce the highly ordered mesostructure and curing the polymer makes

the framework. The templates are removed by calcination at 350 °C and mesoporous polymers are obtained which after carbonisation transform to mesoporous carbon structures.

The structures of porous carbon monoliths prepared by, for example, block copolymers as templates have some macro-cracks due to the large shrinkage. This decreases the mechanical strength of the monoliths prepared by the template method. However, no mechanical strength values for porous carbon structures prepared by the template methods have been reported. In terms of electrical conductivity, for mesoporous carbon monoliths derived from templates of silica SBA-15 powder with hexagonal mesostructure, electrical conductivity of 1.37 S cm⁻¹ has been reported [112] and for ordered mesoporous carbon monolith synthesised from silica monolith, conductivity of 0.43 S cm⁻¹ has been reported [113]. The difference in the conductivities is because the rope-like carbon particles in the mesoporous carbon derived from the SBA-15 powder are connected to each other, while the rope-like carbon particles in the mesoporous carbon derived from the silica monolith are mostly isolated.

1.4.3 Physical Properties of Porous Carbons

Several physical properties of porous carbon electrodes are of particular interest for biofuel cell applications, *i.e.* relative density, electrical conductivity and mechanical strength. These properties are further explained in the following sections.

1.4.3.1 Relative Density

Relative density is one of the important physical properties of carbon foams, as mechanical strength and electrical conductivity of the porous carbon materials are related to this property. Relative density (ρ^*/ρ_s) is defined as the density of the porous material, ρ^* , divided by that of the solid from which the cell walls are made, ρ_s . As the relative density increases, the cell walls become thicker and the pores shrink. Gibson and Ashby [114] have indicated that above the relative density of about 0.3, a porous structure transforms to a solid containing isolated pores. According to Table 1-

3, the relative density of reticulated vitreous carbon (RVC) with pore volume of 97% is 0.034. Decreasing the pore volume will lead to a porous carbon with higher bulk density and therefore a higher relative density. The strut density depends on the type of carbon produced, *e.g.* density of glassy carbon is 1.54 g cm⁻³, whereas, density of moulded graphite is 1.90 g cm⁻³. Moreover, microporosity in the carbon framework affects the strut density of porous carbons.

1.4.3.2 Electrical Conductivity

Electrical conductivity is an inverse of electrical resistivity. Electrical resistivity is a measure of how strongly a material opposes the flow of electric current. A low resistivity (R) indicates a material that readily allows the movement of electrical charge. When a conducting material is foamed, its resistivity increases. The electrical resistivity of porous materials (R*) can be described by equation 1-2 [9]:

$$R^* \propto \frac{R_s}{(\rho^*/\rho_s)} \quad (1-2)$$

Where R_s is the resistivity of the solid and ρ*/ρ_s is the relative density of the porous material. The constant of proportionality reflects the reduction in conductivity due to the tortuosity of the path in the foam. As the density decreases, the average cross-section available for conduction decreases and the tortuosity of the current path increases, both of which increase the resistivity of the foam. The empirical data obtained by Mepura [115] for aluminium foams suggest that electrical resistivity of the conductive foams is described by:

$$R^* = R_s \left(\frac{\rho^*}{\rho_s} \right)^{-3/2} \quad (1-3)$$

In order to investigate the relationship between density and electrical conductivity of porous carbons, Jenkins and Kawamura [116] introduced porosity into the glassy carbon and formed materials with bulk densities of 0.8-1.5 g cm⁻³. Fig. 1-20 shows the relationship between the electrical conductivity and the bulk densities of these

porous carbons. Two linear regions can be seen from this plot. At densities above 1.15 g cm⁻³, the pores are isolated and the conductivity vs. bulk density increases more rapidly than the densities below 1.15 g cm⁻³. By extrapolating this line, the conductivity of a graphite single crystal, with density of 2.26 g cm⁻³, is found to be 1000 S cm⁻¹, which is lower than the conductivity of randomly oriented graphite crystals (2000-4000 S cm⁻¹ along the basal plane). This indicates that the folds of polyaromatic ribbons in the glassy carbons can also affect the electrical conductivity.

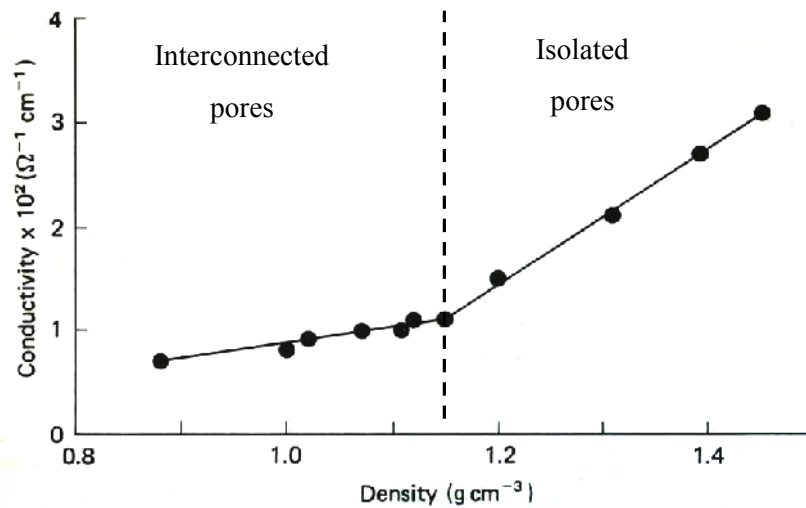


Fig. 1-20: Electrical conductivity of porous glassy carbons annealed at 2700 °C versus density [116].

1.4.3.3 Mechanical Strength

Studies of brittle porous materials have shown that the crushing strength of brittle foams is dependant on relative density (to the power of 3/2). Gibson and Ashby [8] described the crushing strength of brittle foams (by a model) as:

$$\frac{\sigma_f^*}{\sigma_f} = 0.2 \left(\frac{\rho^*}{\rho_s} \right)^{3/2} \quad (1-4)$$

Where σ_f^* is the crushing strength of the foam, ρ^*/ρ is the relative density and σ_f is the fracture strength of the solid material. The crushing strength of porous carbons decreases with increasing porosity. This is due to the decrease of relative density. For example, the compressive strength of carbon foams derived from coal precursors with porosity of 79 and 84% was found 9.9 and 2.9 MPa, respectively [46]. Thus, even

though high surface area carbon electrodes are needed to achieve high efficiency in biofuel cells, the high porosity will lower the mechanical strength of the electrodes and some strategies are needed to improve the mechanical strength.

1.4.4 Summary

Foaming and templating methods can be used to fabricate high surface area carbon electrodes. Comparing foaming and templating methods, it can be concluded that the template method can produce ordered porous carbon structures with homogeneous pore sizes, whereas foaming method is easier and cheaper to process and is more suitable for large-scale production. By using polymer precursors and foaming method, reticulated vitreous carbons are produced which are suitable to be used as electrodes in microbial fuel cells.

Polymer precursors are also used in the template method, which produces porous glassy carbon. Regarding the templates, the most common templates used for fabrication of meso- and macro-porous carbon structures are silica and polymers. Silica templates produce ordered porous carbon structures and the problem of shrinkage that usually exists by using polymer templates is eliminated by using silica templates. However, removal of the polymer templates from the structure is much easier than the silica templates as they can be removed during carbonisation, unlike silica that requires treatment with HF.

Mechanical strength and electrical conductivity of the porous carbon structures depend on their relative density and increase as the relative density increases.

1.5 Porous Carbon as an Electrode

Electrode behaviour during electron transfer and enzyme reaction is an important factor to be controlled. Practically, an electrode should be electrochemically inert to not interfere with the enzyme catalytic reactions, while insuring fast electron transfer. Moreover, it needs to possess appropriate surface chemistry for adequate enzyme/microbe immobilisation. Various electrochemical methods, in particular,

cyclic voltammetry are used to evaluate the electroactivity of carbon electrodes and their ability of transferring electrons and the effect of enzyme/microbe immobilisation. In the following, the basic principles of cyclic voltammetry and the properties of carbon electrodes, in particular, glassy carbon and pyrolytic graphite are summarised.

1.5.1 Basics of Electrochemistry

Cyclic voltammetry has been extensively used to characterise different types of carbon electrodes. In this method, a reference, a working and a counter (auxiliary) electrode are used and referred to as a three-electrode system [117]. The working electrode potential is ramped linearly vs. time and when it reaches a set potential, the working electrode's potential ramp is inverted. This inversion can happen multiple times during a single experiment (cyclic). The potential is measured between the reference electrode and the working electrode and the current is measured between the working electrode and counter electrode. This data is then plotted as current (i) vs. potential (E). As can be seen from Fig. 1-21, the current will increase as the potential reaches the reduction potential of the analyte, but then drops as the analyte is consumed close to the electrode surface. Oxidation peak usually have a similar shape to the reduction peak. Therefore, information about the redox potential and electrochemical reaction rates of the compounds is obtainable with this method.

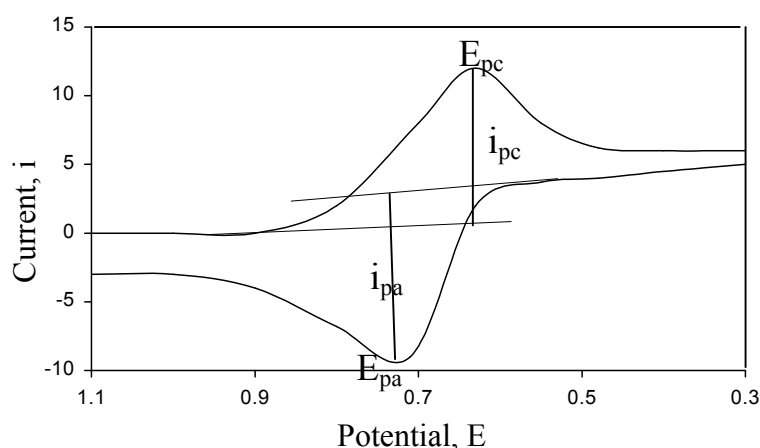


Fig. 1-21: A typical cyclic voltammogram [118], where “pc” is the cathodic peak (reduction peak) and “pa” is the anodic peak (oxidation peak).

Three forms of voltammograms are usually observed depending on the system investigated: reversible, irreversible and quasi-reversible. In a reversible system, the peak current density, I_p , (measured as shown in Fig. 1-21) is proportional to $v^{1/2}$ (scan rate) and a plot of I_p vs. $v^{1/2}$ is linear and passes through the origin. Moreover, the difference between the anodic and the cathodic peak potentials (ΔE_p) equals $59/n$ mV (where n is the number of electrons involved in the electrode reaction) and the peak potential is independent of the scan rate. The anodic and cathodic peak current densities are also equal [118]. In a reversible system, the electron transfer rates at all potentials are much higher than the rate of mass transport, whereas, in an irreversible system the rate of mass transport increases and becomes comparable to the rate of electron transfer. The most observable effect of this increase in the rate of mass transport is an increase in peak separation. The peak current density of an irreversible process is also lower than that of a reversible process. This is related to the shape of the peak as the concentration of reactants on the surface change more slowly with potential and the profile is less steep and the flux to the surface is lower than a reversible process. Furthermore, in the case of an irreversible system, the peak potential varies with the scan rate [119].

In some cases, a process that is reversible at low scan rates becomes irreversible at high scan rates. This happens after passing through a region known as quasi-reversible. The criteria for a quasi-reversible system are: I_p increases with $v^{1/2}$ but does not maintain the proportionality, ΔE_p is larger than $59/n$ mV and increases with increasing v , and the cathodic peak potential (E_{pc}) shifts to negative values with increasing v [118].

In the cyclic voltammetry profile, the peak current intensity can be used to evaluate the specific electrochemical surface area of a porous electrode by equation 1-5 [120]:

$$S_s = \frac{I_{pa}}{2.69 \times 10^5 C_0 V_{el} \sqrt{D_0 v}} \quad (1-5)$$

where, S_s is the specific surface area ($\text{cm}^2 \text{cm}^{-3}$); I_{pa} is the anodic peak current intensity (A); C_0 is the oxidant or reductor concentration (mol cm^{-3}), V_{el} is the electrode

volume immersed in solution (cm^3), D_0 is the oxidant or reductor diffusivity in solution ($\text{cm}^2 \text{s}^{-1}$) and v is the scanning rate (V s^{-1}).

The electrochemical response is also dependant on the surface chemistry of the electrode and the double layer at the electrode surface. Fig. 1-22 illustrates a schematic model of the double layer region. The theory of the electrical double layer is referring to the charge distribution and electrical potentials that are caused by this charge separation [121].

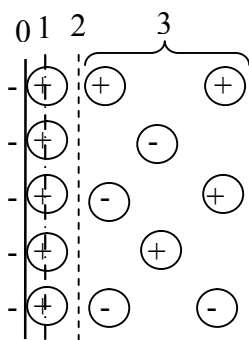


Fig. 1-22: Schematic model of the double-layer region. 0 is electrode-electrolyte interface, 1 is IHP (inner Helmholtz plane), 2 is OHP (outer Helmholtz plane) and 3 is the diffusive layer [121, 122].

The inner and outer Helmholtz planes are defined by Grahame [123] as the locus of the electrical centres of a layer of adsorbed ions and the locus of the electrical centres of the solvated ions, respectively. The electrical potential of the inner and outer Helmholtz planes are different from that of the bulk of the solution. When electrode reactions involve very low concentrations of electroactive species, the charging current can be much larger than the Faradaic current for the reduction or oxidation reaction hence the existence of the double layer capacitance or the presence of a charging current in electrochemical experiments should be taken into account. For instance, at a given potential the double layer capacitance of a metal electrode is usually in the range of $10\text{-}40 \mu\text{F cm}^{-2}$ [122] depending on the potential scan rate and the double layer capacitance of a carbon electrode in a neutral solution is in the range of $8\text{-}12 \mu\text{F cm}^{-2}$ [124].

Double-layer capacitance of porous carbon electrodes can be determined by cyclic voltammetry, using equation 1-6 [14]:

$$C_d = \frac{i_c}{\nu} \quad (1-6)$$

where, C_d is the double layer capacitance, i_c is a differential capacitance current and ν is the potential scan rate. The true double-layer capacitance for porous carbon electrodes is calculated by dividing the apparent capacitance by the BET surface area³ of the porous carbon, assuming all the area of the internal structure of the porous carbon is wetted by electrolyte. Therefore, equation 1-6 can be rewritten for a porous electrode as [125]:

$$C_d = \frac{i_c}{A \times \nu} \quad (1-7)$$

where, A is the BET surface area. For instance, the double layer capacitance of a high surface area ($> 600 \text{ m}^2 \text{ g}^{-1}$) carbon electrode is $20 \text{ } \mu\text{F cm}^{-2}$ at 5 mV s^{-1} , if all the pores are accessible to the electrolyte [126] and if it contains micropores that are not accessible to the electrolyte, the double layer capacitance decreases to about $10 \text{ } \mu\text{F cm}^{-2}$.

Moreover, the electrode reaction rate or current depends on the rates of processes such as mass transfer of species from the bulk solution to the electrode surface, electron transfer at the electrode surface and other surface reactions such as adsorption or desorption (Fig. 1-23). The rate of the electrode reaction usually is controlled by the rate of one of these steps which is the slowest, this rate is called the rate-determining step (RDS) [127]. This can be a heterogeneous electron transfer reaction or the diffusion of the species from the bulk solution to the electrode surface. Obviously, the structure of the double layer and adsorbate at the electrode surface will affect the kinetics.

³ Section C.3 of Appendix C gives details of the BET technique for measuring surface area of a material.

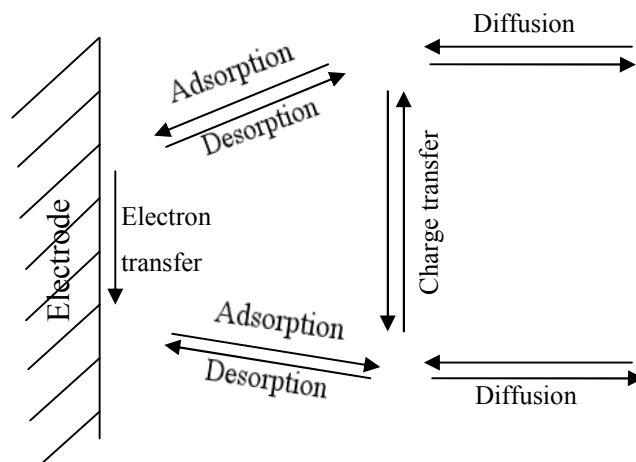


Fig. 1-23: Schematic of electron transfer at an electrode surface [128].

The kinetic behavior of an electrode can be evaluated by determining the standard rate constant for electron transfer. Cyclic voltammetry can be used to measure the heterogeneous rate constant, k_0 , (cm s^{-1}) at the electrode [129]. The difference between the anodic and cathodic peak potentials (ΔE_p) is used to calculate k_0 (for a quasi-reversible system) according to the equation 1-8 [130]:

$$K_0 = \Lambda(D(nF / RT)v)^{1/2} \quad (1-8)$$

where, Λ is a parameter associated with the peak shape and is a quantitative measure of reversibility:

$$\Lambda = \Psi \pi^{1/2} \quad (1-9)$$

where, Ψ is the degree of reversibility and can be obtained from numerical data according to the ΔE_p [130]. D is the diffusion coefficient of the electroactive species ($\text{cm}^2 \text{s}^{-1}$), n is the number of electrons transferred, F is the Faraday constant (C mol^{-1}), R is the gas constant ($\text{J K}^{-1} \text{mol}^{-1}$), T is the temperature (K) and v is the scan rate (V s^{-1}).

If the heterogeneous electron transfer rate at the electrode surface is fast and the rate-determining step is the diffusion of species to the electrode surface, then in the

voltammogram the current peak will be proportional to the square root of the scan rate [118].

1.5.2 Electrochemical Properties of Carbon

As biofuel cells operate under mild conditions; room temperature and neutral pH, the electrochemical properties of carbon is considered in these conditions in this section. Thermodynamic data on the electrochemical stability of carbon in aqueous solutions are usually proposed in the form of potential-pH diagrams. Randin [131] showed potential-pH diagrams of a solid (graphite) and dissolved species such as H_2CO_3 , CH_3OH , HCHO , HCOOH , CH_4 CO and CO_2 . It was found that the two main reactions concerning the electrochemical oxidation of carbon in aqueous solutions are:



and



Reactions 1-10 and 1-11 have standard electrode potentials (*vs.* SHE^4) of 0.207 and 0.518 V at 25 °C, respectively. Carbon monoxide is thermodynamically unstable compare to CO_2 . The CO- CO_2 reaction (1-12) has a standard electrochemical potential of -0.103 V.



As the 1-10 and 1-11 reactions are highly irreversible [14], it can be concluded that carbon has a reasonable corrosion stability in aqueous systems. Glassy carbon electrodes have a wide working potential range of 1 to -2.5 V (*vs.* SCE) in aqueous solutions depending on the pH. For example, electrochemical window of glassy carbon in 1 M NaOH is 0.5 to -1.6 V (*vs.* SCE) [132]. Moreover, pyrolytic graphite, which is the main material used for enzyme electrochemistry, has an electrochemical window of 0.68 to -0.34 V (*vs.* SCE) in 0.1 M NaOH [133].

⁴ Standard hydrogen electrode (SHE) is a reference electrode.

Ferri-/ferro-cyanide is usually used as a probe to determine the electrode surface activity. For example, an untreated glassy carbon, in 1 mM $\text{Fe}(\text{CN})_6^{3-}$ and electrolyte of 1 M KCl, has a separation of cathodic and anodic peak potential (ΔE_p) of 300 mV at scan rate of 1 V s^{-1} . This indicates that the electrode shows slow charge transfer kinetics or it is deactivated [134]. The deactivation of the electrodes is often due to the prolonged exposure to the atmosphere or to a working solution. It is possible to activate the electrode surface by different methods such as polishing, chemical oxidations and heating at low pressures [135-137]. For instance for the electrode mentioned above, it was observed that the ΔE_p decreased to 75 mV after a vacuum heat treatment.

Reticulated vitreous carbon (RVC) is also inert like solid glassy carbon and it has usable potential range of 1.2 to -1 V (vs. SCE) at pH 7 [138]. The voltammetric studies showed that the behaviour of RVC electrodes is quasi-reversible and ΔE_p in 1 mM ferricyanide/0.1 M KCl and at scan rate of 50 mV s^{-1} is 200 mV [69].

1.5.3 Summary

Carbon is a suitable material as an electrode because it is inert to a wide range of reactive chemicals and it has a reasonable electric conductivity. RVC has a wide electrochemical window and a quasi-reversible behaviour. Carbon electrodes usually require some surface modifications to activate their surface and improve their electrochemical reversibility. This can be done for example by heating the electrode under reduced pressure.

1.6 How to Reach the Ideal Properties?

Ideally porous carbon electrodes for biofuel cell applications must have “high” mechanical strength, “high” electrical conductivity and high porosity for enzyme/microbe immobilisation. From the reported data in the literature, as summarised in previous sections, it is not possible to raise all these properties simultaneously because a high porosity leads to a low mechanical strength and low

electrical conductivity. However, some strategies can be derived to balance these properties.

1.6.1 Mechanical Strength

The porous carbon electrodes need to have sufficient strength for handling. For instance, electrodes to be used in biofuel cells should withstand fluid flow. A disadvantage of the foaming method for production of macroporous carbons is that the struts of the reticulated structure often have some cracks which are formed during the pyrolysis of the polymeric template. These strut flaws reduce the final mechanical strength of the porous carbon to levels lower than the strength theoretically predicted for open cell structures [139].

Many efforts have been made to overcome this defect by, for example, performing a second impregnation step to fill the cracks in the struts and increase the density of the foams [140-142], introducing fibres to reinforce the materials structure [143-145] and controlling the sintering temperature of the foams [146]. Sintering temperature affects the microstructure and porosity of the foams and ultimately the strength of the foams. In fibre reinforcement method, the reinforcement phase need to possess superior strength than the matrix otherwise no strength improvement would be achieved. Moreover, short fibres (typically a few tens of μm long) are easier to use and can often be used with conventional systems. Whereas, long continuous fibres usually align in one direction and result in anisotropic properties and special fabrication methods should be adopted when using these fibres. In addition, the coefficient of thermal expansion (CTE) of the fibres and the matrix should match each other. Wang *et al.* [147] have shown the improvement of mechanical properties of carbon foams by adding chopped carbon fibres to carbon-foam preforms. It was observed that the mechanical strength of the carbon foam is improved from 25 to 42 MPa by addition of 3 wt% of carbon fibre (3 mm in length and 7.2 μm in diameter). Addition of fibres to carbon-foam preforms results in the reduction of the brittleness and thus improvement of the density of the foams from 1.38 to 1.45 g cm^{-3} . However, addition of more than 3 wt% fibre to the foams created some micro-cracks because of CTE mismatch between the fibres and the foams.

The effect of sintering temperature on mechanical strength of carbon foams has not been reported. In addition, the effect of successive impregnations for the carbon foams reinforced with carbon fibre can also be examined.

1.6.2 Electrical Conductivity

Electrical conductivity is an important factor for electrodes as it can limit charge transfer at the electrode/enzyme interface and hence the efficiency of the biofuel cells. For graphitisable carbon precursors, electrical conductivity can be improved by graphitising the carbon structure at high temperatures after carbonisation [148]. For example, graphitic mesoporous carbon was synthesised by means of poly-vinyl chloride (PVC) as a carbon precursor. It has been observed that the carbon obtained from carbonisation of PVC presented a conductivity of 0.3 S cm^{-1} , while after heat treatment of the carbon to $2300 \text{ }^\circ\text{C}$, the conductivity increased to 4.2 S cm^{-1} [149]. This increase in conductivity was the result of a high degree of graphitisation obtained from heat treatment of carbon at the high temperature. When using a non-graphitisable carbon precursor, the improvement of conductivity has been reported to be not possible by heat treating at high temperatures and other methods have been used to graphitise the carbon structure which are explained below.

Catalytic graphitisation can be used to improve the crystallinity of carbon by the formation of a graphitic material. This process involves a chemical reaction between the ungraphitised carbon and a metal or inorganic compound which represents the graphitisation catalyst [150]. Graphitisation, in general, is a thermally activated process, involving self-diffusion by which structural defects are removed. Several possible ways of assisting the transformation exist, *e.g.* plastic deformation, high pressure and chemical methods. For non-graphitising carbons, a complete reorganisation is required which can be produced by solution and precipitation using solid or liquid solvents and by compound formation and decomposition. Most of the graphitisation catalysts operate by one or more of these basic mechanisms [151].

It is well known that the artificial resins with a three dimensionally cross-linked structure such as divinyl benzene polymer or polyfurfuryl alcohol produce non-

graphitising carbon. Carbons produced from such resins undergo rapid graphitisation when they are heated with an addition of a small amount of various kinds of metallic compounds, such as Fe_2O_3 [152, 153]. Extents of catalytic graphitisation of non-graphitising carbons are dependant on three factors: heat treatment temperature, soak time and the catalyst type [154, 155].

There are different methods of forming graphitic carbon by means of catalytic graphitisation. One method is to impregnate the carbonaceous material with metallic salts, which is then heat treated under an inert atmosphere. The salt decomposes to the corresponding metallic oxides during heat treatment and the carbon reduces the oxides to elemental metal (*e.g.* Ni, Fe). Eventually, at temperatures above 800 °C, the metal or oxide nanoparticles contained within the carbon matrix act as catalysts for the conversion of amorphous carbon into more ordered carbon (graphitic) [156].

Structure and properties of catalytically graphitised carbon can be characterised by the relative levels of the so-called G-component, T_s -component and T_n -component. The G-component occurs with all carbons when large particles (*e.g.* nickel particles of > 80 nm in diameter [157]) or appreciable quantity of catalysts is added (*e.g.* 10 wt% of boron [158]). T-component is formed when a non-graphitising carbon is heated with a finely-divided catalyst (*e.g.* nickel particles of 20 nm [157]). T-component has a turbostratic structure (Fig. 1-24) and is an intermediate between an ideal graphite and amorphous carbon [159]. Turbostratic carbons consist nano-scale graphite crystallites arranged parallel to one another with a random orientation [160].

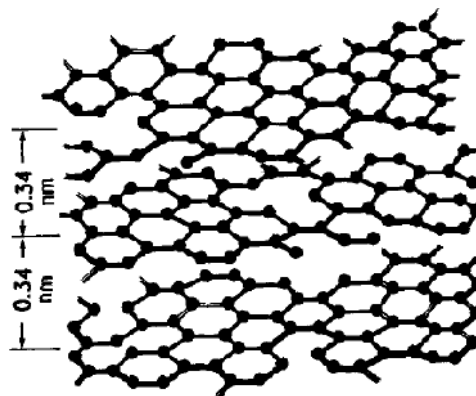


Fig. 1-24: Structure of turbostratic carbon [150].

Two mechanisms have been proposed for the formation of graphitised carbon G-component; one is the solution of carbon into the catalyst particle and precipitation as a graphite material such as when using nickel particles as catalyst [161, 162]. The other mechanism involves the formation and decomposition of carbide intermediates [150]. This mechanism was clearly observed using large particles of silica powder in the carbon precursor of phenolic resin [163]. The G-component has an interlayer (d_{002}) spacing of approximately 0.335 nm and a crystallite size of $L_c > 50$ nm. The X-ray diffraction (002) of such graphitised carbon shows a peak at $2\theta = 26.5^\circ$ [150].

In T_s -component, values of d_{002} and L_c , depending on the catalyst used, vary from 0.338 to 0.342 nm and from 6 to 20 nm, respectively. These are characterised by an X-ray peak at around $2\theta = 26^\circ$ using $\text{CuK}\alpha$. The structure of this material is turbostratic which means it does not have three-dimensionally ordered graphitic structure [150]. T_n -component shows two X-ray diffraction peaks at 26° (T_s -component) and 26.5° (G-component) [164, 165]. This structure has a d_{002} -spacing of 0.343 nm and L_c of 90 nm [166].

In terms of catalyst size, heating a non-graphitising carbon containing finely dispersed metal, results in turbostratic carbon (the T-component), whereas when the dispersion is less fine the resulting structure is three dimensional graphite (the G-component) [167-170]. In addition, with an increasing amount of catalyst in carbon, the extent of graphitisation of carbon increases. However, the formation of the turbostratic carbon (T-component) can be replaced by the G-component, resulting from the coalescence and growth of finely divided catalyst particles [150].

Oya and Otani [171] investigated the catalytic effects of 22 metals on both non-graphitising and graphitising carbons and found out that the majority of graphitisation catalysts had an atomic number of less than 40. Alloys and compounds as catalysts sometimes behave differently from constituent elements. The lower melting point of alloys contributes to lower graphitisation temperatures [172]. Numerous examples of catalytic graphitisation of non-porous glassy carbon can be found in the literature. Catalysts that have been used for graphitisation of carbon include nickel, boron, iron, manganese and cobalt. However, only few catalytic graphitisation of highly porous

carbons have been reported. For example, it has been reported that the electrical conductivity of porous carbon synthesised by silica (SBA-15) template and iron-impregnated polypyrrole (PPy) precursor is 37 times higher than porous carbon obtained from PFA precursor (0.003 S cm^{-1}) [173]. In addition, Sevilla and Fuertes [156] observed that nickel is a better catalyst for graphitisation than iron and manganese, as carbons catalysed by nickel showed greater crystallinity and higher conductivity than the carbon catalysed by the other two catalysts. Catalysing the carbon by nickel increased the conductivity from 0.19 to 19.5 S cm^{-1} , whereas using iron and manganese catalysts increased the conductivity of the carbon to 10.7 and 8.9 S cm^{-1} , respectively.

In catalytic graphitisation of carbon, it is better to remove the catalyst after the graphitisation. This is because the catalyst can decrease the strength of the carbon structure due to the inhomogeneity of the structure. In addition, for electrochemical investigation it is better to have only carbon to avoid the effect of metal particles in the electrochemical behaviour of the electrode. It has been reported that catalytic graphitisation of glassy carbon with iron (by adding 3 wt% ferrocene dicarboxylic acid to FA prior to polymerisation) without removing the catalyst has decreased the tensile strength of carbon from 43 to 20 MPa [174]. This is due to the inhomogeneity caused by different compositions and also the graphitic domains in the carbon structure. This inhomogeneity may have caused localised internal strain that reduced the overall tensile strength of the material.

1.6.3 Surface Chemistry

Surface chemistry of carbon electrodes in biofuel cells usually needs some modifications for better enzyme attachments. For example, it has been observed that laccase molecules weakly adsorb on an unmodified pyrolytic graphite surface, but by modifying the electrode surface with anthracene-2-diazonium, some phenol-like groups were introduced on the surface and high surface coverage and stability of the enzymes were achieved [175]. Moreover, modification of glassy carbon electrodes using electrochemical reduction of aryldiazonium salts, generated *in situ* from the corresponding arylamine, introduced carboxylic acid functional groups on the surface.

Subsequently, glucose oxidase (GO_x) was covalently grafted on the surface and it was observed that the modified electrode was catalytically active even after 6 weeks, whereas, the unmodified electrode lost its activity just after 1 week [176].

Generally, the surface chemistry of carbon materials is determined by the amount and type of oxygen surface complexes. These complexes can be introduced on carbons by different methods, including oxidising agents and electrochemical pretreatment. These treatments fix a certain amount of oxygen surface complexes such as carboxyls, lactones, phenols, ketones, quinines, alcohols and ethers on the carbon surfaces (Fig. 1-3) [177].

Oxidation in a gas or a liquid phase can be used to increase the concentration of surface oxygen groups, whereas heating under an inert atmosphere can be used to selectively remove some of these oxygen groups [178]. Different oxidising agents can be used to introduce oxygen surface complexes. The behaviour of these agents is not the same. For example, when activated carbon is oxidised with HNO_3 , H_2O_2 and $(\text{NH}_4)_2\text{S}_2\text{O}_8$, the highest total oxygen uptake is obtained with the HNO_3 solution, and the lowest with the $(\text{NH}_4)_2\text{S}_2\text{O}_8$ [179]. All the oxidising agents produced single C-O bonds, lactones, carboxyl, quinone or conjugated ketene and carboxyl-carbonate structures. However, the highest total acidity (mainly from carboxyl) was obtained using the HNO_3 and the lowest concentration of acidic functional groups, such as carboxyl, lactone and phenolic groups, was obtained after oxidation with the $(\text{NH}_4)_2\text{S}_2\text{O}_8$.

Oxidising gases such as N_2O may also be used to produce different oxygen groups. Generally, it has been shown that gas phase oxidation of activated carbons increases mainly the concentration of hydroxyl and carbonyl surface groups, while oxidation in the liquid phase increases the concentration of carboxyl groups [180, 181]. Moreover, liquid phase treatments usually have no significant affect on the texture of the carbon, while gas phase oxidation increases the micropores size and volume and also the mesopores surface area. Practically, gas phase oxidation is performed, for example, with 5% O_2 (in N_2) at around 400 °C, or with 50% N_2O (in N_2) at 500 °C. For highly oriented pyrolytic graphite (HOPG) and carbon fibres oxidised in air at 500-750 °C, it

has been observed that the electrochemical behaviour of carbons improved by introducing more edge plane sites on the carbon surfaces [182]. The functional groups on the electrode surface can also act as mediators of electrons between the electrode and the electroactive species [183] and hence increase the electron transfer rate.

In order to obtain reproducible electrochemical results, glassy carbon electrodes require some pretreatments to introduce specific functional groups on the surface. For instance, the pretreatment can be carried out by cycling the applied potential between +1.0 and -1.0 V (*vs.* SCE), for 10 min, and keeping at each potential for 1-2 min [79]. Engstrom and Strasser [184] also activated glassy carbon surface by applying +1.75 V (*vs.* SCE) for 5 min followed by -1.0 V (*vs.* SCE) for 1 min and observed enhancement in electrochemical activity, higher background current and better wettability. The types of oxygen groups obtained by electrochemical pretreatments on glassy carbon are not reported. However, for pyrolytic graphite it has been reported that lactone, carboxyl and quinone groups were introduced on the edge surface by electrochemical treatment [185].

Other electrode pretreatments, such as polishing or heat treatment, are also possible to enhance the electrode's activity. For glassy carbon electrode, the activity depends on the method of pretreatment, the type of material used to activate the surface and the amount and type of oxygen on the surface. For example, it has been observed that the amount of oxygen on electrochemically treated glassy carbon surface is greater than that at a polished surface. However, the activity of the polished electrode is higher than the electrochemically treated electrode [186]. In the case of high surface area porous carbon electrodes, it is not possible to use the polishing pretreatment method therefore other methods need to be considered. Depending on the required oxygen functional groups on the electrode surface for enzyme attachment, a suitable pretreatment method can be selected. For example, as many enzymes have been directly adsorbed on the edge surface of pyrolytic graphite, it can be concluded that the types of oxygen groups exist on the edge surface of pyrolytic graphite need to be introduced on the glassy carbon electrodes for better enzyme attachment. For this purpose, treating the porous glassy carbon electrodes with oxidising agents would be

a good option as it would be possible to control the formation of the desirable types of oxygen groups on the electrode surface.

1.7 Objectives

The objective of this project is to produce a porous carbon electrode for hosting enzymes or microbes in a biofuel cell (see Appendix A for an account of the types of biofuel cells). Mesoporous materials have been used for enzyme immobilisation due to their controlled porosity and high surface area ($> 200 \text{ m}^2 \text{ g}^{-1}$) [187-190]. One of the most commonly used approaches in the immobilisation of enzymes into mesoporous materials is by adsorption. The stability of adsorbed enzymes in mesoporous materials depends on many factors, including surface chemistry and pore size of mesoporous materials. The pore size of a mesoporous material should be similar to or larger than that of enzymes for a successful enzyme adsorption and high stability of adsorbed enzymes [4, 187]. Large pore sizes in mesoporous materials result in poor enzyme stability due to the quick leach out of the adsorbed enzymes from the mesopores. In the particular case of a biofuel cell, the enzyme used at the anode as an oxidising catalyst is hydrogenase [191-193] and laccase is usually used at the cathode for catalytic reduction of oxygen [194, 195]. The size of enzymes is in the nanometric ranges and therefore there is a need to produce porous carbons with nanometric pore sizes. For instance, Deloggio and Graves [196] have used porous silica glass with pore diameters of 55-135 nm as a hydrogenase immobilisation support. In the case of microbial fuel cells, the size of microbes is around few microns [197]; hence a macroporous carbon electrode, with pore sizes in micrometric ranges, would be suitable for hosting the microbes.

In order to prepare these porous electrodes, the templating method was selected as a method for producing 3D mesoporous and macroporous carbon electrodes for hosting enzymes. This method is selected here because it is possible to control the pore sizes by the choice of template size, according to requirement. It is also possible to fabricate a homogeneous structure by means of a homogeneous sized template. In order to prepare porous carbons with larger pores for hosting microbes, a foaming method was selected as this method is easy and inexpensive to use. However, it is

difficult to control the pore size and to obtain nanopores with the foaming method. Even though, the walls may contain some nanoporosity. Moreover, in order to produce porous carbons, polyfurfuryl alcohol was selected as a carbon precursor to infiltrate into the templates and the foams. This is a thermosetting polymer so it hardens by heating and is possible to make the electrodes with the desirable shape. Moreover, this resin has a high carbon yield (see Table 1-1) and its pyrolysis results in a glassy carbon which is relatively high in strength and conductivity (see Table 1-2).

Mechanical strength and conductivity of the carbon decrease by introducing pores in the carbon. The porous carbon electrodes need to have sufficient strength for handling or machining. The maximum theoretical mechanical strength that can be achieved for an open cell glassy carbon, with a specific relative density, can be calculated from equation 1-4. The theoretical strength values are plotted versus the relative densities of the porous glassy carbon structures and the plot is shown in Fig. 1-25. If the mechanical strengths of the porous carbon electrodes produced are less than the theoretical values to a great extent, then they need to be improved by the methods mentioned in section 1.6.1. For example, for improving the mechanical strength of porous carbons, successive impregnation of the material in a resin is suggested. This fills the existing micropores and cracks on the carbon walls and increases the relative density of the porous structure which ultimately leads to a higher mechanical strength.

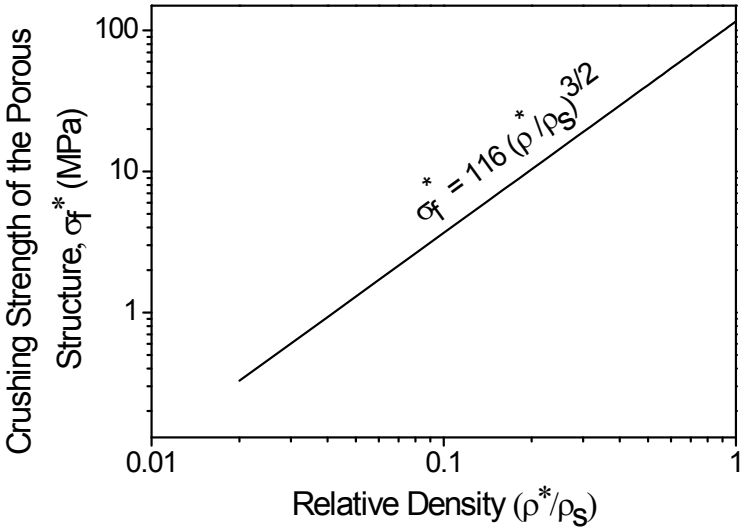


Fig. 1-25: Theoretical values of crushing strength of porous glassy carbon against relative density.

Electrical conductivity of the fabricated porous carbon electrodes should be high enough to not limit the charge transfer. Therefore, we need to know the minimum required conductivity of the electrodes for electron transfer. The electrical conductivity at the zero-field (the lowest energy state of a field) can be calculated from equation 1-13 [198]:

$$\sigma = qN\mu \quad (1-13)$$

where, q is the electronic charge (C), N is the charge carrier density (m^{-3}), μ is the mobility of the charge carrier ($\text{m}^2 \text{V}^{-1} \text{s}^{-1}$) and σ is the electrical conductivity (S m^{-1}).

To estimate the minimum conductivity, we need to estimate the minimum μ and N values. The mobility of charge carrier in a glassy carbon is in the range of 10^{-4} - $10^{-9} \text{ cm}^2 \text{V}^{-1} \text{s}^{-1}$ [199-202], hence, we can consider $10^{-9} \text{ cm}^2 \text{V}^{-1} \text{s}^{-1}$ as the minimum value for μ . For estimating the minimum number of charge carriers per volume, N_{min} , first we need to know the electrode coverage with the enzyme. For a protein of molecular mass 100000, the maximum coverage of a monolayer of the protein is around $3 \times 10^{12} \text{ mol cm}^{-2}$ [203]. As we want to estimate the minimum electrode coverage, we consider the minimum surface area to volume ratio of the electrode (flat electrode). Therefore, there are 18×10^{11} enzymes per cm^3 of the electrode. Assuming the turn over rate of an enzyme, which is the rate at which the catalyst cycle its substrate (fuel or oxidant), to be 100 s^{-1} [5], it can be concluded that the minimum charge carrier density is $18 \times 10^{13} \text{ cm}^{-3}$. In conclusion, by assuming the electric charge of 1 C, the minimum electrical conductivity required for electron transfer is estimated: $18 \times 10^4 \text{ S cm}^{-1}$. This value is close to the conductivity of metals such as gold ($45 \times 10^4 \text{ S cm}^{-1}$) and it won't be possible to achieve it unless the carbon has a graphitic structure and e^- conduction is along the basal plane.

The theoretical electrical resistivity value of an open cell glassy carbon, with a specific relative density, can be calculated from equation 1-3. The theoretical conductivity values are plotted versus the relative densities of the porous glassy carbon structures and the plot is shown in Fig. 1-26. As it can be seen from the figure, the maximum conductivity achievable for glassy carbon without any pores (relative

density of 1) is 200 S cm^{-1} which is 900 times less than the minimum required conductivity. Moreover, for porous structures conductivity decreases as relative density decreases and thus some strategies are needed to improve the conductivity.

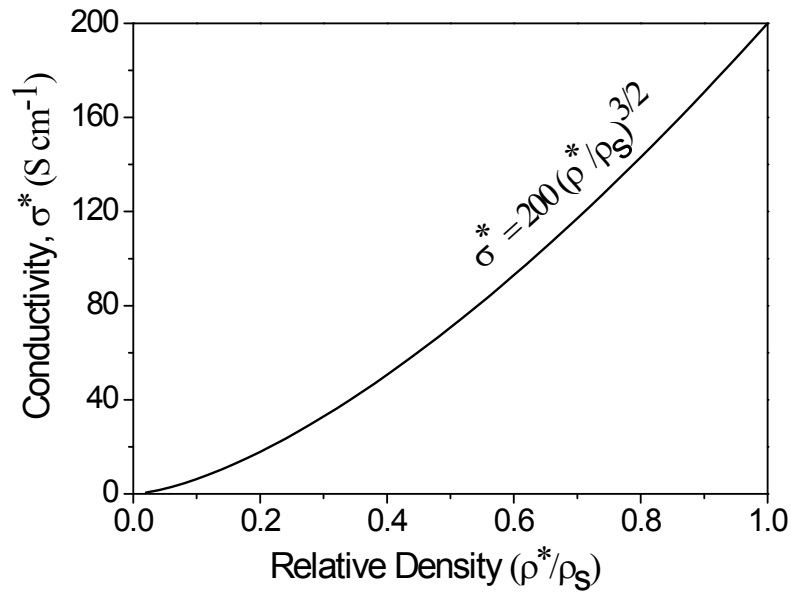


Fig. 1-26: Theoretical values of electrical conductivity of porous glassy carbon against relative density.

Improving electrical conductivity by catalytic graphitisation is explained in section 1.6.2. This method can be used to improve the conductivity of porous glassy carbon and nickel can be used as catalyst. Another suggestion for improving electrical conductivity of the glassy carbon is the addition of some graphite powder to the polymer precursor before curing and carbonisation. Moreover, successive resin impregnation, suggested for improving the mechanical strength of porous carbon materials, can also be used for enhancement of electrical conductivity because successive impregnation will result in higher density and thus higher electrical conductivity.

1.8 Summary

Carbon is a suitable material to be used as electrode material in biofuel cells because it has a relatively high electrical conductivity and corrosion resistant and its surface chemistry is adjustable for enzyme/microbe immobilisation. Carbon can be prepared

from carbonisation of organic materials. Various types of carbon precursors can be used that result in different carbon yields and carbon types. Aromatic hydrocarbons such as pitches and coals have higher carbon yield than polymer precursors but they need some modifications before carbonisation that makes the process complicated and also preparation of porous carbons of controlled pore size with pitches/coals is difficult. Therefore, polymeric precursors are usually used for preparation of high surface area carbon monoliths. These precursors are classified into two groups of thermoplastic and thermosetting polymers. Thermoplastic polymers pass through a liquid stage during the carbonisation but thermosetting polymers harden without passing through a mesophase. Thermosetting resins are suitable precursors for preparing porous carbon materials as they keep their shape during heating but their carbonisation results in a non-graphitisable carbon. This type of carbon does not graphitise by heating to high temperatures and therefore some strategies are needed to enhance their electrical conductivity.

Methods for preparation of porous carbon materials can be classified into two groups of foaming and templating methods. Generally, foaming method is easier and cheaper to use. However, templating method produces ordered porous carbon structures with homogeneous pore size distributions. In foaming method is not possible to control the pore sizes and they are mainly in micrometric ranges which can be suitable for microbe immobilisation. Templating method can be used for preparation of ordered meso- and macro-porous carbon materials. In this method either hard, *e.g.* silica, or soft, *e.g.* polymer, templates can be used. The structures obtain from silica templates usually do not shrink but the removal of hard templates is more difficult than soft templates. They require treatment with HF, whereas, polymer templates burn out during carbonisation process. Most of the porous carbon structures prepared with these methods and reported in the literature are in the forms of films or powders or if they have 3D structures, they are in small scales and they are mechanically weak. Therefore, a challenge of this project is to prepare 3D porous carbon structures with stable mechanical strength in both small and large scales. High surface area 3D structures are needed for high enzyme/microbe loadings.

Mechanical strength and electrical conductivity of porous carbon electrodes depend on their relative density. Some strategies can be used to improve these properties. For example, to improve mechanical strength, successive impregnation of the porous carbon with a resin and also using carbon fibre in the structure were suggested. Furthermore, electrical conductivity of glassy carbons needs to improve to not limit the charge transfer on electrode/enzyme interface. To improve electrical conductivity of glassy carbon, catalytic graphitisation, by using metals such as nickel or iron as catalysts, can be used. Surface chemistry of the porous carbon electrodes also needs some modifications for better enzyme attachments. This can be done by creating some oxygen functional groups on the carbon surface using either chemical oxidation or electrochemical pretreatment. This will result in better activity, reversibility and stability of the electrodes and ultimately higher efficiency of biofuel cell.

Chapter 2: Carbon Preparation from Polyfurfuryl Alcohol

2.1 Introduction

Polyfurfuryl alcohol (PFA) is a thermosetting resin which is used as a carbon precursor in all the fabrication methods in this project. As explained in the previous chapter, the pyrolysis of this resin results in a vitreous (glassy) carbon. The synthesis of this resin and the properties obtained from carbonisation of the resin are reported in this chapter. The structure of the resin and the physical and mechanical properties of the pyrolysed resin are compared with the ones reported in the literature.

2.2 Synthesis of PFA

To prepare polyfurfuryl alcohol, furfuryl alcohol (FA) was mixed with a solution containing an equal volume of distilled water as the FA and sulphuric acid, according to the literature [204]. The mixture was heated over a water bath until two layers formed. Prolonging the heating at this stage resulted in a furan resin of higher viscosity. The bottom resin layer was separated from the aqueous layer with a separating funnel and washed with distilled water. The synthesised polyfurfuryl alcohol (PFA) can be seen in Fig. 2-1. After reaction, the yellow solution of FA becomes black.



Fig. 2-1: Furfuryl alcohol, picture at the left hand side, and Polyfurfuryl alcohol, at the right.

Depending on the amount of added catalyst (H₂SO₄) and duration of polymerisation, the PFA obtained will be of different viscosity. Overall, the viscosity of the PFA is related to the degree of polymerisation. Therefore, polyfurfuryl alcohol with different viscosities was prepared (see Table 2-1) in order to examine the effect of viscosity on the process of making porous carbons. The viscosity of the resin was measured with a viscometer as described in Appendix E. Typical viscosity for given experimental conditions are summarised in Table 2-1. Obviously, a higher concentration of acid, temperature and reaction time lead to a higher viscosity.

Table 2-1: Preparation of PFA with different viscosities.

Amount of FA (mL)	Amount of water (mL)	Amount of acid (mL)	Temperature (°C)	Time (h)	Viscosity of PFA (cP)
50	50	4	60	3	765
50	50	4	60	5	1150
150	150	12	60	6	1650
150	150	24	40	5	3650
300	300	6	40	1/2	80
300	300	6	40	1	332
150	150	3	40	3/4	95

2.3 Confirmation of the PFA Synthesis

The synthesis of PFA was confirmed by FTIR spectroscopy and TGA/MS.

2.3.1 Chemical Structure

In order to confirm the structure of synthesised PFA, the resin was dried (cured) to remove any solvent (water) and crushed and mixed with potassium bromide *i.e.* transparent to the infrared light and does not introduce any lines onto the spectra. The resulting FTIR spectrum is given in Fig. 2-2. On the spectrum peaks at 3410 cm⁻¹ and 3120 cm⁻¹ related to OH stretching and CH stretching can be observed. These correspond to intermolecular hydrogen bonds and furan ring hydrogen, respectively. Moreover, peaks at 2920 and 2870 cm⁻¹ can be seen on the spectrum and are related to

aliphatic CH₂ and CH stretching. Peaks appeared at 1600, 1550 and 1500 cm⁻¹ are related to C=C stretching in aromatic rings and the peak observed at 1710 cm⁻¹ is related to C=O stretching due to acid-catalysed ring opening of furan rings. Therefore, the synthesised PFA is primarily comprised of furan rings linked together by methylene (-CH₂-) bridges (Fig. 1-10a). The IR spectrum of the synthesised PFA is consistent with data reported in the literature [62, 205].

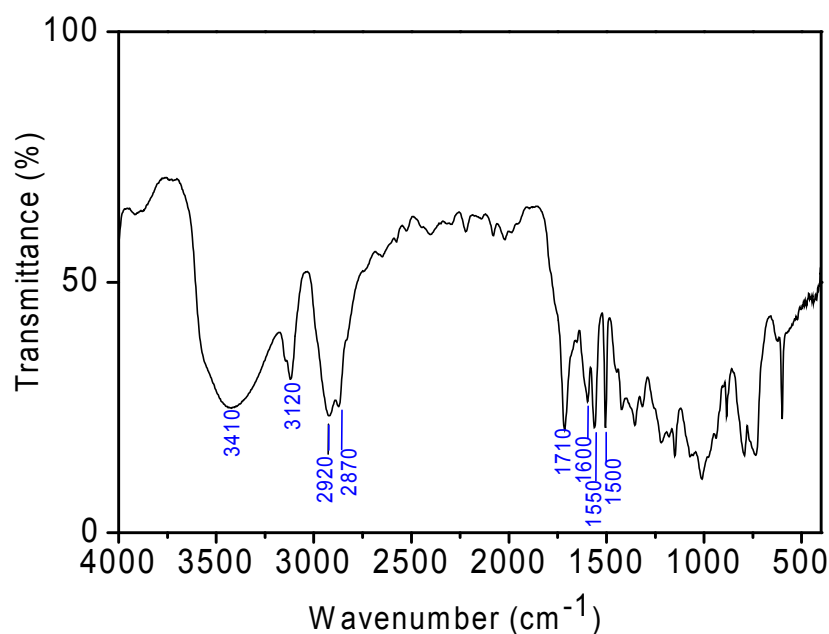


Fig. 2-2: Infrared spectrum of PFA as synthesised.

2.3.2 Thermal Behaviour

Thermal behaviour of the synthesised PFA needs to be examined in order to determine the decomposition trend. The pyrolysis of PFA was examined by thermogravimetric (TG) technique. The sample was heated under a flowing argon atmosphere at 10 °C min⁻¹ from room temperature to 700 °C. The weight loss (TG) and differential thermal analysis (DTA) curves are represented in Fig. 2-3. It can be seen from the DTA curve that the thermal decomposition of synthesised PFA is an exothermic process due to the formation of pyrolysis gases. Weight loss occurred in two distinct temperature regimes. The weight loss in the temperature range of 100-200 °C corresponds to evaporation of water as confirmed by mass spectrometry (Fig. 2-4),

which was formed as a by-product of the polymerisation reaction. The maximum weight loss rate is found in the range of 300-400 °C. Within this temperature range, the decomposition of PFA occurs with the release of several gases as found by MS, see Fig. 2-4.

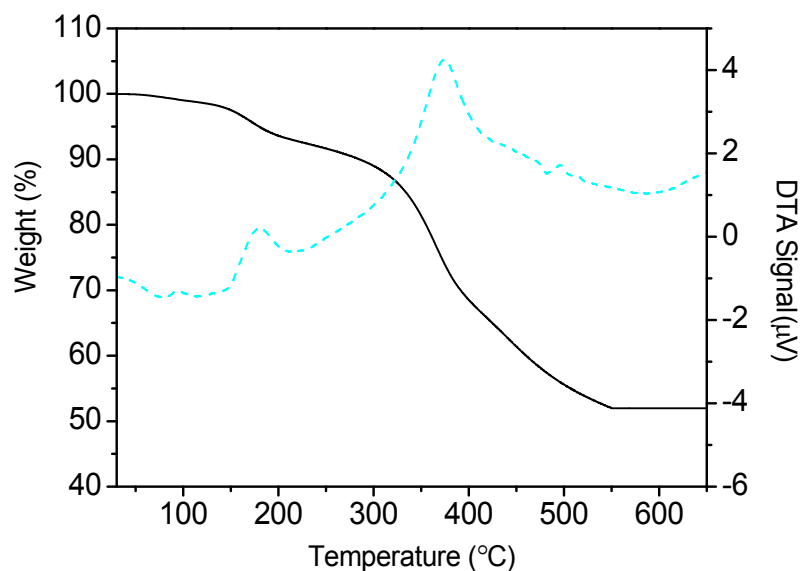


Fig. 2-3: TGA (-) and DTA (--) profiles of pyrolysis of PFA in argon at 10 °C min⁻¹.

MS results show that the main pyrolysis gases are water and carbon monoxide. Other by-products are carbon dioxide, methane and hydrogen gases. In the region of 100-200 °C water evaporation was observed and in the region of 200-300 °C the by-products were mainly CO₂, CH₄, H₂O and CO. The production of CO₂ and CO decreased in the region of 300-400 °C and CH₄ and H₂O release stopped in this region. An hydrogen loss occur at 400 °C. Above 550 °C the decomposition of PFA and production of majority of gases was stopped.

The decomposition of the synthesised resin corresponds to that of PFA [61]. It is reported that water is the first product and hydrogen is the last during decomposition of PFA. Thus, TGA/DTA confirms the synthesis of PFA which agrees with the IR result.

From the TG curve of the synthesised PFA, the carbon yield of this resin was found to be 50-55%. This is in agreement with the one reported in the literature (see Table 1-1 in Chapter 1).

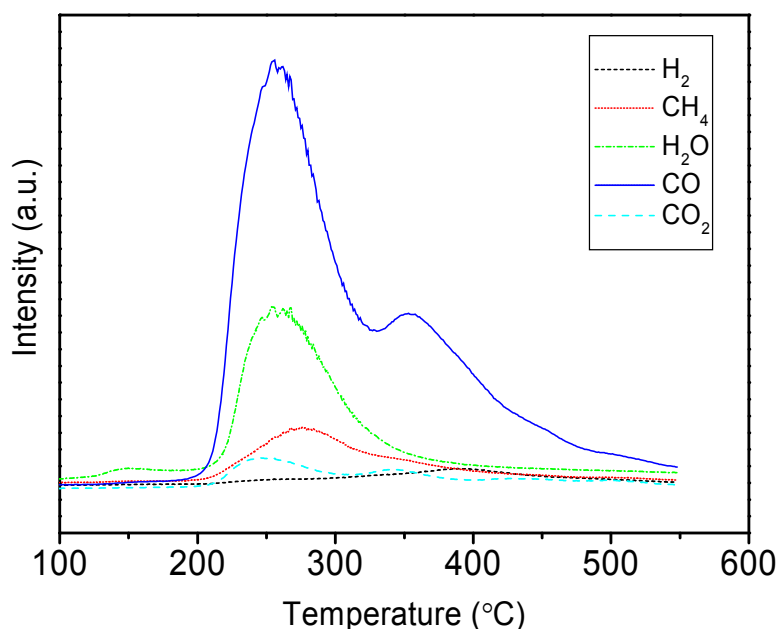


Fig. 2-4: Gas evolution profiles of pyrolysis of PFA in argon at 10 °C min⁻¹.

2.4 Properties of the Pyrolysed PFA

The synthesised PFA was cured and carbonised under nitrogen flow at 80 °C and 1000 °C, respectively. The curing time depended on the viscosity of the PFA; the more viscous the resin was, the less the time required for curing (due to water evaporation showed by TGA). Pyrolysis of the synthesised PFA resulted in a glassy carbon. The physical and mechanical properties of the carbon are investigated in the following.

2.4.1 Structure

The pyrolysed PFA was crushed to powders and characterised by X-ray diffraction (XRD) technique. Fig. 2-5 shows the XRD pattern obtained for the carbonised PFA. A broad band appeared in the XRD pattern at a 2θ value of 23-25° indicating the presence of an amorphous structure. Two other carbon peaks also appeared at 43 and 44.8° and a wide low intensity band at around 78° which can be assigned to (100), (101) and (110) diffraction peaks of a graphitic framework, respectively. Therefore, structure of the carbonised PFA is amorphous with some degree of crystallinity. However, since the (002) peak of graphite is broad, it is difficult to determine its

accurate position and the full-width-half-maximum (FWHM) and hence to calculate the (002) plane spacing (d_{002}) and the crystallite size, L_c , (see Appendix B, Section B.1).

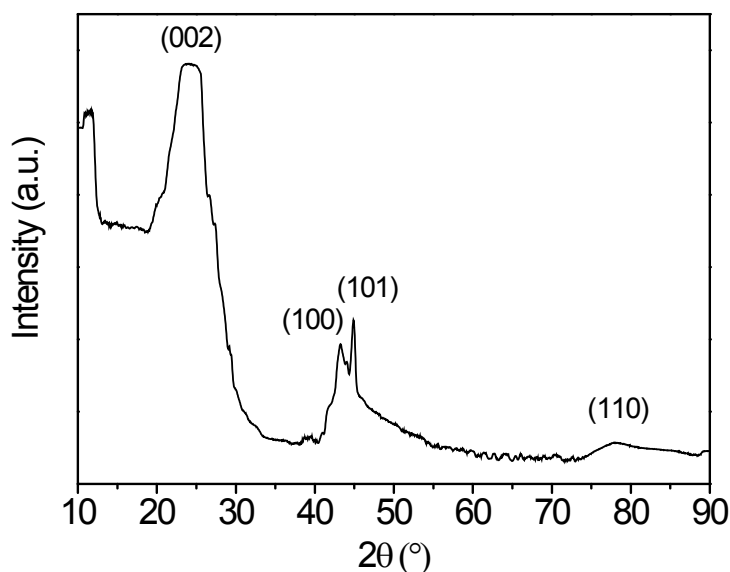


Fig. 2-5: XRD pattern of the carbonised PFA.

To further examine the structure of PFA pyrolysed, Raman spectrum of the carbonised PFA was obtained and is shown in Fig. 2-6. Here, two bands can be observed at around 1350 cm^{-1} and 1580 cm^{-1} . These bands correspond to the disordered carbon (D-band) and graphitic carbon (G-band) [206].

In theory, a single Raman line at 1575 cm^{-1} is expected in hexagonal lattice of graphite [207, 208]. An additional Raman line has been observed in glassy carbon at around 1355 cm^{-1} . This line results from graphite crystallites containing disorganised regions near crystal edges and lattice defects such as vacancies. It can be seen from Fig. 2-6 that it contains two broad bands which are characteristic of disordered carbon [208]. This together with the XRD result suggests that the pyrolysis of synthesised PFA resulted in an amorphous carbon structure.

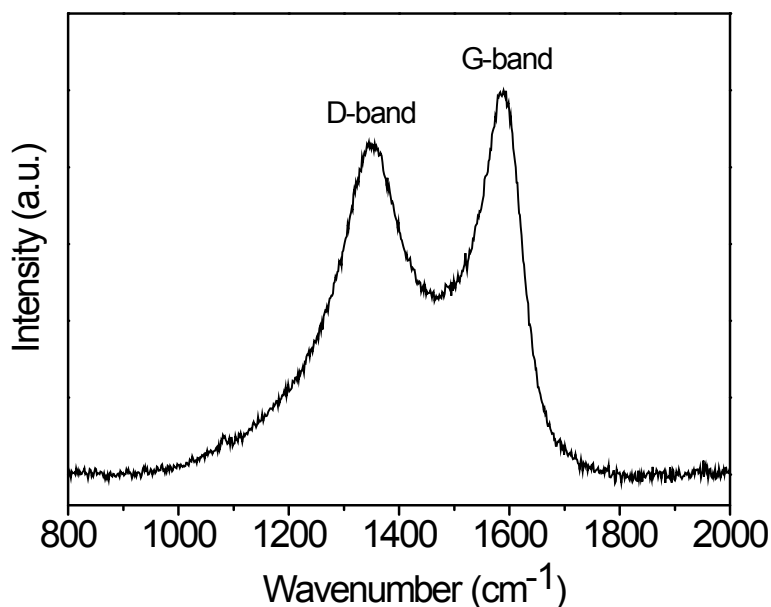


Fig. 2-6: Raman spectrum of the carbonised PFA.

2.4.2 Density

The density of the carbonised PFA was measured by a pycnometer (see Appendix B, Section B.4). The density of the PFA cured in air and carbonised was found $1.607 \pm 0.0013 \text{ g cm}^{-3}$ and the density of the PFA cured in nitrogen and carbonised was $1.899 \pm 0.0176 \text{ g cm}^{-3}$. These values are higher than the one reported in the literature (Table 1-2). This can be due to a different pyrolysis condition such as carbonisation temperature.

2.4.3 Mechanical Strength

The mechanical strength of the carbonised PFA was investigated by compression test (see Appendix B, Section B.6). Mechanical strength of two carbonised PFA under different curing conditions was tested. One sample was cured under nitrogen and the other in air at 80 °C. All the other parameters and carbonisation conditions were the same for both samples. Two of the graphs obtained from the compression tests for the two mentioned samples are shown in Fig. 2-7.

The maximum loads that the samples could tolerate before crumbling were 1306 and 2508 N for the PFA cured in air and nitrogen, respectively. The areas of the samples that were under load were measured before the tests. The cross sectional area of the sample cured in air was $18.216 \pm 0.0004 \text{ mm}^2$ and the sample cured in nitrogen was $17.5 \pm 0.0004 \text{ mm}^2$. The mechanical strength of the samples can be calculated by dividing the maximum load that the sample could withstand before crumbling to the area that the load was applied to. Therefore, the mechanical strength was 72 MPa for the sample cured in air and 143 MPa for the one cured in nitrogen. The compression test was repeated for other samples of carbonised PFA, cured in air and nitrogen, and the range of mechanical strengths obtained are shown on the graph by error bars. Therefore, it can be concluded that the resin cured under nitrogen has better compressive strength than the one cured in air. This can be due to the higher density of the carbon obtained from the PFA cured in nitrogen compared to the one cured in air. It was also found that the compressive strength of the glassy carbon obtained from the synthesised PFA is lower than the one reported in the literature (see Table 1-2 in Chapter 1).

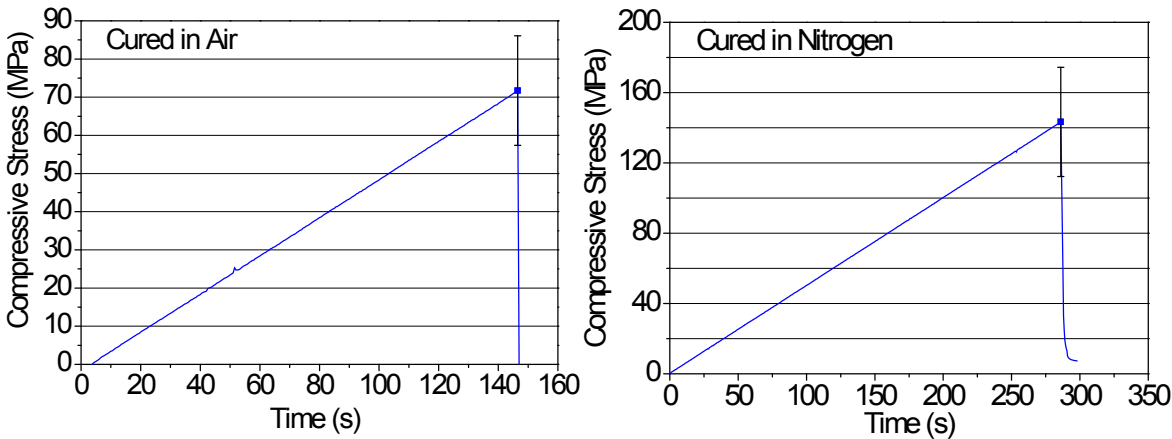


Fig. 2-7: Compressive stress (MPa) vs. time (s) graphs obtained from the compression tests for two samples of PFA that have been cured in air and nitrogen, respectively and carbonised at the same conditions.

2.4.4 Electrical Conductivity

Electrical resistivity of the carbonised PFA was measured by the four point technique as described in Section B.5 of Appendix B. The resistivity was calculated using

equation (B-9), $\rho = 2\pi S \frac{V}{I}$ where ρ is the resistivity of the material ($\Omega \text{ cm}$), S is the

probe spacing (cm), V is the potential difference between the inner probes (V) and I is the current (A). The voltage at 1 mA current was measured to be 0.011 mV and therefore the resistivity of the glassy carbon was found to be $48 \times 10^{-4} \Omega \text{ cm}$. This value is similar to the one reported in the literature (Table 1-3 in Chapter 1). Moreover, the theoretical resistivity at room temperature can be determined from equation 2-1 [209]:

$$\log_{10}[\log_{10}(\rho/\rho_{\infty})] = -\theta/\theta_c + I \quad (2-1)$$

where, ρ is the resistivity of the pyrolysed polymer ($\Omega \text{ cm}$), $\rho_{\infty} = 3 \times 10^{-3} \Omega \text{ cm}$, θ is the heat-treatment temperature (K), $\theta_c = 300 \text{ K}$ and $I = 3.6$. From this equation, resistivity of the pyrolysed PFA at $1000 \text{ }^{\circ}\text{C}$ would be $50 \times 10^{-4} \Omega \text{ cm}$ which is consistent with the result obtained.

2.5 Summary

Polyfurfuryl alcohol has been synthesised and pyrolysed successfully. The properties of the synthesised resin were confirmed to be that of PFA. The structure, physical and mechanical properties of the pyrolysed resin were characterised by different characterisation techniques. The structure of the carbon obtained found to be amorphous as expected. The density and mechanical strength of the prepared glassy carbon from PFA cured in nitrogen were higher than from the PFA cured in air. Mechanical strength of these carbons was lower than the one reported in the literature. Whereas, electrical conductivity of the glassy carbons prepared was in good agreement with the literature.

Chapter 3: Macroporous Carbon Materials Derived from Foaming Method

3.1 Introduction

Macroporous carbon materials with pore sizes in micrometric ranges are needed for hosting microbes in microbial fuel cells. In order to fabricate macroporous carbon electrodes, foaming method was chosen for the simplicity of the method. Previously, methods based on foaming of aqueous polyurethane systems have been reported for preparation of ceramic foams [210] and two-part polyurethane mixtures have been shown to produce fine reticulated ceramic foams with more than 90% porosity [211]. However, these foams had low mechanical strength and therefore, the foaming method needs to be modified for preparation of mechanically stable carbon foams. Moreover, in order to obtain high current densities, microbial fuel cells usually require large electrodes. Developing large and mechanically stable porous carbon electrodes with high electrical conductivity is a big challenge.

In this part of the project, a two-part polyurethane mixture was used to prepare carbon foams and the properties of the carbon foams, especially mechanical strength, were improved by modifying the preparation method. The properties of the carbon foams obtained from different methods of fabrication are reported in this chapter. Furthermore, Electrical conductivity of the carbon foams need to be improved as polyfurfuryl alcohol (PFA) was used as a carbon precursor which produced a non-graphitisable carbon. Electrical conductivity was improved by catalytic graphitisation using nickel as a catalyst and different catalytic structures were produced. The electrochemical properties of the original and the graphitised carbon foams were examined.

3.2 Fabrication of Carbon Foams and Their Properties

Foaming method was used for preparation of macroporous carbon foams. The properties of the carbon foams were improved by the processing method. The three

methods of foam fabrication used for preparation of carbon foams are reported in the following sections.

3.2.1 Method-1: Sintering

The foaming method used for fabrication of macroporous carbon materials is illustrated schematically in Fig. 3-1. This method of fabrication was based on previous work reported in our group for preparation of metal foams [212, 213]. In this method, graphite powder was added to each component of the foaming agent (polyurethane) separately and hand stirred for 1 min. The total amount of the powder in the mixture was 30 vol.% (this is the optimum amount of powder to achieve the best structure and minimum shrinkage, see Section 3.2.2.2). The compounds were then mixed together for a further period of ~1 min. These mixtures were then poured into a box and allowed to rise. After storage for 24 h that the foaming process was finished and the foams were dry, specimen cubes were cut.

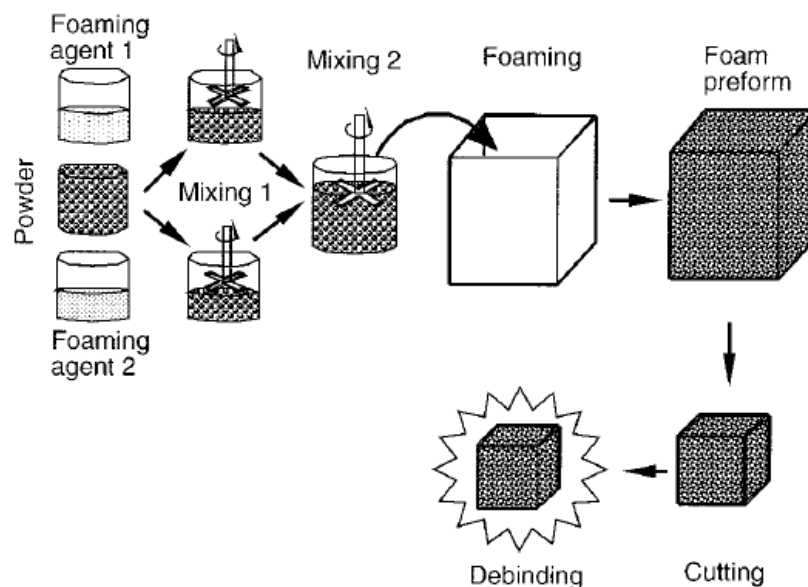


Fig. 3-1: Schematic diagram of foaming process [213].

The procedure of debinding (polymer burn out) is illustrated schematically in Fig. 3-2. The preform specimens were heated at $1\text{ }^{\circ}\text{C min}^{-1}$ to $120\text{ }^{\circ}\text{C}$ followed by $0.1\text{ }^{\circ}\text{C min}^{-1}$ to $400\text{ }^{\circ}\text{C}$ in flowing air and held for 2 h before furnace cooling [212]. This procedure is performed at a low heating rate of $0.1\text{ }^{\circ}\text{C min}^{-1}$ to avoid rupture of the preform

structure. After burning the polymer out of the structure, the preform was sintered to bond the graphite particles by two different techniques: 1) sintering in a vacuum tube furnace at 1000 °C for different periods of time, up to 16 h; and 2) sintering by spark plasma sintering (SPS) method (see Appendix E for further details), where the carbon foam was sintered at 2000 and 2175 °C for 3, 5 and 15 min. Two samples for each condition were prepared (twelve samples in total).

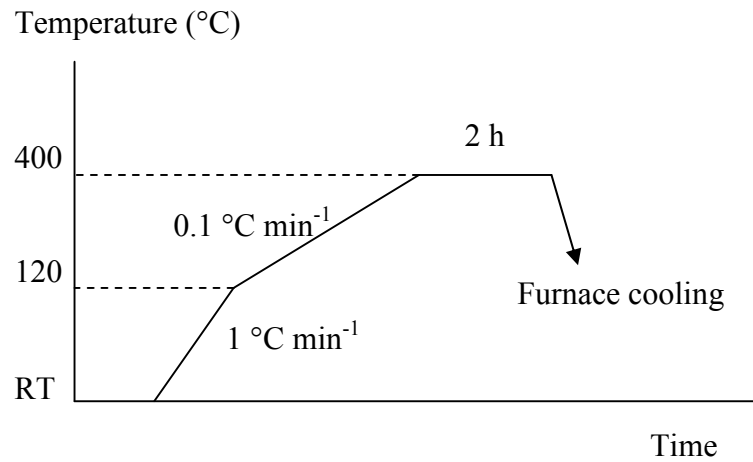


Fig. 3-2: Schematic diagram of debinding procedure.

Morphology of the fabricated carbon foams was examined by scanning electron microscopy (SEM) before and after sintering. Structures of the carbon foams sintered in the vacuum tube furnace were very weak that could not stand the preparations for SEM.

Fractured surface of a foam preform after debinding and before sintering is shown in Fig. 3-3 and fractured surfaces of sintered carbon foams can be seen in Fig. 3-4 (A) and (B). The samples were sintered by spark plasma sintering (SPS) technique at 2175 °C for 5 and 15 min. It can be seen from the figures that pores in the sample sintered for 5 min are in the range of $310 \pm 80 \mu\text{m}$ and pores of the sample sintered for 15 min are in the $163 \pm 20 \mu\text{m}$ ranges. Moreover, it can be seen from the figures that the walls of the carbon structures have some cracks that weakens the structures. These cracks were present in all the sintered foams. Strength of the samples sintered at various times (3, 5 and 15 min) were similar and did not improve by prolonging the sintering.

The structures obtained from the above sintering methods were mechanically very weak (less than 1 MPa) even after sintering at high temperatures with the SPS technique or after prolonged sintering. This could be because the sintering temperatures were not high enough as the melting point of carbon is 3500 °C and therefore the sintering need to be performed at around 3000 °C. Therefore, this method was modified (Method-2) to improve the mechanical strength of the carbon foams.

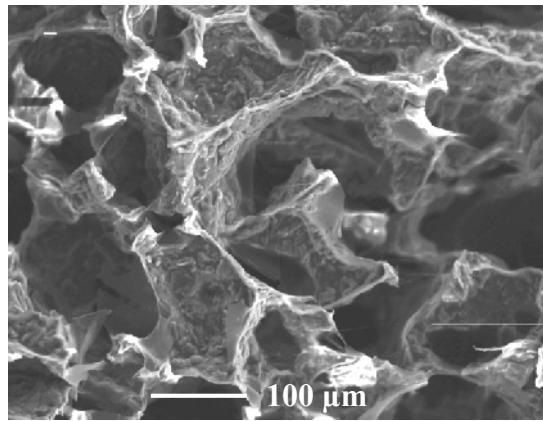


Fig. 3-3: SEM image of a carbon foam after polymer burn out.

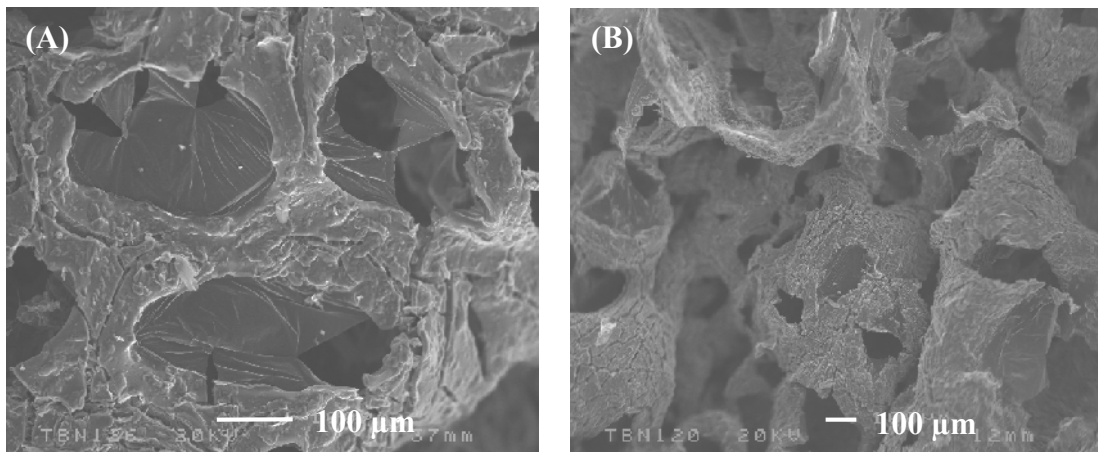


Fig. 3-4: SEM images of sintered carbon foams (prepared with Method-1 and using SPS process) at 2175 °C for (A) 5 min and (B) 15 min.

3.2.2 Method-2: Impregnation with PFA

In order to improve the mechanical strength, the foam preforms were impregnated with polyfurfuryl alcohol (instead of sintering the structures) after the polymer is burnt out of the structure. The viscosity of the PFA used for impregnation was $120 \pm$

10 cP. To impregnate the samples with PFA, the samples were soaked in the PFA for ~10 min. The optimum impregnation time was obtained after impregnating the carbon foam preforms (cubes of approximately 1.5 cm) with the PFA for various times and cutting the samples to half to check if they are fully impregnated. After the impregnation, the excess PFA on the surface of the foams was removed with tissue to prevent blockage of the pores. The samples were placed on the tissue for 30, 60 and 120 min (two samples for each time) and they were turned occasionally. The best result in terms of structure homogeneity after carbonisation was obtained for the samples placed on the tissue for 1 h.

The foams were cured at 80 °C for approximately 20 h under a nitrogen flow (850 mL min⁻¹). These are the optimum curing conditions obtained after various experiments at different temperatures and times. The carbonisation of the foams was also performed under a nitrogen flow of 850 mL min⁻¹ at 1000 °C for 2 h at a heating rate of 1 °C min⁻¹ [63]. Fig. 3-5a and b show pictures of a carbon foam before and after the polymer burnt out, respectively and Fig. 3-5c shows a carbon foam after impregnation with PFA and carbonisation.

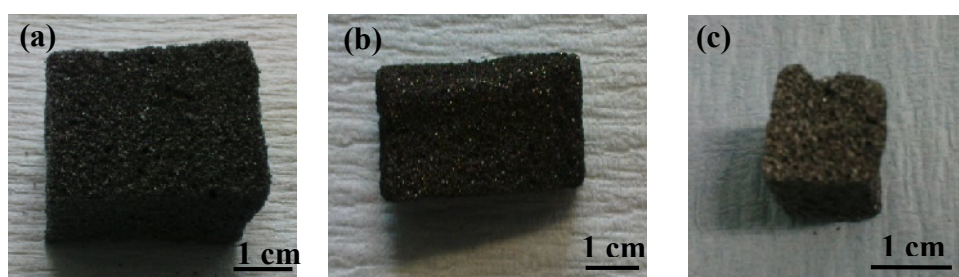


Fig. 3-5: Pictures of the carbon foams fabricated (a) before polymer burn out, (b) after polymer burn out and (c) after impregnation with PFA and carbonisation (Method-2).

Different properties of the foams fabricated with Method-2 were examined and are reported below. To examine the properties, approximately fifty samples were prepared with Method-2.

3.2.2.1 Morphology and Porosity

In order to investigate the morphology of the carbon foams produced with Method-2 field emission scanning electron microscopy (SEM) was used. The SEM images of

carbonised foams after first, second and third impregnations with polyfurfuryl alcohol are shown in Fig. 3-6. It can be seen from the images that the majority of pore sizes in the impregnated foams are less than 100 μm , whereas the majority of pore sizes in the carbon foams prepared with Method-1 (sintered) were more than 100 μm . The other factor to be noted is the walls of the foams that are more continuous in the impregnated foams (Method-2) than in the sintered ones (Method-1). The sintered foams had cracks on the walls that weakened the structures.

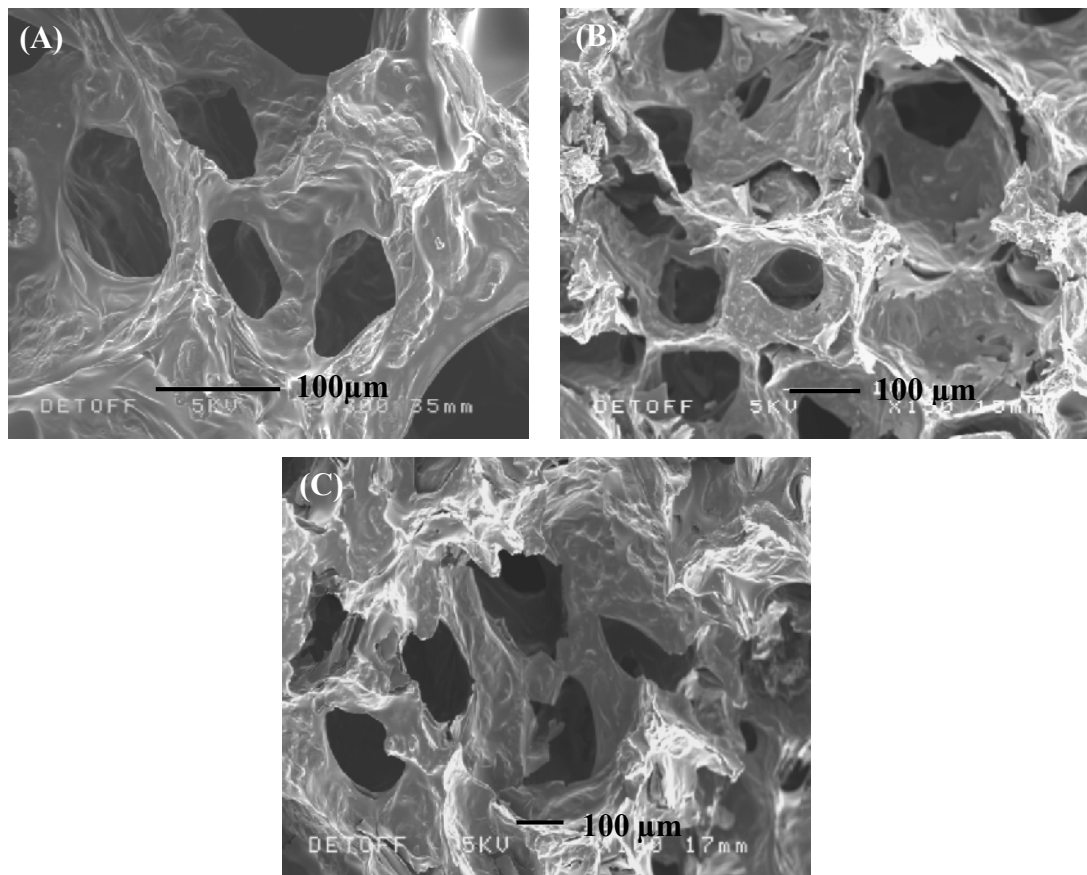


Fig. 3-6: Field emission scanning electron microscopy images of the carbonised foams prepared with Method-2 after (A) first, (B) second and (C) third impregnation with PFA.

Porosity of the carbon foams prepared with Method-2 was further studied with the mercury porosimetry technique. This technique and the theory behind it are explained in Appendix C, Section C.2. The porosity investigations with this technique was not possible for the carbon foams prepared by Method-1, as the structure of the foams produced by Method-1 was very weak and could not withstand any pressure. The pore size ranges of the carbon foams produced by Method-2 and impregnated with PFA once (porous carbon 1), twice (porous carbon 2) and three times (porous carbon 3)

were examined and are shown in Fig. 3-7. Moreover, to compare pore size distribution of porous carbons 1, 2 and 3, one graph for each impregnation is chosen and they are plotted in Fig. 3-8 against Log differential intrusions of each impregnation. It was found that the pore size ranges for the porous carbon 1 is between 1 and 200 μm , for porous carbon 2 is between 0.4 and 180 μm , and for porous carbon 3 is between 0.1 and 180 μm . The majority of the pore diameters for porous carbons 1 and 2 are at $60 \pm 10 \mu\text{m}$ and for porous carbon 3 are at $50 \pm 10 \mu\text{m}$. The porous carbon 1 has another peak of smaller pore sizes (at 25 μm) which is disappeared for porous carbon 2 and 3 as a result of successive impregnations with PFA. It can also be seen that the pore sizes, in general, reduce by successive impregnations.

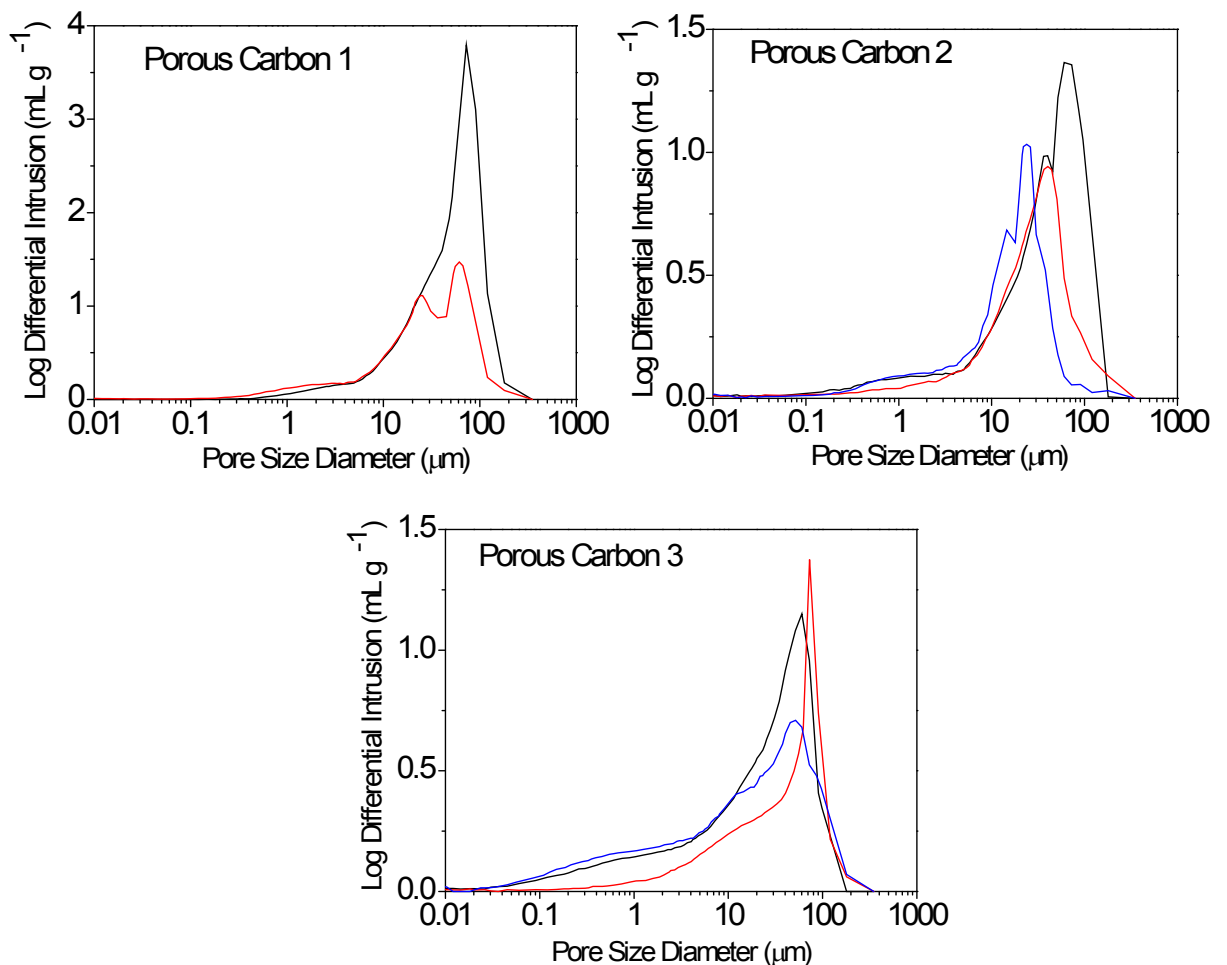


Fig. 3-7: Pore size distribution curves of two samples of carbon foam prepared by Method-2 and impregnated with PFA once (porous carbon 1) and three samples of carbon foams prepared by Method-2 and impregnated with PFA twice (porous carbon 2) and three samples of carbon foams prepared by Method-2 and impregnated with PFA three times (porous carbon 3).

Pore volume of the foams was also obtained using the porosimetry technique. It was found that the pore volume of the foams prepared by Method-2 after first, second and third impregnations were 71 ± 5 , 59 ± 5 and $55 \pm 5\%$, respectively (see Table 3-1). The pore volume of the foams reduced after successive impregnations with PFA as it was expected.

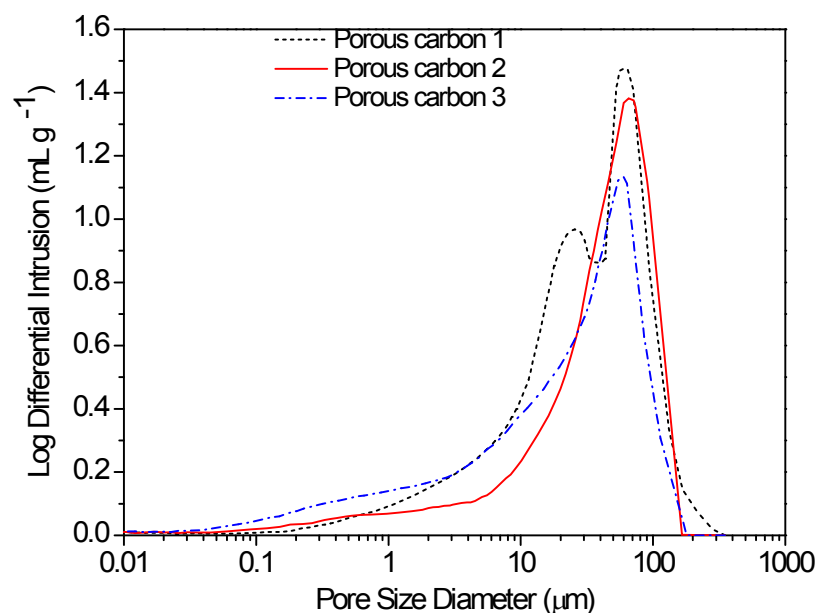


Fig. 3-8: Log differential intrusion (mL g^{-1}) vs. average pore size diameter (μm) of carbon foams prepared by Method-2 and impregnated with PFA once (porous carbon 1), twice (porous carbon 2) and three times (porous carbon 3).

3.2.2.2 Shrinkage

Shrinkage of the carbon foams prepared by Method-2 and with different amounts of graphite powder (in vol.%) was investigated by measuring the dimensions of the foams before and after polymer burn out. Three samples were prepared for each volume of graphite (twelve samples in total). Fig. 3-9 shows the average shrinkage values of the foams after polymer burn out versus different amounts of graphite added. It can be seen that the minimum shrinkage of the foams obtained when 30 vol.% of graphite powder was added to the structure. Furthermore, shrinkage of the foams after impregnation with PFA and carbonisation was investigated by measuring the dimensions of the foams before and after carbonisation. It was found that the shrinkage of the carbon foams after first, second and third impregnations with PFA

and carbonisation was 43 ± 8 , 42 ± 7 and $42 \pm 7\%$, respectively (Table 3-1). Thus, shrinkage of the foams after carbonisation did not change by successive impregnations with PFA.

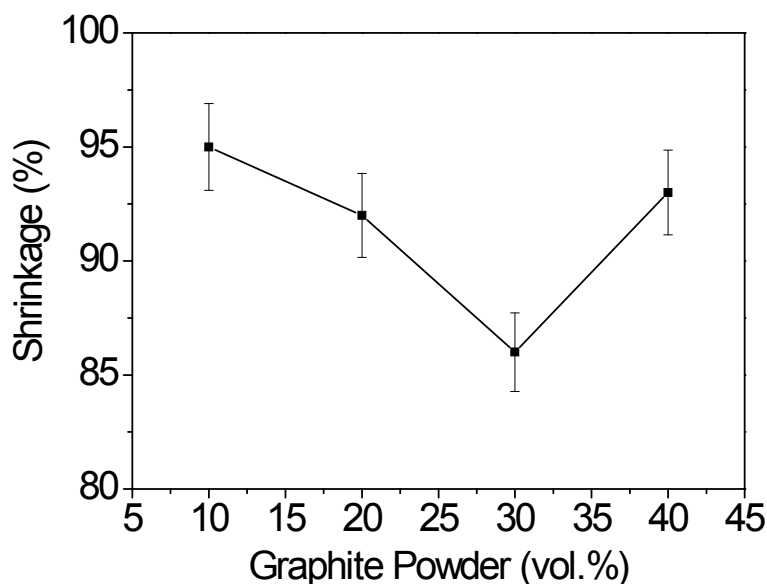


Fig. 3-9: Shrinkage of the carbon foams, prepared by Method-2, after polymer burn out vs. different amounts of graphite powder (vol.%) added.

Overall shrinkage of the foams prepared by Method-2 after polymer burn out (86%) and impregnation with PFA and carbonisation (42%) was very high, making it difficult to prepare large electrodes with desirable shapes.

3.2.2.3 Structure

Structure of the carbon foams prepared with Method-2 was examined by XRD. Foams were crushed into powders and XRD pattern of the carbon foams prepared by Method-2 and impregnated with PFA once is shown in Fig. 3-10. It can be seen from the figure that the structure of the foams exhibited a sharp single (002) graphite peak at 26.4° which was due to the graphite powder used in the structure.

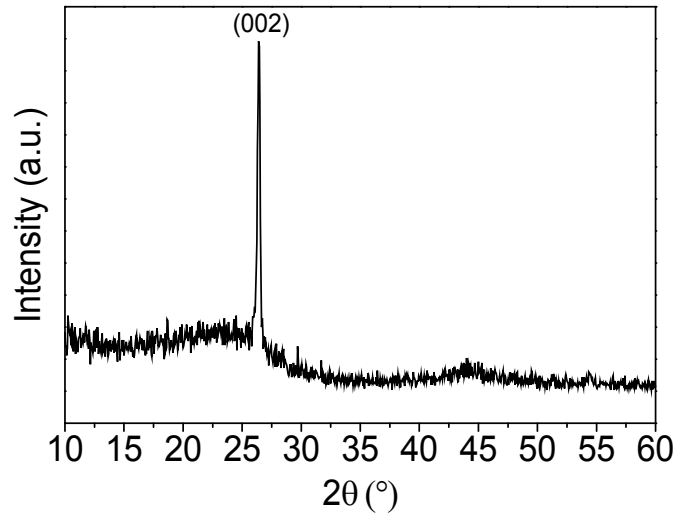


Fig. 3-10: Structure of the carbon foams prepared by Method-2 and impregnated with PFA once.

3.2.2.4 Density and Mechanical Strength

In order to estimate the density of the carbon foam walls (struts), pycnometer was used (see Section B.4 of Appendix B for further explanation). In addition, the density of the foams as a bulk material was estimated using equation (3-1):

$$\rho^* = \frac{m}{V} \quad (3-1)$$

where ρ^* is the bulk density (g cm^{-3}), m is the mass (g) and V is the volume (cm^3) of the material. Strut (helium) density, ρ_s , and bulk density, ρ^* , of the carbon foams produced by Method-2 are summarised in Table 3-1. The bulk density of the foams after first, second and third impregnation with PFA was found to be 0.32 ± 0.01 , 0.34 ± 0.02 and $0.38 \pm 0.01 \text{ g cm}^{-3}$, respectively. It was found that the bulk density of the foams increased by successive impregnations with PFA which is reasonable, as the weight of the foams increase after each impregnation whereas the volume of the foams does not change by successive impregnations. With the strut and bulk densities, relative densities of the foams were calculated as ρ^*/ρ_s . The relative densities were found to be 0.20 ± 0.01 , 0.22 ± 0.01 and 0.26 ± 0.01 for the foams impregnated with PFA once, twice and three times, respectively. Therefore, the relative densities of the foams increased as the pore volume of the foams decreased by successive impregnations.

Mechanical strength of the foams improved dramatically with Method-2 compared to Method-1. The mechanical strengths of the foams after first, second and third impregnations with PFA were estimated from compression tests (see Section B.6 of Appendix B for details) and are summarised in Table 3-1. Three samples were prepared for each impregnation with PFA. The mechanical strength of the carbon foams impregnated with PFA once, twice and three times was found 9 ± 1 , 11 ± 1 and 11 ± 2 MPa, respectively. Fig. 3-11 shows the result of compression test for carbon foam prepared from Method-2 and impregnated with PFA twice. Mechanical strength of the foams after second impregnation with PFA improved to some extent over the first impregnation but did not change after third impregnation compared to the second impregnation.

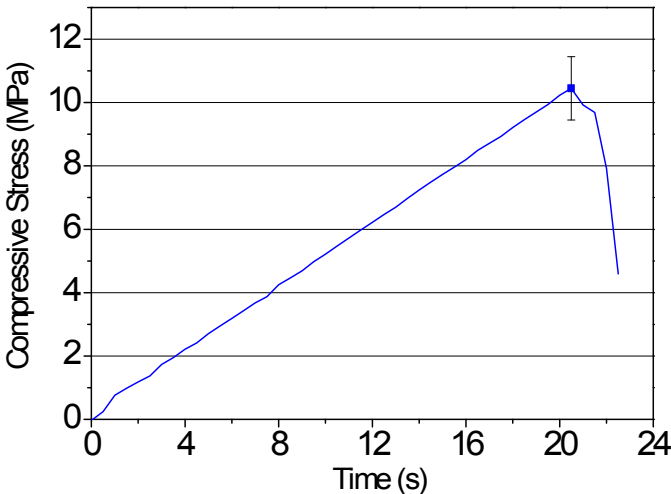


Fig. 3-11: Compressive stress (MPa) vs. time (s) obtained from the compression test of carbon foam prepared by Method-2 after second impregnation with PFA.

Fig. 3-12 shows theoretical values of compressive strength versus relative density of glassy carbon (as it was discussed in Chapter 1, Section 1.7), as well as compressive strengths of the foams produced by Method-2 versus their relative densities. It can be seen from the figure that the strength values for the carbon foams after first and second impregnations with PFA are close to the theoretical values. For example, carbon foam after second impregnation with relative density of 0.22 showed a mechanical strength of 11 MPa which is very close to the theoretical strength value with the same relative density; 12 MPa.

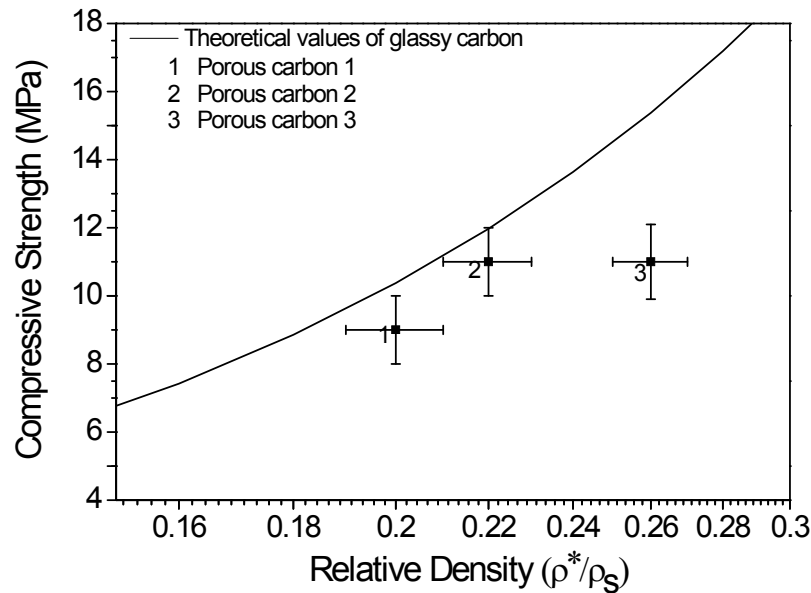


Fig. 3-12: Theoretical values of compressive strength (MPa) of glassy carbon vs. relative density (—) and compressive strength vs. relative density of the carbon foams impregnated with PFA once (porous carbon 1), twice (porous carbon 2) and three times (porous carbon 3).

Furthermore, by comparing these results with the ones reported in the literature, it can be seen that the carbon foams prepared from Method-2 are higher in mechanical strength than the ones reported, for example, by Kett [81] with even higher densities. The carbon foams were prepared from pitch precursor and compressive strength of 3.4 MPa was reported for foams with 0.53 g cm^{-3} bulk density (relative density of about 0.48).

Another factor found to affect the mechanical strength of the foams was the heating rate in the carbonisation cycle. Three samples were carbonised at 1000°C for 2 h, at $0.5 \text{ }^\circ\text{C min}^{-1}$. Slow heating rate resulted in diffusing the PFA to the outer surface of the structure and as a consequent a structure with a hard surface and soft core was obtained.

3.2.2.5 Electrical Conductivity

Electrical conductivity of the carbon foams was estimated by the four point technique as described in Section B.5 of Appendix B. For the foams prepared by Method-2, it was found that the resistivity of the foams decreased by increasing the number of impregnations with PFA. The electrical conductivity of the foams impregnated with PFA three times was about five times higher than the one impregnated with PFA once

(Table 3-1). This could be due to more solid walls as the successive impregnations with PFA might have filled in some voids and cracks in the walls of the structure.

Table 3-1: Summary of the physical properties of the carbon foams prepared by Method-2.

Carbon foam	After first impregnation	After second impregnation	After third impregnation
Porosity (%)	71 ± 5	59 ± 5	55 ± 5
Mechanical strength (MPa)	9 ± 1	11 ± 1	11 ± 2
Shrinkage (%)	43 ± 8	42 ± 7	42 ± 7
Bulk density (g cm^{-3})	0.32 ± 0.01	0.34 ± 0.02	0.38 ± 0.01
Strut (helium) density (g cm^{-3})	1.56 ± 0.09	1.55 ± 0.11	1.48 ± 0.07
Electrical conductivity (S cm^{-1})	102 ± 36	204 ± 47	492 ± 134

3.2.3 Method-3: Foaming with No Powder

In order to overcome the shrinkage problem of the foams prepared by Method-2, Method-3 was tested. In this method, addition of graphite powder to the foaming agents was eliminated. The polyurethane foams were impregnated with PFA (viscosity: 120 ± 10 cP) and they were cured at $80\text{ }^{\circ}\text{C}$ for 20 h. Their polymer burn out occurred as the foams were heating to the carbonisation temperature. Therefore, a higher heating rate was used for the debinding process compared to the previous methods to obtain homogenous structures from carbonisation of PFA. Fig. 3-13 shows the heating cycle of the impregnated foams prepared by Method-3.

Different properties of the carbon foams produced with this method investigated and are reported below.

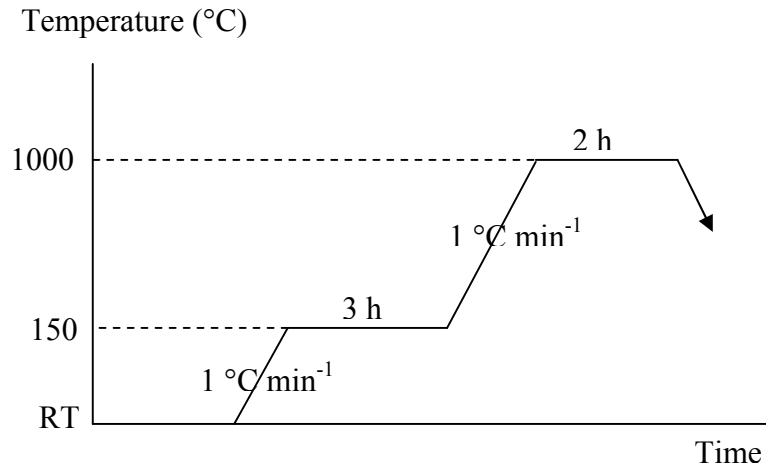


Fig. 3-13: Schematic diagram of heating cycle for debinding and carbonisation of the foams prepared by Method-3.

3.2.3.1 Morphology and Porosity

Field emission scanning electron microscopy of carbonised foam prepared by Method-3 after second impregnation with PFA is shown in Fig. 3-14. It can be seen from this figure that the pores were larger in Method-3 ($170 \pm 20\ \mu\text{m}$), compared to the two previous methods. Moreover, the structure obtained by Method-3 is not as uniform as the two previous methods and some closed pores were observed in the foams prepared by Method-3.

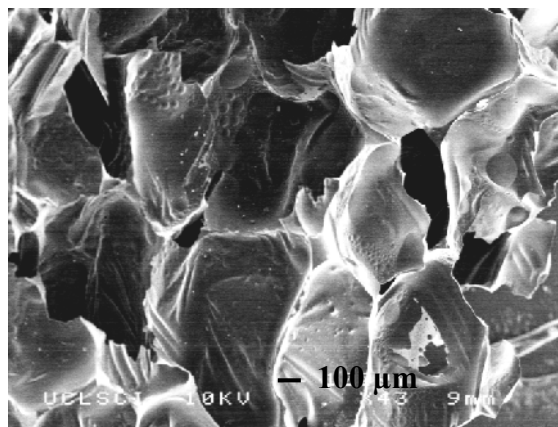


Fig. 3-14: Field emission scanning electron microscopy image of a carbonised foam prepared by Method-3 after second impregnation with PFA.

In order to investigate pore size distribution of the carbon foams produced by Method-3 mercury porosimetry technique was used. The pore size range of carbon foam prepared by Method-3 and impregnated with PFA once was examined and is shown in Fig. 3-15. It can be seen that the pore size ranges are between 1 to 300 μm with the majority of pores at $85 \pm 15 \mu\text{m}$. Therefore, the pores obtained by Method-3 were larger than the pores obtained by Method-2. This is in agreement with the results obtained from SEM and it could be due to a higher heating rate used during the debinding process in Method-3. Moreover, pore volume of the foams prepared by Method-3 and impregnated with PFA once found to be $37 \pm 3\%$ which was less than the foams prepared by Method-2. This could be due to some closed pores in the foams prepared by Method-3 that was also observed with SEM.

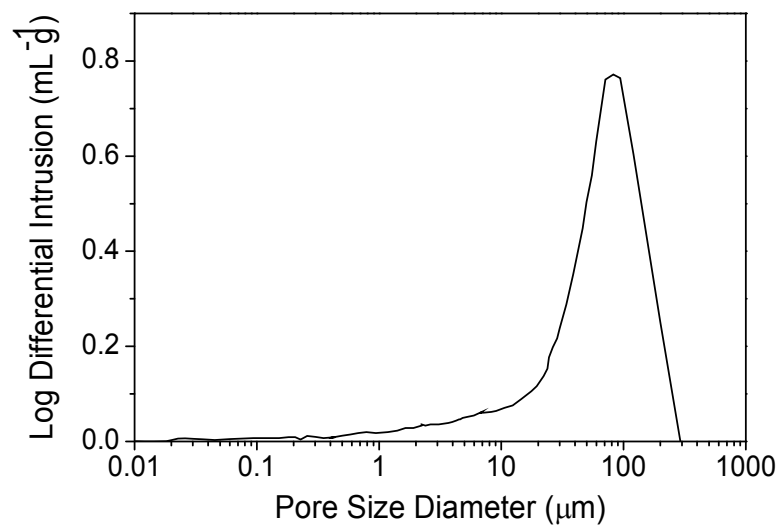


Fig. 3-15: Log differential intrusion (mL g^{-1}) vs. pore size diameter (μm) for carbon foam prepared by Method-3 and after first impregnation with PFA.

3.2.3.2 Shrinkage

Shrinkage of the carbon foams produced by Method-3, after polymer burn out and carbonisation, was $27 \pm 3\%$ which was much lower than the one prepared by Method-2. However, the foam samples in Method-3 reshaped after impregnation with PFA and therefore it was difficult to control their shape. This would especially be a problem for large-scale production where we want to shape the material.

3.2.3.3 Structure

Structure of the carbon foams prepared by Method-3 was examined with XRD and Raman spectroscopy. The XRD pattern and Raman spectrum of the foams prepared by Method-3 are shown in Fig. 3-16. The XRD pattern of the foams showed two broad bands at around 21 and 44° and a low intensity broad band at around 80° which represented an amorphous structure. Raman spectrum of the foams showed two broad bands of disordered carbon (D-band) and graphitic carbon (G-band) at 1357 and 1589 cm^{-1} , respectively which was also representative of an amorphous structure. The structures of the carbon foams prepared by Method-3 were similar to the structure observed for glassy carbon obtained from carbonisation of PFA in the previous chapter.

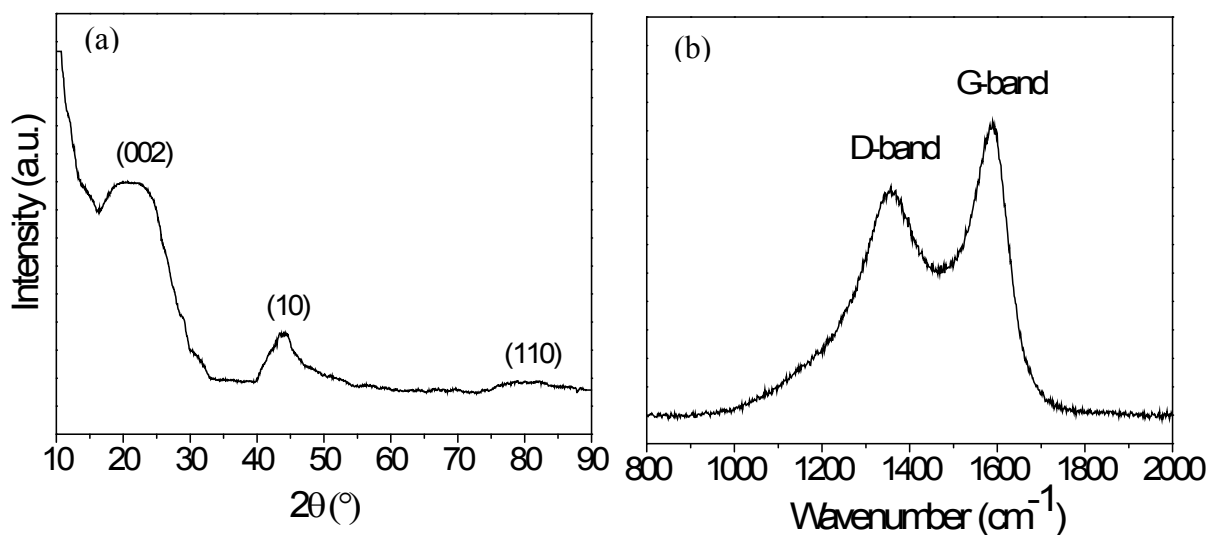


Fig. 3-16: (a) XRD pattern and (b) Raman spectrum of carbon foam prepared by Method-3 and impregnated with PFA once.

3.2.3.4 Density and Mechanical Strength

The density of the walls of the carbon foams prepared from Method-3 was measured by pycnometer and the density of the foams after first and second impregnations with PFA was found 1.585 ± 0.008 and 1.805 ± 0.012 g cm^{-3} , respectively. These densities are close to the density of the non-porous glassy carbon prepared from carbonisation of the synthesised PFA (1.899 ± 0.0176 g cm^{-3}). Bulk densities of the foams prepared by Method-3 after first and second impregnations were 0.14 ± 0.01 and 0.15 ± 0.01 g

cm⁻³, respectively; thus relative density of these foams was 0.085 ± 0.005 . These foam densities are lower than the densities obtained from Method-2. This could be because of the graphite powder in the structure of the foams prepared with Method-2 that has increased the relative density. Moreover, pore volume of the foams prepared with Method-3 was lower than Method-2 so we expected to have higher densities but the densities were found to be lower, thus foams prepared by Method-3 contained some closed pores.

Compression tests of carbon foams produced by Method-3 and impregnated with PFA once, twice and three times showed that the mechanical strengths of the foams were 0.08 ± 0.005 MPa. Fig. 3-17 shows typical compression behaviour of carbon foams prepared with Method-3. It can be seen from the figure that the foam had a brittle fracture and the first failure of the foams was considered as their compressive strength.

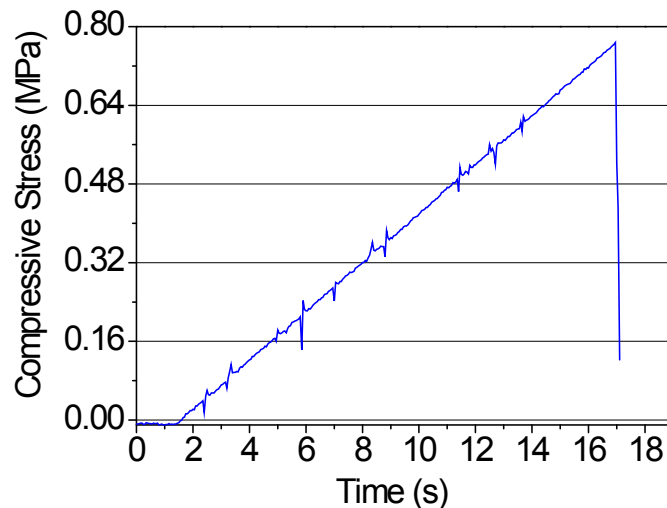


Fig. 3-17: Compressive stress (MPa) vs. time (s) graph obtained from the compression test for carbon foam prepared by Method-3 after polymer burn out.

Mechanical strengths of the carbon foams produced by Method-3 are less than the theoretical values to a great extent. For instance, a carbon foam impregnated with PFA once with a relative density of 0.085 would have a theoretical compressive strength of 2.9 MPa, whereas the compressive strength of the foams produced by Method-3 were less than 0.1 MPa. Therefore, by comparing the mechanical strengths of the foams produced by Methods 2 and 3 it can be concluded that the addition of

graphite powder to carbon foam structures in Method-2 improved the mechanical strength to a great extent.

3.2.3.5 Electrical Conductivity

Electrical conductivity of the carbon foams prepared by Method-3 was found $6 \pm 0.4 \text{ S cm}^{-1}$. This value found to be the same as the theoretical conductivity value for a porous glassy carbon with the same relative density (see Chapter 1, Fig. 1-24). The conductivity of the foams prepared by Method-3 was less than the foams prepared by Method-2 to a great extent. This was due to their much lower relative density and also not having graphite powder in their structures. Conductivity of the foams prepared by Method-3 did not change with successive impregnations with PFA.

3.2.4 Summary

Three different foaming methods were used to prepare carbon foams and their physical properties were examined. The carbon foams prepared with sintering (Method-1) were not very desirable as they were very low in mechanical strength and could not stand any pressure. This could be due to low sintering temperatures of the carbon (1000-2175 °C). These foams were impregnated with PFA (Method-2) to increase the mechanical strength. The foams prepared by Method-2 showed high mechanical strength close to the theoretical values due to the graphite powder in their structures. Their conductivity improved by successive impregnations with PFA however, it was still lower than the ideal value and needed improvement. For the carbon foams prepared by Method-2, it was found that the shrinkage of the foams was very high, hence another method without using any graphite powder (Method-3) was tested and the shrinkage reduced to a great extent. However, electrical conductivity and mechanical strength of these foams were very low and they were very brittle. This is especially not in favour because these foams reshaped during impregnation with PFA and they needed to be machined for a proper shape and they could not withstand machining due to their low mechanical strength. Moreover, they contained some closed pores that are not favourable as we want structures with continuous open pores to facilitate the reactant/product flow. Therefore, the carbon foams prepared with

Method-2 were the most suitable in terms of the objective properties set in Chapter 1 and the foams prepared by this method were used for further experiments. However, electrical conductivity of these foams needed to be improved which is discussed in the following sections.

3.3 Improving Electrical Conductivity of the Foams

In order to improve electrical conductivity of the carbon foams produced, catalytic graphitisation method was used (see Chapter 1 for further details). Nickel was selected as the catalyst due to its ability to enhance the electrical conductivity more than other catalysts such as iron and manganese [156], and also because of a relatively low heat treatment temperature required (due to a relatively low melting point). By adding different concentrations of nickel and different methods of addition to the carbon foams, different levels of graphitic carbon may be obtained to improve the electrical conductivity.

3.3.1 Materials Preparation

Nickel (II) nitrate hexahydrate ($\text{Ni}(\text{NO}_3)_2 \cdot 6\text{H}_2\text{O}$), was used as a graphitising catalyst and three methods were used for addition of the catalyst to the carbons. Four samples were prepared for each nickel concentration (approximately thirty samples for all the graphitisation tests). The three methods of nickel addition are explained below:

A. The carbon foams were impregnated with a solution of different concentrations of nickel nitrate in ethanol (0.01, 0.05 and 0.22 mol L⁻¹) and heated to evaporate the ethanol. Afterwards, the foams were heat treated under nitrogen flow (850 mL min⁻¹) at 1500 °C (slightly above the melting point of nickel, 1453 °C), with a heating rate of 2 °C min⁻¹, and held at this temperature for 5 h. Nickel particles were removed from the structure in order not to reduce the strength of the carbon due to inhomogeneity of the structure as well as, to avoid the effect of the metal particles in the electrochemical behaviour of the electrode. To remove the nickel particles, the carbon materials were washed with hydrochloric acid (~36%).

B. Polyfurfuryl alcohol (PFA) was prepared as described in Section 2.2 of Chapter 2, except that nickel nitrate was dissolved in the acid catalyst prior to addition to the monomeric alcohol and polymerisation. The catalyst concentrations of 0.004 and 0.11 mol L⁻¹ inside the furfuryl alcohol were examined. The carbonisation of the carbon foams impregnated with PFA, with nickel inside the FA, were carried out at 1500 °C under nitrogen flow (850 mL min⁻¹), at a heating rate of 2 °C min⁻¹, for 5 h. Removal of the nickel particles from the carbon material was done using hydrochloric acid as in Method-A.

C. PFA was synthesised according to Section 2.2 of Chapter 2 and was mixed with nickel nitrate (0.045 and 0.3 mol L⁻¹) before impregnation in carbon foams. The carbonisation and nickel removal were carried out the same as in Method-A.

3.3.2 Characterisation and Properties

3.3.2.1 Structure and Morphology

In order to investigate the effect of nickel addition to the structure of the foams, foams were prepared by addition of carbon powder to the structure instead of graphite powder. This was because the structure of the foams using carbon powders in their structure had an amorphous structure after impregnation with PFA and carbonisation (Fig. 3-18), whereas the foams that used graphite powder in their structures showed a graphite peak (Fig. 3-10). Thus in order to be able to recognise the graphitic peak from catalytic graphitisation, carbon foams with carbon powder in their structure was used for the graphitisation investigations.

X-ray diffraction (XRD) pattern of polyfurfuryl alcohol mixed with 0.3 mol L⁻¹ nickel nitrate, after carbonisation at 1500 °C for 5 h is shown in Fig. 3-19. It can be seen that the amorphous vitreous carbon resulted from carbonisation of PFA (Chapter 2, Section 2.4.1) was graphitised by adding Ni(NO₃)₂ to PFA prior to carbonisation.

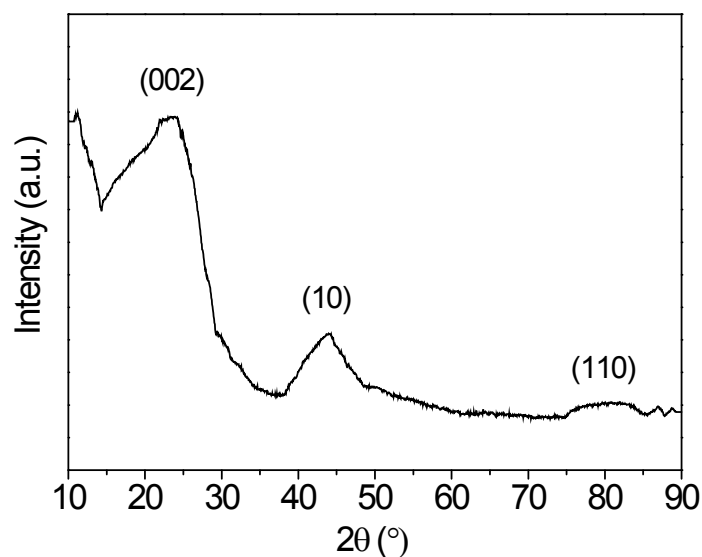


Fig. 3-18: XRD pattern of carbon foam prepared by Method-2 but using amorphous carbon powder instead of graphite powder.

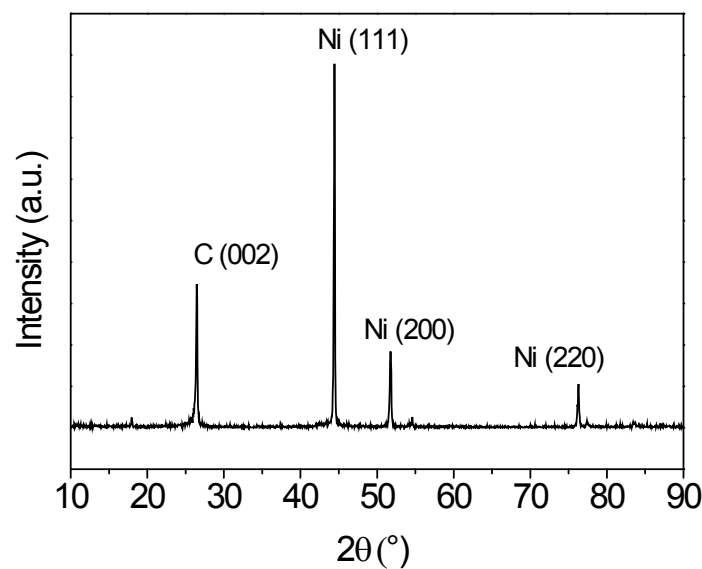


Fig. 3-19: XRD pattern of carbonised PFA+Ni(NO₃)₂.

Carbon foams were treated with different concentrations of nickel nitrate and their structures were examined by XRD. The XRD spectra of carbon foams with and without nickel treatments are shown in Fig. 3-20. As expected, the carbon foams without any treatments did not exhibit any characteristic diffraction peak, which is consistent with an amorphous framework. In contrast, the carbon foams treated with nickel exhibited intense XRD peaks at 26° and 26.5° which are denoted as graphitic

carbons T-component and G-component, respectively (as explained in Chapter 1, Section 1.6.2). However, they are not true graphite.

Impregnation of carbon foams with 0.01 mol L^{-1} nickel salt (Method-A) resulted in graphitic carbons T-component, whereas impregnations with 0.05 and 0.22 mol L^{-1} of nickel solutions resulted in graphitic carbons G-component. Therefore, depending on the catalyst concentration different graphitic components were obtained (see Appendix F for all the XRD patterns of the samples).

Adding different amounts of nickel nitrate to the FA before polymerisation (Method-B) also ended up in different graphitic components; T-component when adding 0.004 mol L^{-1} and G-component when adding 0.11 mol L^{-1} of nickel nitrate. XRD patterns of the samples produced by this method are presented in Appendix F.

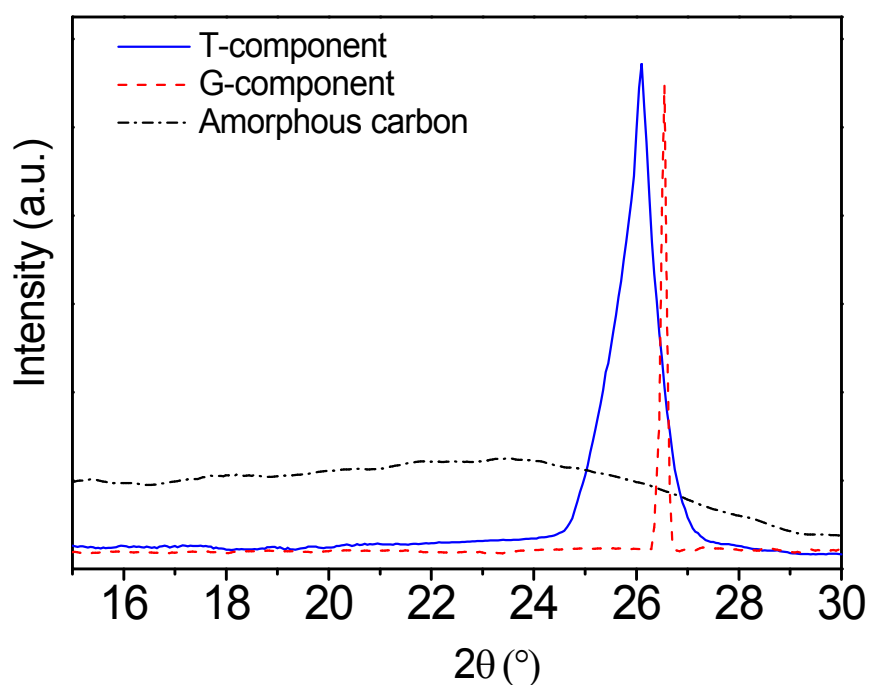


Fig. 3-20: XRD patterns of carbon foams before any nickel treatments (amorphous carbon) and after addition of 0.01 and 0.05 mol L^{-1} nickel salts by Method-A, produced T-component and G-component, respectively.

Mixing different concentrations of nickel nitrate to PFA before impregnation in carbon foams and eventually carbonisation (Method-C) resulted in amorphous structures (with the same XRD patterns as Fig. 3-18). This could be caused by uneven

distribution of nickel inside the resin. When the foams impregnated with the resin only a small amount of resin remained on the foam walls and therefore maybe the amount of nickel was too small to diffuse into the structure and change the amorphous carbon to graphitic. Moreover, examining with XRD shows the structure of the bulk material and if there are only some graphitic structures on the surfaces it does not reveal them.

Morphology of the treated carbons with nickel was studied by transmission electron microscopy (TEM). Fig. 3-21 presents the TEM image obtained for the carbon foam treated by addition of 0.004 mol L^{-1} nickel nitrate and using Method-B for the addition. XRD patterns showed that graphitic carbons T-component were produced by this treatment. In this image, presence of both types of graphitic and amorphous carbon structures was revealed which is a characteristic of turbostratic structure of T-component [160].

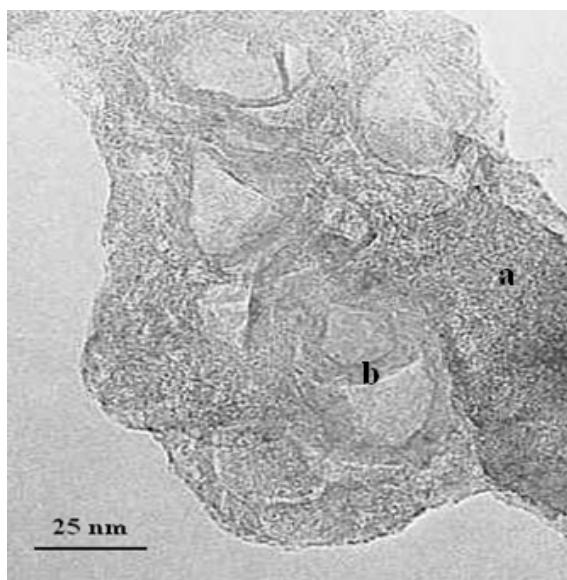


Fig. 3-21: TEM image of a graphitised carbon T-component obtained by addition of 0.004 mol L^{-1} nickel nitrate and using Method-B for catalyst addition. (a) amorphous carbon and (b) graphitic carbon.

Fig. 3-22 shows a TEM image of the graphitic carbon G-component obtained by addition of 0.22 mol L^{-1} nickel nitrate by Method-A. For this graphitic component 002 lattice fringes were observed. Moreover, some nickel particles left in the structure can be seen. No amorphous structure was observed in this structure.

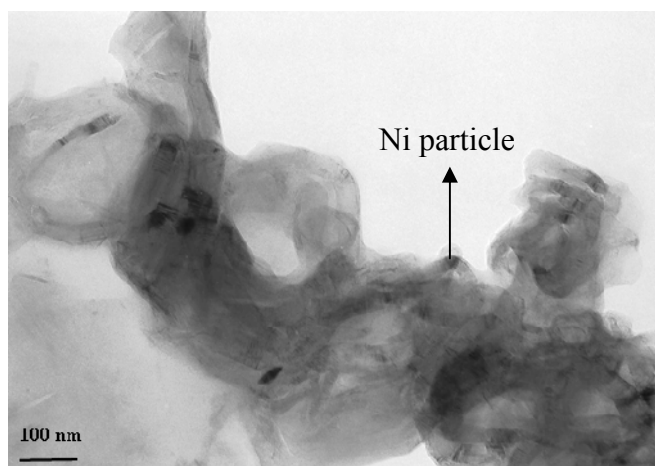


Fig. 3-22: TEM image of the produced graphitic carbon G-component obtained by addition of 0.22 mol L^{-1} nickel by Method-A.

In order to study the structure of the produced graphitic carbons further, interlayer spacing and crystallite sizes of the structures were calculated and are presented in the following sections. They are also compared to the values reported in the literature.

a) Interplanar Spacing

A structural parameter deduced from an analysis of the XRD spectra of the produced carbons was 002 plane spacing (d_{002}). Bragg's equation (Appendix B, equation B-1), $n\lambda = 2d\sin\theta$, was used to calculate d_{002} , where the wavelength of the X-ray beam (λ) for $\text{CuK}\alpha$ radiation was 0.15405 nm and the order of diffraction $n = 1$. The interplanar spacing obtained for the graphitic carbons T-component from Method-A was 0.341 nm, and from Method-B was 0.343 nm. The interlayer spacing of the graphitic carbons G-component obtained from Method-A and Method-B was 0.337 and 0.336 nm, respectively. These values are in the ranges reported in the literature for graphitic carbons T- and G-components (0.338-0.343 nm for T-component and \sim 0.335 nm for G-component [150]). The values obtained for d_{002} of the produced graphitic carbons G-component are closer to that of graphite (0.335 nm) than the ones for T-component.

b) Crystallite Size

Crystallite size along the c-axis (L_c) was obtained by applying Scherrer's formula (Appendix B, equation B-2), $L = K \lambda / B \cos \theta$, to the 002 XRD diffraction peak. In

the calculations the shape factor K was given a value of 0.9 [159], λ for $\text{CuK}\alpha$ radiation was 0.15405 nm, and B was the full-width-half-maximum of the diffracted beam. The calculated crystallite sizes of the T- and the G-components obtained by Method-A were 7.7 and 81 nm, respectively and for the T- and G-components obtained by Method-B were 9 and 54 nm, respectively. Therefore, the crystallite sizes of graphitic carbons produced of different components were in the ranges reported in literature (6-20 nm for T-component and > 50 nm for G-component [150]). Moreover, the crystallite sizes of the graphitic carbons G-component were larger than the T-component ones.

3.3.2.2 Degree of Graphitisation

Raman spectroscopy can be used to determine the degree of graphitisation of the carbon foams produced. Generally in graphite lattice, defects break down the hexagonal symmetry of the lattice and change the lattice vibrational modes which can be observed in Raman scattering. In theory, a single Raman line is expected for the hexagonal lattice of graphite and has been observed at 1575 cm^{-1} in natural graphite (G-band) [207, 208]. An additional Raman line was observed in glassy carbon and polycrystalline graphite at around 1355 cm^{-1} (D-band). This line resulted from graphite crystallites containing disorganised regions near crystal edges and lattice defects such as edge dislocation and lattice vacancies [208].

Raman spectra of the produced carbon foams with no nickel treatment, graphitic carbons T-component and graphitic carbons G-component produced by Method-A are shown in Fig. 3-23. It can be seen from the figure that the Raman spectrum obtained for the carbon foam without any treatments contain two broad bands, as might be expected for a disordered carbon [208]. Whereas, for the G-component, a strong G-band at 1580 cm^{-1} and a weak D-band at 1350 cm^{-1} was observed which clearly indicates the presence of graphitic structure. The increase of intensity and narrowing of the D-band was observed for the T-component compare to the G-component. A G-band at 1575 cm^{-1} was observed for the T-component. Raman spectra of the graphitic carbons T- and G-components produced by Method-B are presented in Appendix F.

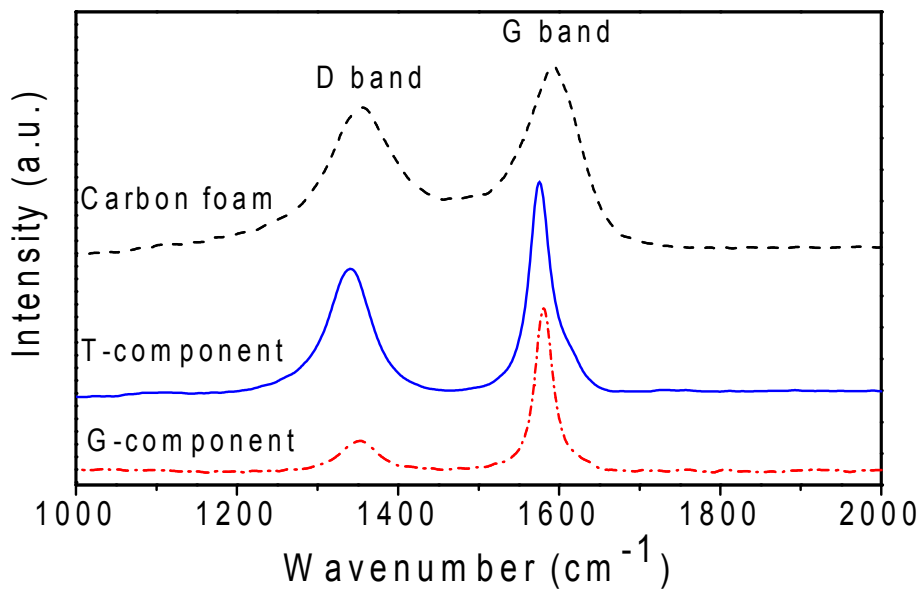


Fig. 3-23: Raman spectra of the amorphous carbon foam and the graphitic carbons of T-component and G-component produced by Method-A and by addition of 0.01 and 0.05 mol L⁻¹ nickel nitrate, respectively.

It was stated by Nakamizo *et al.* [207] that the intensity ratio of D-band to G-band, $R = I(1355 \text{ cm}^{-1}) / I(1575 \text{ cm}^{-1})$, is a measure of the extent of imperfection of order within the carbon structure. It increases with increasing imperfection. The Raman intensity ratios, R , for carbon foams produced with different structures of amorphous, T-component and G-component are given in Table 3-2. These values are the average of different regions of measurement as it was observed that the obtained Raman spectra depended on the selected region of measurement. The produced graphitic carbon G-component showed the lowest R values (0.21-0.28) and amorphous carbon showed the highest R value (0.67). These results indicate that the amorphous carbon is the least graphitic, and the G-component contains least imperfection in its structure. However, these results are contrary to the ones reported by Oya and co-workers [214]. They used phenol formaldehyde as the carbon precursor and the resin was doped with nickel to produce T- and G-components. Their results indicated that the T-component had a lower R value (0.23) than the G-component (0.90-1.05). However, they have mentioned this result as an unusual feature and have related it to the finely divided nickel used to produce the T-component compared to the larger sized particles of nickel used to prepare the G-component.

To investigate the effect of the widths of D- and G-bands (half-widths) on the R values, R_a value which represents the ratios of the area under the D-band over the area

under the G-band, was calculated for each produced carbon structure and the averages of different region of measurements are shown in Table 3-2. These values found to be consistent with the R values (the lowest R_a was obtained for the produced graphitic carbon G-component and the highest for the amorphous carbon foam).

Table 3-2: Different structures of the produced carbon foams and their structural properties.

Sample (Structure)	Method of fabrication*	L_c (nm)	d_{002} (nm)	$R = I_D/I_G$	$R_a = A_D/A_G$	σ ($S\ cm^{-1}$)
Carbon foam (amorphous)	---	---	---	0.67 ± 0.04	0.77 ± 0.06	5.5 ± 1
T-component	A	7.7 ± 0.2	0.341 ± 0.001	0.56 ± 0.13	0.70 ± 0.17	178 ± 40
G-component	A	81 ± 3	0.337 ± 0.001	0.28 ± 0.10	0.43 ± 0.13	263 ± 45
T-component	B	9 ± 0.2	0.343 ± 0.001	0.36 ± 0.19	0.48 ± 0.22	159 ± 50
G-component	B	54 ± 1	0.336 ± 0.001	0.21 ± 0.01	0.35 ± 0.04	250 ± 50

* Explained in Section 3.3.1

3.3.2.3 Electrical Conductivity

Electrical conductivity of the foams was estimated by the four point technique. This method is described in Appendix B and equation (B-9), $\rho = 2\pi S \frac{V}{I}$ where ρ is the resistivity of the material ($\Omega\ cm$), S is the probe spacing (cm), V is the potential difference between the inner probes (V) and I is the current (A), was used to calculate the resistivity of the foams and the conductivities are reported in Table 3-2. It can be seen from the table that the nickel doping was successful in improving the electrical conductivity and the conductivity of the produced carbon foams increased in the order of amorphous < T-component < G-component. This is in agreement with the degree of graphitisation of the produced carbon foams *i.e.* the more graphitic and ordered structures (G-component) showed higher conductivity.

3.3.3 Summary

In order to improve electrical conductivity of the produced carbon foams, catalytic graphitisation was used. Different concentrations of nickel (catalyst) and different methods of addition of nickel to the amorphous carbon foams were tested. Graphitic structures of T- and G-components were successfully produced. The results obtained showed that the G-component had crystallite size and interplanar spacing approaching that of graphite and its structure was more ordered than the T-component. Moreover, it was observed that the presence of graphitic carbon improved the electrical conductivity considerably (by a factor of up to 50), compared to the carbon foams with an amorphous framework

3.4 Electrochemical Behaviour of the Fabricated Foams

Cyclic voltammetry technique was used to examine the electrochemical behaviour of the different types of produced carbon electrodes. The charging and discharging capacitance at the electrode/electrolyte interface was evaluated using the cyclic voltammograms. A series of experiments was carried out to study the electrochemical behaviour of the carbon electrodes in the presence of ferricyanide. The main objectives were to examine the electrodes electrochemical activity and reversibility of the ferricyanide redox reactions. Electrochemical response also permitted to evaluate the Specific Electrochemical Surface Area (SESA) of the electrodes and heterogeneous rate constant (K_0) of ferricyanide at the electrodes.

Cyclic voltammetry measurements of the fabricated carbon electrodes were performed using a three electrode cell. A platinum counter electrode and a Ag/AgCl reference electrode were used in a 0.1 M NaCl solution as electrolyte (Fig. 3-24). The carbon electrode activity was assessed in terms of the heterogeneous electron transfer reversibility using 1 mM of potassium ferricyanide as the redox probe. Argon was used to de-aerate solutions and to keep air-free atmosphere over the solution during the measurements. All experiments were performed at room temperature (25 °C) and the solution was not stirred during the tests. The carbon foam electrodes were

sonicated in the electrolyte before electrochemical tests for 1-2 min, to remove the air bubbles trapped in the pores.

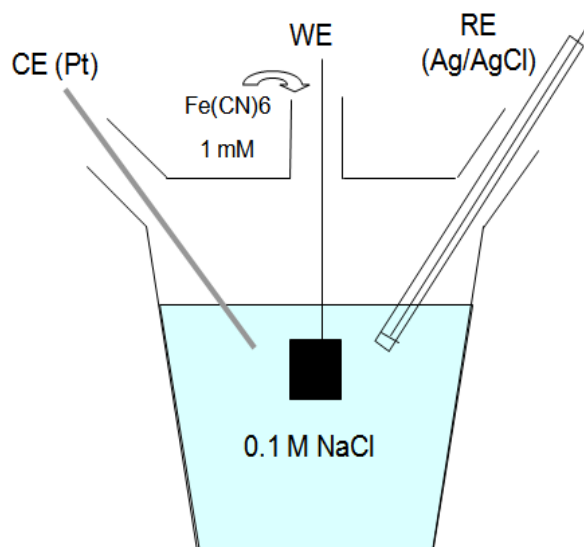


Fig. 3-24: Three electrode cell used for investigating the electrochemical behaviour of the produced carbon foams.

Carbon foams produced using amorphous carbon powder in their structures are named as “carbon foams” and the foams prepared using graphite powder are named “graphite foams” in the following investigations. For the carbon and graphite foams graphitised by nickel, all the electrochemical tests were performed after removing nickel from the electrodes. Nickel was removed with hydrochloric acid and elemental analysis indicated that all the foams contained < 25 ppm nickel after washing with the acid.

To examine the electrochemical properties of the carbon and graphite foams, twelve samples of each structure were prepared *i.e.* thirty six samples of carbon foams and thirty six samples of graphite foams. All the samples were impregnated with PFA twice and the graphitised foams T- and G-components were prepared by addition of 0.01 and 0.05 mol L⁻¹ nickel nitrates, respectively by Method-A explained in Section 3.3.1. Preparations of the produced foams to be used as electrodes in the three electrode cell for electrochemical investigations are explained in Appendix E.

Cyclic voltammograms of carbon foam and graphite foam are shown in Fig. 3-25a and b. In these voltammograms (as well as other voltammograms present), the

currents are normalised per unit surface area of the electrode obtained from nitrogen adsorption isotherm using the BET method (see Section C.3 of Appendix C for further explanation). It can be seen from the figure that the voltammograms obtained are relatively flat at potential ranges of -0.5 to 0.5 V for the carbon foam and -0.5 to 0.6 V for the graphite foam.

In order to investigate the effect of electrode pretreatment on the electrochemical behaviour of the electrodes and reduce OH concentration [215], graphite foam was heated from room temperature to 540 °C at a rate of 2 °C min⁻¹ and kept at this temperature for 10 h. From the CV curve of this electrode (Fig. 3-25b) it can be seen that the electrochemical window potential of this electrode is smaller (-0.1 to 0.1 V) than the graphite foam without any pretreatment and the background current is increased compared to the untreated electrode. The increase in background current of pretreated glassy carbon electrode has been reported previously in the literature [184]. This may be due to the change in the chemical nature of the carbon surface.

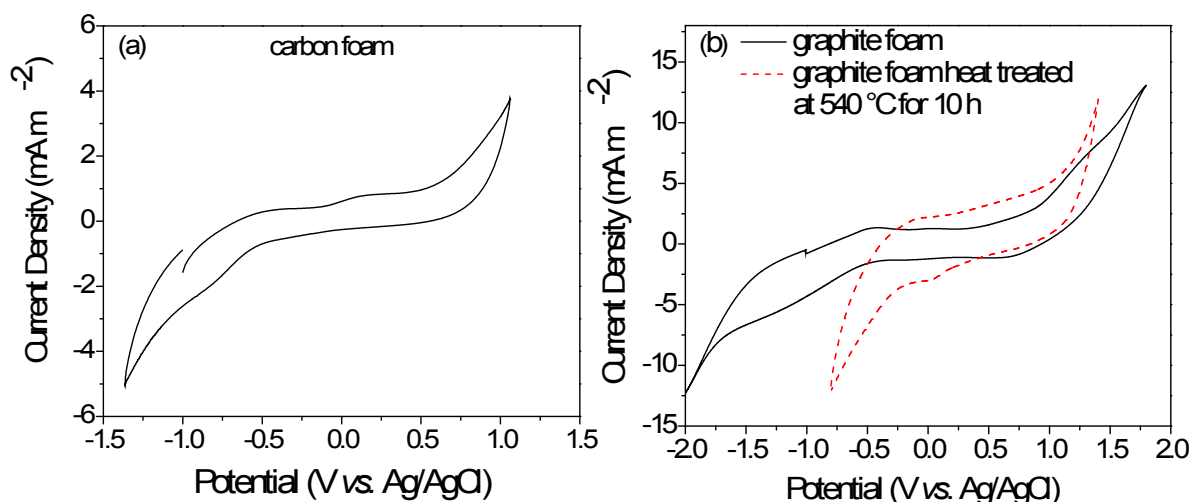


Fig. 3-25: CV curves of carbon foams produced by (a) carbon powder and (b) graphite powder, at a 100 mV s⁻¹ scan rate in an aqueous 0.1 M NaCl solution.

Electrochemical behaviour of the graphitised carbon foams using nickel as catalyst was investigated from the CV curves obtained for the graphitic structures of T-component and G-component. It can be seen from the voltammogram of the T-component (Fig. 3-26a) that the current increased compared to the ungraphitised carbon foam and the electrochemical window of this structure is relatively flat and no oxidation or reduction of nickel is observed. However, in the CV curve of the G-

component (Fig. 3-26b) no flat electrochemical window is observable. This may be due to the effect of nickel remained in the structure.

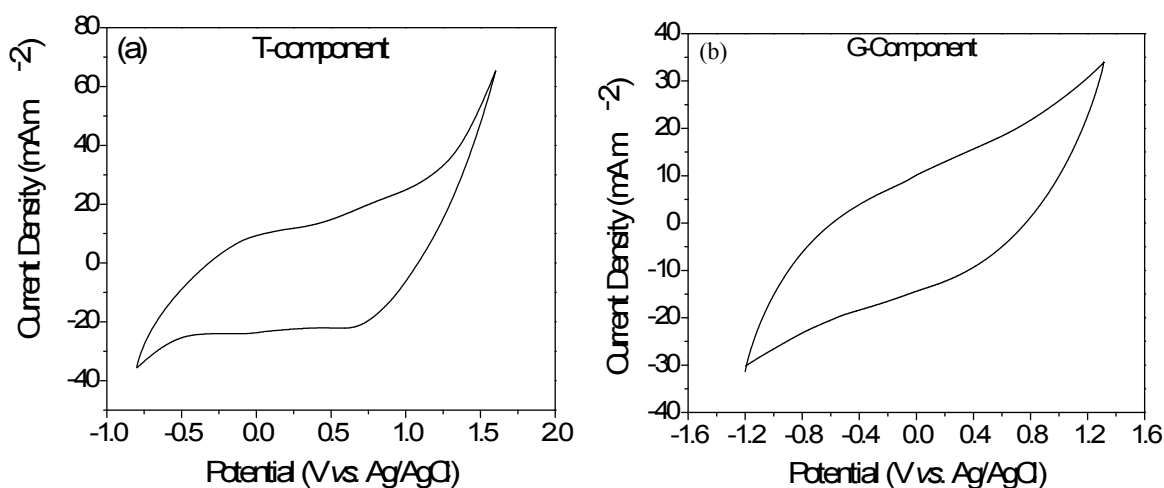


Fig. 3-26: CV curves of graphitised carbon foams produced by carbon powder and with different structures of (a) T-component and (b) G-component, at 100 mV s^{-1} scan rate in an aqueous 0.1 M NaCl solution.

Fig. 3-27 presents voltammetric curves of typical carbon and graphite foams with different structures and treatment in $1 \text{ mM ferricyanide}/0.1 \text{ M NaCl}$. In all the voltammograms obtained for different electrodes, it was observed that increase in scanning rate resulted in increase of the current peak intensity in cathodic and anodic reactions. In Fig. 3-27a it can be seen that the anodic peak shifted from -0.043 to 0.106 V and the cathodic peak shifted from -0.197 to -0.358 V . As it can be seen from Fig. 3-27b, carbon and graphite foams with G-component did not show any clear oxidation/reduction peaks. This could be due to the effect of nickel remained in the structure. For the other produced carbon and graphite foams, a quasi-reversible behaviour was observed from the voltammetric studies; the difference between the anodic and cathodic peak potentials (ΔE_p) was greater than $59/n \text{ mV}$ (n is the number of electrons involved in the reaction) and it increased with the scan rate (ν) (Fig. 3-28), the cathodic peak potential, E_{pc} , shifted to negative value when ν increased, and the anodic peak current increased with $\nu^{1/2}$ but did not keep the proportionality [118]. Fig. 3-27c shows that the anodic peak shifted from 0.0009 to 0.074 V and the cathodic peak shifted from -0.272 to -0.395 V by increasing the scan rate from 25 to 100 mV s^{-1} . The difference between the anodic and cathodic peak potentials at the scan rate of 100 mV s^{-1} , for graphite foam with turbostratic structure (T-component) is 0.47 V and for the heat treated graphite foam is 0.35 V (Fig. 3-27d). In both cases the reversibility

of the electrode has improved compared to the graphite foam. The graphite foam appeared to be irreversible at high scan rates ($\Delta E_p = 0.73$ V at the 100 mV s^{-1} scan rate, Fig. 3-28). Carbon foam T-component with $\Delta E_p = 0.26$ V at 100 mV s^{-1} scan rate showed the best reversibility among all the prepared electrodes. Moreover, reversibility of the carbon foam T-component ($\Delta E_p = 0.17$ V at 50 mV s^{-1} as it is shown in Fig. 3-28) is better than the reversibility of the reticulated vitreous carbon electrodes (RVC) with $\Delta E_p = 0.20$ V at scan rate of 50 mV s^{-1} in 1 mM ferricyanide/ 0.1 M KCl [69].

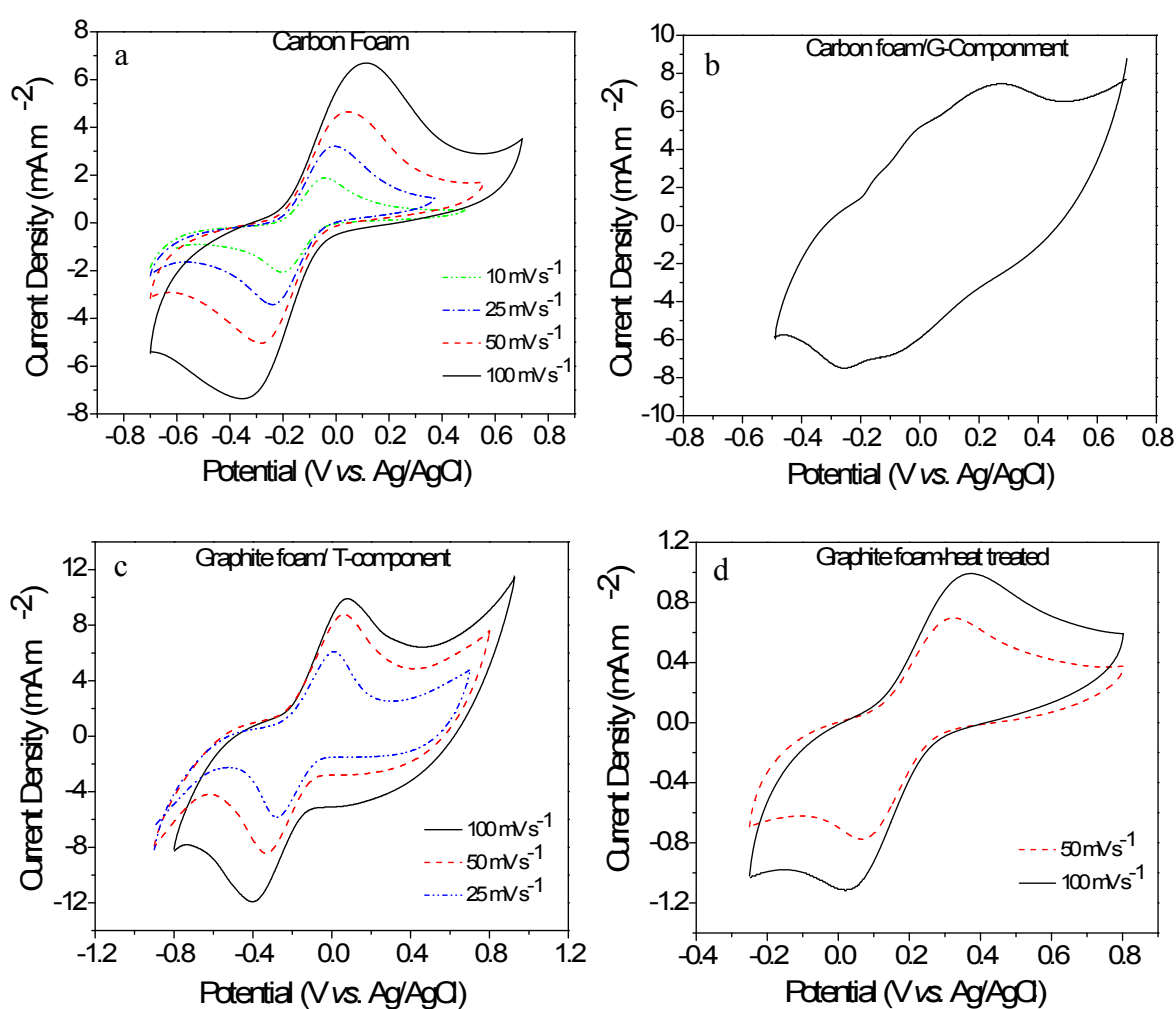


Fig. 3-27: Cyclic voltammetric behaviour of (a) carbon foam at different scan rates and (b) carbon foam/G-component at 100 mV s^{-1} (c) graphite foam-T-component at different scan rates (d) graphite foam heat treated at $540 \text{ }^\circ\text{C}$ for 10 h, at different scan rates and all in 1 mM ferricyanide/ 0.1 M NaCl.

The anodic current was used to evaluate the specific electrochemical surface area (by equation 1-5 in Section 1.5.1 of Chapter 1) of the produced foams and the values are shown in Table 3-3. Graphite foams showed greater specific electrochemical surface area (SESA) than carbon foams and among carbon foams it was observed that graphitisation increased the SESA from 31 to 107 $\text{cm}^2 \text{cm}^{-3}$. Moreover, the kinetic behaviour of the systems was studied by analysing the heterogeneous rate constant (K_0) value using equation 1-8 in Section 1.5.1 of Chapter 1. It was observed that the electron transfer rate of the carbon foam T-component was the highest (3.34 cm s^{-1}) amongst different types of the fabricated electrodes (Table 3-3).

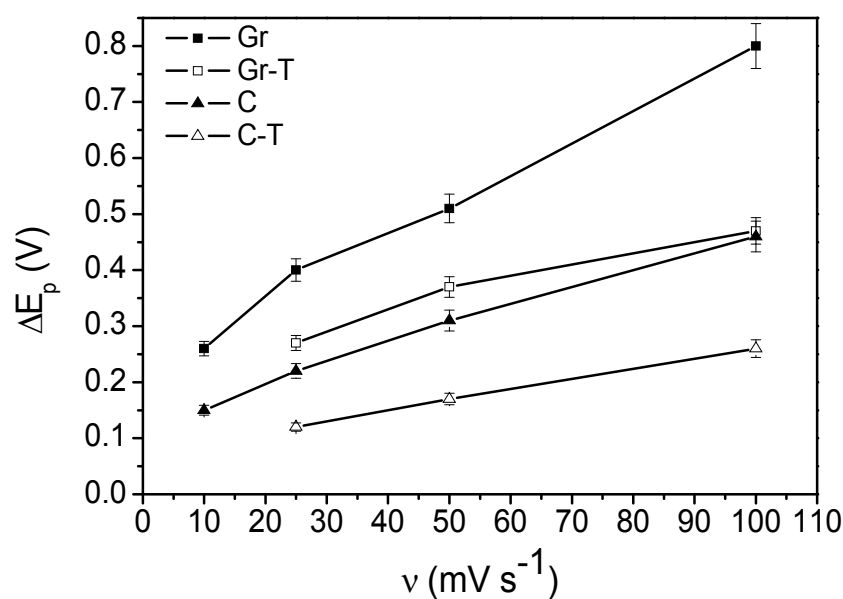


Fig. 3-28: ΔE_p as a function of scan rate in 1 mM ferricyanide/0.1 M NaCl for different produced electrodes.

The double-layer charging and discharging capacitance of the foams was estimated by cyclic voltammetry and using equation 1-7 (described in Section 1.5.1 of Chapter 1) and are shown in Table 3-3. It can be seen from this table that the capacitance of the graphitised foams are higher than the non-graphitised foams and the carbon foam T-component showed the highest capacitance.

Table 3-3: Calculated parameters of 1 mM ferricyanide/0.1 M NaCl and capacitance values at produced carbon electrodes from the CV curves.

Electrode	ΔE_p^a (V)	SESA ^b (cm ² cm ⁻³)	$10^2 K_0^c$ (cm s ⁻¹)	Capacitance ($\mu\text{F cm}^{-2}$)	
				Charge	Discharge
Graphite foam	0.73 ± 0.04	–	–	1.1	1.1
Graphite foam (T-component)	0.47 ± 0.02	180	1.38	8	8
Carbon foam	0.46 ± 0.03	31	1.24	1.6	0.8
Carbon foam (T-component)	0.26 ± 0.01	107	3.34	12	16

^a At 100 mV s⁻¹ scan rate.

^b D_0 of 1 mM ferricyanide in 0.1 M NaCl was assumed 7.2×10^{-6} cm² s⁻¹ [216, 217].

^c K_0 was calculated with the following equation: $K_0 = 2.78 \times 10^{-2} \Psi_0^{1/2}$.

3.5 Summary

Carbon foams with micrometric pore sizes were prepared by foaming method. The foams that contained carbon or graphite powder in their structure showed relatively high mechanical strength, close to the theoretical values, when impregnated with PFA. The electrical conductivity of the foams was improved by catalytic graphitisation using nickel as catalyst. Different graphitic components were produced and electrochemical behaviour of the amorphous and the graphitic structures was examined by cyclic voltammetry. In terms of reversibility and electron transfer rate, carbon foam T-component showed the best behaviour. The G-component did not show oxidation/reduction peaks for ferri-/ferro-cyanide.

Chapter 4: Ordered Porous Carbon Materials Derived from Templating Method

4.1 Introduction

Two critical issues in enzymatic biofuel cells are short lifetime (couple of weeks) and poor power density (in the order of sub-mW cm⁻²). These are related to enzyme stability, electron transfer rate and enzyme loading [218]. Many nanostructured materials, such as mesoporous media, nanoparticles and nanotubes, have been reported to be efficient hosts for enzyme immobilisation [219-221]. By means of nanostructures, the large surface area of these materials can increase enzyme loading and improve the reaction kinetics and hence the power density of biofuel cells.

Synthesis of mesoporous carbons with adjustable structures and properties has been a subject of research over the past decade and has been recorded in various reviews [10, 12, 86, 88]. Most of these mesoporous carbon materials are obtained in the form of powders. However, in recent years more people have reported the preparation of monolithic carbon materials from the templating route [49, 112, 222-224]. Nevertheless, the fabrication of carbon monoliths that are mechanically stable is still an important issue in the area of mesoporous carbons.

In this work, the sphere templating method has been used to fabricate ordered mesoporous and macroporous, high surface area carbon electrodes with homogenous pore size distribution. This method consists of using template spheres of a specific size and connecting them by annealing to create necks between the spheres. Hence, after infiltration of a resin, curing, carbonisation and removal of the template, a three-dimensional porous carbon structure can be obtained with interconnections between the spherical pores in the resulting carbons. Two different types of templates have been selected due to their high uniformity, *i.e.* polystyrene (PS) and silica spheres. These soft and hard spheres have been used to compare the resulting porous carbon structures from soft and hard templates as well as, to compare their processing methods. Polyfurfuryl alcohol (PFA) was used as the carbon precursor.

4.2 Preparation of Porous Carbon Monoliths and the Properties

Meso- and macro-porous carbon materials have been prepared using the templating method. Two types of templates *i.e.* soft and hard, were used with different methods of fabrication as explained below.

4.2.1 Using Polystyrene Template

Polymers are good candidates as templates for fabrication of porous carbon materials as they can be easily removed from the structure during heating in the carbonisation process. Polystyrene (PS) spheres were selected as the template because they can be synthesised with narrow particle size distribution. The commercially available PS spheres are expensive and also they are limited in particle sizes. The synthesis technique, properties of the synthesised particles, method of preparation of the porous carbon materials and the properties of the porous carbons are described in the following sections.

4.2.1.1 Synthesis of Polystyrene Spheres and the Properties

In order to synthesise monodispersed polystyrene spheres, an emulsifier-free emulsion polymerisation technique was used [225]. This technique is derived from conventional emulsion polymerisation in which polymerisation is carried out in the absence of emulsifiers. It is used for the preparation of polymer colloids with narrow particle size distribution and size range of 100-1000 nm [226].

Water used in the synthetic steps was deionised to a resistivity of 18 M Ω cm. 105 mL of styrene monomer was purified in a separatory funnel by washing four times with 100 mL of 0.1 M NaOH, followed by washing four times with 100 mL of water to wash the NaOH away. A five-necked round bottomed flask was connected to a mechanical stirrer, condenser and nitrogen inlet. Deionised water (850 mL) was added to the flask and heated to 70 °C before adding the 100 mL of the purified styrene.

In a separate bottle, 0.3315 g of potassium persulphate initiator was added to 50 mL of water and the solution was then heated to 70 °C and then added to the flask. The temperature was kept at 70 ± 2 °C while the solution was stirred. Depending on the stirring speed different sphere sizes were obtained. Two stirring speeds of 247 and 650 rpm were used for comparison of their effect on particle size and each test lasted for 24 h. The resulting latex spheres were filtered through glass wool to remove any large agglomerates.

Particle sizes of synthesised polystyrene spheres were examined by transmission electron microscopy (TEM) and the size distribution was determined using a particle size analyser. Figs. 4-1 and 4-2 show TEM images of PS spheres prepared at a stirring speed of 247 and 650 rpm, respectively. Figs. 4-1 (a) and (b) show the uniformity of the prepared spheres. It was found from the TEM images that the PS sphere sizes are 610 ± 10 nm when using a stirring speed of 247 rpm.

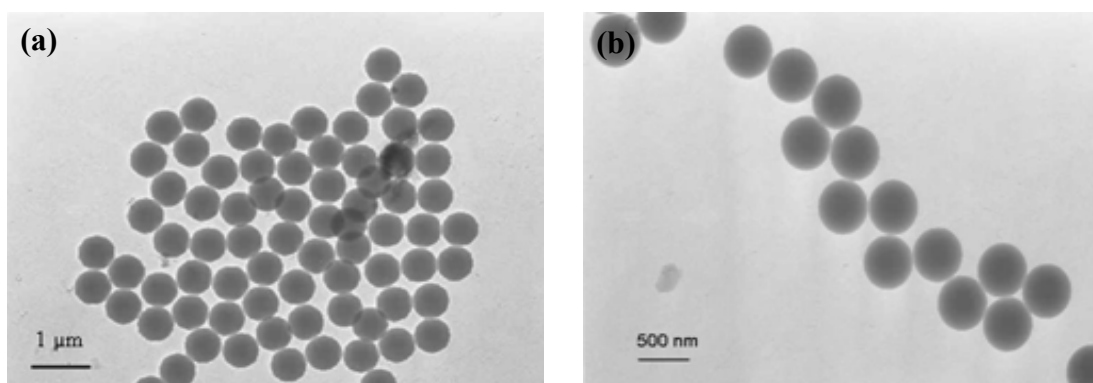


Fig. 4-1: TEM images of PS spheres synthesised using a stirring speed of 247 rpm and at (a) 8K and (b) 12K magnifications.

A TEM image of PS spheres prepared using a stirring speed of 650 rpm is shown in Fig. 4-2. It can be seen from this image that the diameters of the spheres are 163 ± 5 nm and which is much smaller than those due to a speed of 247 rpm. This decrease in particle size is due to the smaller sizes of nuclei formed at the high stirring speed. The size distribution of the synthesised PS spheres was further determined using a particle size analyser and the result is shown in Fig. 4-3. The majority of particle sizes synthesised at the stirring speed of 247 rpm were 651 ± 200 nm and the PS particle sizes prepared at the stirring speed of 650 rpm were 190 ± 4 nm. Thus, the results obtained from particle size analyser and TEM were close and matching. Therefore, PS

particles in different sizes, with narrow size distribution, were successfully synthesised by changing the stirring speed.

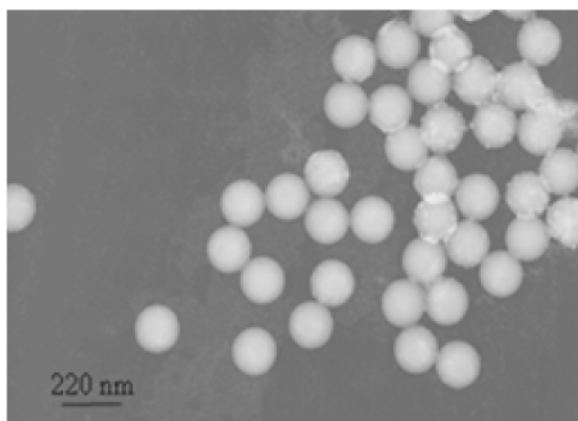


Fig. 4-2: TEM image of PS spheres synthesised using a stirring speed of 650 rpm.

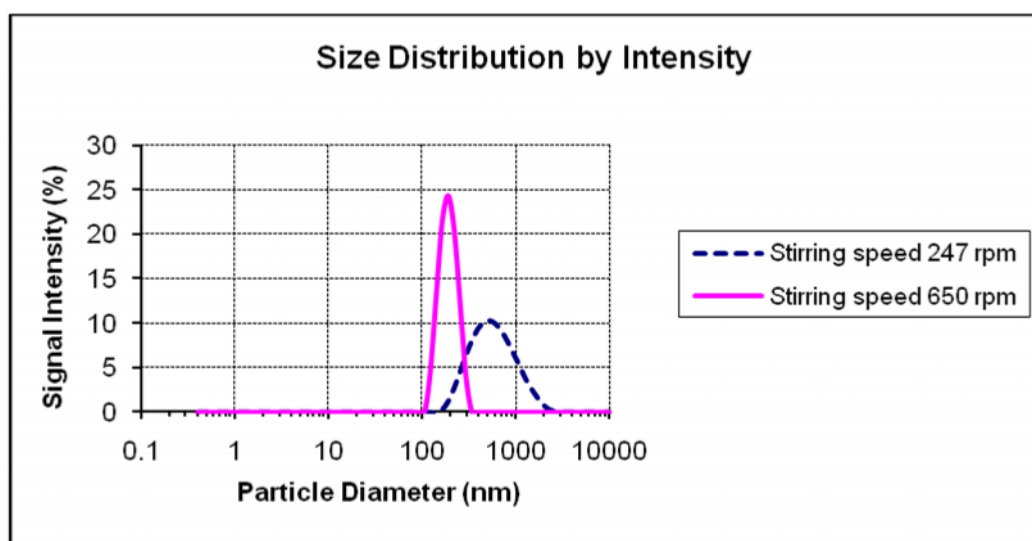


Fig. 4-3: Particle size distributions of the PS spheres prepared at a stirring speed of 247 and 650 rpm, respectively.

In order to identify the decomposition behaviour of the synthesised PS particles, thermogravimetric (TG)/differential thermal analysis (DTA) technique was used and the results are shown in Fig. 4-4. The synthesised PS was heated from room temperature to 600 °C at 2 °C min⁻¹. It was found that above 350 °C, the weight loss accelerated due to combustion of the polystyrene, following a highly exothermic process. The exothermic decomposition of PS can be detrimental to the formation of porous carbons with intact structures (free from “cracks” and wall “defects”) if the gas production results in excessive bubbling.

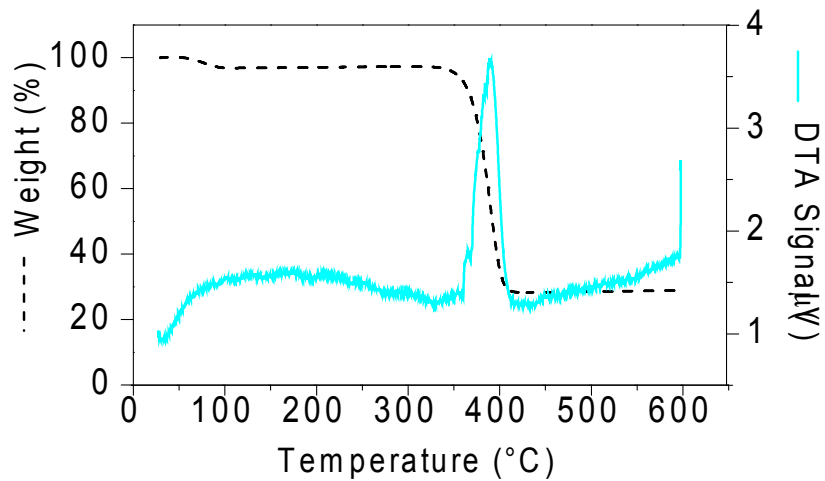


Fig. 4-4: TGA (--) and DTA (-) curves of PS spheres heated from RT to 600 °C at 2 °C min⁻¹ in nitrogen.

4.2.1.2 Fabrication of Porous Carbon Monoliths and Their Properties

In order to prepare porous carbon monoliths from PS templates, the colloidal crystals of the PS need to be shaped and ordered by centrifugation. This method speeds up sedimentation significantly, so that close-packed spheres can be obtained in a matter of hours. A schematic diagram of synthesising porous carbon from PS template is shown in Fig. 4-5. The synthesised polystyrene spheres suspended in water were placed inside blocked syringes and centrifuged at 900-1500 rpm for 15 to 22 h, depending on the sphere sizes.

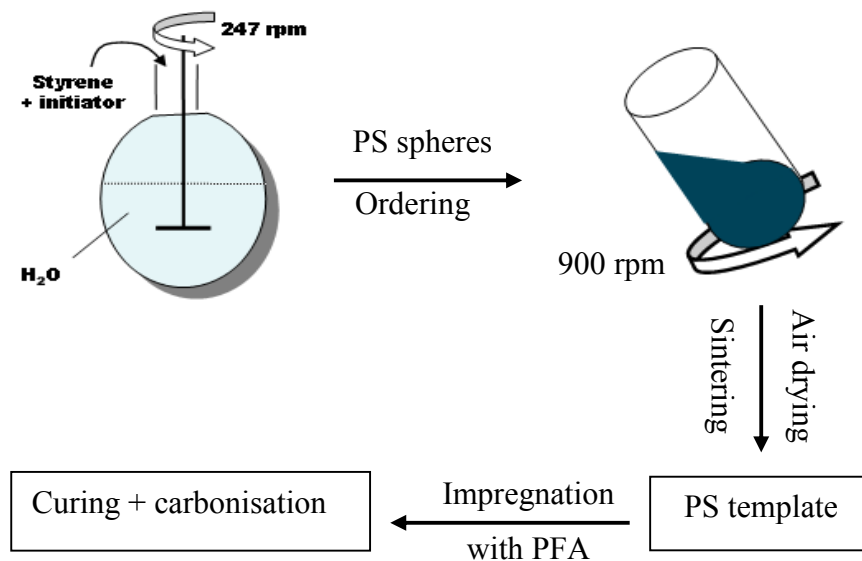


Fig. 4-5: Schematic diagram of synthesising porous carbon from PS template.

The ordering of the PS spheres was investigated by field emission scanning electron microscopy (Fig. 4-6). It can be seen from this figure that centrifugation of the latex spheres resulted in a hexagonal close packed (hcp) structure. Some disorderness was observed by SEM that was likely created during the preparation of colloidal crystals for the SEM examinations.

After centrifugation, the chunks of PS spheres were air dried for 3 to 5 days and sintered at 90 °C (around the glass transition temperature of polystyrene [105]) for 10 min to improve bonding between the spheres and strengthen the structure. The sintering time was optimised by sintering the PS spheres at 90 °C for 5, 10, 15, 30 and 60 minutes and examining the structures after sintering, as well as after impregnation with polyfurfuryl alcohol (PFA) and carbonisation.

The PS templates were removed from the syringes and impregnated with PFA by immersing the templates into the resin. PFA of viscosities of 100-2000 cP were used and the templates were firstly soaked in a low viscose resin of approximately 100 cP for 2 days to completely wet the templates and facilitate impregnation of high viscose PFA into the templates. To achieve carbon structures with strong walls, the templates were impregnated with high viscose resins. The templates were soaked in resins with viscosities of approximately 1000 and 2000 cP and left in each viscosity for 2-4 days. The viscosity of the PFA was adjusted by adding ethanol to the resin.

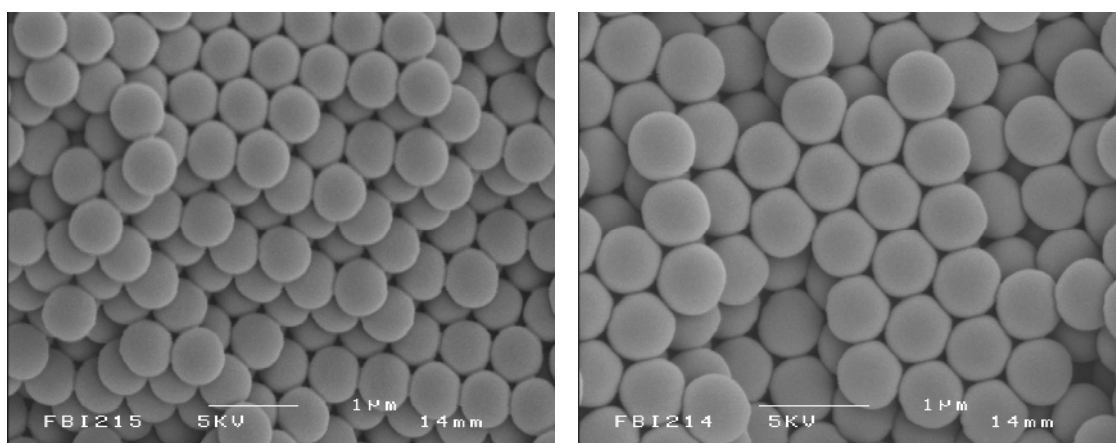


Fig. 4-6: SEM images of PS spheres after centrifugation at 950 rpm for 15 h.

The excess PFA on the surfaces of the samples was wiped off by tissue and the samples were cured under a nitrogen flow of 850 mL min^{-1} at $80 \text{ }^\circ\text{C}$ for 20 h. After curing, the samples were carbonised under nitrogen flow (1000 mL min^{-1}) at a heating rate of $0.5 \text{ }^\circ\text{C min}^{-1}$ from RT to $1000 \text{ }^\circ\text{C}$ and kept at this temperature for 3 h. The carbonisation cycle including removal of the latex template from the structure is shown in Fig. 4-7. According to the decomposition behaviour of PS obtained from TGA, the removal of PS template starts from $320 \text{ }^\circ\text{C}$ thus a plateau of 3 h was placed at this temperature. In this carbonisation cycle, a slow heating rate of $0.5 \text{ }^\circ\text{C min}^{-1}$ was used to facilitate more even melting and decomposition of PS templates and avoid excessive bubbling. A slower heating rate of $0.1 \text{ }^\circ\text{C min}^{-1}$ was also tested however, a better structure was obtained for the porous carbons carbonised with a $0.5 \text{ }^\circ\text{C min}^{-1}$ heating rate. Moreover, a fast nitrogen flow of 1000 mL min^{-1} was used to aid transport of the by-products.

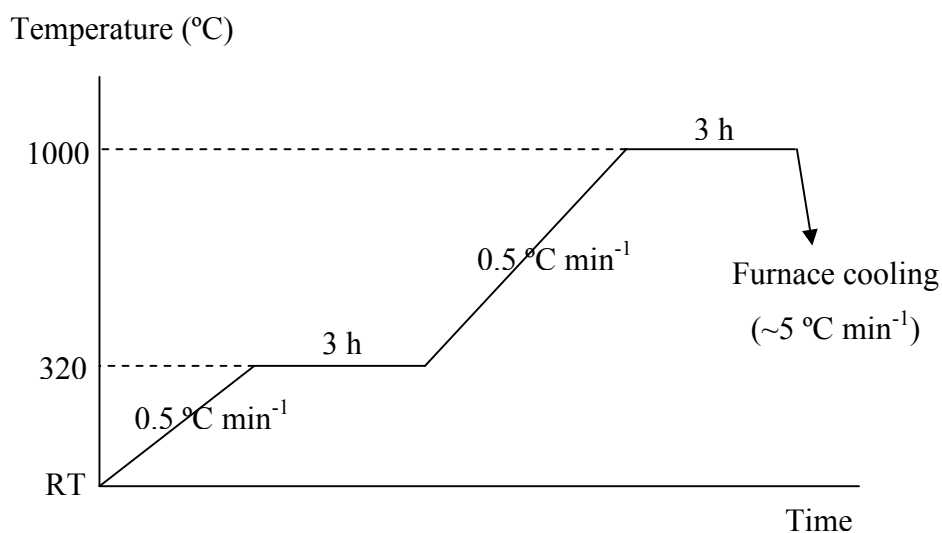


Fig. 4-7: Carbonisation cycle of PFA resin + PS template.

Fig. 4-8 shows field emission scanning electron microscopy (SEM) images of porous carbon resulted from the $610 \pm 10 \text{ nm}$ PS templates. It can be seen from the figure that the pores were $400 \pm 30 \text{ nm}$ in diameter and the diameters of windows between the pores were $170 \pm 20 \text{ nm}$. Shrinkage of the structure after template removal was estimated according to the size of latex spheres and pore size diameters which was found to be 31-35%. This result is similar to the shrinkage reported in the literature (26-34%) for macroporous structures of inorganic solids resulted from PS templates

[225]. As a result of this shrinkage, some cracks were observed in the structure and it was not possible to prepare porous carbon monoliths with intact structure from this type of template and therefore no further property examinations were carried out.

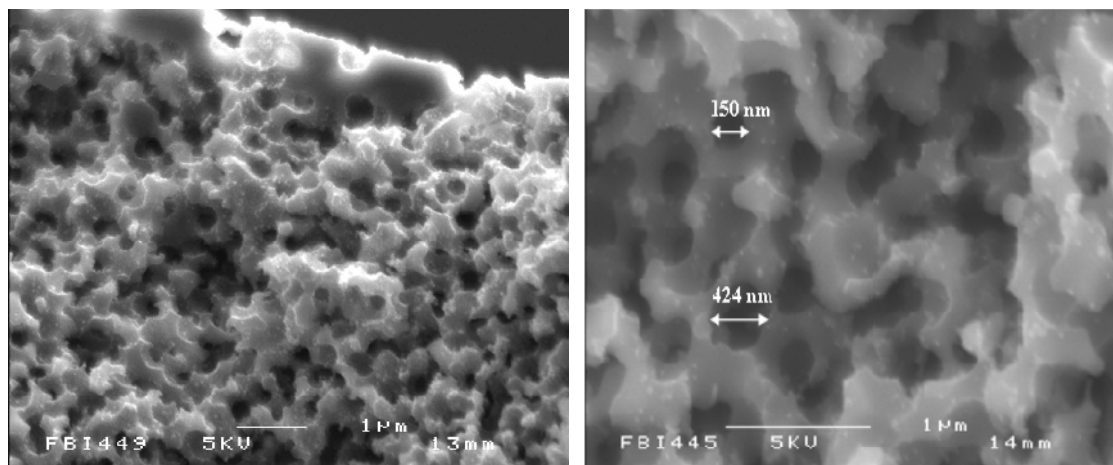


Fig. 4-8: Porous carbon resulted from PS template of an initial PS sphere size of 610 nm.

4.2.2 Using Silica Template

Silica beads are another suitable type of templates that can be used for preparation of porous carbon monoliths. Two kinds of colloidal silica have been used for preparation of meso- and macro-porous carbon materials. They were both commercially available and one had particle sizes of 70-100 nm, Snowtex-Z (Fig. 4-9a) and the other had an average particle size of 22 nm, Ludox AS-40 (Fig. 4-9b).

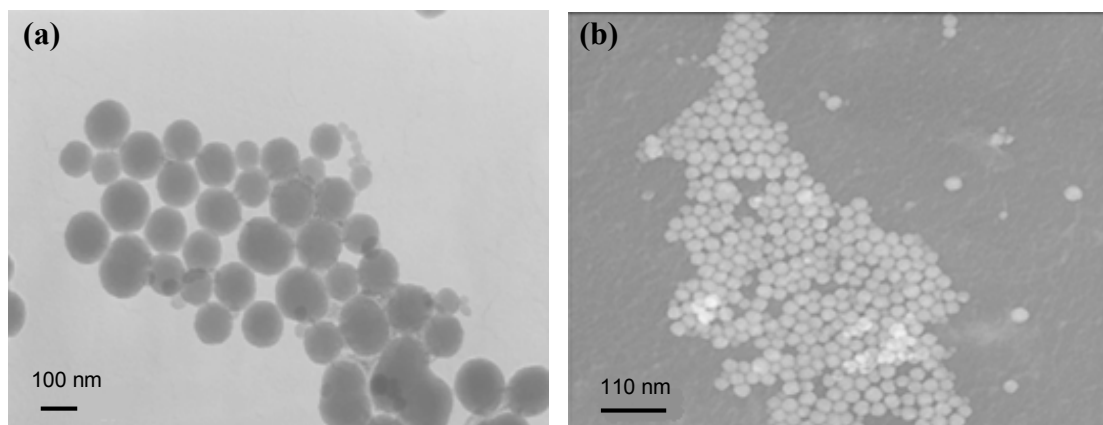


Fig. 4-9: Transmission electron micrographs of the colloidal silica as received (a) Snowtex-ZL with particle sizes of 70-100 nm and (b) Ludox AS-40 with an average particle size of 22 nm.

4.2.2.1 Fabrication of Porous Carbon Monoliths

Two different methods have been used for fabrication of meso- and macro-porous carbon monoliths from the silica templates and are reported below.

Method-I

In this method centrifugation was used to order the silica spheres, whereby it is possible to collect the small particles floating on top of the colloidal solution and therefore obtain a more uniform silica particle size distribution in the resulting template structure. After centrifugation the spheres were dried at 120 °C for about 3 days [87]. Sintering of the spheres was performed at 750 °C according to the thermal analysis of SiO₂ particles obtained from Nissan Chemicals (Fig. 4-10). Sintering time was optimised by sintering the silica templates for 0.5, 1 and 2 h and the best carbon structure was obtained after 1 h of sintering. It can be seen from the TG and DTA analysis of silica dry gel that at about 150 °C water evaporates from the silica gel results in a weight loss. Furthermore, dehydration of the silanol groups at 400-700 °C causes another small weight reduction. Up to this temperature the particles remain unchanged but at approximately 800 °C, surface fusion between the silica particles takes place [227].

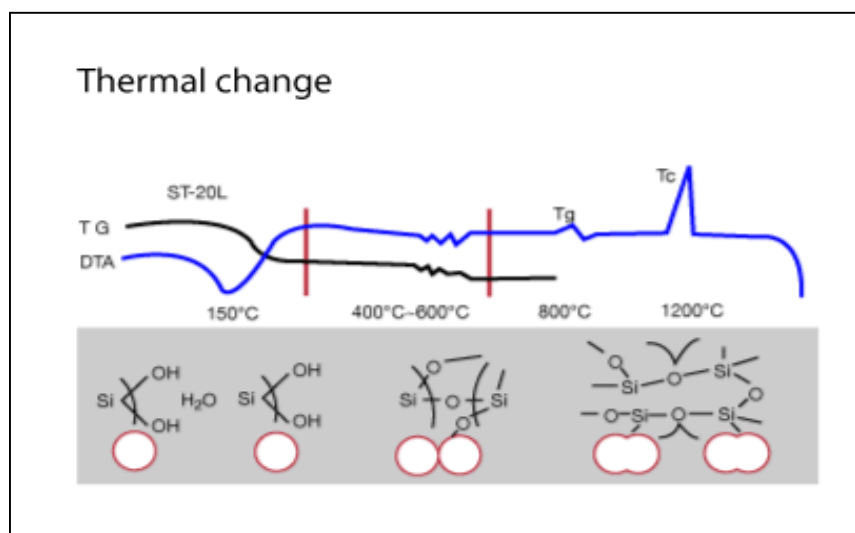


Fig. 4-10: Differential thermal analysis (DTA) and thermal gravimetric (TG) analysis of silica dry gel. The transition of the silica particles is highlighted in the illustration [227].

After preparation of the silica templates (Fig. 4-11a), the templates were impregnated with PFA (viscosity: 2200 ± 100 cP). Impregnation of PFA into the silica templates was facilitated by centrifugation at 1000 rpm for 48 h. After removal of the excess PFA from the samples surfaces, the impregnated samples were cured under a nitrogen flow of 850 mL min^{-1} at $80 \text{ }^\circ\text{C}$ for one day. Afterwards, they were carbonised under a nitrogen flow of 850 mL min^{-1} from 80 to $1000 \text{ }^\circ\text{C}$ at a heating rate of $1 \text{ }^\circ\text{C min}^{-1}$ and kept at this temperature for 2 h (Fig. 4-11b). After carbonisation, the samples were soaked in 40% hydrofluoric acid (HF) at room temperature for two days to dissolve the silica templates. The resulting carbon monoliths were soaked in a solution of calcium carbonate (CaCO_3) in water for ~ 12 h to neutralise the HF and then were washed with distilled water to remove the CaCO_3 and dried in an oven.

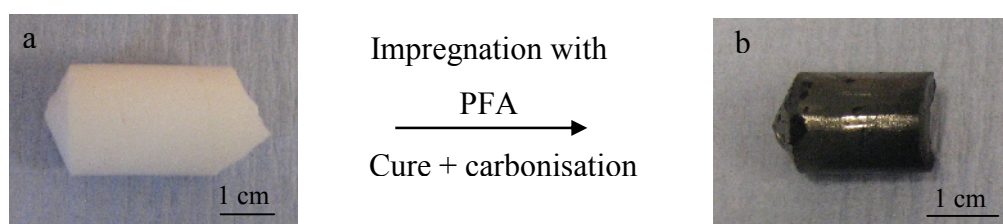


Fig. 4-11: A silica template and resulted macroporous carbon from the template produced by Method-I.

Method-II

To facilitate the template fabrication and impregnation and also to prepare more stable template and carbon structures, silica templates were prepared (according to the method reported in the literature [228]) by drying the colloidal silica, filling a cylindrical steel die (1.25 cm in diameter) with the dried silica powders and compressing the powders under a pressure of 40 MPa (this is an optimised pressure after testing various pressures to get strong silica templates and carbon structures). This resulted in mesoporous silica monoliths (Fig. 4-12a) that were sintered from RT to $750 \text{ }^\circ\text{C}$ at a heating rate of $1 \text{ }^\circ\text{C min}^{-1}$ and then kept at $750 \text{ }^\circ\text{C}$ for 1 h. Afterwards, the mesoporous silica templates were impregnated with oxalic acid (with a template to OxA weight ratio of 100/4), which was used as a catalyst for polymerisation of furfuryl alcohol (FA). This impregnation was performed by immersing the templates in an ethanol solution of oxalic acid and evaporating the ethanol from the templates. The oxalic acid treated templates were then impregnated with FA by immersing the samples in the FA for 7 h. The impregnation time was optimised after immersing the

samples in the FA for various times and cutting the samples to half to check whether the FA has penetrated to the middle of the sample.

The polymerisation of FA was carried out at 80 °C for 24 h (Fig. 4-12b). Afterwards, the monoliths were cured at 150 °C for 3 h under a nitrogen flow of 850 mL min⁻¹ and subsequently heated to 1000 °C at a heating rate of 1 °C min⁻¹ and kept at this temperature for 2 h for carbonisation. The silica templates were removed by immersing the samples in a 40% HF with the same procedure as explained in Method-I. A picture of the resulting mesoporous carbon monolith can be seen in Fig. 4-12c.

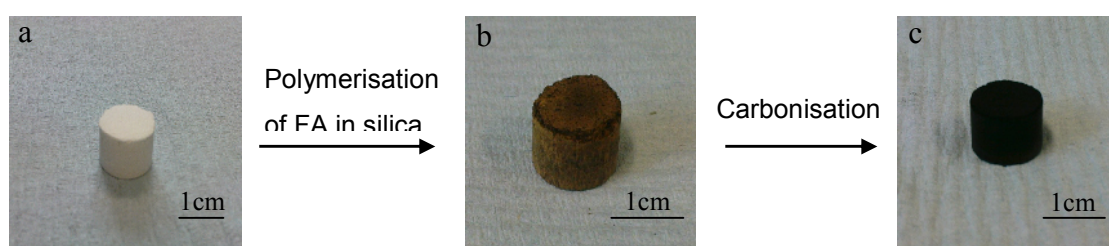


Fig. 4-12: Picture of (a) mesoporous silica template, (b) silica template after impregnation with OxA and FA and in situ polymerisation, (c) mesoporous carbon resulted from carbonisation and silica removal, all were produced by Method-II.

4.2.2.2 Properties of the Fabricated Carbon Monoliths

The morphological and physical properties of the meso- and macro-porous carbon monoliths prepared using the silica templates were examined with different techniques and are reported in the following sections.

a) Carbon Yield

Carbon yield of the porous carbons prepared using the silica templates by Method-II was estimated by considering the weights of template, template + polymer and template + carbon after carbonisation of the polymer. Carbon yield of the mesoporous carbon monoliths prepared by the silica with average particle size of 22 nm was found to be $30 \pm 4\%$ and carbon yield of the macroporous carbon monoliths prepared using 100 nm silica particles was found $37 \pm 2\%$. These carbon yields are lower than carbon yield of polyfurfuryl alcohol (50-55%) found in Section 2.3.2 of Chapter 2. This might be due to a low degree of polymerisation of the FA. To improve the

polymerisation, more oxalic acid was used and it was observed that by increasing the weight ratio of the 22 nm silica templates to oxalic acid from 100/4 to 100/9, the carbon yield increased from 30 to 36%.

b) Morphology and Shrinkage

Morphologies of macroporous and mesoporous carbon monoliths prepared by Methods-I and II examined by SEM and the images are presented in Figs. 13 and 14, respectively. The pores in Fig. 4-13 were found 87 ± 16 nm in diameter and shrinkage of this structure was estimated according to the size of silica particles and pore size diameters and found to be $14 \pm 8\%$. From Fig. 4-14 it was observed that the pores were very uniform and were 20 ± 2 nm in diameter. Shrinkage of $9 \pm 5\%$ was found for this structure. The shrinkage observed for the porous carbon structures obtained from the silica templates is mainly due to the carbonisation of the PFA and not the thermal treatment of the silica templates during the carbonisation [48].

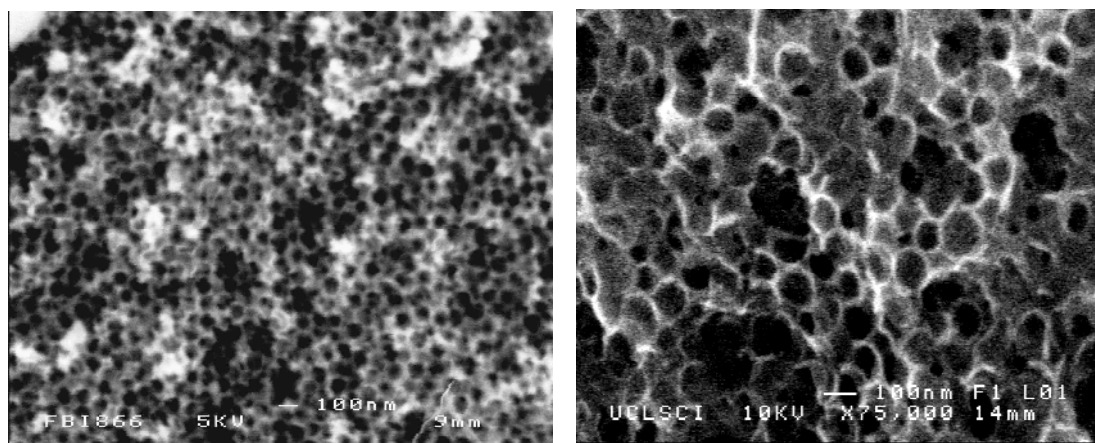


Fig. 4-13: Ordered macroporous carbon prepared from silica template using Method-I.

Comparing the carbon structures prepared by Methods-I and II, it can be seen that the structure of the macroporous carbon materials obtained by Method-I (preparing the silica templates by centrifugation) contains some big holes and the structure is not as intact as the mesoporous carbon monoliths obtained by Method-II (preparing the silica templates by applying pressure). Moreover, carbon monoliths were easily prepared in different shapes and sizes using different die shapes and sizes, by Method-II. Therefore, Method-II is more suitable for producing porous carbon monoliths and

this method of fabrication were also used for preparation of macroporous carbon materials from silica template and the obtained structures were improved significantly compared to the structures obtained using Method-I and thus only the properties of the porous carbon monoliths produced by Method-II were further examined.

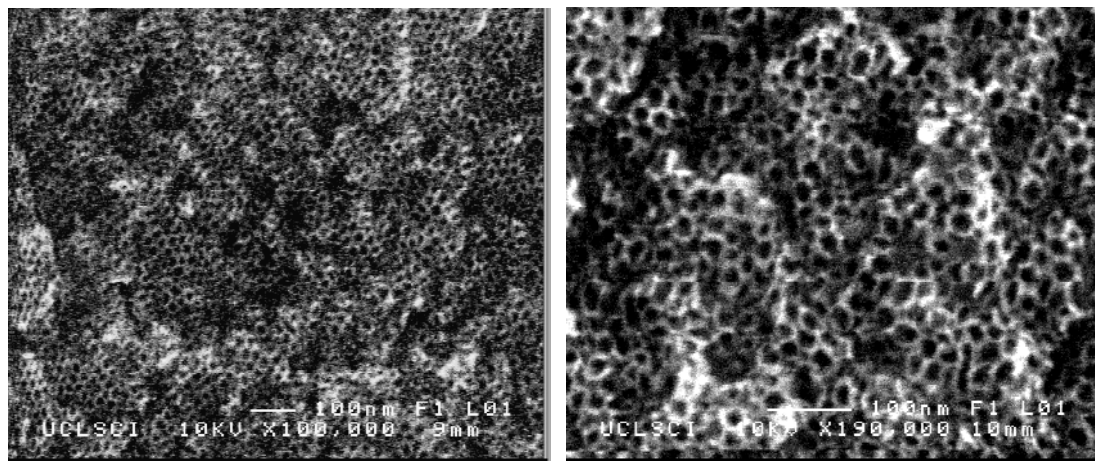


Fig. 4-14: Highly ordered mesoporous carbon prepared from silica template using Method-II.

c) Porosity and Surface Area

Nitrogen adsorption isotherms of the mesoporous silica template and the prepared carbon monolith are shown in Fig. 4-15. It can be seen from the figure that the isotherms were of type IV with hysteresis loops of type H2 (see Section C-3 of Appendix C for further explanation). This reflected the mesoporous character of these materials with relatively uniform channel-like pores [229]. The BET surface areas of the mesoporous silica template and the carbon monolith were found 119 and 325 m² g⁻¹, respectively. Pore size distribution (PSD) curves of these samples are shown in Fig. 4-15, inset. It can be seen from the PSD curves that the estimated values of the pore widths of the silica template and the carbon monolith at the PSD maximum were 7.7 and 10.4 nm, respectively. Pore volumes of the silica template and the carbon monolith were estimated from the volume adsorbed at a relative pressure close to the saturation vapour pressure *i.e.* a relative pressure of ~0.99 [230], and are reported in Table 4-1.

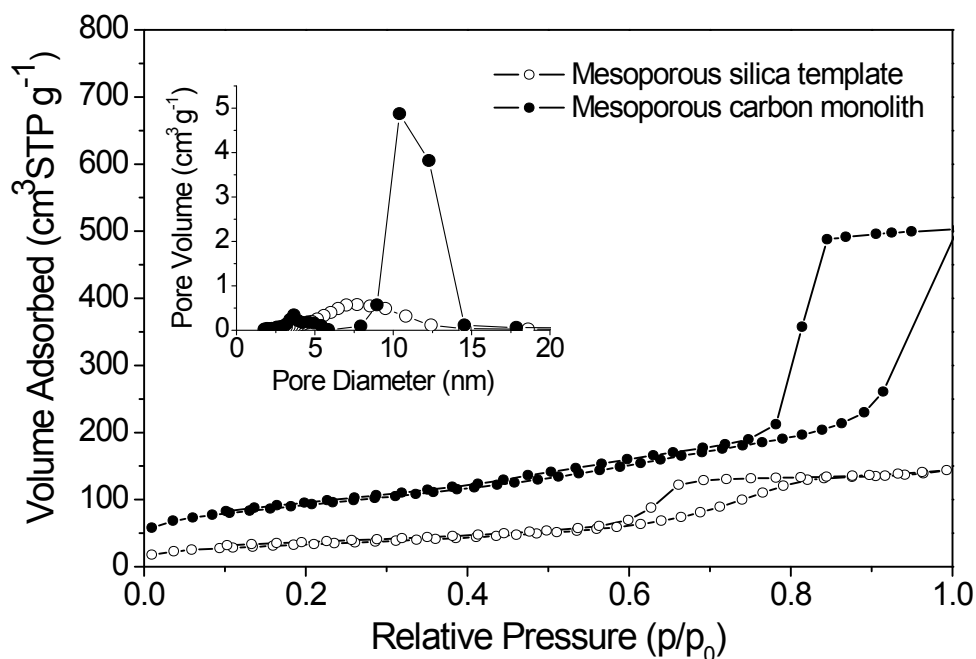


Fig. 4-15: Nitrogen sorption isotherms and pore size distribution (inset) of the mesoporous silica template and the carbon monoliths prepared by Method-II.

Fig. 4-16 shows nitrogen adsorption isotherms of the macroporous silica template and the carbon monolith. The isotherms were of type IV with hysteresis loops of types H1 and H3 for silica template and carbon monolith, respectively. This indicated that the silica template had a highly uniform pore size with a good connectivity [72], and carbon monoliths from this silica template consisted of aggregates of plate like particles with slit-like pores [230]. The BET surface areas, pore volumes and pore widths from PSD curves of the macroporous silica template and the carbon monolith are reported in Table 4-1. The pore volume and the pore widths of the silica template and the carbon monolith were found lower than what it was expected for macroporous materials. This was because the BET method is not very accurate for characterising macroporous materials as the pores are wide and the pore fillings occur at pressures too close to the saturation vapour pressure and therefore the relative pressures (p/p_0) are very close to unity and it is not possible to map out the isotherms in details [231]. The BET surface areas of the macroporous silica template and the carbon monolith were found to be 24 and 187 $\text{m}^2 \text{g}^{-1}$, respectively. These values were lower than the BET surface areas found for the mesoporous silica template and the carbon monolith as was expected due to bigger pores.

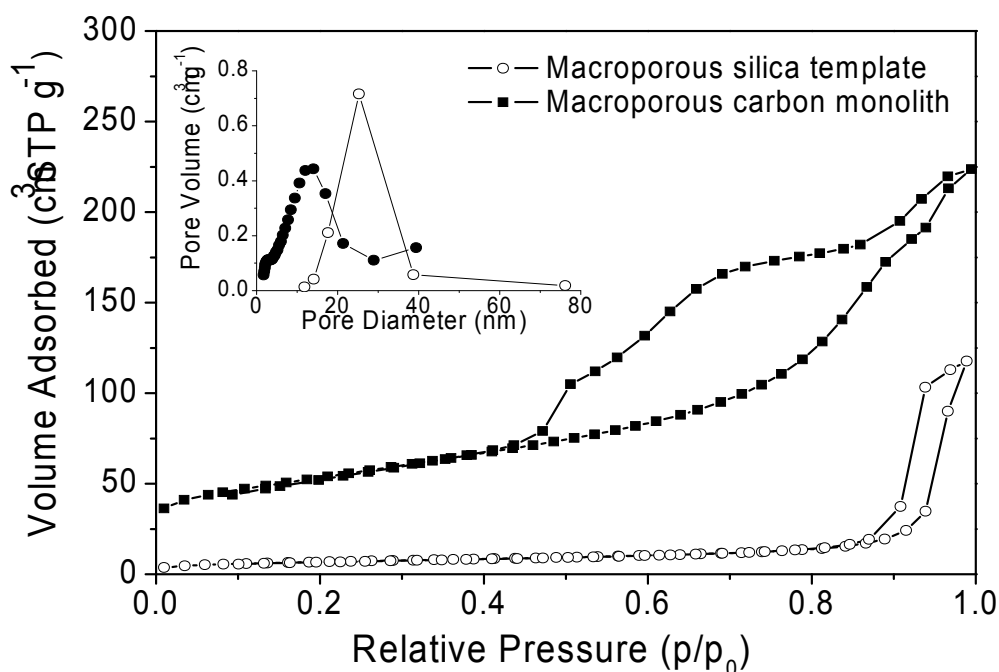


Fig. 4-16: Nitrogen sorption isotherms and pore size distribution (inset) of the macroporous silica template and the carbon monoliths prepared by Method-II.

Table 4-1: Structural parameters of the silica templates and the carbon monoliths produced by Method-II.

Sample	BET Surface Area ($\text{m}^2 \text{g}^{-1}$)	Pore Volume* ($\text{cm}^3 \text{g}^{-1}$)	Pore Width (nm)
Mesoporous silica template	119.2150 ± 0.2152	0.212	7.7
Macroporous silica template	24.1835 ± 0.1567	0.054	12
Mesoporous carbon monolith	324.7866 ± 1.1981	0.778	10.4
Macroporous carbon monolith	187.0689 ± 0.7126	0.296	25

* Single-point pore volumes correspond to a relative pressure of ~ 0.99 .

d) Density and Mechanical Strength

Density of the walls of mesoporous and macroporous carbon materials was measured using a pycnometer and were determined to be 2.2621 ± 0.0146 and 2.3102 ± 0.0152 g cm^{-3} , respectively. Bulk densities of the samples were estimated by measuring the weight and dimensions of the samples and were 0.84 ± 0.05 g cm^{-3} for the mesoporous carbons prepared by 22 nm silica and 0.57 ± 0.07 g cm^{-3} for the macroporous carbon prepared by 100 nm silica. Therefore, relative densities of the mesoporous and

macroporous carbon materials prepared were 0.37 ± 0.02 and 0.25 ± 0.02 , respectively. This indicates that increasing pore size would decrease the relative density of the material. Wen *et al.* [232] used equation (4-1) to calculate porosity of ceramic foams and found that increasing pore sizes leads to an increase in porosity or decrease in relative density.

$$Porosity = \frac{\rho_s - \rho^*}{\rho_s} \quad (4-1)$$

where, ρ_s and ρ^* are the density of the solid material that the walls of the porous material are made of (helium density) and the bulk density of the porous material, respectively. Considering this equation for calculating porosity of the fabricated porous carbon materials, pore volumes of the produced mesoporous and the macroporous carbons were found to be 63 and 75%, respectively.

Mechanical strengths of the porous carbons were examined by compression tests. Fig. 4-17 shows compressive strengths of the mesoporous and the macroporous carbons prepared by silica templates which are 13 ± 0.65 and 10.7 ± 0.53 MPa, respectively. Therefore, structures with smaller pore sizes were mechanically stronger.

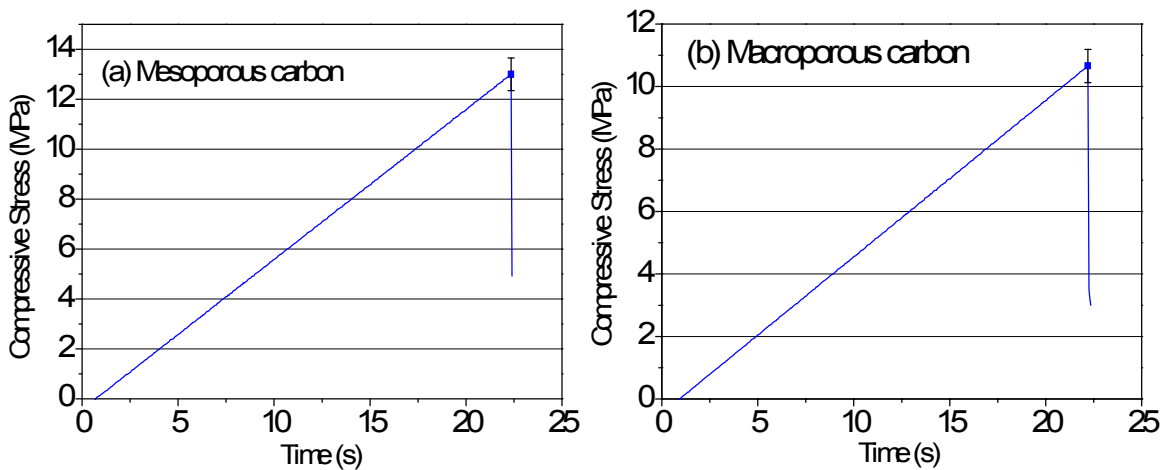


Fig. 4-17: Compressive stress (MPa) vs. time (s) obtained from the compression tests of (a) mesoporous and (b) macroporous carbon materials prepared from silica templates by Method-II.

Compressive strengths of the mesoporous and macroporous carbons were compared with the theoretical values of porous glassy carbons with the same relative densities

(Fig. 4-18). The theoretical strength values (the curve) is calculated from the Gibson and Ashby equation (equation 1-4 [8] in Chapter 1) and they are plotted against the relative densities as it was shown in Chapter 1, Fig. 1-23. Theoretical values of mechanical strength for a porous glassy carbon with relative densities of 0.25 and 0.37 are 14.4 and 26 MPa, respectively whereas the mechanical strengths of the prepared macroporous and mesoporous carbon materials were found to be 10.7 and 13 MPa. Therefore, no considerable change in mechanical strength of the prepared porous carbons was observed at different relative densities. The mesoporous carbons were also re-impregnated with FA and oxalic acid to examine the effect on the mechanical strength of the carbon structures. The resulting mechanical properties of the re-impregnated mesoporous carbons did not change, despite an increase of the relative densities from 0.37 to 0.47. Hence, this deviation of mechanical strength of the porous carbons from the theoretical values is most likely due to weak carbon bonding of such structures. One method to improve the carbon bonding could be to sinter or heat-treat the carbon structures at relatively high temperature ($> 2000\text{ }^{\circ}\text{C}$), which is unfortunately beyond the capability of our current experimental facilities.

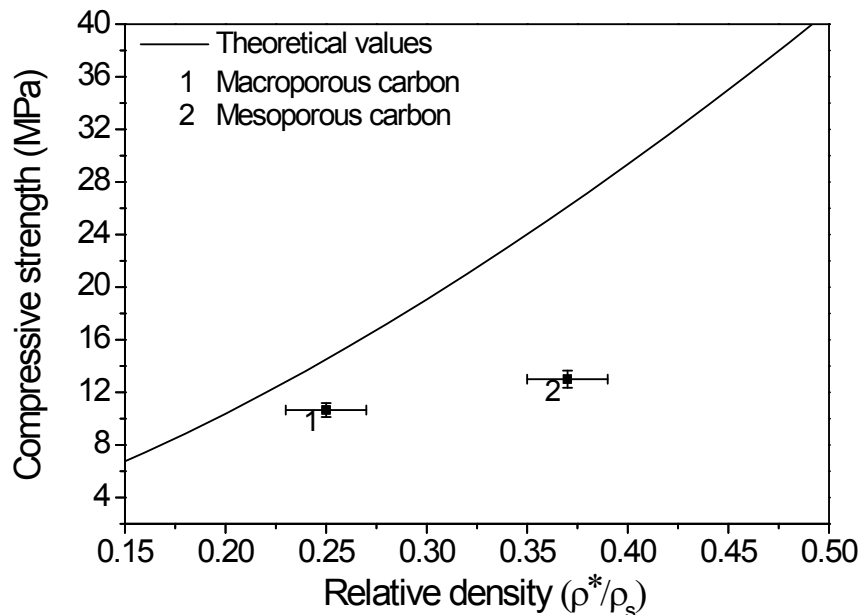


Fig. 4-18: Theoretical values of compressive strength (MPa) of glassy carbon vs. relative density (—) and compressive strength vs. relative density of (1) the macroporous and (2) the mesoporous carbon materials prepared from silica templates by Method-II.

e) Electrical Conductivity

Electrical conductivity of the mesoporous and macroporous carbon materials prepared by silica templates was estimated using the four point technique as described in Section B.5 of Appendix B. Conductivity of the mesoporous carbons was found $23 \pm 2 \text{ S cm}^{-1}$ and conductivity of the macroporous carbons was found $19 \pm 1 \text{ S cm}^{-1}$. Therefore, porous carbons with smaller pore sizes showed higher conductivity due to higher relative density of the mesoporous carbons compared to the macroporous carbons but not to a great extent. Moreover, the measured conductivities of the fabricated porous carbons were compared with the theoretical values (calculated in Section 1.7 of Chapter 1) with the same relative densities (Fig. 4-19). The theoretical values of electrical conductivity of porous glassy carbons with relative densities of 0.25 and 0.37 are 25 and 45 S cm^{-1} , respectively. The theoretical value and measured value were close for the macroporous carbons, but for the mesoporous carbons the deviation of the measured conductivity and the theoretical value was more probably due to the weak carbon bonding as discussed in the previous section.

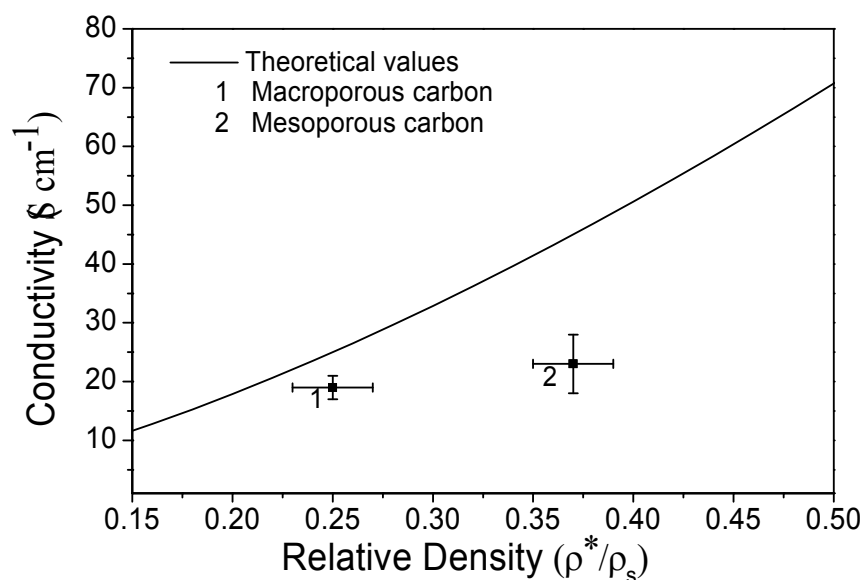


Fig. 4-19: Theoretical values of electrical conductivity (S cm^{-1}) for glassy carbon vs. relative density (—) and conductivity vs. relative density of (1) the macroporous and (2) the mesoporous carbon materials prepared from silica templates by Method-II.

4.2.3 Summary

High surface area mesoporous and macroporous carbon monoliths (324 and $187 \text{ m}^2 \text{ g}^{-1}$, respectively) with homogenous pores were prepared by the templating method. Two types of hard and soft templates were used. Polystyrene spheres were synthesised and used as a soft template. It was found that the meso- and macro-porous carbon structures prepared by polystyrene templates had some cracks in their structures due to shrinkage because of the PS removal during the carbonisation process. Therefore, colloidal silica was used to prepare hard templates. The carbon structures prepared with silica templates were very uniform in porosity with a small shrinkage. However, HF had to be used for removal of the silica templates from the structures. It was found that the mechanical strength and the electrical conductivity of the porous carbons prepared by silica template only increased slightly when the relative density increased, due to weak carbon bonding; the mechanical strength and the electrical conductivity of the mesoporous carbons were slightly higher than the macroporous carbons.

4.3 Electrochemical Behaviour of the Porous Carbons Fabricated

The electrochemical behaviour of the mesoporous and macroporous carbon monoliths produced by silica templates was studied by cyclic voltammetry. Cyclic voltammetry (CV) measurements of the fabricated carbon electrodes were performed using a three electrode cell with a platinum counter electrode and a Ag/AgCl reference electrode in a 0.1 M NaCl solution as electrolyte at room temperature ($25 \text{ }^\circ\text{C}$). Argon was used to remove oxygen from the solution and to maintain an air-free atmosphere over the solution during the measurements. The electrolyte solution was not stirred during the tests and the carbon electrodes were sonicated in the electrolyte solution for 2-3 min before the electrochemical tests. Cyclic voltammograms of mesoporous and macroporous carbons produced by silica templates are shown in Figs. 4-20 and 4-21, respectively. The CV curves were obtained between potentials of -0.2 and 0.6 V at scan rates of $0.5, 10$ and 100 mV s^{-1} . It can be seen from the figures that at high scan rates the curves were not flat (no electrochemical window was observed). However, at

slower scan rates more pores could be penetrated and the curves were found to be more flat. Moreover, it was observed that at lower scan rates the capacitance of the mesoporous and macroporous carbon electrodes (calculated from equation 1-7 in Chapter 1) at the midrange potentials were higher (see Table 4-2). This was also because more pores could be penetrated by ions at slower scan rates.

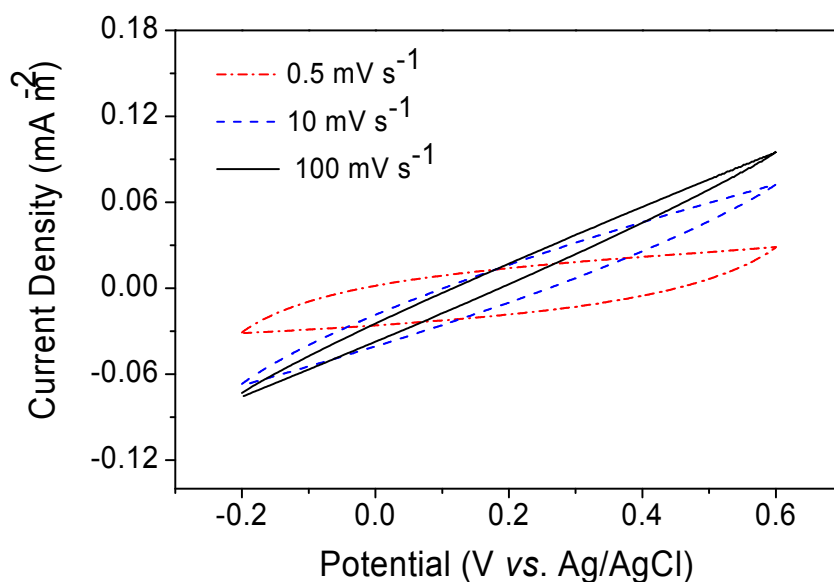


Fig. 4-20: Cyclic voltammograms of mesoporous carbon monoliths prepared by silica templates in 0.1 M NaCl solution at various scan rates (0.5, 10 and 100 mV s⁻¹).

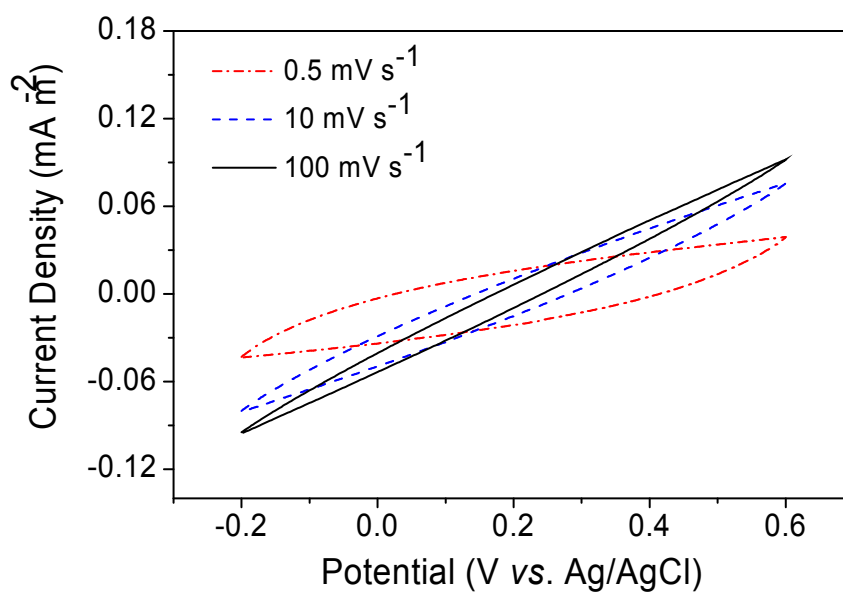


Fig. 4-21: Cyclic voltammograms of macroporous carbon monoliths prepared by silica templates in 0.1 M NaCl solution at various scan rates (0.5, 10 and 100 mV s⁻¹).

Table 4-2 illustrates the estimated capacitance values obtained from the CV curves of the porous carbons. By comparing the capacitance values at lower scan rates, it was observed that the charging/discharging capacitance values at the macroporous carbon electrodes were higher than the mesoporous carbon electrodes.

Table 4-2: Capacitance values of the mesoporous and macroporous carbons at various scan rates.

Carbon	Scan rate (mV s ⁻¹)	Capacitance (μF cm ⁻²)	
		Charge	Discharge
Mesoporous	0.5	2.8	3.6
	10	0.17	0.10
	100	0.017	0.003
Macroporous	0.5	3.2	4.2
	10	0.11	0.15
	100	0.006	0.01

1 mM potassium ferricyanide was added to the aqueous solution as a redox probe. Fig. 4-22 presents the voltammetric curves of the macroporous carbons from the silica templates in 1 mM ferricyanide/0.1 M NaCl at various scan rates. Broad oxidation/reduction peaks with low intensities were observed for these electrodes. These broad peaks reflected poor surface properties of the carbon electrodes with respect to the redox process of ferri-/ferro-cyanide couple. Moreover, it was observed that an increase of the scanning rate results in an increase of the current peak intensity in the cathodic and anodic reactions. The anodic peak shifted from 0.28 to 0.38 V and the cathodic peak shifted from 0.19 to 0.10 V by increasing the scan rate from 2 to 100 mV s⁻¹. Thus the difference between the anodic and cathodic peak potentials (ΔE_p) at 2, 10 and 100 mV s⁻¹ scan rates were 90, 140 and 280 mV, respectively. As the peaks were very broad, calculation of the other properties of the electrodes such as Specific Electrochemical Surface Area (SESA) and heterogeneous rate constant (K_0) of ferricyanide at the electrodes would not be very accurate and were disregarded. CV curves of mesoporous carbon monoliths in 1 mM ferricyanide/0.1 M NaCl showed a similar behaviour to the macroporous carbon electrodes, *i.e.* broad oxidation/reduction peaks with low intensities.

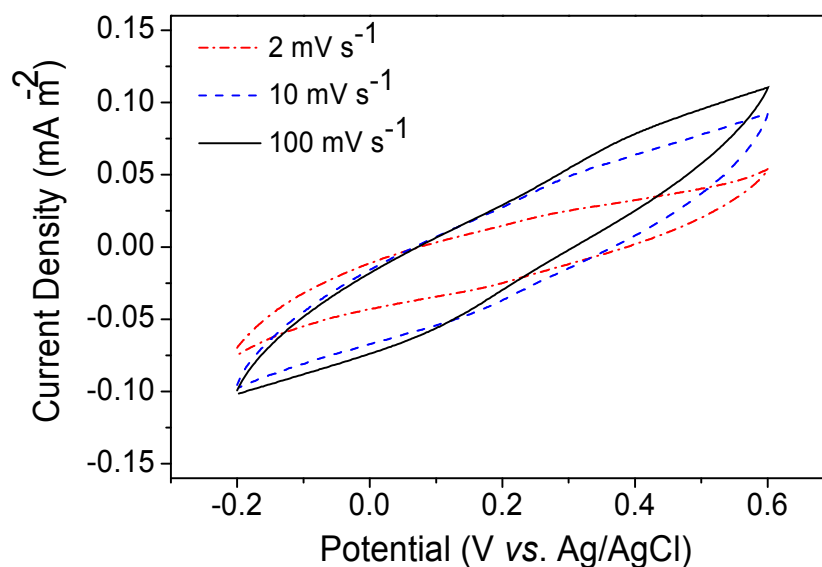


Fig. 4-22: Cyclic voltammetric behaviour of the macroporous carbons prepared from silica templates in 1 mM ferricyanide/ 0.1 M NaCl at various scan rates (2, 10 and 100 mV s⁻¹).

4.4 Summary

High surface area porous carbon monoliths ($> 180 \text{ m}^2 \text{ g}^{-1}$) with homogenous pore size distributions were fabricated using silica templates. The structure of these carbons was more intact (without any apparent cracks and holes) than the structures of porous carbons prepared from polymer templates due to the large shrinkage of the structures occurred after polymer removal during the carbonisation process. Mechanical strength and electrical conductivity of the macroporous carbon electrodes prepared from silica templates were more close to the theoretical values than the mesoporous carbon electrodes.

Electrochemical behaviour of the prepared carbon structures were examined by CV and it was found that at high scan rates the electrochemical windows were not flat because the majority of the pores could not be penetrated during the time scale of the CV measurements. The charge/discharge capacitance at the electrodes was found higher at the lower scan rates. Moreover, the oxidation/reduction peaks of ferri-/ferrocyanide were very broad and low in intensity due to the poor surface properties of the fabricated carbon electrodes with respect to the redox process of ferri-/ferro-cyanide.

Chapter 5: Carbon Electrodes in Large-Scales

5.1 Introduction

Microbial fuel cells normally require large electrodes to increase the efficiency of the biofuel cell. It has been reported that the use of three-dimensional electrodes enabled higher power output compared to two-dimensional or flat electrodes [233, 234]. This is due to a higher surface to volume ratios which results in more bacteria attachment. Therefore, there is a need of large three-dimensional carbon electrodes to be used in microbial fuel cells. The meso- and macro-porous carbon materials prepared in the previous chapters are suitable to be used in enzymatic fuel cells but not in microbial fuel cells due to the difficulty in preparation of the electrodes in large-scales. In the foaming method used in Chapter 3 for producing macroporous carbon materials, the problem with shrinkage makes the process difficult to be used for producing large electrodes. Moreover, the macroporous carbon electrodes prepared with the templating method in Chapter 4 were highly porous and thus were not strong enough to be produced in large-scales. Therefore, another method was developed for preparing large porous carbon structures.

In this method two kinds of polymers with different thermal stabilities were used as starting materials. One of them was a carbon precursor that tended to carbonise at high temperatures while the other was a thermally decomposable polymer which decomposed to gaseous product by heating under an inert atmosphere. In this work polyfurfuryl alcohol (PFA) and polyethylene (PE) were used as the carbon precursor and thermally decomposable polymer, respectively. After mixing the two polymers and moulding, the mixture was pressed, cured and carbonised. A macroporous carbon structure with walls containing mesopores was obtained. The structure was mechanically stable and could be produced in different shapes and sizes. The electrochemical behaviour of these structures was examined.

5.2 Preparation of Porous Carbon Electrodes

Polymer blend technique was used to fabricate porous carbon electrodes in large-scales. In this method a mixture of polyethylene powder (particle size 180 μm), polyfurfuryl alcohol (viscosity: 7500 cP), with a volume ratio of 12 to 1 (this volume ratio is an optimum after testing various volume ratios and checking the structures after the carbonisation), respectively and a solution of oxalic acid in ethanol (concentration of oxalic acid in the whole mixture was 0.25 mol L⁻¹), were prepared. Afterwards, the mixture was placed in a mould and pressed. A schematic of this process is shown in Fig. 5-1. After moulding, the samples were dried at 80-100 °C for 2-12 h depending on the sample size. This step polymerised the PFA further and helped the hardening of the structure. Subsequently, samples were removed from the moulds, cured and carbonised at 150 and 1000 °C, respectively under a nitrogen flow. The nitrogen flow needed to be selected carefully as a high nitrogen flow (1500 mL min⁻¹) resulted in bending of the samples (Fig. 5-2). This was due to a temperature gradient created in the tube furnace as a result of the nitrogen flow hence the flow was set to 800 mL min⁻¹. Some of the samples were impregnated with PFA in low viscosity (~65 cP) and carbonised at 1000 °C for 2 h at a heating rate of 1 °C min⁻¹, after polymer burn out and carbonisation to make the structures stronger. Impregnation of PFA in the carbon structures was facilitated by sonicating the samples for 10 min to 1 h depending on the sample size.

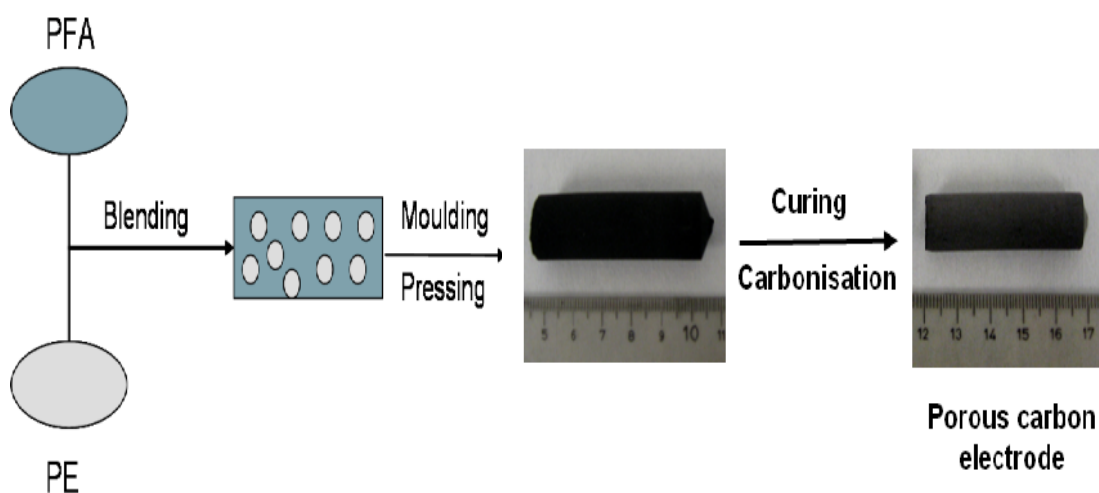


Fig. 5-1: Schematic diagram of the polymer blend technique used for preparation of large porous carbon electrodes.

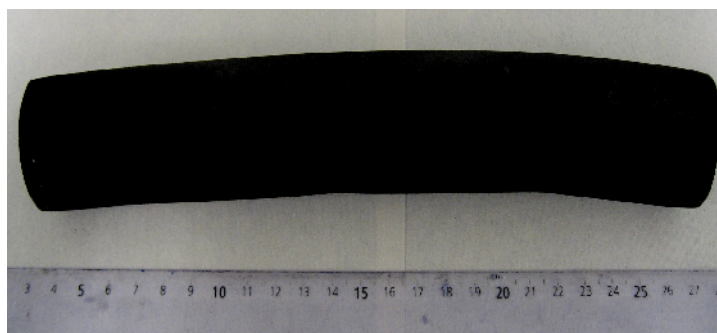


Fig. 5-2: A picture of porous carbon material (bended) prepared by the polymer blend technique and carbonised under a nitrogen flow of 1500 mL min^{-1} .

The curing and carbonisation cycle of the samples are shown in Fig. 5-3. It can be seen from the figure that the samples were heated from room temperature to $150 \text{ }^\circ\text{C}$ at a heating rate of $1 \text{ }^\circ\text{C min}^{-1}$ and were kept at this temperature for 4 h to complete the curing process. In order to carbonise the samples, they were further heated from 150 to $400 \text{ }^\circ\text{C}$ at a heating rate of $1 \text{ }^\circ\text{C min}^{-1}$ and from 400 to $600 \text{ }^\circ\text{C}$ they were heated very slowly ($0.1 \text{ }^\circ\text{C min}^{-1}$) to avoid rupture of the structure. This temperature range is the decomposition temperature range of polyethylene according to the data reported in the literature [235]. Subsequently, the samples were heated from 600 to $1000 \text{ }^\circ\text{C}$ at a heating rate of $1 \text{ }^\circ\text{C min}^{-1}$ and kept at $1000 \text{ }^\circ\text{C}$ for 2 h.

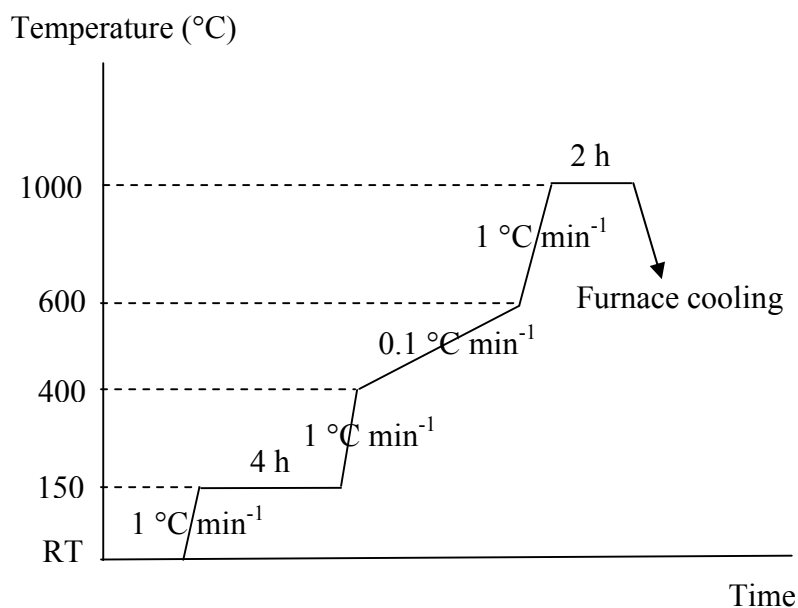


Fig. 5-3: A schematic diagram of curing and carbonisation cycle of the samples prepared by the polymer blend technique.

Porous carbon materials in different shapes and sizes were produced successfully with the method described above. Fig. 5-4 shows picture of the prepared materials, in each set of samples the larger sample is before the carbonisation and the smaller one is after the polymer burn out and carbonisation. The properties of the fabricated materials were examined with different characterisation techniques and are reported in the following sections.

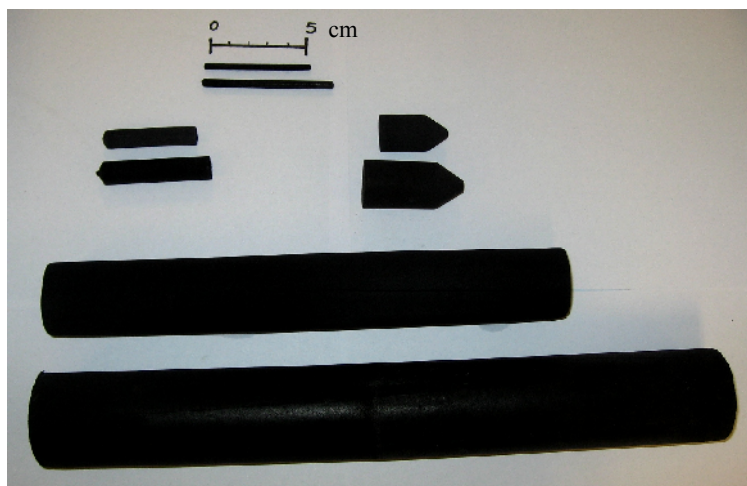


Fig. 5-4: Picture of porous carbon materials prepared in different shapes and sizes by the polymer blend technique. In every set of samples the larger sample is before the carbonisation and the smaller one is after the carbonisation.

5.3 Properties of the Fabricated Carbon Electrodes

5.3.1 Morphology and Porosity

Morphology of the porous carbons prepared by the polymer blend technique was examined with field emission scanning electron microscopy and is shown in Fig. 5-5. It can be seen from the figure that the porous structure was consisted of large pores (in micrometric ranges) and small pores (in nanometric ranges) in the walls of the structure. The large pores were resulting from the polyethylene (PE) particles removed from the structure during the carbonisation of PFA and the small pores on the walls were similar in morphology to the morphology of the PE particles (Fig. 5-6).

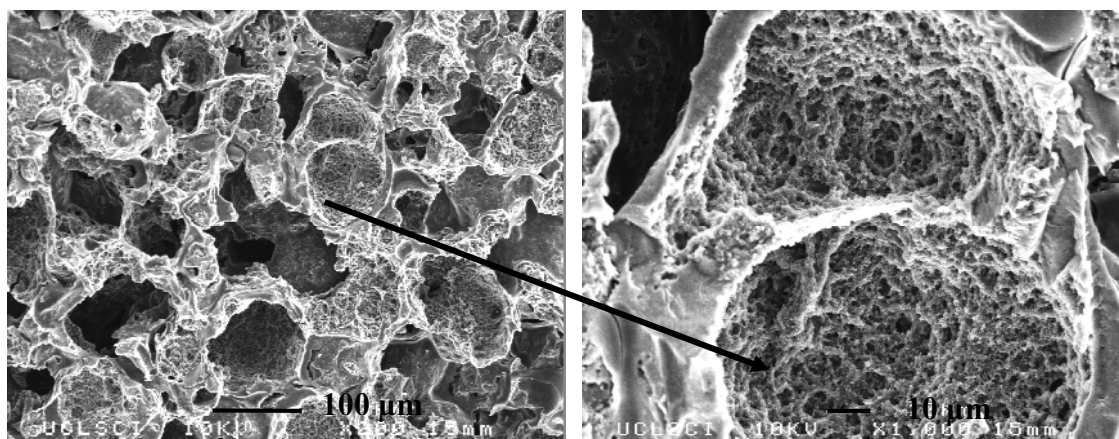


Fig. 5-5: Field emission scanning electron microscopy images of porous carbon electrode prepared with the polymer blend technique after impregnation with PFA at different magnifications.

Fig. 5-6 shows SEM images of PE particles at different magnifications. It can be seen that the particle sizes were $160 \pm 30 \mu\text{m}$ and the particles were not block solid and they contained some porosity that PFA penetrated inside and resulted in the porous carbon structure with porosity on the walls.

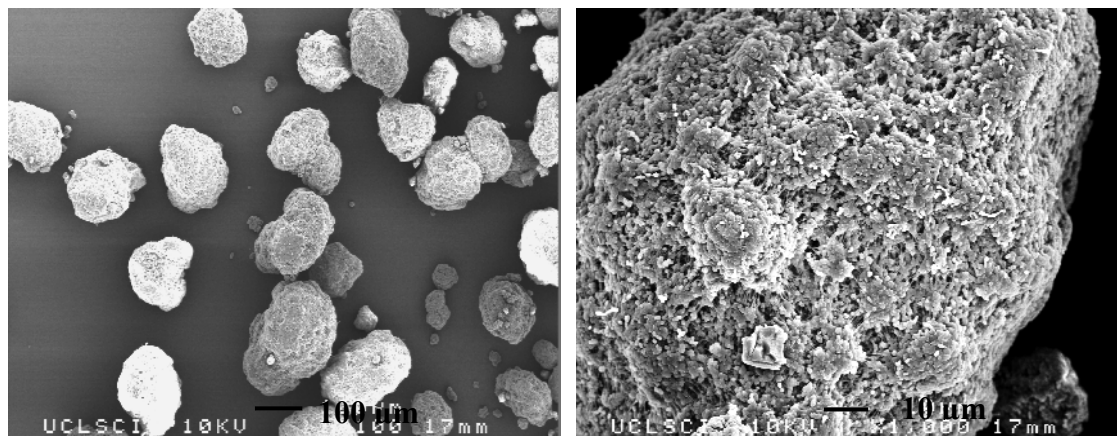


Fig. 5-6: Field emission scanning electron microscopy images of the polyethylene particles at different magnifications.

Porosity of the porous carbons was further studied with the mercury porosimetry technique. Pore size distributions of porous carbons after polymer burn out and after impregnation with PFA are presented in Fig. 5-7. Three peaks at 28, 5 and $0.4 \mu\text{m}$ were observed for the porous carbon after polymer burn out and three peaks at 29, 6.5 and $0.25 \mu\text{m}$ were observed for the porous carbon after impregnation with PFA. The pore size range for the porous carbon after polymer burn out was between 0.25 and $200 \mu\text{m}$ with the majority of pores at $28 \mu\text{m}$, and for the porous carbon after

impregnation with PFA was between 0.15 and 60 μm with the majority of pores at 29 μm .

As mercury porosimetry technique can only determine macroporosity of the porous materials, in order to investigate mesopores on the porous carbon walls, nitrogen adsorption/desorption method (see Section C.3 of Appendix C for further details) was used. Pore size distributions of porous carbons prepared with the polymer blend technique after polymer burn out and after impregnation with PFA are presented in Fig. 5-8. It can be seen from the figure that the pore diameters decreased from 32 to 14 nm after impregnation with PFA. The porous carbon after impregnation with PFA showed another pore diameter peak at about 4 nm. Moreover, it was observed that the mesoporosity volume of the porous carbons after polymer burn out was less than the porous carbons after impregnation with PFA whereas, the macroporosity volume of porous carbons after polymer burn out was more than porous carbons after impregnation with PFA (Fig. 5-7).

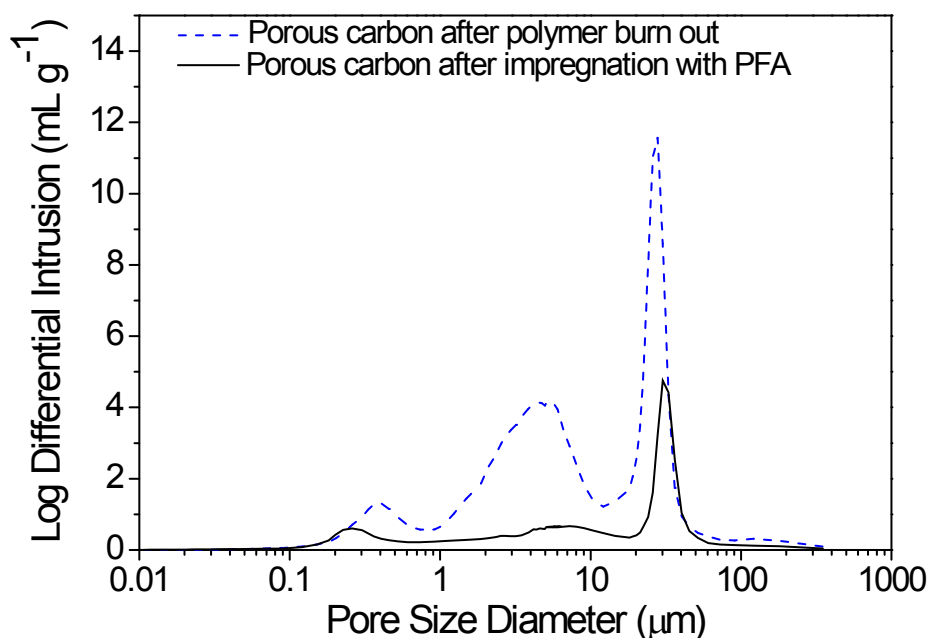


Fig. 5-7: Pore size diameter (μm) vs. Log differential intrusion (mL g^{-1}) for porous carbons prepared by the polymer blend technique after polymer burn out (---) and after impregnation with PFA (—).

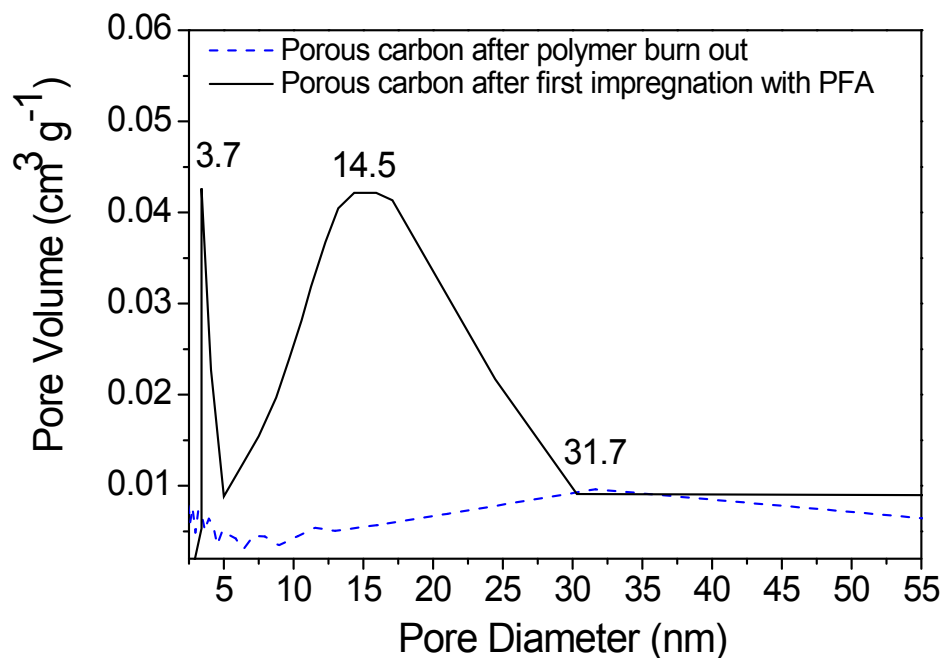


Fig. 5-8: Pore size distributions (mesopore) of porous carbons prepared by the polymer blend technique, after polymer burn out (---) and after impregnation with PFA (—).

5.3.2 Structure

Structure of the porous carbons prepared by the polymer blend technique was examined by XRD and Raman spectroscopy. In order to investigate the structures by XRD, the carbon materials were crushed to powders and the XRD pattern together with the Raman spectrum of the carbons after impregnation with PFA are presented in Fig. 5-9. The XRD pattern of the carbon materials showed three broad bands at 24, 43.5 and 80° which were assigned to (002), (01) and (110) diffraction peaks of graphitic structure, respectively. Therefore, structure of the porous carbons was amorphous with some degree of crystallinity. Moreover, the Raman spectrum showed two broad bands at 1348 cm^{-1} (D-band) and 1580 cm^{-1} (G-band) which were characteristic of disordered carbon. Thus, the XRD and Raman spectra indicated that the carbon materials presented an amorphous structure similar to the structure of carbonised PFA (glassy carbon) presented in Chapter 2.

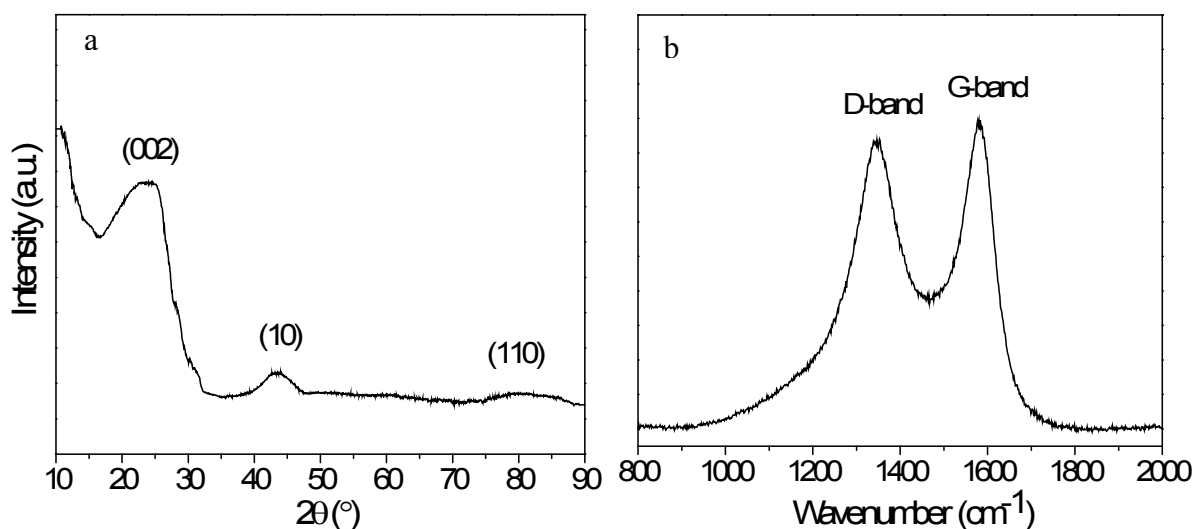


Fig. 5-9: (a) XRD pattern and (b) Raman spectrum of the porous carbons prepared by the polymer blend technique and impregnated with PFA.

5.3.3 Shrinkage and Density

Shrinkage of the porous carbons prepared after polymer burn out and carbonisation was examined by measuring the dimensions of the structures before and after polymer burn out. It was found that the shrinkage of the materials were $22 \pm 2\%$ after polymer burn out and carbonisation. Shrinkage after impregnation with PFA and carbonisation was small and thus negligible.

Density of the walls of the porous carbon structures was measured by pycnometer (see Section B.4 of Appendix B for further explanation) and for the porous carbon materials after polymer burn out and after impregnation with PFA and carbonisation was found $2.0541 \pm 0.038 \text{ g cm}^{-3}$ and $2.1241 \pm 0.051 \text{ g cm}^{-3}$, respectively. These densities were slightly higher than the density of glassy carbon obtained from carbonisation of PFA in Chapter 2 ($1.899 \pm 0.0176 \text{ g cm}^{-3}$). This could be due to a higher degree of polymerisation of PFA. Furthermore, bulk density of the structures was estimated by dividing weight of the materials to their volumes. The bulk density of the materials after polymer burn out and carbonisation was found $0.14 \pm 0.02 \text{ g cm}^{-3}$ and the bulk density of the structures after impregnation with PFA and carbonisation was found to be dependant on the size of the materials due to the different amount of PFA impregnated in the materials. For example, bulk density of the materials with a relatively small cross section (diameter of $10 \pm 1 \text{ mm}$) was found $0.48 \pm 0.02 \text{ g cm}^{-3}$.

and bulk density of the materials with a greater cross section (diameter of 35 ± 0.03 mm) was found $0.32 \pm 0.01 \text{ g cm}^{-1}$. Thus, it was found that after impregnation with PFA, the bigger the materials were, the smaller the bulk densities and hence the relative densities were. This was because penetration of the PFA in the smaller samples was easier and thus the resulting structures had thicker walls than the bigger samples and therefore were denser.

Relative densities of the porous carbons prepared with the polymer blend technique after polymer burn out did not depend on the materials size and were found to be 0.07 ± 0.005 whereas, relative densities of the porous carbon materials after impregnation with PFA and carbonisation depended on the materials size and found to be in the range of 0.15 ± 0.01 to 0.22 ± 0.01 for the fabricated materials.

5.3.4 Mechanical Strength

Mechanical strength of the porous carbons prepared by the polymer blend technique was estimated by compression tests and typical graphs obtained for the compressive stresses of porous carbons after polymer burn out and after impregnation with PFA and carbonisation are shown in Fig. 5-10. It was observed that the compressive strength of the carbons increased by impregnation with PFA. Moreover, the tests showed that the compressive strengths of the carbon materials changed by changing the cross sectional area of the samples. This effect was investigated and is shown in Fig. 5-11.

Fig. 5-11 illustrates the relation observed between compressive strengths of the porous carbons and the sample diameters. Samples with diameters of (a) 11 ± 0.1 , (b) 20 ± 0.1 and (c) 37.7 ± 0.5 mm after polymer burn out and samples with diameters of (a) 10 ± 0.02 , (b) 18.5 ± 0.2 and (c) 35.5 ± 0.3 mm after impregnation with PFA were tested. It was observed that the compressive strengths of the materials decreased by increasing the cross sectional area of the samples. However, this change of strength with the samples' cross sectional area was not strong for the samples after polymer burn out. This could be because the relative densities of the samples after polymer burn out with different diameters were found to be the same whereas, the relative

density of the carbon materials after impregnation with PFA was different for materials with different diameters as discussed in the previous section.

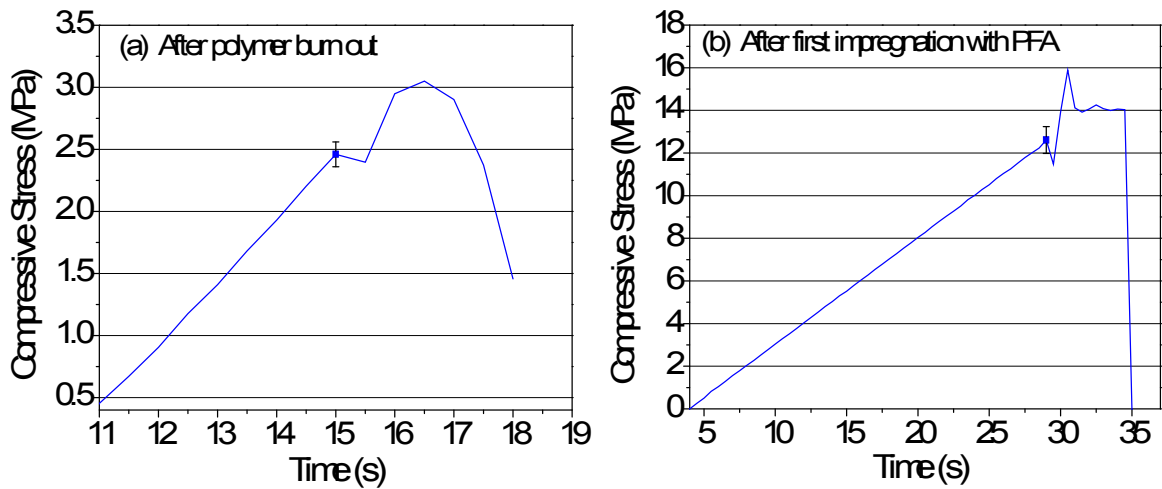


Fig. 5-10: Compressive stress (MPa) vs. time (s) obtained from the compression tests of the carbon materials (sample a) prepared by the polymer blend technique (a) after polymer burn out and (b) after impregnation with PFA.

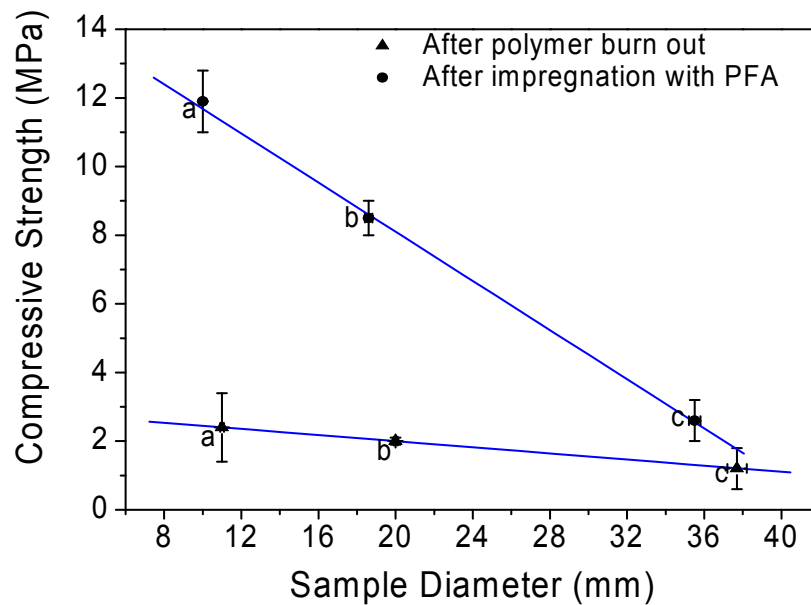


Fig. 5-11: Compressive strength (MPa) vs. sample diameter (mm) obtained for the porous carbons prepared by the polymer blend technique with different diameters (a: 11, b: 20 and c: 37.7 mm) after polymer burn out and after impregnation with PFA (a: 10, b: 18.5 and c: 35.5 mm).

The compressive strengths of samples a, b and c after polymer burn out and after impregnation with PFA obtained from compression tests were compared with the theoretical strength values of porous glassy carbons (calculated in Section 1.7 of Chapter 1) and is shown in Fig. 5-12. It can be seen from the figure that the

compressive strengths of the carbon materials with different diameters after polymer burn out were very close to the theoretical values and compressive strengths of the carbons after PFA impregnation with smaller diameters were closer to the theoretical values compared to the samples with greater diameters. For instance, compressive strength of sample (a) with a diameter of 10 mm was 11.9 MPa and the theoretical value with the same relative density was 12 MPa whereas, sample (c) with a diameter of 35.5 mm showed a compressive strength of 2.6 MPa and the theoretical value of compressive strength with the same relative density was 6.7 MPa. The relatively low mechanical strength of the big samples could be because the impregnation of the big samples with PFA was more difficult than the small samples and thus the structures after carbonisation was not as uniform as the small samples. However, the big samples were strong enough to withstand machining and to be used in microbial fuel cells (see Appendix F for pictures of the machined sample).

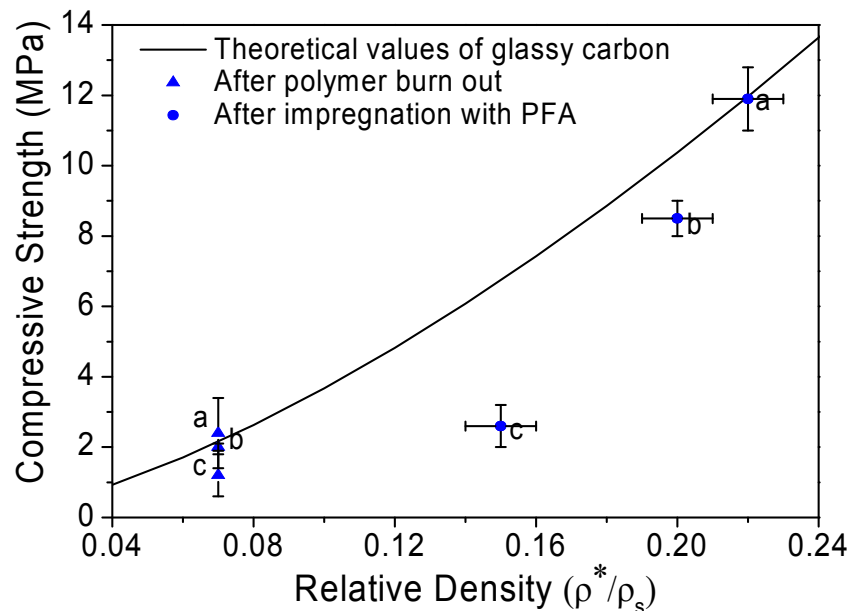


Fig. 5-12: Theoretical values of compressive strength (MPa) of glassy carbon vs. relative density (—) and compressive strength vs. relative density of porous carbons with different diameters (samples a, b and c) after polymer burn out (▲) and after impregnation with PFA (●).

5.3.5 Electrical Conductivity

Electrical conductivity of the porous carbons was estimated by the four point technique as described in Section B.5 of Appendix B. Electrical conductivity of the porous carbons after polymer burn out was found $1.96 \pm 0.08 \text{ S cm}^{-1}$ and it was found

that the conductivities of the carbons improved by impregnation with PFA. Electrical conductivities of the porous carbons with different diameters (samples a, b and c) after impregnation with PFA were found close to each other, in the range of 8-19.5 S cm⁻¹ depending on their relative density. The conductivities of the porous carbons after polymer burn out and after impregnation with PFA were compared to the theoretical values of conductivity of glassy carbon (calculated in Chapter 1, Section 1.7) with the same relative densities and are shown in Fig. 5-13. It can be seen from the figure that the conductivities of the samples after polymer burn out as well as samples (a) and (b) after impregnation with PFA were close to the theoretical values. Deviation of the conductivity of sample (c) from the theoretical value was more than samples (a) and (b), most probably because the structure of the big sample was not as uniform as the other two samples.

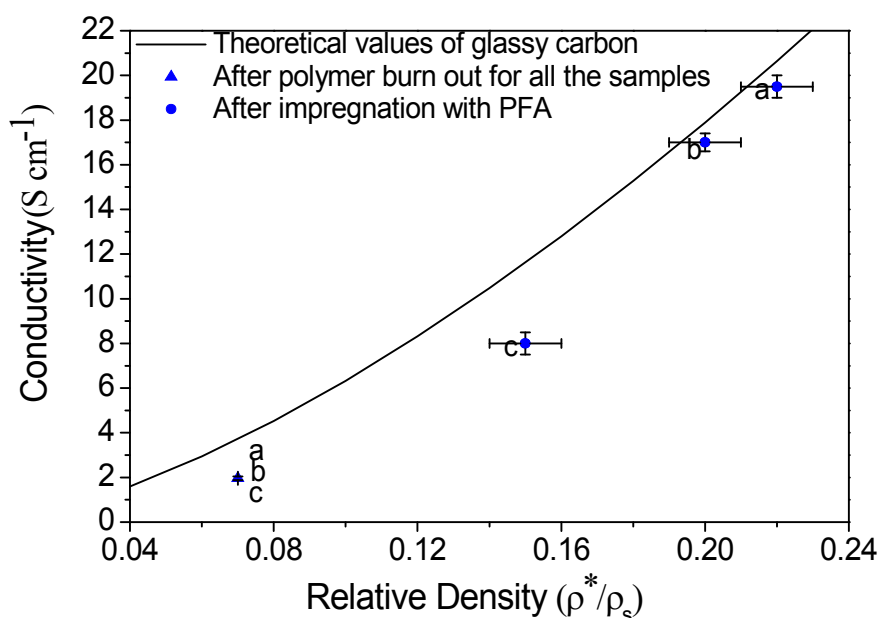


Fig. 5-13: Theoretical values of electrical conductivity (S cm⁻¹) for glassy carbon vs. relative density (—) and conductivity vs. relative density of the porous carbons with different diameters (samples a, b and c) prepared by the polymer blend technique after polymer burn out (▲) and after impregnation with PFA (●).

5.3.6 Electrochemical Behaviour

Cyclic voltammetry was used to examine the electrochemical behaviour of the produced porous carbons. Cyclic voltammetry measurements of the carbon electrodes were performed using a three electrode cell with a platinum counter electrode and a

Ag/AgCl reference electrode in a 0.1 M NaCl solution as electrolyte at room temperature (25 °C). Argon was used to remove oxygen from the solution and to keep air-free atmosphere over the solution during the measurements and the electrolyte solution was not stirred during the tests. Before the electrochemical tests, the electrodes were sonicated in the electrolyte solution for 1-2 min to remove the air bubbles from the pores.

Cyclic voltammogram of porous carbon produced by the polymer blend technique after polymer burn out is shown in Fig. 5-14. The CV curves were obtained between potentials of -2.5 and 0.6 V at scan rates of 10-100 mV s⁻¹. It was observed that the curves were flat in this potential range and the same behaviour was observed for the carbon electrodes after impregnation with PFA.

In all the voltammograms presented here, the currents are normalised per unit surface area of the electrodes, obtained from nitrogen adsorption isotherm using the BET method (described in Section C.3 of Appendix C), which were found to be 7.7 m² g⁻¹ for the porous carbons after polymer burn out as well as after impregnation with PFA.

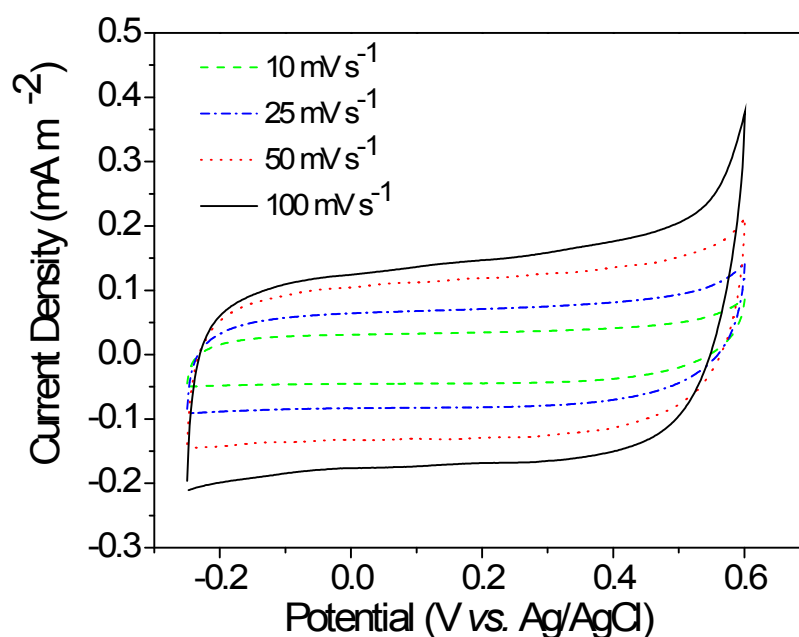


Fig. 5-14: Cyclic voltammograms of porous carbon electrodes after polymer burn out in 0.1 M NaCl solution at various scan rates.

Charging and discharging capacitance at the electrode/electrolyte interface was evaluated using the cyclic voltammograms and equation 1-7 in Chapter 1, $C = i/A.v$ (where, i is the current intensity, A is the BET surface area and v is the scan rate). The charging and discharging capacitance of the porous carbons after polymer burn out at different scan rates are reported in Table 5-1. The capacitance were found to be very low compared to the values reported in the literature for porous carbon electrodes ($10-20 \mu\text{F cm}^{-2}$) [125]. Furthermore, the capacitance were found higher at lower scan rates and therefore the low capacitance might be due to high scan rates used in this study. The majority of pores might have not been penetrated because of too high scan rates.

Table 5-1: Capacitance of porous carbon electrodes after polymer burn out at various scan rates.

Scan rate (mV s^{-1})	Capacitance ($\mu\text{F cm}^{-2}$)	
	Charge	Discharge
10	0.32	0.44
25	0.24	0.32
50	0.20	0.26
100	0.12	0.18

Activity of the carbon electrodes was assessed in terms of the heterogeneous electron transfer reversibility using 1 mM of potassium ferricyanide as a redox probe. Fig. 5-15 presents voltammetric curves of porous carbons after polymer burn out in 1 mM ferricyanide/0.1 M NaCl at different scan rates. It can be seen from the figure that an increase in the scanning rate resulted in an increase of the current peak intensity in the cathodic and the anodic reactions. The anodic peak shifted from 0.204 to 0.282 V and the cathodic peak shifted from 0.107 to 0.024 V by increasing the scan rate from 10 to 100 mV s^{-1} .

Fig. 5-16 shows voltammetric curves of porous carbon electrodes after impregnation with PFA in 1 mM ferricyanide/0.1 M NaCl at different scan rates. It can be seen that the behaviour of the carbon electrodes after impregnation with PFA is similar to the carbon electrodes after polymer burn out. The current peak intensity of the cathodic

and the anodic reactions shifted from 0.212 to 0.296 V and from 0.099 to 0.020 V, respectively by increasing the scan rate from 10 to 100 mV s^{-1} . It was observed that the difference between the anodic and the cathodic peak potentials (ΔE_p) of the porous carbon electrodes after polymer burn out and after impregnation with PFA were very close to each other and increased with increasing the scan rate (ν) (see Fig. 5-17).

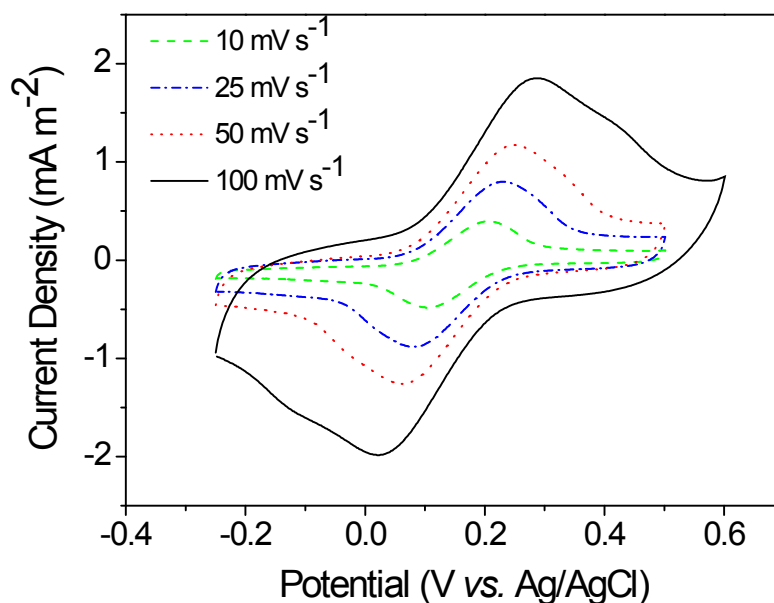


Fig. 5-15: Cyclic voltammetric behaviour of the porous carbons after polymer burn out in 1 mM ferricyanide/ 0.1 M NaCl at various scan rates.

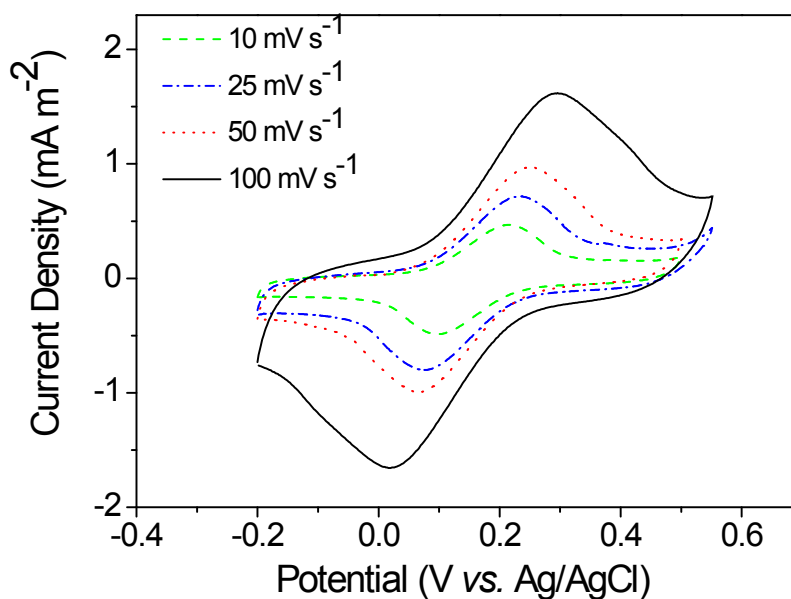


Fig. 5-16: Cyclic voltammetric behaviour of the porous carbons after impregnation with PFA in 1 mM ferricyanide/ 0.1 M NaCl at various scan rates.

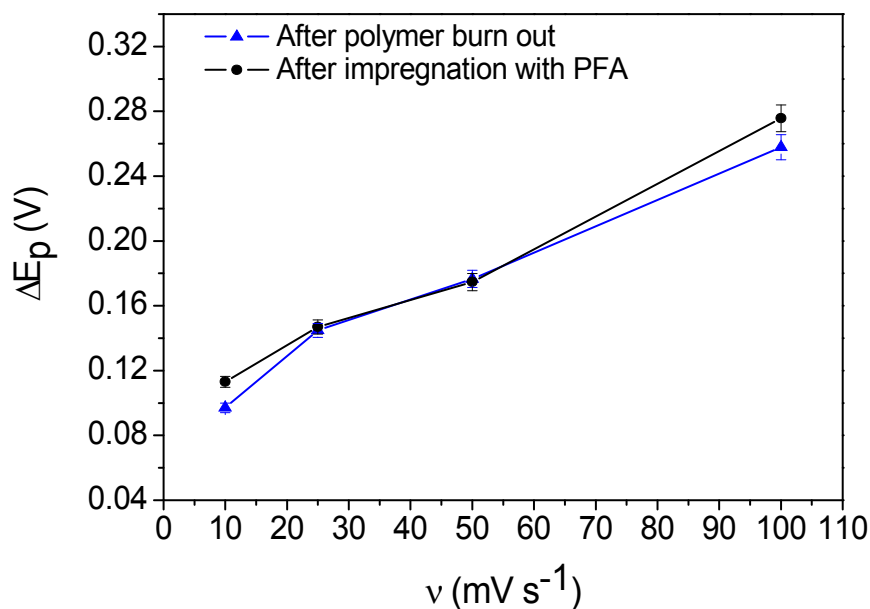


Fig. 5-17: ΔE_p as a function of scan rate (ν) in 1 mM ferricyanide/0.1 M NaCl for the porous carbons after polymer burn out (▲) and after impregnation with PFA (●).

Specific Electrochemical Surface Area (SESA) of the electrodes and heterogeneous rate constant (K_0) of ferricyanide at the electrodes were evaluated by the electrochemical response of the porous carbons. For estimating the SESA, anodic peak currents from the CV curves were used in the equation 1-5 (in Chapter 1) and diffusion coefficient of 1 mM ferricyanide in 0.1 M NaCl was assumed $7.2 \times 10^{-6} \text{ cm}^2 \text{ s}^{-1}$ [216, 217]. The SESA of the porous carbon electrodes after polymer burn out and after impregnation with PFA was found 8.5 ± 0.3 and $10.7 \pm 0.6 \text{ cm}^2 \text{ cm}^{-3}$, respectively (see Table 5-2). The lower SESA of the electrodes after polymer burn out compared to after impregnation with PFA might correlate to a lower conductivity which is determinant for the electrodes electrochemical response.

The heterogeneous rate constant, K_0 , was estimated using the equation below derived from the equation 1-8 in Chapter 1:

$$K_0 = 2.78 \times 10^{-2} \Psi \nu^{1/2} \quad (5-1)$$

where, Ψ is the degree of reversibility and ν is the scan rate. The K_0 values for carbon electrodes after polymer burn out and after impregnation with PFA at different scan rates are reported in Table 5-2. Carbon electrodes after polymer burn out showed slightly higher K_0 values. This might be due to different surface states of electrodes

after impregnation with PFA and after polymer burn out as it has been shown that the electron transfer rate of ferri-/ferro-cyanide at glassy carbon electrodes is very sensitive to the state of the electrodes surface. For instance, the heterogeneous rate constant of a bare glassy carbon electrode increased from $1 \times 10^{-4} \text{ cm s}^{-1}$ to $2 \times 10^{-2} \text{ cm s}^{-1}$ when it was chemically oxidised [236]. The K_0 values obtained for the carbon electrodes after polymer burn out and after impregnation with PFA were in the range reported in the literature for heterogeneous rate constant of polished glassy carbon, *i.e.* 0.45×10^{-2} [237]- 0.14 cm s^{-1} [137], depending on the surface cleanliness and electrode pretreatment.

Cathodic peak current intensities of the porous carbon electrodes after polymer burn out and after impregnation with PFA increased as a function of square root of scan rate (see Fig. 5-18), thus the electron transfer rate at the electrode surface was fast and the reactions at the electrodes were controlled by diffusion [118].

Table 5-2: Calculated parameters of 1 mM ferricyanide/0.1 M NaCl at the carbon electrodes after polymer burn out and after impregnation with PFA from the CV curves at various scan rates.

Porous carbon	ν (mV s^{-1})	I_{pa} (mA)	SESA ($\text{cm}^2 \text{ cm}^{-3}$)	ΔE_p (V)	Ψ	$10^2 K_0$ (cm s^{-1})
After polymer burn out	10	0.87 ± 0.02	8.25	0.097 ± 0.011	0.60	5.27
	25	1.47 ± 0.03	8.82	0.145 ± 0.014	0.24	3.34
	50	2.08 ± 0.04	8.82	0.177 ± 0.019	0.16	3.14
	100	2.76 ± 0.06	8.28	0.258 ± 0.028	0.066	1.83
After impregnation with PFA	10	0.93 ± 0.02	11.35	0.113 ± 0.012	0.42	3.69
	25	1.30 ± 0.03	10.04	0.147 ± 0.014	0.23	3.20
	50	2.00 ± 0.04	10.92	0.175 ± 0.018	0.16	3.14
	100	2.70 ± 0.05	10.42	0.276 ± 0.030	0.056	1.56

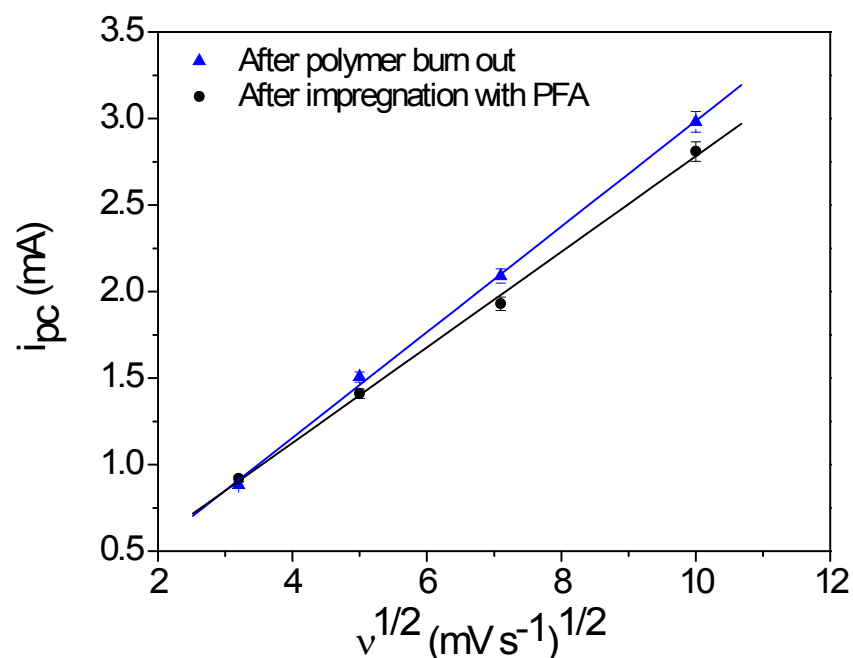


Fig. 5-18: Cathodic peak current as a function of (scan rate)^{1/2} in 1 mM ferricyanide/0.1 M NaCl for the porous carbons after polymer burn out and after impregnation with PFA.

5.4 Summary

Polymer blend technique was used to prepare porous carbons in large-scales and carbon electrodes in different sizes and shapes with mechanically stable structures were successfully fabricated with this method. The structures were composed of pores in the micrometric ranges with mesopores in the walls of the structures. The mechanical strength and electrical conductivity of the carbon structures were improved by impregnation with PFA. It was found that after impregnation and carbonisation, size of carbon samples affected the mechanical strength and the electrical conductivity due to different relative densities. The mechanical strength and electrical conductivity of the samples after impregnation with PFA were close to the theoretical values of glassy carbon with the same relative densities.

Electrochemical behaviour of the fabricated electrodes was examined by cyclic voltammetry. The difference between the anodic and the cathodic peak potentials (ΔE_p) of the porous carbon electrodes after impregnation with PFA was close to the electrodes after polymer burn out. The specific Electrochemical Surface Area (SESA) of the electrodes after impregnation with PFA was higher than after polymer burn out due to the higher electrical conductivity of the electrodes.

Chapter 6: General Discussion

The proposed aim of this project was to fabricate porous carbon electrodes for hosting catalytic enzymes and microbes in biofuel cells. These electrodes should possess some specific properties for optimal use in biofuel cells: i) pore sizes of the porous carbon electrodes match with the sizes of enzymes and microbes; ii) the electrodes should have “high” mechanical strength and “high” electrical conductivity; and iii) suitable surface chemistry for enzyme immobilisation. The sizes of enzymes are in the nanometric ranges and the sizes of microbes are in the micrometric ranges. Therefore, mesoporous and macroporous carbon materials should be fabricated for such properties.

For all the carbon preparations in this project, polyfurfuryl alcohol (PFA) was used as a carbon precursor. This polymer was chosen because it has a high carbon yield and it is a thermoset resin so it maintains its shape during heating. Carbonisation of this polymer produced glassy (vitreous) carbon with a high compressive strength (~143 MPa).

To prepare macroporous carbons for hosting microbes, a foaming method was used. Three different methods of preparation were tested and the best method, in terms of mechanical strength of the carbon foams, was chosen. In this method a two part polyurethane mixture was mixed with a graphite powder. After polymer burn out by heating to 400 °C slowly (0.1 °C min⁻¹), the foams were impregnated with PFA and carbonised to 1000 °C. In this method, graphite powder helped to reinforce the structure as it is reported in the literature that addition of carbon fibres to the structure would improve the mechanical strength of the carbon foams by reduction of the brittleness and improvement of the density of the foams [147].

The majority of the pore diameters for carbon foams after first and second impregnation with PFA was found to be $60 \pm 10 \mu\text{m}$, and after third impregnation was found to be $50 \pm 10 \mu\text{m}$. The mechanical strength of the carbon foams impregnated with PFA once, twice and three times was found 9 ± 1 , 11 ± 1 and 11 ± 2 MPa,

respectively. The strength of the foams was compared with the theoretical mechanical strength values for glassy carbon with the same relative density and found to be close (the theoretical strength value for glassy carbon with the same relative density as the carbon foam after second impregnation is 12 MPa). The theoretical mechanical strength values of glassy carbon in relation to relative density of the carbon was calculated from the Gibson and Ashby equation [8]. Moreover, the compressive strengths of the produced carbon foams were either similar or higher than the strength reported in the literature for carbon foams. For example, the compressive strength of carbon foams produced from coal precursors were reported to be 3 to 10 MPa depending on their density (bulk density of 0.32-0.40 g cm⁻³) [46] and compressive strength of highly porous reticulated vitreous carbon (RVC) was reported in the range of 0.07-3.4 MPa depending on the porosity [63].

For producing mesoporous and macroporous carbons with pore sizes in the nanometre ranges and homogenous pore size distribution, a templating method was used. Using this method porous carbons with high surface areas (325 m² g⁻¹ and 187 m² g⁻¹ for the mesoporous and macroporous carbons, respectively) were produced. The high surface area of the carbons results in high enzyme loading and improves the reaction kinetics and hence improves the power density of the biofuel cells.

In the templating method, two types of hard and soft templates were used. The carbon structures obtained from the soft templates had some cracks as a result of large shrinkage caused by the removal of the template during carbonisation. Silica beads were used as hard templates and resulted in structures with homogenous pores. Silica particles were slightly sintered to settle, which resulted in windows between the pores in the carbon materials. These hierarchically porous structures usually have better properties compared to single sized porous structures [238, 239]. This is due to increased mass transport through the material from the large pores (macropores) and at the same time having a high surface area because of the fine pores (mesopores).

Moulding and pressing of the silica particles resulted in stable silica templates which were used for producing mesoporous and macroporous carbons by *in situ* polymerisation of furfuryl alcohol (FA) in the pores of the templates. The method of

in situ polymerisation of FA is easier than the impregnation of the templates with PFA because in order to get stable and strong structures, PFA with high viscosity (high degree of polymerisation) should be used which makes the impregnation into the nanometric pores of the templates difficult and time consuming. Mesoporous and macroporous carbons with pore diameters of 19 ± 2 and 87 ± 16 nm, respectively were produced. The only problem with using the silica templates was the removal of silica from the carbon structures which had to be performed using hydrofluoric acid (HF) that is a very strong and corrosive acid.

Compressive strengths of the mesoporous and macroporous carbons prepared by silica templates were found 13 ± 0.65 MPa and 10.7 ± 0.53 MPa, respectively. No mechanical strength values for porous carbon structures prepared by the templating methods are reported in the literature. Moreover, electrical conductivity of the mesoporous and macroporous carbons prepared by silica templates were found 23 ± 2 S cm⁻¹ and 19 ± 1 S cm⁻¹, respectively. These electrical conductivity values are higher to a great extent than the electrical conductivity of the porous carbons prepared by the templating methods reported in the literature. For example, for ordered mesoporous carbon monolith (pores of ~7 nm) synthesised from a silica monolith and sucrose as a carbon precursor, conductivity of 0.43 S cm⁻¹ is reported [113]. Moreover, it was observed that the mechanical strength and the electrical conductivity of the carbon structures prepared by the templating method did not change much by increasing the relative densities. This could be due to weak carbon bonding in the structures. Carbon bonding can probably be improved by sintering the carbon structures at high temperatures (> 2000 °C).

An essential property of the electrodes in biofuel cells is high electrical conductivity. The minimum required conductivity of an electrode in biofuel cell was estimated from the mobility of charge carrier in glassy carbon and the charge carrier density. Thus, the minimum required conductivity of the carbon electrodes estimated to be 18×10^4 S cm⁻¹. This value was close to the conductivity of metals and for carbon materials was only possible to get close to this value if the carbon was in the graphitic form and the electron conduction was in the *ab* direction.

As carbonisation of PFA led to a glassy carbon, with a conductivity of 900 times less than the minimum conductivity required for an effective electron transfer (as mentioned above), the electrical conductivity of the carbon materials needs improving. Some methods such as addition of graphite powder to the carbon precursor prior to carbonisation, as well as successive impregnations of the carbon materials with the PFA helped improving the conductivity. It was found that addition of graphite powder to the amorphous carbon structures increased the conductivity 17 times (from 6 to 102 S cm⁻¹) and graphite foams after impregnation with PFA three times showed 5 times higher electrical conductivity than the foams impregnated with PFA only once.

Another method tested for enhancing the electrical conductivity of the produced carbon electrodes was catalytic graphitisation of the amorphous carbons. Catalytic graphitisation was used to improve the crystallinity of the carbons by formation of a graphitic material. In this method nickel was used as a catalyst and two types of graphitic carbons (T-component and G-component) were produced by addition of different amounts of nickel to the glassy carbons. It was observed that the presence of graphitic carbons improved the electrical conductivity (up to 50 times) compared to the carbons with an amorphous framework.

Electrochemical behaviour of the amorphous and the graphitic carbon foams was examined by cyclic voltammetry (CV) and the charge/discharge capacitance, specific electrochemical surface area (SESA) and the electron transfer rate of the produced electrodes were studied from the CV curves. It was observed that graphitisation of the amorphous structures increased the SESA of the electrodes (from 31 to 107 cm² cm⁻³) and the carbon foam T-component showed the best reversibility ($\Delta E_p = 0.26$ V at 100 mV s⁻¹ scan rate) and electron transfer rate (3.34×10^{-2} cm s⁻¹ at 100 mV s⁻¹ scan rate). Moreover, reversibility of the carbon foam T-component ($\Delta E_p = 0.17$ V at 50 mV s⁻¹) was better than the reversibility of the reticulated vitreous carbon electrodes (RVC) with $\Delta E_p = 0.20$ V at the same scan rate [69]. The graphitic carbon G-component did not show good electrochemical behaviour probably because of more nickel added to the structure, even though nickel in the carbon electrodes was washed out by acid before any investigations but a little amount might have left in the structures that

made the electrodes heterogeneous. Furthermore, by examining the CV curves of the porous carbons prepared by the templating method, it was found that at high scan rates ($> 0.5 \text{ mV s}^{-1}$) the electrochemical windows were not flat because the majority of the pores could not be penetrated by ions at the high scan rates.

Microbial fuel cells normally require large three-dimensional electrodes to increase the efficiency of the biofuel cells. The foaming method could not be used to prepare electrodes in large scales as the shrinkage was too high after the polymer burn out and after the impregnation with PFA and carbonisation. Templating method was also difficult to be used as obtaining stable large electrodes with open pores in micrometric size ranges was very hard. Therefore, a polymer blend technique was used to produce electrodes in large scales. In this method two kinds of polymers with different thermal stabilities were used. One was the carbon precursor and the other was a thermally decomposable polymer.

Electrodes with various shapes and sizes with mechanically stable structures were successfully fabricated with this method. High viscosity of the PFA used in this technique (7500 cP), as well as applying pressure to the PFA, that helps more cross-linking of the polymer, were accounted for the strong and stable structures of the electrodes. It should be noted that high viscous PFA was either not possible or very time consuming to be used in the foaming and the templating methods. It was observed that the electrical conductivity and the mechanical strength of the electrodes improved by impregnation with PFA. Moreover, these electrodes were composed of pores in the micrometric ranges (20-60 μm) with mesopores (200-400 nm) on the walls of the structures which made them suitable for hosting either enzymes or microbes. Electrochemically, the electrodes were found to be active and they showed a quasi-reversible behaviour. The heterogeneous rate constant (K_0) values obtained for the carbon electrodes after the polymer burn out and after the impregnation with PFA were in the range reported in the literature for K_0 of polished glassy carbon, *i.e.* 0.45×10^{-2} [237]- 0.14 cm s^{-1} [137], depending on the surface cleanliness and electrode pretreatment.

Chapter 7: Conclusions and Future Work

7.1 Conclusions

1. A foaming method was used for producing macroporous carbons for hosting microbes. Porous carbons with pores of $\sim 60 \mu\text{m}$ were prepared. This method was easy to apply but was difficult to control pore sizes; particularly producing macroporous carbons with pore sizes in the nanometre ranges was difficult.

2. In the foaming method, different process modifications were tested to improve the mechanical strength of the foams and the best result was obtained when a mixture of carbon precursor and graphite powder was used to produce the carbon walls of the foams. The mechanical strength of the foams ($\sim 11 \text{ MPa}$) was found close to the theoretical strength values of glassy carbon with the same relative density (12 MPa). Successive impregnations of the foams with PFA did not improve the mechanical strength.

3. Mesoporous and macroporous carbons with pore sizes in the nanometre ranges (~ 19 and 87 nm , respectively) were produced by a templating method. This method produced porous carbons with homogeneous pore size distributions. Porous carbon structures prepared by soft templates (polystyrene) resulted in some cracks in the structure due to a high shrinkage ($31\text{-}35\%$), whereas carbon structures prepared with hard templates (silica) were very uniform in porosity with a small shrinkage ($\sim 9\%$).

4. Mechanical strengths of the porous carbons prepared by the templating method are reported here for the first time. Mechanical strength and electrical conductivity of the mesoporous carbons of $\sim 19 \text{ nm}$ pore diameter and 0.37 relative density are $\sim 13 \text{ MPa}$ and $\sim 23 \text{ S cm}^{-1}$, respectively, which are higher than those of the macroporous carbons of $\sim 87 \text{ nm}$ and 0.25 relative density ($\sim 10.7 \text{ MPa}$ and $\sim 19 \text{ S cm}^{-1}$, respectively), due to the higher relative density in the former case. The electrical conductivities of the porous carbons prepared by the templating method are higher to a great extent than those reported in the literature ($0.43\text{-}1.37 \text{ S cm}^{-1}$ [112, 113]). However, the mechanical

strength and the electrical conductivity of the mesoporous carbons deviates considerably from the theoretical values of glassy carbon - more from the macroporous carbon structures, due to weak carbon bonding of the structures.

5. Catalytic graphitisation of produced porous carbons by nickel improved the degree of graphitization (from 0.67 for amorphous carbon to 0.21 for the G-component), which in turn enhances the electrical conductivity of the amorphous carbons up to 50 times.

6. Electrochemical studies of the produced carbon foams by cyclic voltammetry (CV) showed that the porous carbons had a quasi-reversible behaviour. Moreover, it was observed that graphitisation of the amorphous structures increased the specific electrochemical surface area (SESA) of the electrodes (from 31 to 107 cm² cm⁻³) and the carbon foam T-component showed the best reversibility (better than the reversibility of RVC) and electron transfer rate (0.26 V and 3.34 × 10⁻² cm s⁻¹, respectively at 100 mV s⁻¹ scan rate).

7. Porous carbon electrodes in large-scales with mechanically stable structures (2.6-12 MPa compressive strength, depending on their size) in various shapes and sizes were produced with the polymer blend technique. These monolithic carbons were composed of pores in the micrometric ranges (20-60 μm) that help efficient mass transfer, with mesopores (200-400 nm) on the walls that enhance the surface areas of the structures and hence improve enzyme and microbe loadings.

7.2 Future Work

1. Engineering design of the carbon electrodes for biofuel cells should be considered. For example, the electrodes fabricated in this work were all in cylindrical or cubic shapes whereas, other electrode shapes might be better in terms of flow control. Furthermore, according to the literature the use of three-dimensional electrodes increased the volumetric power density of microbial fuel cells compared to the use of two-dimensional electrodes [233, 240] thus in this work all the electrodes were designed three-dimensionally, to host more enzymes and microbes. However,

two-dimensional electrodes might be useful to use in other designs such as around a solid block carbon electrode so that the high conductivity of the solid block combine with the high enzyme loading in the pores of the carbon felt.

2. Surface chemistry of the carbon electrodes in biofuel cells usually needs some modifications for better enzyme attachments. Therefore, surface chemistry of the produced carbon electrodes need to be analysed and the desirable surface functional groups, for instance the oxygen groups exist on the edge planes of a pyrolytic graphite, should be created on the electrode surfaces.
3. Improvement of the electrical conductivity of the produced carbon electrodes by the templating method and the polymer blend technique, by catalytic graphitisation or by addition of graphite powder to the resin prior to carbonisation, should be examined.
4. The fabricated carbon electrodes should be tested in the real conditions to be compared with the ones currently available in the market. They need to be tested in terms of stability and oxidation. Moreover, the achievable efficiencies of the biofuel cells using these electrodes need to be compared with the biofuel cells using other types of electrodes.

References

1. Moore, C.M., Akers, N.L., Hill, A.D., Johnson, Z.C., and Minteer, S.D., Improving the environment for immobilized dehydrogenase enzymes by modifying nafion with tetraalkylammonium bromides. *Biomacromolecules*, 2004. 5(4): p. 1241-1247.
2. Mano, N., Mao, F., and Heller, A., A Miniature Biofuel Cell Operating in A Physiological Buffer. *Journal of the American Chemical Society*, 2002. 124(44): p. 12962-12963.
3. Barbieri, O., Hahn, M., Herzog, A., and Kötz, R., Capacitance limits of high surface area activated carbons for double layer capacitors. *Carbon*, 2005. 43(6): p. 1303-1310.
4. Takahashi, H., Li, B., Sasaki, T., Miyazaki, C., Kajino, T., and Inagaki, S., Immobilized enzymes in ordered mesoporous silica materials and improvement of their stability and catalytic activity in an organic solvent. *Microporous and Mesoporous Materials*, 2001. 44-45: p. 755-762.
5. Cracknell, J.A., Vincent, K.A., and Armstrong, F.A., Enzymes as working or inspirational electrocatalysts for fuel cells and electrolysis. *Chemical Reviews*, 2008. 108(7): p. 2439-2461.
6. Aelterman, P., Versichele, M., Marzorati, M., Boon, N., and Verstraete, W., Loading rate and external resistance control the electricity generation of microbial fuel cells with different three-dimensional anodes. *Bioresource Technology*, 2008. 99(18): p. 8895-8902.
7. He, Z., Minteer, S.D., and Angenent, L.T., Electricity generation from artificial wastewater using an upflow microbial fuel cell. *Environmental Science & Technology*, 2005. 39(14): p. 5262-5267.
8. Gibson, L.J. and Ashby, M.F., *Cellular solids; structure and properties*, 1997. Cambridge University Press: Cambridge. p. 213.
9. Gibson, L.J. and Ashby, M.F., *Cellular solids; structure and properties*, 1997. Cambridge University Press: Cambridge. p. 296-297.
10. Ryoo, R., Joo, S.H., Kruk, M., and Jaroniec, M., Ordered mesoporous carbons. *Advanced Materials*, 2001. 13(9): p. 677-681.

11. Subramoney, S., Novel Nanocarbons - Structure, Properties, and Potential Applications. *Advanced Materials*, 1998. 10(15): p. 1157-1171.
12. Kyotani, T., Control of pore structure in carbon. *Carbon*, 2000. 38(2): p. 269-286.
13. Jinwoo, L., Jaeyun, K., and Taeghwan, H., Recent progress in the synthesis of porous carbon materials. *Advanced Materials*, 2006. 18: p. 2073-2094.
14. Kinoshita, K., Carbon, electrochemical and physiochemical properties, 1987. John Wiley & Sons: California. p. 293-379.
15. Szucs, A., Hitchens, G.D., and Bockris, J.O.M., On the adsorption of glucose oxidase at a gold electrode. *Journal of the Electrochemical Society*, 1989. 136(12): p. 3748-3755.
16. Pierson, H.O., Handbook of carbon, graphite, diamond and fullerenes: properties, processing and applications, 1993. Noyes Publications: New Jersey. p. 107.
17. Marsh, H. and Rodriguez-Reinoso, F., Activated carbon, 2006. Elsevier: Oxford. p. 25-26.
18. Pierson, H.O., Handbook of carbon, graphite, diamond and fullerenes: properties, processing and applications, 1993. Noyes Publications: New Jersey. p. 13-36.
19. Pierson, H.O., Handbook of carbon, graphite, diamond and fullerenes: properties, processing and applications, 1993. Noyes Publications: New Jersey. p. 61.
20. Savage, G., Carbon - carbon composites, 1993. Chapman & Hall: London. p. 8-10.
21. Bundy, F.P., Bassett, W.A., Weathers, M.S., Hemley, R.J., Mao, H.U., and Goncharov, A.F., The pressure-temperature phase and transformation diagram for carbon; updated through 1994. *Carbon*, 1996. 34(2): p. 141-153.
22. Healey, F.H., Yu, Y.-F., and Chessick, J.J., The detection of hydrophilic heterogeneities on a carbon surface. *The Journal of Physical Chemistry*, 1955. 59(5): p. 399-402.
23. Mahajan, O.P., Moreno-castilla, C., and Walker, P.L., Surface-treated activated carbon for removal of phenol from water. *Separation Science and Technology*, 1980. 15(10): p. 1733 - 1752.

24. Kwon, S., Vidic, R., and Borguet, E., Enhancement of adsorption on graphite (HOPG) by modification of surface chemical functionality and morphology. *Carbon*, 2002. 40(13): p. 2351-2358.
25. Rodríguez-Reinoso, F., The role of carbon materials in heterogeneous catalysis. *Carbon*, 1998. 36(3): p. 159-175.
26. Collins, P.G., Bradley, K., Ishigami, M., and Zettl, A., Extreme oxygen sensitivity of electronic properties of carbon nanotubes. *Science*, 2000. 287(5459): p. 1801-1804.
27. Bandoz, T.J., Jagiello, J., and Schwarz, J.A., Effect of surface chemical groups on energetic heterogeneity of activated carbons. *Langmuir*, 1993. 9(10): p. 2518-2522.
28. Kong, J., Franklin, N.R., Zhou, C., Chapline, M.G., Peng, S., Cho, K., and Dai, H., Nanotube molecular wires as chemical sensors. *Science*, 2000. 287(5453): p. 622-625.
29. Rodríguez-Reinoso, F. and Molina-Sabio, M., Textural and chemical characterization of microporous carbons. *Advances in Colloid and Interface Science*, 1998. 76-77: p. 271-294.
30. Otake, Y. and Jenkins, R.G., Characterization of oxygen-containing surface complexes created on a microporous carbon by air and nitric acid treatment. *Carbon*, 1993. 31(1): p. 109-121.
31. Pierson, H.O., *Handbook of carbon, graphite, diamond and fullerenes: properties, processing and applications*, 1993. Noyes Publications: New Jersey. p. 63-66.
32. Pierson, H.O., *Handbook of carbon, graphite, diamond and fullerenes: properties, processing and applications*, 1993. Noyes Publications: New Jersey. p. 73-80.
33. Savage, G., *Carbon - carbon composites*, 1993. Chapman & Hall: London. p. 120-123.
34. Franklin, R.E., The structure of graphitic carbons. *Acta Crystallographica* 1951. 4: p. 253-261.
35. Jenkins, G.M. and Kawamura, K., *Polymeric carbons - carbon fibre, glass and char*, 1976. Cambridge University Press: New York. p. 11-35.

36. Inagaki, M., Harada, S., Sato, T., Nakajima, T., Horino, Y., and Morita, K., Carbonization of polyimide film "Kapton". *Carbon*, 1989. 27(2): p. 253-257.
37. Kajiura, H., Tanabe, Y., and Yasuda, E., Carbonization and graphitization behavior of iodine-treated coal tar pitch. *Carbon*, 1997. 35(2): p. 169-174.
38. Savage, G., *Carbon - carbon composites*, 1993. Chapman & Hall: London. p. 158-178.
39. Eser, S. and Jenkins, R.G., Carbonization of petroleum feedstocks I: Relationships between chemical constitution of the feedstocks and mesophase development. *Carbon*, 1989. 27(6): p. 877-887.
40. Lewis, I.C., *Chemistry of carbonization*. *Carbon*, 1982. 20(6): p. 519-529.
41. Savage, G., *Carbon - carbon composites*, 1993. Chapman & Hall: London. p. 28.
42. Seki, H., Kumagai, J., Matsuda, M., Ito, O., and Iino, M., Fluidity of coal residues after extraction with mixed solvents. *Fuel*, 1989. 68(8): p. 978-982.
43. Clemens, A.H. and Matheson, T.W., The effect of selected additives and treatments on Gieseler fluidity in coals. *Fuel*, 1995. 74(1): p. 57-62.
44. Kipling, J.J. and Shooter, P.V., Factors affecting the graphitization of carbon: evidence from polarized light microscopy. *Carbon*, 1966. 4: p. 1-4.
45. Dollimore, D. and Heal, G.R., The degradation of selected polymers to carbons in an inert atmosphere. *Carbon*, 1967. 5: p. 65-72.
46. Chen, C., Kennel, E.B., Stiller, A.H., Stansberry, P.G., and Zondlo, J.W., Carbon foam derived from various precursors. *Carbon*, 2006. 44(8): p. 1535-1543
47. Pascault, J.-P., Sautereau, H., Pascault Pascault, J.-P., Verdu, J., and Williams, R.J.J., *Thermosetting polymers*, 2002. Marcel Dekker: New York. p. 1.
48. Fuertes, A.B. and Nevskaja, D.M., Control of mesoporous structure of carbons synthesised using a mesostructured silica as template. *Microporous and Mesoporous Materials*, 2003. 62(3): p. 177-190.
49. Lu, A.-H., Li, W.-C., Schmidt, W., and Schüth, F., Fabrication of hierarchically structured carbon monoliths via self-binding and salt templating. *Microporous and Mesoporous Materials*, 2006. 95(1-3): p. 187-192.

50. Tennison, S.R., Phenolic-resin-derived activated carbons. *Applied Catalysis A: General*, 1998. 173(2): p. 289-311.
51. Streitwieser, A., Clayton, J., and Heathcock, H., *Introduction to organic chemistry*, 1985. Macmillan Publishing Company: New York. p. 12.
52. Streitwieser, A., Clayton, J., and Heathcock, H., *Introduction to organic chemistry*, 1985. Macmillan Publishing Company: New York. p. 808.
53. Rego, R., Adriaensens, P.J., Carleer, R.A., and Gelan, J.M., Fully quantitative carbon-13 NMR characterization of resol phenol-formaldehyde prepolymer resins. *Polymer*, 2004. 45(1): p. 33-38.
54. Zhenglong Yang, J.W.K.H.J.M.Z.Y.Y.L., Functional mesoporous polymers from phenolic building oligomers. *Macromolecular Rapid Communications*, 2008. 29(5): p. 442-446.
55. Savage, G., *Carbon - carbon composites*, 1993. Chapman & Hall: London. p. 128-129.
56. Makarevich, N.I., Sushko, N.I., Ivanov, A.I., Lingart, E.N., Glazova, T.I., and Prutkov, L.M., Pyrolysis of some commercial phenol-formaldehyde bonding agents. *Journal of Applied Spectroscopy*, 1977. 26(4): p. 531-535.
57. Gandini, A. and Belgacem, M.N., Furans in polymer chemistry. *Progress in Polymer Science*, 1997. 22(6): p. 1203-1379.
58. Choura, M., Belgacem, N.M., and Gandini, A., Acid-catalyzed polycondensation of furfuryl alcohol: mechanisms of chromophore formation and cross-linking. *Macromolecules*, 1996. 29: p. 3839-3850.
59. Wang, Z., Lu, Z., Huang, X., Xue, R., and Chen, L., Chemical and crystalline structure characterizations of polyfurfuryl alcohol pyrolyzed at 600 °C. *Carbon*, 1998. 36(1-2): p. 51-59.
60. Fitzer, E. and Schäfer, W., The effect of crosslinking on the formation of glasslike carbons from thermosetting resins. *Carbon*, 1970. 8(3): p. 353-364.
61. Fitzer, E., Schaefer, W., and Yamada, S., The formation of glasslike carbon by pyrolysis of polyfurfuryl alcohol and phenolic resin. *Carbon*, 1969. 7(6): p. 643-646.
62. Shindo, A. and Izumino, K., Structural variation during pyrolysis of furfuryl alcohol and furfural-furfuryl alcohol resins. *Carbon*, 1994. 32(7): p. 1233-1243.

63. Pierson, H.O., Handbook of carbon, graphite, diamond and fullerenes: properties, processing and applications, 1993. Noyes Publications: New Jersey. p. 122-140.
64. Jenkins, G.M. and Kawamura, K., Polymeric carbons - carbon fibre, glass and char, 1976. Cambridge University Press: New York. p. 65-73.
65. Jenkins, G.M. and Kawamura, K., Structure of glassy carbon. Nature, 1971. 231(5299): p. 175-176.
66. Cowlard, F.C. and Lewis, J.C., Vitreous carbon — A new form of carbon. Journal of Materials Science 1967. 2(6): p. 507 - 512
67. Lausevic, Z. and Jenkins, G.M., Anodic oxidation of glassy carbon surfaces. Carbon, 1986. 24(5): p. 651-652.
68. Van der Linden, W.E. and Dieker, J.W., Glassy carbon as electrode material in electro- analytical chemistry. Analytica Chimica Acta, 1980. 119(1): p. 1-24.
69. Gonçalves, E.S., Rezende, M.C., Takahashi, M.F.K., and Ferreira, N.G., Electrochemical reversibility of reticulated vitreous carbon electrodes heat treated at different carbonization temperatures. Materials Research, 2006. 9: p. 147-152.
70. Kaneko, K., Determination of pore size and pore size distribution:1. Adsorbents and catalysts. Journal of Membrane Science, 1994. 96(1-2): p. 59-89.
71. International Union of Pure and Applied Chemistry Physical Chemistry Division Commission on Colloid and Surface Chemistry, Subcommittee on Characterization of Porous Solids: Recommendations for the characterization of porous solids (Technical Report), in *Pure & Applied Chemistry*. 1994: 66 (8). Great Britain. p. 1739-1758.
72. Sing, K.S.W., Everett, D.H., GHAul, R.A.W., Moscou, L., Pierotti, R.A., Rouquerol, J., and Siemieniewska, T., Reporting physisorption data for gas/solid systems with special reference to the determination of surface area and porosity. *Pure & Applied Chemistry*, 1985. 57(4): p. 603-919.
73. Haber, J., Manual on catalyst characterization. *Pure & Applied Chemistry*, 1991. 63: p. 1227-1246.
74. Ford, W., Method of making cellular refractory thermal insulating material. 1964, 3121050: US Patent.

75. WJ, M., Light-weight porous carbon. 1967, 3342555: US Patent.
76. Googin, J., Napier, J., and Scrivner, M., Method for manufacturing foam carbon products. 1967, 3345440: US Patent.
77. Wang, J., Reticulated vitreous carbon—a new versatile electrode material. *Electrochimica Acta*, 1981. 26(12): p. 1721-1726
78. J.M. Friedrich, C. Ponce-de-Le on, G.W. Reade, and Walsh, F.C., Reticulated vitreous carbon as an electrode material. *Journal of Electroanalytical Chemistry*, 2004. 561: p. 203–217.
79. Wang, J., Reticulated vitreous carbon--a new versatile electrode material. *Electrochimica Acta*, 1981. 26(12): p. 1721-1726.
80. Hager, J.W. *Materials research society symposium proceedings 270*, 29-46 1992.
81. Klett, J., Process for making carbon foam. 2000, 6033506: US Patent
82. Gallego, N.C. and Klett, J.W., Carbon foams for thermal management. *Carbon*, 2003. 41(7): p. 1461–1466.
83. Kanno, K. and Tsuruya, H., Manufacture of carbon foam and graphite foam. 2002, 1225160A2: Eur Patent
84. Hager, J.W. and Anderson, D.P. *Carbon extended abstracts in 21st Biennial Conference 1993*. New York.
85. Kyotani, T., Ma, Z., and Tomita, A., Template synthesis of novel porous carbons using various types of zeolites. *Carbon*, 2003. 41(7): p. 1451-1459.
86. Lee, J., Han, S., and Hyeon, T., Synthesis of new nanoporous carbon materials using nanostructured silica materials as templates. *Journal of Materials Chemistry*, 2004. 14(4): p. 478-486.
87. Zakhidov, A.A., Baughman, R.H., Iqbal, Z., Cui, C., Khayrullin, I., Dantas, S.O., Marti, J., and Ralchenko, V.G., Carbon structures with three-dimensional periodicity at optical wavelengths. *Science* 1998. 282(5390): p. 897-901.
88. Sakintuna, B. and Yurum, Y., Templated porous carbons: a review article. *Industrial and Engineering Chemistry Research*, 2005. 44(9): p. 2893-2902.
89. Ma, Z., Kyotani, T., and Tomita, A., Synthesis methods for preparing microporous carbons with a structural regularity of zeolite Y. *Carbon*, 2002. 40(13): p. 2367-2374.

90. Su, F., Zhao, X.S., Lv, L., and Zhou, Z., Synthesis and characterization of microporous carbons templated by ammonium-form zeolite Y. *Carbon*, 2004. 42(14): p. 2821-2831.
91. Kyotani, T., Nagai, T., Inoue, S., and Tomita, A., Formation of new type of porous carbon by carbonization in zeolite nanochannels. *Chemistry of Materials*, 1997. 9(2): p. 609-615.
92. Gaslain, F.O.M., Parmentier, J., Valtchev, V.P., and Patarin, J., First zeolite carbon replica with a well resolved X-ray diffraction pattern. *Chemical Communications*, 2006(9): p. 991-993.
93. Rodriguez-Mirasol, J., Cordero, T., Radovic, L.R., and Rodriguez, J.J., Structural and textural properties of pyrolytic carbon formed within a microporous zeolite template. *Chemistry of Materials*, 1998. 10(2): p. 550-558.
94. Ma, Z., Kyotani, T., and Tomita, A., Preparation of a high surface area microporous carbon having the structural regularity of Y zeolite. *Chemical Communications*, 2000(23): p. 2365-2366.
95. Ryoo, R., Joo, S.H., and Jun, S., Synthesis of highly ordered carbon molecular sieves via template-mediated structural transformation. *The Journal of Physical Chemistry B*, 1999. 103(37): p. 7743-7746.
96. Lee, J., Yoon, S., Hyeon, T., Oh, S.M., and Kim, K.B., Synthesis of a new mesoporous carbon and its application to electrochemical double-layer capacitors. *Chemical Communications*, 1999(21): p. 2177-2178.
97. Kim, J.M. and Stucky, G.D., Synthesis of highly ordered mesoporous silica materials using sodium silicate and amphiphilic block copolymers. *Chemical Communications*, 2000(13): p. 1159-1160.
98. Lee, J.S., Joo, S.H., and Ryoo, R., Synthesis of mesoporous silicas of controlled pore wall thickness and their replication to ordered nanoporous carbons with various pore diameters. *Journal of the American Chemical Society*, 2002. 124(7): p. 1156-1157.
99. Zhao, D., Feng, J., Huo, Q., Melosh, N., Fredrickson, G.H., Chmelka, B.F., and Stucky, G.D., Triblock copolymer syntheses of mesoporous silica with periodic 50 to 300 angstrom pores. *Science*, 1998. 279(5350): p. 548-552.

100. Joo, S.H., Choi, S.J., Oh, I., Kwak, J., Liu, Z., Terasaki, O., and Ryoo, R., Ordered nanoporous arrays of carbon supporting high dispersions of platinum nanoparticles. *Nature*, 2001. 412(6843): p. 169-172.
101. Kruk, M., Jaroniec, M., Ryoo, R., and Joo, S.H., Characterization of ordered mesoporous carbons synthesized using MCM-48 silicas as templates. *The Journal of Physical Chemistry B*, 2000. 104(33): p. 7960-7968.
102. Lee, J., Yoon, S., Oh, S.M., Shin, C.-H., and Hyeon, T., Development of a new mesoporous carbon using an HMS aluminosilicate template. *Advanced Materials*, 2000. 12(5): p. 359-362.
103. Stein, A., Sphere templating methods for periodic porous solids. *Microporous and Mesoporous Materials*, 2001. 44-45: p. 227-239.
104. Johnson, S.A., Ollivier, P.J., and Mallouk, T.E., Ordered mesoporous polymers of tunable pore size from colloidal silica templates. *Science*, 1999. 283(5404): p. 963-965.
105. Yan, H., Blanford, C.F., Holland, B.T., Smyrl, W.H., and Stein, A., General synthesis of periodic macroporous solids by templated salt precipitation and chemical conversion. *Chemistry of Materials*, 2000. 12(4): p. 1134-1141.
106. Nishiyama, N., Zheng, T., Yamane, Y., Egashira, Y., and Ueyama, K., Microporous carbons prepared from cationic surfactant-resorcinol/formaldehyde composites. *Carbon*, 2005. 43(2): p. 269-274.
107. Lee, K.T. and Oh, S.M., Novel synthesis of porous carbons with tunable pore size by surfactant-templated sol-gel process and carbonisation. *Chemical Communications*, 2002(22): p. 2722-2723.
108. Wan, Y., Shi, Y., and Zhao, D., Supramolecular aggregates as templates: ordered mesoporous polymers and carbons. *Chemistry of Materials*, 2008. 20(3): p. 932-945.
109. Tanev, P.T. and Pinnavaia, T.J., A Neutral templating route to mesoporous molecular sieves. *Science*, 1995. 267(5199): p. 865-867.
110. Meng, Y., Gu, D., Zhang, F., Shi, Y., Yang, H., Li, Z., Yu, C., Tu, B., and Zhao, D., Ordered mesoporous polymers and homologous carbon frameworks: amphiphilic surfactant templating and direct transformation. *Angewandte Chemie International Edition*, 2005. 44: p. 7053-7059.

111. Meng, Y., Gu, D., Zhang, F., Shi, Y., Cheng, L., Feng, D., Wu, Z., Chen, Z., Wan, Y., Stein, A., and Zhao, D., A family of highly ordered mesoporous polymer resin and carbon structures from organic-organic self-assembly. *Chemistry of Materials*, 2006. 18(18): p. 4447-4464.
112. Wang, L., Lin, S., Lin, K., Yin, C., Liang, D., Di, Y., Fan, P., Jiang, D., and Xiao, F.-S., A facile synthesis of highly ordered mesoporous carbon monolith with mechanically stable mesostructure and superior conductivity from SBA-15 powder. *Microporous and Mesoporous Materials*, 2005. 85(1-2): p. 136-142.
113. Yang, H., Shi, Q., Liu, X., Xie, S., Jiang, D., Zhang, F., Yu, C., Tu, B., and Zhao, D., Synthesis of ordered mesoporous carbon monoliths with bicontinuous cubic pore structure of Ia3d symmetry. *Chemical Communications* 2002(23): p. 2842-2843.
114. Gibson, L.J. and Ashby, M.F., *Cellular solids; structure and properties*, 1997. Cambridge University Press: Cambridge. p. 2.
115. Mepura, Metaapulvergesellschaft m.b.h., Ranshofen, A-5282 Braunau-Ranshofen. 1995: Austria.
116. Jenkins, G.M. and Kawamura, K., *Polymeric carbons - carbon fibre, glass and char*, 1976. Cambridge University Press: New York. p. 94-96.
117. Bard, A.J. and Faulkner, L.R., *Electrochemical methods: fundamentals and applications*, 2001. John Wiley & Sons: New York. p. 26.
118. Greef, R., Peat, R., Peter, L.M., Pletcher, D., and Robinson, J., *Instrumental methods in electrochemistry*, 1985. Ellis Horwood: London. p. 178-227.
119. Nicholson, R.S. and Shain, I., *Theory of stationary electrode polarography. Single scan and cyclic methods applied to reversible, irreversible, and kinetic systems*. *Analytical Chemistry*, 1964. 36(4): p. 706-723.
120. Trasatti, S. and Petrii, O.A., *Real surface area measurements in electrochemistry*. *Pure & Applied Chemistry*, 1991. 63(5): p. 711-734.
121. Greef, R., Peat, R., Peter, L.M., Pletcher, D., and Robinson, J., *Instrumental methods in electrochemistry*, 1985. Ellis Horwood: London. p. 149-176.
122. Bard, A.J. and Faulkner, L.R., *Electrochemical methods: fundamentals and applications*, 2001. John Wiley & Sons: New York. p. 12-13.

123. Grahame, D.C., The electrical double layer and the theory of electrocapillarity. *Chemical Reviews*, 1947. 41(3): p. 441-501.
124. Soffer, A. and Folman, M., The electrical double layer of high surface porous carbon electrode. *Journal of Electroanalytical Chemistry*, 1972. 38(1): p. 25-43.
125. Salitra, G., Soffer, A., Eliad, L., Cohen, Y., and Aurbach, D., Carbon electrodes for double-layer capacitors: I. Relations between ion and pore dimensions. *Journal of the Electrochemical Society*, 2000. 147(7): p. 2486-2493.
126. Lin, C., Ritter, J.A., and Popov, B.N., Correlation of double-layer capacitance with the pore structure of sol-gel derived carbon xerogels. *Journal of The Electrochemical Society*, 1999. 146(10): p. 3639-3643.
127. Bard, A.J. and Faulkner, L.R., *Electrochemical methods: fundamentals and applications*, 2001. John Wiley & Sons: New York. p. 23.
128. Brett, C.M.A. and Oliveira Brett, A.M., *Electrochemistry, principles, methods and applications*, 1993. Oxford University Press: New York. p. 70-71.
129. Nicholson, R.S., Theory and application of cyclic voltammetry for measurement of electrode reaction kinetics. *Analytical Chemistry*, 1965. 37(11): p. 1351-1355.
130. Brett, C.M.A. and Oliveira Brett, A.M., *Electrochemistry, principles, methods and applications*, 1993. Oxford University Press: New York. p. 174-187.
131. Randin, J.P., *Encyclopedia of electrochemistry of the elements*, A.J. Bard, Editor, 1976. Dekker: New York. p. 1.
132. Thornton, D.C., Corby, K.T., Spindel, V.A., Jordan, J., Robbat, A., Rutstrom, D.J., Gross, M., and Ritzler, G., Pretreatment and validation procedure for glassy carbon voltammetric indicator electrodes. *Analytical Chemistry*, 1985. 57(1): p. 150-155.
133. Adams, R.N., *Electrochemistry at solid electrodes*, 1969. Dekker: New York. p. 19.
134. Fagan, D.T., Hu, I.F., and Kuwana, T., Vacuum heat-treatment for activation of glassy carbon electrodes. *Analytical Chemistry*, 1985. 57(14): p. 2759-2763.

135. Wightman, R.M., Deakin, M.R., Kovach, P.M., Kuhr, W.G., and Stutts, K.J., Methods to Improve Electrochemical Reversibility at Carbon Electrodes. *Journal of The Electrochemical Society*, 1984. 131(7): p. 1578-1583.
136. Rusling, J.F., Variations in electron-transfer rate at polished glassy carbon electrodes exposed to air. *Analytical Chemistry*, 1984. 56(3): p. 575-578.
137. Hu, I.-F., Karweik, D.H., and Kuwana, T., Activation and deactivation of glassy carbon electrodes. *Journal of Electroanalytical Chemistry*, 1985. 188(1-2): p. 59-72.
138. Norvell, V.E. and Mamantov, G., Optically transparent vitreous carbon electrode. *Analytical Chemistry*, 1977. 49(9): p. 1470-1472.
139. Gibson, L.J. and Ashby, M.F., *Cellular solids; structure and properties*, 1997. Cambridge University Press: Cambridge. p. 183-217.
140. Pu, X., Liu, X., Qiu, F., and Huang, L., Novel method to optimize the structure of reticulated porous ceramics. *Journal of the American Ceramic Society*, 2004. 87(7): p. 1392-1394.
141. Brown, D.D. and Green, D.J., Investigation of strut crack formation in open cell alumina ceramics. *Journal of the American Ceramic Society*, 1994. 77(6): p. 1467-1472.
142. Zhu, X., Jiang, D., Tan, S., and Zhang, Z., Improvement in the strut thickness of reticulated porous ceramics. *Journal of the American Ceramic Society*, 2001. 84(7): p. 1654-1656.
143. Wu, M. and Messing, G.L., SiC-whisker-reinforced cellular SiO₂ composites. *Journal of the American Ceramic Society*, 1990. 73(11): p. 3497-3499.
144. Davidge, R.W., Fibre-reinforced ceramics. *Composites*, 1987. 18(2): p. 92-98.
145. Paiva, A.E.M., Sepulveda, P., and Pandolfelli, V.C., Processing and thermomechanical evaluation of fibre-reinforced alumina filters. *Journal of Materials Science*, 1999. 34(11): p. 2641-2649.
146. Han, Y.-s., Li, J.-b., Wei, Q.-m., and Tang, K., The effect of sintering temperatures on alumina foam strength. *Ceramics International*, 2002. 28(7): p. 755-759.
147. Wang, X., Luo, R., Ni, Y., Zhang, R., and Wang, S., Properties of chopped carbon fiber reinforced carbon foam composites. *Materials Letters*, 2009. 63(1): p. 25-27.

148. Brooks, J.D. and Taylor, G.H., Chemistry and physics of carbon, L. Philip and J. Walker, Editors, 1968. Marcel Dekker: New York. p. 243-285.
149. Fuertes, A.B. and Alvarez, S., Graphitic mesoporous carbons synthesised through mesostructured silica templates. Carbon, 2004. 42(15): p. 3049-3055.
150. Ōya, A. and Marsh, H., Phenomena of catalytic graphitization. Journal of Materials Science, 1982. 17(2): p. 309-322.
151. Fischbach, D.B., Chemistry and physics of carbon, P.L. Walker, Jr., Editor, 1971. Marcel Dekker, INC.: New York. p. 83-91.
152. Yokokawa, C., Hosokawa, K., and Takegami, Y., Low temperature catalytic graphitization of hard carbon. Carbon, 1966. 4: p. 459-465.
153. Marsh, H., Crawford, D., and Taylor, D.W., Catalytic graphitization by iron of isotropic carbon from polyfurfuryl alcohol, 725-1090 K. A high resolution electron microscope study. Carbon, 1983. 21(1): p. 81-87.
154. Mochida, I., Ohtsubo, R., Takeshita, K., and Marsh, H., Catalytic graphitization of graphitizable carbon by chromium, manganese and molybdenum oxides. Carbon, 1980. 18(1): p. 25-30.
155. Mochida, I., Ohtsubo, R., and Takeshita, K., Catalytic graphitization of non-graphitizable carbon by chromium and manganese oxides. Carbon, 1980. 18: p. 117-123.
156. Sevilla, M. and Fuertes, A.B., Catalytic graphitization of templated mesoporous carbons. Carbon, 2006. 44(3): p. 468-474.
157. Oya, A., Mochizuki, M., Otani, S., and Tomizuka, I., An electron microscopic study on the turbostratic carbon formed in phenolic resin carbon by catalytic action of finely dispersed nickel. Carbon, 1979. 17(1): p. 71-76.
158. Oya, A., Yamashita, R., and Otani, S., Catalytic graphitization of carbons by borons. Fuel, 1979. 58: p. 495-500.
159. Warren, B.E., X-ray diffraction in random layer lattices. Physical Review, 1941. 59(9): p. 693.
160. Badami, D.V., X-ray studies of the formation of graphite from silicon carbide. Carbon, 1964. 1(3): p. 375-375.
161. Hansen, M., Constitution of binary alloys, 1958. McGraw-Hill: New York. p. 374-375.

162. Marsh, H. and Warburton, A.P., Catalysis of graphitization. *Journal of Applied Chemistry*, 1970. 20: p. 133-142.
163. Oya, A. and Otani, S., Catalytic graphitization of phenolic resin carbon by silicon. *High Temperature-High Pressures*, 1975. 7: p. 563-572.
164. Loebner, E.E., Thermoelectric power, electrical resistance, and crystalline structure of carbons. *Physical Review*, 1956. 102(1): p. 46.
165. Honda, H., Kobayashi, K., and Sugawara, S., X-ray characteristics of non-graphitizing-type carbon. *Carbon*, 1968. 6(4): p. 517-523.
166. Oua, A., Otani, S., and Tomizuka, I., On the structure of turbostratic carbon formed in charcoal by catalytic action of calcium vapor. *Carbon*, 1979. 17(3): p. 305-306.
167. Oya, A. and Otani, S., The effects of aluminum on structural development of a carbon derived from phenolic resin. *Carbon*, 1976. 14(4): p. 191-194.
168. Courtney, R.L. and Duliere, S.F., The catalytic graphitization of naphthalenediol and a urethane foam -- a feasibility study. *Carbon*, 1972. 10(1): p. 65-72.
169. Wewerka, E.M. and Imprescia, R.J., The use of organometallic additives to promote graphitization of carbons derived from furfuryl alcohol resins. *Carbon*, 1973. 11(4): p. 289-294.
170. Otani, S., Oya, A., and Akagami, J., The effects of nickel on structural development in carbons. *Carbon*, 1975. 13(5): p. 353-356.
171. Oya, A. and Otani, S., Catalytic graphitization of carbons by various metals. *Carbon*, 1979. 17(2): p. 131-137.
172. Baraniecki, C., Pinchbeck, P.H., and Pickering, F.B., Some aspects of graphitization induced by iron and ferro-silicon additions. *Carbon*, 1969. 7(2): p. 213-224.
173. Fuertes, A.B. and Centeno, T.A., Mesoporous carbons with graphitic structures fabricated by using porous silica materials as templates and iron-impregnated polypyrrole as precursor. *Journal of Materials Chemistry*, 2005. 15(10): p. 1079-1083.
174. Kammereck, R., Nakamizo, M., and Walker, P.L., Structure and properties of iron containing glassy carbons. *Carbon*, 1974. 12: p. 281-289.

175. Blanford, C.F., Heath, R.S., and Armstrong, F.A., A stable electrode for high-potential, electrocatalytic O₂ reduction based on rational attachment of a blue copper oxidase to a graphite surface. *Chemical Communications*, 2007: p. 1710-1712.
176. Pellissier, M., Barrière, F., Downard, A.J., and Leech, D., Improved stability of redox enzyme layers on glassy carbon electrodes via covalent grafting. *Electrochemistry Communications*, 2008. 10(6): p. 835-838.
177. Moreno-Castilla, C., Carrasco-Marin, F., and Mueden, A., The creation of acid carbon surfaces by treatment with (NH₄)₂S₂O₈. *Carbon*, 1997. 35(10-11): p. 1619-1626.
178. Kwon, S., Vidic, R., and Borguet, E., The effect of surface chemical functional groups on the adsorption and desorption of a polar molecule, acetone, from a model carbonaceous surface, graphite. *Surface Science*, 2003. 522: p. 17-26.
179. Moreno-Castilla, C., Lopez-Ramon, M.V., and Carrasco-Marin, F., Changes in surface chemistry of activated carbons by wet oxidation. *Carbon*, 2000. 38(14): p. 1995-2001.
180. Figueiredo, J.L., Pereira, M.F.R., Freitas, M.M.A., and Orfao, J.J.M., Modification of the surface chemistry of activated carbons. *Carbon*, 1999. 37(9): p. 1379-1389.
181. Moreno-Castilla, C., Ferro-Garcia, M.A., Joly, J.P., Bautista-Toledo, I., Carrasco-Marin, F., and Rivera-Utrilla, J., Activated carbon surface modifications by nitric acid, hydrogen peroxide, and ammonium peroxydisulfate treatments. *Langmuir*, 1995. 11: p. 4386-4392.
182. Chu, X. and Kinoshita, K., Surface modification of carbons for enhanced electrochemical activity. *Materials Science and Engineering B*, 1997. 49(1): p. 53-60.
183. Evans, J.F., Kuwana, T., Henne, M.T., and Royer, G.P., Electrocatalysis of solution species using modified electrodes. *Journal of Electroanalytical Chemistry*, 1977. 80(2): p. 409-416.
184. Engstrom, R.C. and Strasser, V.A., Characterization of electrochemically pretreated glassy carbon electrodes. *Analytical Chemistry*, 1984. 56(2): p. 136-141.

185. Nakahara, M. and Sanada, Y., FT-IR ATR spectroscopy of the edge surface of pyrolytic graphite and its surface/PVC interface. *Journal of Materials Science*, 1995. 30(17): p. 4363-4368.
186. Kamau, G.N., Surface preparation of glassy carbon electrodes. *Analytica Chimica Acta*, 1988. 207: p. 1-16.
187. Takahashi, H., Li, B., Sasaki, T., Miyazaki, C., Kajino, T., and Inagaki, S., Catalytic Activity in Organic Solvents and Stability of Immobilized Enzymes Depend on the Pore Size and Surface Characteristics of Mesoporous Silica. *Chemistry of Materials*, 2000. 12(11): p. 3301-3305.
188. Lei, C., Shin, Y., Liu, J., and Ackerman, E.J., Entrapping Enzyme in a Functionalized Nanoporous Support. *Journal of the American Chemical Society*, 2002. 124(38): p. 11242-11243.
189. Fan, J., Lei, J., Wang, L., Yu, C., Tu, B., and Zhao, D., Rapid and high-capacity immobilization of enzymes based on mesoporous silicas with controlled morphologies. *Chemical Communications*, 2003: p. 2140-2141.
190. Wang, P., Dai, S., Waezsada, S.D., Tsao, A.Y., and Davison, B.H., Enzyme stabilization by covalent binding in nanoporous sol-gel glass for nonaqueous biocatalysis. *Biotechnology and Bioengineering*, 2001. 74(3): p. 249-255.
191. Jones, A.K., Sillery, E., Albracht, S.P.J., and Armstrong, F.A., Direct comparison of the electrocatalytic oxidation of hydrogen by an enzyme and a platinum catalyst. *Chemical Communications*, 2002(8): p. 866-867.
192. Karyakin, A.A., Morozov, S.V., Karyakina, E.E., Zorin, N.A., Pereygin, V.V., and Cosnier, S., Hydrogenase electrodes for fuel cells. *Biochemical Society Transactions* 2005. 33: p. 73-75.
193. Hambourger, M., Gervaldo, M., Svedruzic, D., King, P.W., Gust, D., Ghirardi, M., Moore, A.L., and Moore, T.A., [FeFe]-hydrogenase-catalyzed H₂ production in a photoelectrochemical biofuel cell. *Journal of the American Chemical Society* 2008. 130(6): p. 2015-2022.
194. Shumakovich, G.P., Shleev, S.V., Morozova, O.V., Khohlov, P.S., Gazaryan, I.G., and Yaropolov, A.I., Electrochemistry and kinetics of fungal laccase mediators. *Bioelectrochemistry*, 2006. 69(1): p. 16-24.

195. Stolarczyk, K., Nazaruk, E., Rogalski, J., and Bilewicz, R., Nanostructured carbon electrodes for laccase-catalyzed oxygen reduction without added mediators. *Electrochimica Acta*, 2008. 53(11): p. 3983-3990.
196. Deloggio, T.J. and Graves, D.J., An immobilized hydrogenase from *Alcaligenes eutrophus* H-16. *Biotechnology and Bioengineering*, 1988. 32(3): p. 295-300.
197. Fumihito, A., Masanobu, O., and Toshio, F., Selective manipulation of a microbe in a microchannel using a teleoperated laser scanning manipulator and dielectrophoresis. *Advanced Robotics*, 1999. 13(3): p. 343-345.
198. Rand, B., Appleyard, S.P., and Yardim, M.F., Design and control of structure of advanced carbon materials for enhanced performance, in *NATO Science Series*, 2001. Kluwer Academic Publishers: The Netherlands. p. 68.
199. Foulani, A., Laurent, C., Mebarki, B., and Segui, Y., Determination of space-charge dynamics and transport parameters in hydrogenated carbon layers by time-resolved electroluminescence measurements. *Journal of Applied Physics*, 1996. 80(1): p. 470-476.
200. Mycielski, W., Staryga, E., Lipinski, A., Mitura, S., and Sokolowska, A., Open-circuit mode drift mobility measurements in DLC films. *Diamond and Related Materials*, 1994. 3(4-6): p. 858-860.
201. Maeng, S.L., Uchikoga, S., Clough, F.J., Tagliaferro, A., Flewitt, A.J., Robertson, J., and Milne, W.I., A carbon based bottom gate thin film transistor. *Diamond and Related Materials*, 2000. 9(3-6): p. 805-810.
202. Klibanov, L., Oksman, M., Seidman, A., and Croitoru, N., The drift mobility and decay of photocurrent in doped amorphous diamond-like carbon films. *Diamond and Related Materials*, 1997. 6(9): p. 1152-1156.
203. Armstrong, F.A., Heering, H.A., and Hirst, J., Reaction of complex metalloproteins studied by protein-film voltammetry. *Chemical Society Reviews*, 1997. 26: p. 169-179.
204. Chanda, M. and Dinesh, S.R., Monitoring the curing of furan resins through the exothermic heat of reaction. *Die Angewandte Makromolekulare Chemie*, 1978. 69(1): p. 85-98.

205. Burket, C.L., Rajagopalan, R., Marencic, A.P., Dronvajjala, K., and Foley, H.C., Genesis of porosity in polyfurfuryl alcohol derived nanoporous carbon. *Carbon*, 2006. 44(14): p. 2957-2963.
206. Marsh, H. and Rodriguez-Reinoso, F., *Activated carbon*, 2006. Elsevier: Oxford. p. 14.
207. Nakamizo, M., Honda, H., Inagaki, M., and Hishiyama, Y., Raman spectra, effective Debye parameter and magnetoresistance of graphitized cokes. *Carbon*, 1977. 15(5): p. 295-298.
208. Tuinstra, F. and Koenig, J.L., Raman spectrum of graphite. *The Journal of Chemical Physics*, 1970. 53(3): p. 1126-1130.
209. Jenkins, G.M. and Kawamura, K., *Polymeric carbons - carbon fibre, glass and char*, 1976. Cambridge University Press: New York. p. 90.
210. Wood, L.L., Messina, P., and Frisch, K.C., Porous ceramic from polyurethane foam. 1974, 3833386: US Patent.
211. Powell, S.J. and Evans, J.R.G., The structure of ceramic foams prepared from polyurethane-ceramic suspensions. *Materials and Manufacturing Processes* 1995. 10(4): p. 757 - 771.
212. Jee, C., Guo, Z., Evans, J., and Özgüven, N., Preparation of high porosity metal foams. *Metallurgical and Materials Transactions B*, 2000. 31(6): p. 1345-1352.
213. Guo, Z.X., Jee, C.S.Y., Özgüven, N., and Evans, J.R.G., Novel polymer-metal based method for open cell metal foams production. *Materials Science and Technology*, 2000. 16: p. 776-780.
214. Oya, A., Ida, Y., Takabatake, M., Otani, S., and Marsh, H., Oxidation with Simon's reagent and $\text{HNO}_3/\text{H}_2\text{SO}_4$ of turbostratic graphitic carbon prepared catalytically by nickel particles (20nm) in a carbonized resin *Journal of Materials Science*, 1981. 16: p. 1809-1814.
215. Stutts, K.J., Kovach, P.M., Kuhr, W.G., and Wightman, R.M., Enhanced electrochemical reversibility at heat-treated glassy carbon electrodes. *Analytical Chemistry*, 1983. 55(9): p. 1632-1634.
216. Konopka, S.J. and McDuffie, B., Diffusion coefficients of ferri- and ferrocyanide ions in aqueous media, using twin-electrode thin-layer electrochemistry. *Analytical Chemistry*, 1970. 42(14): p. 1741-1746.

217. Kawagoe, K.T., Jankowski, J.A., and Wightman, R.M., Etched carbon-fiber electrodes as amperometric detectors of catecholamine secretion from isolated biological cells. *Analytical Chemistry*, 1991. 63(15): p. 1589-1594.
218. Kim, J., Jia, H., and Wang, P., Challenges in biocatalysis for enzyme-based biofuel cells. *Biotechnology Advances*, 2006. 24(3): p. 296-308.
219. Liu, B., Cao, Y., Chen, D., Kong, J., and Deng, J., Amperometric biosensor based on a nanoporous ZrO₂ matrix. *Analytica Chimica Acta*, 2003. 478(1): p. 59-66.
220. Díaz, J.F. and Balkus, K.J., Enzyme immobilization in MCM-41 molecular sieve. *Journal of Molecular Catalysis B: Enzymatic*, 1996. 2(2-3): p. 115-126.
221. Han, Y.-J., Watson, J.T., Stucky, G.D., and Butler, A., Catalytic activity of mesoporous silicate-immobilized chloroperoxidase. *Journal of Molecular Catalysis B: Enzymatic*, 2002. 17(1): p. 1-8.
222. Lu, A.-H., Smått, J.-H., Backlund, S., and Lindén, M., Easy and flexible preparation of nanocasted carbon monoliths exhibiting a multimodal hierarchical porosity. *Microporous and Mesoporous Materials*, 2004. 72(1-3): p. 59-65.
223. Klepel, O., Strau, H., Garsuch, A., and Böhme, K., Several ways to produce porous carbon monoliths by template assisted routes. *Materials Letters*, 2007. 61(10): p. 2037-2039.
224. Zhao, Y., Zheng, M.-b., Cao, J.-m., Ke, X.-f., Liu, J.-s., Chen, Y.-p., and Tao, J., Easy synthesis of ordered meso/macroporous carbon monolith for use as electrode in electrochemical capacitors. *Materials Letters*, 2008. 62(3): p. 548-551.
225. Holland, B.T., Blanford, C.F., Do, T., and Stein, A., Synthesis of highly ordered, three-dimensional, macroporous structures of amorphous or crystalline inorganic oxides, phosphates, and hybrid composites. *Chemistry of Materials*, 1999. 11(3): p. 795-805.
226. Arshady, R., Preparation of polymer nano- and microspheres by vinyl polymerization techniques. *Journal of Microencapsulation*, 1988. 5: p. 101-114.
227. Nissan Chemical America Corporation Home Page 2007. Snowtex 2009 <<http://www.nissanchem-usa.com/snowtex.php>>.

228. Jaroniec, M., Choma, J., Gorka, J., and Zawislak, A., Colloidal silica templating synthesis of carbonaceous monoliths assuring formation of uniform spherical mesopores and incorporation of inorganic nanoparticles. *Chemistry of Materials*, 2008. 20(3): p. 1069-1075.
229. Kruk, M., Jaroniec, M., and Sayari, A., Application of large pore MCM-41 molecular sieves to improve pore size analysis using nitrogen adsorption measurements. *Langmuir*, 1997. 13(23): p. 6267-6273.
230. Kruk, M. and Jaroniec, M., Gas adsorption characterization of ordered organic-inorganic nanocomposite materials. *Chemistry of Materials*, 2001. 13(10): p. 3169-3183.
231. Gregg, S.J. and Sing, K.S.W., *Adsorption, surface area and porosity*, 1982. Academic Press: London. p. 25.
232. Wen, Z.-H., Han, Y.-S., Liang, L., and Li, J.-B., Preparation of porous ceramics with controllable pore sizes in an easy and low-cost way. *Materials Characterization*, 2008. 59(9): p. 1335-1338.
233. Rabaey, K., Clauwaert, P., Aelterman, P., and Verstraete, W., Tubular microbial fuel cells for efficient electricity generation. *Environmental Science & Technology* 2005. 39(20): p. 8077-8082.
234. Sell, D., Krämer, P., and Kreysa, G., Use of an oxygen gas diffusion cathode and a three-dimensional packed bed anode in a bioelectrochemical fuel cell. *Applied Microbiology and Biotechnology*, 1989. 31: p. 211-213.
235. Jinno, D., Gupta, A.K., and Yoshikawa, K., Thermal decomposition characteristics of critical components in solid wastes. *Environmental Engineering Science*, 2004. 21(1): p. 65-72.
236. Taylor, R.J. and Humffray, A.A., Electrochemical studies on glassy carbon electrodes: I. Electron transfer kinetics. *Journal of Electroanalytical Chemistry*, 1973. 42(3): p. 347-354.
237. Xu, J., Chen, Q., and Swain, G.M., Anthraquinonedisulfonate electrochemistry: a comparison of glassy carbon, hydrogenated glassy carbon, highly oriented pyrolytic graphite, and diamond electrodes. *Analytical Chemistry*, 1998. 70(15): p. 3146-3154.

238. Sel, O., Kuang, D., Thommes, M., and Smarsly, B., Principles of hierarchical meso- and macropore architectures by liquid crystalline and polymer colloid templating. *Langmuir*, 2006. 22(5): p. 2311-2322.
239. Yuan, Z.-Y.S., Bao-Lian Insights into hierarchically meso–macroporous structured materials. *Journal of Materials Chemistry*, 2006. 16: p. 663-677.
240. Freguia, S., Rabaey, K., Yuan, Z., and Keller, J., Non-catalyzed cathodic oxygen reduction at graphite granules in microbial fuel cells. *Electrochimica Acta*, 2007. 53(2): p. 598-603.

Appendix A: Biofuel Cells

A biological fuel cell (biofuel cell) is a device which directly converts energy stored in substrate such as glucose and methanol into electricity using a microorganism or an enzyme as catalyst. Its working principle is similar to that of chemical fuel cells. The main differences are that catalyst in the biofuel cell is microorganism or enzyme and therefore there is no need for a noble metal. Moreover, it tends to operate under mild conditions (room temperature and neutral pH) [1]. These properties make biofuel cells a useful device for applications where generating high temperatures is difficult, or where harsh reaction conditions are undesirable. However, the performance of biofuel cells is still far below the chemical fuel cells due to low power density, poor stability and short lifetime.

The concept of biofuel cells is known for almost one century since the first microbial fuel cell was presented by Potter in 1912 [2]. Further work by Cohen at Cambridge led to development of batteries of microbial fuel cells capable of generating potentials of more than 35 V [3]. The first enzyme-based biofuel cell was reported in 1964 by Yahiro *et al.* using glucose oxidase as the anodic catalyst and glucose as the fuel [4] and considerable improvements have been made since that time [5, 6].

A generalised scheme of a half-biofuel cell is presented in Fig. A-1. Two electrodes are separated by a membrane and placed into a solution. A biological species such as a microbial cell or an enzyme can either be in the solution or as a suspension within the anodic compartment of the cell or alternatively can be immobilised at the electrode. Once a suitable fuel is introduced, it becomes either partially or totally oxidised at the anode and the electrons released by this process are usually employed to reduce oxygen at the cathode [7].

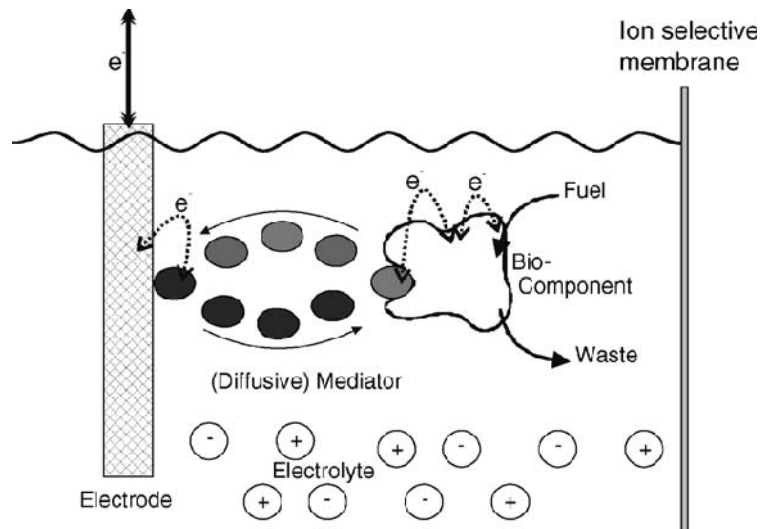
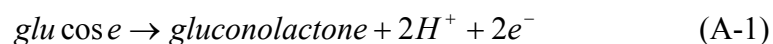


Fig. A-1: Schematic diagram of half-biofuel cell [8].

According to the source of the biocatalysts used, biofuel cells can be divided into two groups, which are enzymatic fuel cells and microbial fuel cells.

1) Enzymatic biofuel cells

Enzyme-based fuel cells are a popular focus for research due to the high biocatalysis rate. In this type of biofuel cell, biocatalysts are directly involved in the redox reaction to produce electricity. Fig. A-2 shows a schematic of an enzyme-based biofuel cell. The fuel is enzymatically oxidised at the anode, producing protons and electrons. At the cathode, the oxidant (usually oxygen or peroxides) reacts with electrons and protons, generating water [9]. For example, reactions of oxidation of glucose at the anode with glucose oxidase (GOx) as catalyst, and reduction of oxygen at the cathode with laccase as catalyst, are as below [10]:



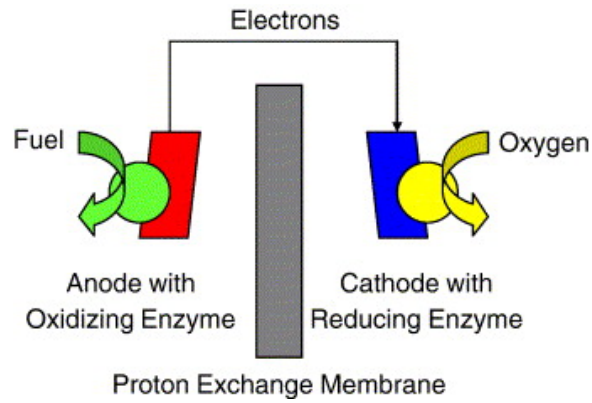


Fig. A-2: Schematic of enzyme-based biofuel cells [9].

The conventional low-temperature fuel cells generally use only H_2 or primary alcohols as fuels but enzymatic biofuel cells can use any substance that can be oxidised by an organism. If the cathode catalyst is not sensitive to the fuel and the anode catalyst is not suppressed by the oxidant, a membrane should not be necessary which simplifies the design and hence the enzymatic fuel cells can be very small [11]. However, using enzymes as electrocatalysts has some disadvantages which are as follows [12]: 1) Even though the active sites of the enzymes may be very active compared to the catalytic site of a conventional metal electrode, but the catalytic density is low because of their large molecules, thus in order to produce enough current, multilayer of enzymes are needed. 2) Electron transfer to or from the electrodes are usually slow because of the position of the catalytically active sites and use of an intrinsic electron relay system, such as a series of FeS clusters, in the protein or an extrinsic mediator that can penetrate close to the active site is necessary. 3) Long-term durability of the enzymes is difficult to achieve because they are unstable outside the ambient conditions of temperature and pH.

One of the critical challenges in developing biofuel cells is inefficient electron transfer between biocatalysts and electrodes. Recent progresses in enzyme immobilisations at electrode surfaces have greatly facilitated the transfer of the electrons and has made these molecules more desirable [13, 14]. Enzyme immobilisation can be achieved in two different ways: physically or chemically (Fig. A-3). Examples of physical enzyme immobilisation are adsorption on the electrode

surface or entrapping the enzymes in polymeric matrices which usually keep the enzymes better than surface adsorption [9].

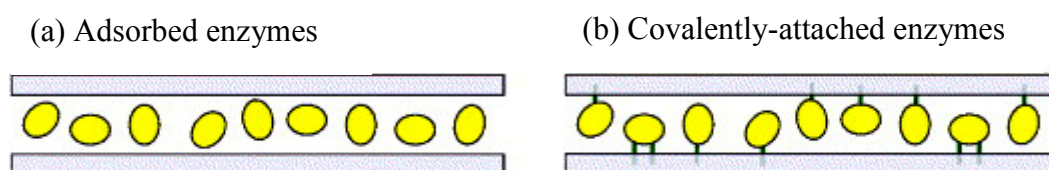


Fig. A-3: Different methods of enzyme immobilisation; (a) adsorption, (b) covalent attachment [9].

2) Microbial fuel cells

Microbes have some advantages over enzymes; they are usually cheaper to use as they can be used as a whole living organisms and don't need to be isolated or purified, they can catalyse a more thorough oxidation of many fuels and can be less susceptible to poisoning and loss of activity under normal operating conditions [7, 8]. However, by using microbes it can be very difficult to use the electrons generated by the reactions in the cell. To overcome this problem, mediators can be used which assist the shuttling of electrons between the bacteria and the electrode. However, the compounds chosen as mediators must satisfy a number of criteria. For instance, they must be capable of being transported across the cell membranes of the microorganisms, and they must be non-toxic. The mediators can be coupled to the microbes in three ways [15] (see Fig. A-4): (1) mediator shuttling between the microbe suspension and the anode surface in the solution, (2) the mediator covalently linked to the electrode surface, (3) the mediator adsorbed on the microbes.

Some microorganisms such as Fe(III)-reducing microorganisms are found to be electrochemically active because they have cytochromes in their outer membranes [15]. These microorganisms can directly transfer electrons on the electrodes without using any mediators. However, these organisms can only use simple organic acids such as acetate as the electron donor. In general, mediator-less fuel cells are more advantageous compared to those with mediators in terms of cost and toxicity of some mediators.

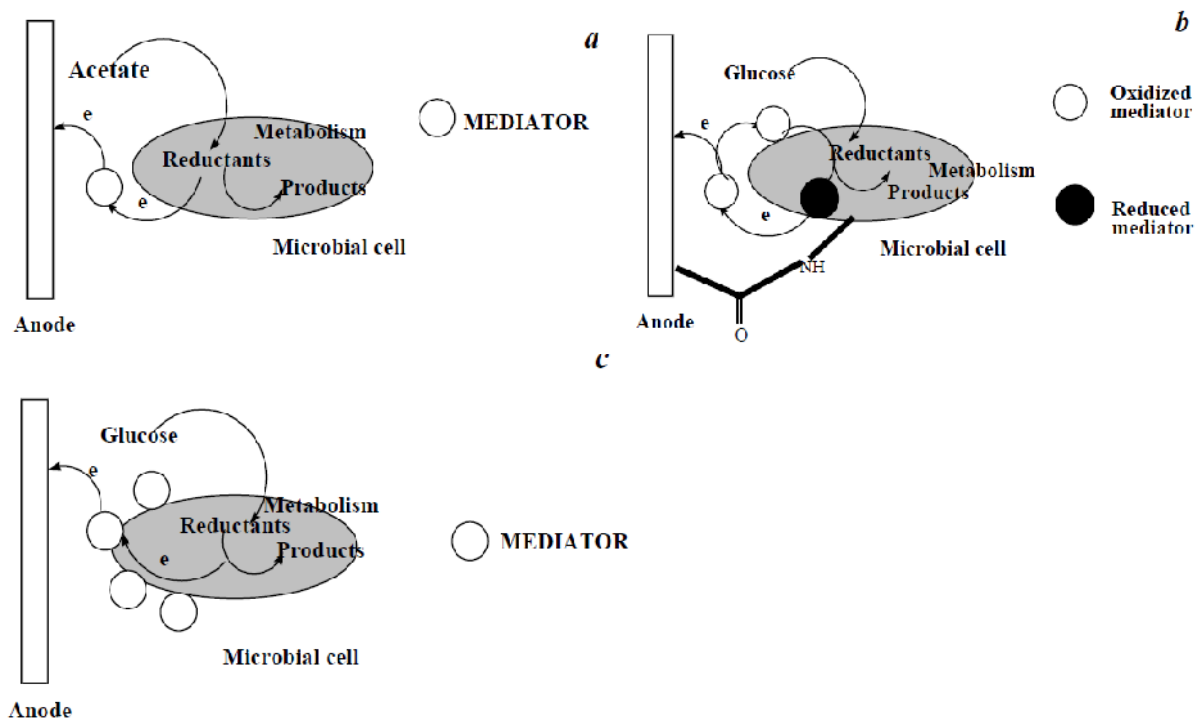


Fig. A-4: Various ways of mediators' attachment to the microorganisms: a, mediator and microorganisms are present in the solution; b, microorganisms are covalently linked to the electrode surface; c, mediators are covalently attached to the outer membrane of microorganisms [15].

There are many different potential applications of biofuel cells. For instance, *in vivo* applications where the fuel used could be withdrawn without limit from the flow of blood to provide a long-term or permanent power supply for devices such as pacemakers, or glucose sensors for diabetics. A biosensor for glucose has been developed using a glucose oxidase-based anode and cytochrome *c* cathode to generate electrical current [16]. This process can be used in a biosensor format to measure the glucose concentrations. Other potential uses of miniature fuel cells include power sources for drug delivery systems [11].

Ex vivo potential applications of biofuel cells are diverse and include wastewater treatment that microorganisms can generate electricity by degrading effluent [17]. Another potential application would be generating power for vehicles which would be environmentally beneficial.

References

1. Yue, P.L. and Lowther, K., Enzymatic oxidation of C₁ compounds in a biochemical fuel cell. *The Chemical Engineering Journal*, 1986. 33B: p. 69-77.
2. Potter, M., Electrical effects accompanying the decomposition of organic compounds. *Proceedings of the Royal Society B: Biological Sciences*, 1912. 84: p. 260-76.
3. Cohen, B., The bacterial culture as an electrical half-cell. *Journal of Bacteriology*, 1931. 21: p. 18.
4. Yahiro, A.T., Lee, S.M., and Kimble, D.O., Bioelectrochemistry I. Enzyme utilizing biofuel cell studies. *Biochimica et Biophysica Acta* 1964. 88: p. 375-383.
5. Mano, N., Mao, F., and Heller, A., A Miniature Biofuel Cell Operating in A Physiological Buffer. *Journal of the American Chemical Society*, 2002. 124(44): p. 12962-12963.
6. Moore, C.M., Akers, N.L., Hill, A.D., Johnson, Z.C., and Minteer, S.D., Improving the environment for immobilized dehydrogenase enzymes by modifying nafion with tetraalkylammonium bromides. *Biomacromolecules*, 2004. 5(4): p. 1241-1247.
7. Davis, F. and Higson, S.P.J., Biofuel cells--Recent advances and applications. *Biosensors and Bioelectronics*, 2007. 22(7): p. 1224-1235.
8. Bullen, R.A., Arnot, T.C., Lakeman, J.B., and Walsh, F.C., Biofuel cells and their development. *Biosensors and Bioelectronics*, 2006. 21(11): p. 2015-2045.
9. Kim, J., Jia, H., and Wang, P., Challenges in biocatalysis for enzyme-based biofuel cells. *Biotechnology Advances*, 2006. 24(3): p. 296-308.
10. Chen, T., Barton, S.C., Binyamin, G., Gao, Z., Zhang, Y., Kim, H.-H., and Heller, A., A miniature biofuel cell. *Journal of the American Chemical Society*, 2001. 123(35): p. 8630-8631.
11. Mano, N., Mao, F., and Heller, A., Characteristics of a miniature compartment-less glucose-O₂ biofuel cell and its operation in a living plant. *Journal of the American Chemical Society*, 2003b. 125(21): p. 6588-6594.

12. Cracknell, J.A., Vincent, K.A., and Armstrong, F.A., Enzymes as working or inspirational electrocatalysts for fuel cells and electrolysis. *Chemical Reviews*, 2008. 108(7): p. 2439-2461.
13. Davis, F. and Higson, S.P.J., Structured thin films as functional components within biosensors. *Biosensors and Bioelectronics*, 2005. 21(1): p. 1-20.
14. Scouten, W.H., Luong, J.H.T., and Brown, R.S., Enzyme or protein immobilization techniques for applications in biosensor design. *Trends in Biotechnology*, 1995. 13(5): p. 178.
15. Shukla, A.K., Suresh, P., Berchmans, S., and Rajendram, A., Biological fuel cells and their applications. *Current Science*, 2004. 87(4): p. 455-468.
16. Katz, E., Buckmann, A.F., and Willner, I., Self-powered enzyme-based biosensors. *Journal of the American Chemical Society*, 2001. 123(43): p. 10752-10753.
17. He, Z., Minteer, S.D., and Angenent, L.T., Electricity generation from artificial wastewater using an upflow microbial fuel cell. *Environmental Science & Technology*, 2005. 39(14): p. 5262-5267.

Appendix B: Techniques for Characterising Structure and Properties of Carbon Materials

B.1 X-Ray Diffraction

X-ray diffraction (XRD) technique is used to obtain information regarding the bulk structure of carbon materials. This method provides a measure of the amount of ordered material present and can be used to give an indication of the size of the crystallites in the ordered structure. Samples are prepared as powders either in capillaries or spread on a flat sample holder [1].

When a beam of X-radiation is directed to a crystalline material, diffraction of the X-rays is observed at different angles with respect to the primary beam. The relationship between the wavelength of the X-ray beam, λ , the angle of diffraction, 2θ , and the distance between the planes of the crystal lattice, d , is given by the Bragg equation:

$$n\lambda = 2d \sin \theta \quad (\text{B-1})$$

where n is the order of diffraction. Using this equation, the interplanar distances of the crystalline material can be calculated. The interplanar spacing depends on the arrangement of atoms in the crystal unit cell while the intensities of the diffracted rays relate to both the diffracting power and the placement of the atoms within the unit cell [2].

The crystallite size can be estimated from the Scherrer equation [3, 4]:

$$L = K\lambda / B \cos \theta \quad (\text{B-2})$$

In which L is a crystallite size (nm), B is the full-width-half-maximum (FWHM) of the diffracted beam in radians, λ is the wave length of the X-ray (nm), θ is the Bragg angle and K is a constant known as the Scherrer constant.

All the XRD patterns presented in this project was obtained using a Siemens D500 instrument operating at 40 kV and 30 mA, using Cu K α radiation ($\lambda = 0.15406$ nm). A step width of $2\theta = 0.05^\circ$ and a count time of 4 s per step was used for all the samples.

B.2 Transmission Electron Microscopy

Transmission electron microscopy (TEM) is used to study the structure and morphology of materials by examining the diffracted and transmitted electron intensities. A beam of high energy electrons is paralleled by electromagnetic lenses and passed through the specimen [5]. The transmitted beam contains information about electron density, phase and periodicity which are used to form an image on a screen below the specimen. Fig. B-1 shows a schematic of TEM with its three essential systems; electron gun and condenser system, the image-producing system and the image-recording system. An electron gun produces the electron beam and the condenser focuses the beam onto the specimen. The image-producing system consists of the movable specimen stage, objective lens, and intermediate and projector lenses, which focus the electrons passing through the specimen to form a highly magnified image.

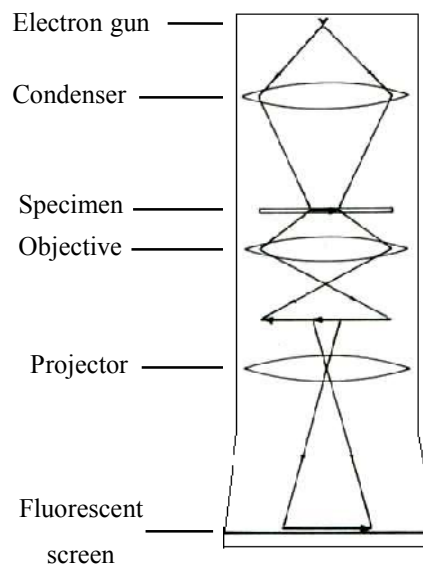


Fig. B-1: Schematic of transmission electron microscope [6].

TEM images presented in this project were obtained using a JEOL JEM 2010 instrument with an accelerating voltage of 200 KV. Samples for TEM observations were prepared by deposition of dilute suspension of the sample drops (*e.g.* 1 ml of colloidal polystyrene was diluted with 5 ml of deionised water) on a copper grid and drying.

B.3 Raman Spectroscopy

Raman Spectroscopy is based on the Raman Effect which is the inelastic scattering of photons by molecules. When light is scattered from a molecule most photons are elastically scattered. The scattered photons have the same energy (frequency) and, therefore, wavelength, as the incident photons. However, a small fraction of light, approximately 1 in 10^7 photons, is scattered at optical frequencies different from, and usually lower than, the frequency of the incident photons. The process leading to this inelastic scatter is termed as the Raman Effect [7].

The difference in energy between the incident photon and the Raman scattered photon is equal to the energy of a vibration of the scattering molecule. A plot of intensity of scattered light versus energy difference is a Raman spectrum.

Raman spectra presented in this report were all collected with a Renishaw Raman microscope. A laser operating at a wavelength of 514.5 nm was used as a radiation source.

B.4 Pycnometry

Pycnometer determines density and volume of a sample in any shape by measuring the pressure change of helium in a calibrated volume. A simplified diagram of the pycnometer is shown in Fig. B-2 [8].

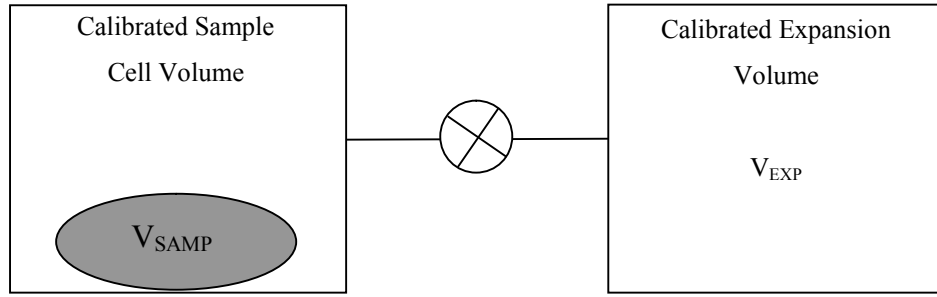


Fig. B-2: Simplified diagram of the pycnometer [8].

Presumably, both V_{CELL} and V_{EXP} are at ambient pressure (P_a) and ambient temperature (T_a) and the valve is closed. V_{CELL} is then charged to an elevated pressure P_1 . The mass balance equation across the sample cell, V_{CELL} , is:

$$P_1(V_{CELL} - V_{SAMP}) = n_c RT_a \quad (B-3)$$

Where n_c is the number of moles of gas in the sample cell, and R is the gas constant. The mass equation for the expansion volume is:

$$P_a V_{EXP} = n_e RT_a \quad (B-4)$$

Where, n_e is the number of moles of gas in the expansion volume. When the valve is opened, the pressure falls to an intermediate value, P_2 , and the mass balance equation becomes:

$$P_2(V_{CELL} - V_{SAMP} + V_{EXP}) = n_c RT_a + n_e RT_a \quad (B-5)$$

By substituting equations (B-3) and (B-4) into (B-5) and making some rearrangements, equation (B-6) is derived and is the working equation for the pycnometer.

$$V_{SAMP} = V_{CELL} - \frac{V_{EXP}}{\frac{P_{1g}}{P_{2g}} - 1} \quad (B-6)$$

P_{1g} and P_{2g} are gauge pressures and are defined as below:

$$P_{1g} = P_1 - P_a \quad (\text{B-7})$$

$$P_{2g} = P_2 - P_a \quad (\text{B-8})$$

V_{CELL} and V_{EXP} are determined by a calibration procedure and the pressures are measured by a gauge pressure transducer [8].

Density of the produced foams in this project was measured using a Micromeretics AccuPyc 1330 pycnometer, Fig. B-3.



Fig. B-3: Micromeretics AccuPyc 1330 Pycnometer [9].

B.5 Four- Point Probe Method for Electrical Resistivity

The oldest method of finding electrical resistivity (ρ) is to use a rectangular sample of known dimensions and measure the electrical resistance (R) and use the relation $R = \rho L/A$, L is the sample length and A is the cross section. A disadvantage of this method is that ρ will also contain a contact-resistance term which affects the calculated electrical resistivity. The effect of contact resistance can be eliminated by use of the two-point probe method. However, measurement with this method has also some restrictions including; the current should be kept low to prevent sample heating, the voltmeter must have a high input impedance, and the specimen cross section needs to be uniform [10].

Due to the drawbacks mentioned above, another method is introduced that offers the most convenient mode of resistivity measurement, *i.e.* the four-point probe technique. The four-point probe is a tool for measuring the resistivity of a material by contacting its surface. The method is widely used in the semiconductor industry. The method is normally non-destructive. However, the probe points may damage certain materials when excessive probe pressure is applied. Current is passed through the outer two probes and the potential developed across the two inner probes is measured (Fig. B-4) [11].

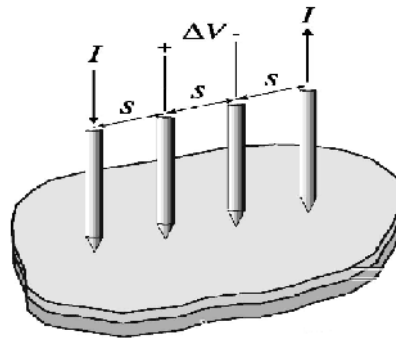


Fig. B-4: Schematic of the linear four-point resistivity probe [11].

Resistivity measurements are geometry-dependent and quite sensitive to boundary conditions. Due to this sensitivity, many correction factors have been calculated. For example, for a thick sample with boundaries of larger than 10 times of probe spacing and equally spaced probes, no correction is required and the resistivity is calculated by equation (B-9) [12],

$$\rho = 2\pi S \frac{V}{I} \quad (\text{B-9})$$

Where S is the probe spacing (cm), V is the measured potential difference between the inner probes (V), I is the current through the outer pair of probes (A), and ρ is the resistivity of the material (Ω cm).

Electrical resistivity of all the samples in this project was measured by the four point technique using a Jandel four point probing system, Fig. B-5. The probe spacing of 0.635 mm and a current of 1 mA were used for all the tests.

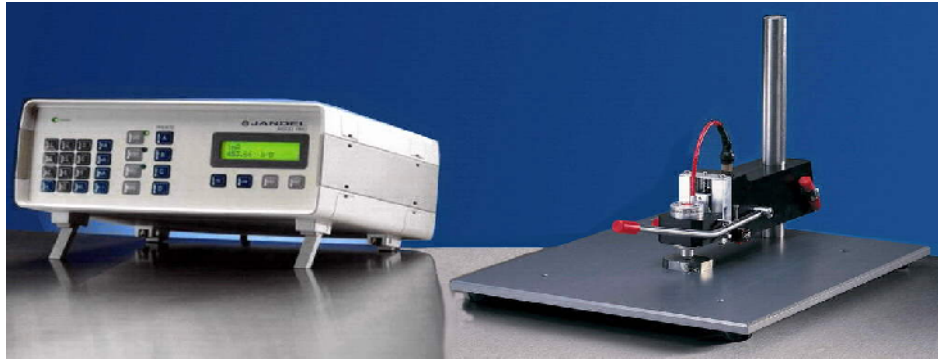


Fig. B-5: Jandel four point probing system. Multi height probe with RM3-AR test unit [13].

B.6 Compression Test for Mechanical Strength

A compression test determines behaviour of materials under crushing loads. The sample is compressed until it breaks and the compressive strength (MPa) is calculated by dividing the maximum load (N) taken by the sample before crushing, by the original cross-sectional area (mm^2) of the sample.

All the mechanical strengths reported in this thesis were measured by compression test using an Instron 8500 machine with a loading rate of 0.5 MPa s^{-1} . To obtain flat surfaces for the compression tests, cross-sections of the samples were grinded before the tests.

References

1. Klug, H.P. and Alexander, L.E., X-ray diffraction procedures for polycrystalline and amorphous materials, 1974. Wiley: New York. p. 202-216.
2. Klug, H.P. and Alexander, L.E., X-ray diffraction procedures for polycrystalline and amorphous materials, 1974. Wiley: New York. p. 130-132.
3. Scherrer, P., Göttinger Nachrichten Gesell, 1918: Göttingen. p. 98.
4. Zsigmondy, R., Kolloidchemie. 3rd Edn. 1920. p. 394.
5. Chescoe, D. and Goodhew, P.J., The operation of transmission and scanning electron microscopes, in *Royal microscopical society microscopy handbooks* 1990. Oxford University Press: New York. p. 21-24.

6. Chescoe, D. and Goodhew, P.J., The operation of transmission and scanning electron microscopes, in *Royal microscopical society microscopy handbooks* 1990. Oxford University Press: New York. p. 5.
7. Raman, C.V. and Krishnan, K.S., A new type of secondary radiation. *Nature*, 1928. 121: p. 501.
8. AccuPyc 1330 Pycnometer Manual. 1996: London. p. B1-B3.
9. Center for Materials Research, Queen Mary University of London. 2010 <<http://www.cmr.qmul.ac.uk/facilities/item.php?eid=123>>.
10. Runyan, W.R., Semiconductor measurements and instrumentation, in *Texas instruments incorporated*, 1975. McGraw-Hill Kogakusha: Tokyo. p. 65-75.
11. Weller, R.A., An algorithm for computing linear four-point probe thickness correction factors. *Review of Scientific Instruments*, 2001. 72(9): p. 3580-3586.
12. Valdes, L.B., Resistivity measurements on Germanium for transistors. *Proceedings of the IRE*, 1954. 42: p. 420-427.
13. Maintenance and use of the multiheight probe. 2007: Linslade. p. 1-8.

Appendix C: Techniques for Characterising Porous Carbons

C.1 Scanning Electron Microscopy

In scanning electron microscopy (SEM), the sample surface is imaged in a cathode ray tube (CRT) by scanning the surface with a high-energy beam of electrons (primary electrons). This electron beam is produced from a tungsten filament and is focused on an area of the surface with magnetic lenses in a high vacuum chamber (Fig. C-1). The electrons interact with the atoms that make up the sample and produce signals that contain information about the surface topography and composition of the sample. The types of signals made by an SEM can include secondary electrons and back scattered electrons coming from the beam of electrons striking the surface of the specimen and interacting with the sample at or near its surface [1].

If the primary electrons (with their energy much higher than the energy of the electrons bound to the nuclei) reflect from the surface without any energy interchange, the electrons from the atoms on the top surface will be knocked out which are called the secondary electrons. A high resolution image can be produced from these secondary electrons. The morphology of the surface is determined by the contrast in the image.

Backscattered electrons vary in their amount and direction with the composition surface topography and crystallinity of the specimen. The contrast of an image produced by backscattered electrons varies with the atomic number of the sample (the higher the atomic number, the higher the contrast). This is useful to detect different phases in specimens especially alloys.

In field emission scanning electron microscopy, a field-emission cathode in the electron gun of a scanning electron microscope provides narrower probing beams as well as high electron energy, resulting in both improved spatial resolution and minimised sample charging compared to the conventional SEM.

Scanning electron microscopy (SEM) of all the fabricated porous carbons in this project was carried out using a Jeol JSM 6300 microscope. Field emission scanning electron microscopy images of these samples have been taken using a Jeol JSM 6300F microscope.

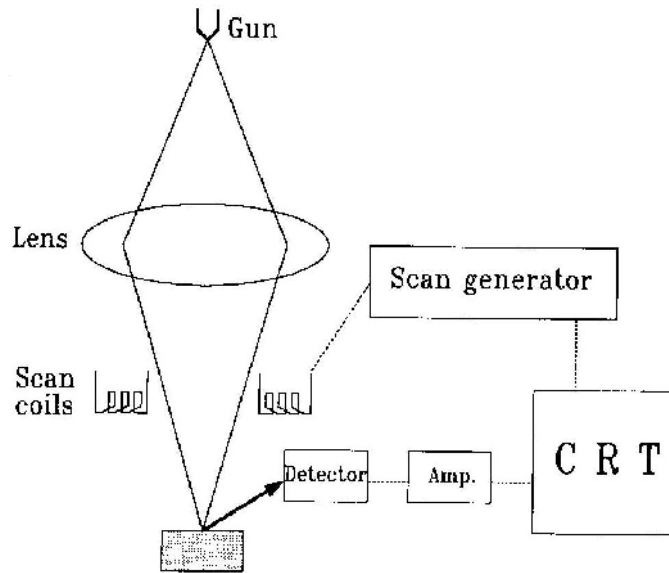


Fig. C-1: Schematic drawing of a scanning electron microscope. CRT=cathode ray tube display [2].

C.2 Mercury Intrusion Porosimetry

Mercury porosimetry characterises a material's porosity by applying various levels of pressure to a sample immersed in mercury. The pressure required to intrude mercury into the sample's pore is inversely proportional to the size of the pores [3].

Mercury porosimetry is based on the capillary law governing liquid penetration into small spaces. This law, in the case of a non-wetting liquid like mercury, is expressed by the Washburn equation [4]:

$$D = (1/P) 4 \sigma \cos \theta \quad (C-1)$$

D: Pore diameter

P: Applied pressure

σ : Surface tension of mercury

θ : Contact angle between the mercury and the sample

Washburn equation states briefly that the pressure required to force a non-wetting liquid to enter a capillary of circular cross-section is inversely proportional to the diameter of the capillary and directly proportion to the surface tension of the liquid and the angle of contact with the solid surface. The assumption that is used by Washburn equation is that the pore or capillary is cylindrical and the opening is circular in cross-section [3].

Porosity of the fabricated carbon foams in this project was studied with the mercury porosimetry technique using a Micromeretics Mercury Intrusion Autopore IV Series (Fig. C-2).

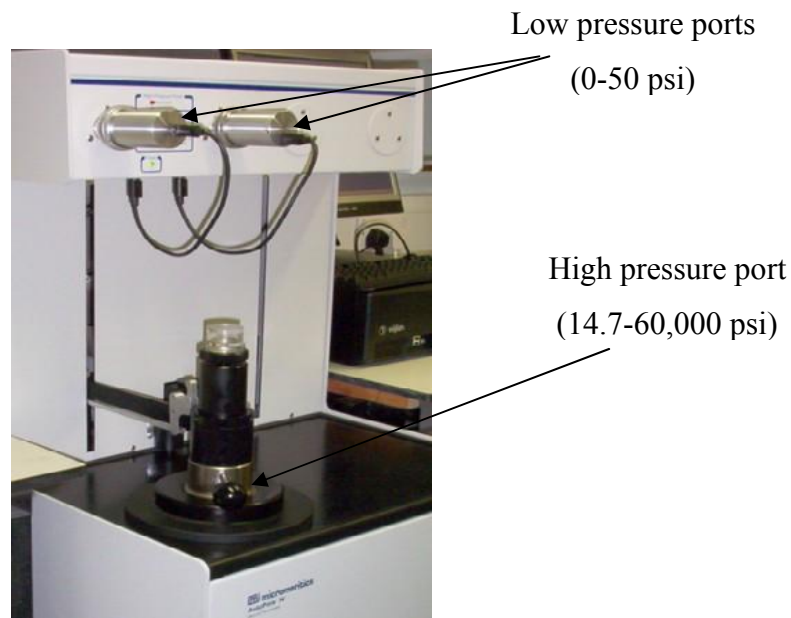


Fig. C-2: Micromeretics Mercury Intrusion Autopore IV [5].

C.3 Brunauer-Emmett-Teller (BET) Surface Area Analyser

Gas sorption (both adsorption and desorption) at the surface of porous materials is the most widely used technique for determination of the surface area and pore size distribution of porous materials. In a gas sorption experiment, the material is heated and degassed by vacuum force or inert gas purging to remove adsorbed foreign

molecules. Controlled doses of an inert gas, such as nitrogen, krypton or argon, are introduced and the gas is adsorbed, or alternatively, withdrawn and desorbed. The sample material is placed in a vacuum chamber at a constant and very low temperature, usually at the temperature of liquid nitrogen (-195.6 °C), and subjects to a wide range of pressures, to generate adsorption and desorption isotherms.

The amounts of gas molecules adsorbed or desorbed are determined by the pressure variations due to the adsorption or desorption of the gas molecules by the material (the adsorbent). Various amounts of gas molecules will be adsorbed or desorbed at different doses of the gas (the adsorbate). Knowing the area occupied by one adsorbate molecule, for example 16.2 Å² for nitrogen, and using an adsorption model, the total surface area of the material can be determined. The most well known and widely used is the BET equation for multilayer adsorption [6]:

$$\frac{P}{n(P_0 - P)} = \frac{1}{cn_m} + \frac{c-1}{cn_m} \frac{P}{P_0} \quad (\text{C-2})$$

where, P, P₀, c, n and n_m are the adsorption pressure, the saturation vapour pressure, a constant, the amount adsorbed (moles per gram of adsorbent) at the relative pressure P/P₀ and the monolayer capacity (moles of molecules needed to make a monolayer coverage on the surface of one gram of adsorbent), respectively. Through the slope and intercept of a plot of P/[n(P₀-P)] against (P/P₀), n_m can be resolved. The specific surface area, S, can then be derived:

$$S = N_A n_m \sigma \quad (\text{C-3})$$

where, N_A is the Avogadro's number and σ is the area occupied by one adsorbate molecule. Determination of pore size and pore size distribution of porous materials can be made from the adsorption/desorption isotherm using an assessment model, suitable for the shape and structure of the pores. Various classifications of gas adsorption isotherms and adsorption/desorption hysteresis loops are described in the following sections.

C.3.a Classification of Gas Adsorption Isotherms

Gas adsorption isotherms are classified into six categories (see Fig. C-3). Isotherms Type I show large adsorption at low relative pressures and then become even. This type of isotherm is considered to indicate adsorption in micropores or monolayer adsorption. However, it may also be observed for mesoporous materials with pore sizes close to micropore ranges. It has been derived from the results of some studies that when a Type I isotherm does not level below the relative pressure of 0.1, the sample is mostly or entirely consisted of mesopores [7].

In Type II and III isotherms the adsorption and desorption branches of the isotherm coincide and there is no adsorption/desorption hysteresis. Both isotherms exhibit the multilayer formation of the adsorbate on macroporous solids as the relative pressure increases [8]. Type IV and V isotherms show the adsorption on mesoporous solids that is initially similar to the adsorption on macroporous solids but at higher pressures the amount adsorbed rises steeply due to the capillary condensation in mesopores. After the pores are filled, the adsorption isotherms level off. The hysteresis loops appear because the capillary condensation and capillary evaporation do not usually occur at the same pressure. However, it was suggested [9] that the capillary condensation-evaporation in mesopores may also be reversible (Type IVc isotherm [8]).

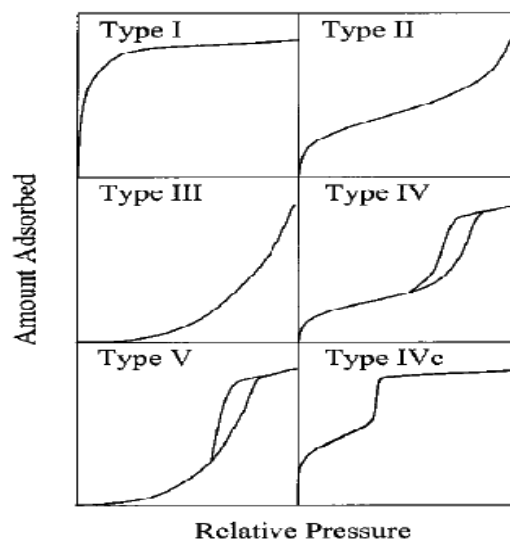


Fig. C-3: Classification of gas adsorption isotherms [8, 10].

C.3.b Classification of Adsorption-Desorption Hysteresis Loops

As mentioned in the previous section, the adsorption process on mesoporous solids usually accompanies by adsorption-desorption hysteresis. These hysteresis loops are classified into four types, according to the IUPAC recommendations [10]. The Type H1 loop presents almost vertical and parallel branches (see Fig. C-4). This type of hysteresis loop is observed in the materials that consist of agglomerates or compacts of spherical particles that are arranged uniformly and the appearance of the H1 hysteresis loop on the adsorption isotherm of porous solid indicates the high pore size uniformity and pore connectivity. The Type H2 hysteresis loop presents materials with relatively uniform channel-like pores [11] and the Type H3 hysteresis loop that does not level off at relative pressures close to the saturation vapour pressure shows aggregates of plate-like particles. Type H4 hysteresis loop with parallel and horizontal branches, shows the presence of large mesopores in a matrix with pores of smaller size.

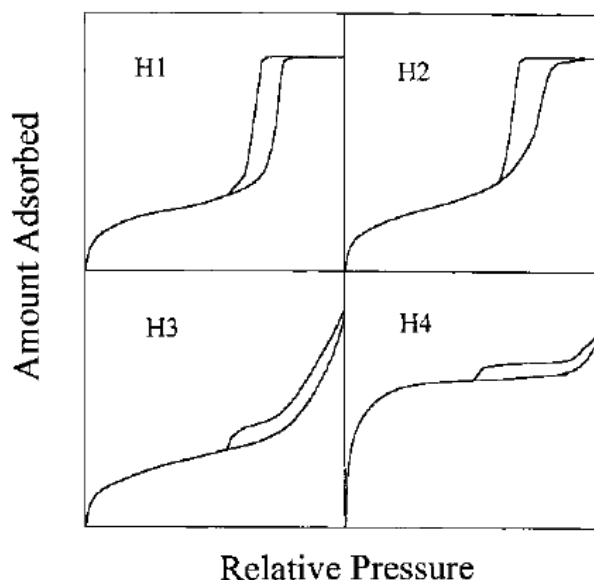


Fig. C-4: Classification of adsorption-desorption hysteresis loops [10].

All the nitrogen sorption isotherms in this report were measured at $-195.85\text{ }^{\circ}\text{C}$ on ASAP 2420 accelerated surface area and porosimetry system, micromeritics (Fig. C-5). Before adsorption measurements each sample was outgassed under vacuum for 5 h at $200\text{ }^{\circ}\text{C}$. All the BET surface areas were calculated from the nitrogen adsorption isotherm in the range of relative pressures from 0.06 to 0.26. Pore size distribution

curves of all the samples were calculated by the Barrett-Joyner-Halenda (BJH) method [12].

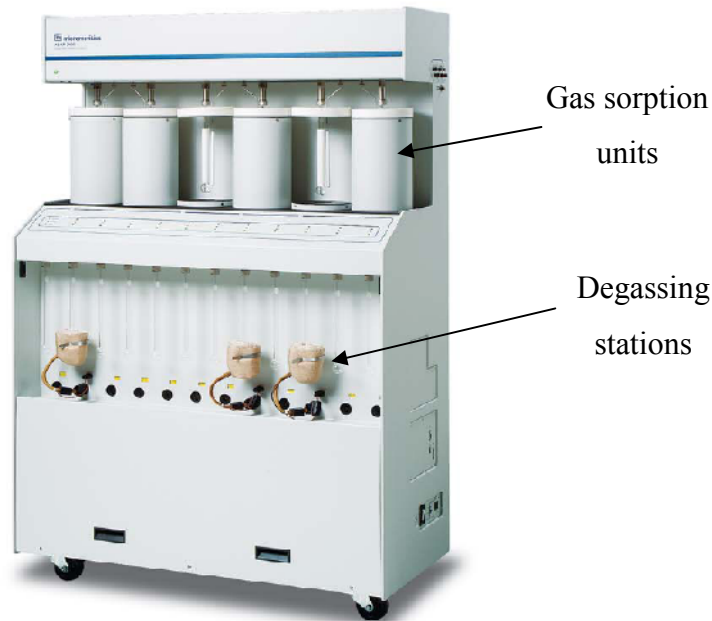


Fig. C-5: Micromeritics ASAP 2420 surface area and porosimetry system [13].

References

1. Rochow, T.G. and Tucker, P.A., Introduction to microscopy by means of light, electrons, X rays, or acoustics, 1994. Plenum Press: New York. p. 297-300.
2. Chescoe, D. and Goodhew, P.J., The operation of transmission and scanning electron microscopes, in *Royal microscopical society microscopy handbooks* 1990. Oxford University Press: New York. p. 2.
3. Webb, P.A., An introduction to the physical characterization of materials by mercury intrusion porosimetry with emphasis on reduction and presentation of experimental data. 2001, Micromeritics Instrument Corp.: Norcross, Georgia. p. 4-8.
4. Washburn, E.W., Note on a method of determining the distribution of pore sizes in a porous material. *Proceedings of the National Academy of Sciences* 1921. 7(4): p. 115-116.
5. Center for Materials Research, Queen Mary University of London. 2010 <<http://www.cmr.qmul.ac.uk/facilities/item.php?eid=124>>.

6. Brunauer, S., Emmet, P.H., and Teller, E., Adsorption of gases in multimolecular layers. *Journal of the American Chemical Society*, 1938. 60(2): p. 309-319.
7. Kruk, M. and Jaroniec, M., Accurate method for calculating mesopore size distributions from argon adsorption data at 87 K developed using model MCM-41 materials. *Chemistry of Materials*, 2000. 12(1): p. 222-230.
8. Kruk, M. and Jaroniec, M., Gas adsorption characterization of ordered organic-inorganic nanocomposite materials. *Chemistry of Materials*, 2001. 13(10): p. 3169-3183.
9. Gregg, S.J. and Sing, K.S.W., *Adsorption, surface area and porosity*, 1982. Academic Press: London. p. 1-38.
10. Sing, K.S.W., Everett, D.H., Ghaul, R.A.W., Moscou, L., Pierotti, R.A., Rouquerol, J., and Siemieniewska, T., Reporting physisorption data for gas/solid systems with special reference to the determination of surface area and porosity. *Pure & Applied Chemistry*, 1985. 57(4): p. 603-919.
11. Liu, H., Zhang, L., and Seaton, N.A., Analysis of sorption hysteresis in mesoporous solids using a pore network model. *Journal of Colloid and Interface Science*, 1993. 156(2): p. 285-293.
12. Barrett, E.P., Joyner, L.G., and Halenda, P.P., The determination of pore volume and area distributions in porous substances. I. Computations from nitrogen isotherms. *Journal of the American Chemical Society*, 1951. 73(1): p. 373-380.
13. Micromeritics Instrument Corporation 2010 <<http://www.micromeritics.com/Pressroom/Press-Release-List/Micromeritics-New-ASAP-2420-Accelerated-Surface-Area-and-Porosimetry-System.aspx>>.

Appendix D: Analysis of Surface Functional Groups

There are traditional methods as well as modern instrumentation to analyse the surface functional groups on carbon surfaces which are summarised below.

D.1 Titration

Titration is a common laboratory method that is used to determine the unknown concentration of a known reactant. This method can be used to evaluate acidic and basic surface groups and is particularly useful when is used in combination with other methods [1]. However, this method has its drawbacks such as requirement of large amount of sample for quantitative analysis and is very time consuming. For instance, to differentiate carboxyl, lactones, hydroxyl and carbonyl groups in carbon materials, they should be suspended in solutions of sodium bicarbonate (NaHCO_3), sodium carbonate (Na_2CO_3), sodium hydroxide (NaOH) or sodium ethoxide, respectively for several hours to determine their acidic surface groups. However, not all the existing oxygen on the carbon surfaces can be determined by this method. Some oxygen could be bonded within the graphene layers (in-ring) and therefore, would be non-reactive. In addition, some carbonyl groups might not be able to react with the alkaline solutions [2, 3].

D.2 Fourier Transform Infrared (FTIR) Spectroscopy

In IR spectroscopy, radiation in the infrared region interacts with the material and excitation of vibrational modes of the chemical bonds between molecules is probed with wavelength dependent attenuation of the incident beam. Resonance occurs when the energy of the incident beam corresponds to the vibrational energy level of a bond and this is when the energy from the incident beam is absorbed and detected. The position of a vibrational band in the spectrum is related to the type of the chemical bond and deviations from typical positions contain information about the chemical nature surrounding this bond [4]. There is a limitation of using IR spectroscopy for carbon materials due to the high absorbance of carbon. Development of diffuse reflectance infrared Fourier transform spectroscopy (DRIFTS) has helped to

overcome this limitation. In this method, one part of the IR beam is reflected at the solid surface and another part of the beam is transmitted through the solid where it can interact in many directions. This transmission-reflectance can occur many times and the scattered IR energy is collected by a spherical mirror and focused on to the detector. This method is a useful method in analysis of the functional groups on carbon surfaces [5-7].

Some of the oxygen groups on carbon surfaces and their assignments in infrared spectra are shown in Table D-1.

Table D-1: Infrared spectra assignments of functional groups on carbon surfaces [6].

Oxygen groups	Assignment regions (cm ⁻¹)		
	1000-1500	1500-2950	2950-3700
C-O stretch in ethers	1000-1300		
Alcohols	1049-1276		3200-3640
Phenolic groups			
C-OH stretch	1000-1220		
O-H	1160-1200		2500-3620
Carbonates: carboxyl carbonates	1100-1500	1590-1600	
Aromatic C = C stretching		1585-1600	
Quinones		1550-1680	
Carboxylic acids	1120-1200	1665-1760	2500-3300
Lactones	1160-1370	1675-1790	
Anhydrides	980-1300	1740-1880	
Ketenes			2080-2200
C-H stretching			2600-3000

As it can be seen from Table D-1, the interpretation of the IR spectra can be complicated. This is because each group develops several bands at different wave numbers and therefore each band may include contributions from various groups. In addition, this method can only be applied to highly oxidised carbons; otherwise the intensity of the absorption bands is not high enough to be detected [8].

The infrared spectrum presented in this work was recorded on an Excalibur HE series FTS 3100 instrument from Digilab.

D.3 X-ray Photoelectron Spectroscopy (XPS)

In XPS, a beam of X-ray irradiate a material and core electrons of the material are excited and leave the atoms while simultaneously measuring the kinetic energy and number of electrons that have escaped. The measured kinetic energies are used to estimate the binding energy. The differences in binding energy for various binding states are small, especially with electronegative elements such as oxygen, compared to the line width and hence a deconvolution of overlapping peaks is necessary [2].

As an example, functional groups of a fibre treated with ozone, determined by XPS from O1s peaks and the corresponding binding energies, are shown in Fig. D-1 and Table D-2.

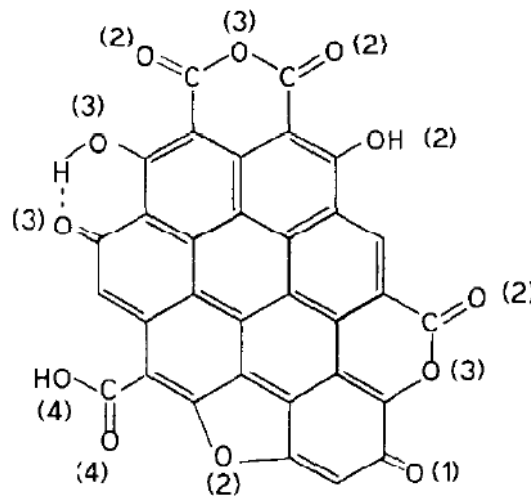


Fig. D-1: Functional groups determined with XPS showing the relevant oxygen atoms at their corresponding binding energies in Table D-2 [9].

Table D-2: Functional groups determined by XPS from the O1s peaks [9].

Group	Binding energy (eV)	Functional groups
1	531.1	C=O groups
2	532.3	Carbonyl oxygen atoms in esters, amides, anhydrides and oxygen atoms in hydroxyls or ethers.
3	533.3	Ether oxygen atoms in esters and anhydrides.
4	534.2	Oxygen atoms in carboxyl groups.

D.4 Temperature Programmed Desorption (TPD)

This technique involves heating of an oxidised carbon in vacuum or in a flow of helium with a constant heating rate (often 10 K min^{-1}) and measuring the evolved gases (usually water, carbon dioxide and carbon monoxide) by a mass spectrometer. Carbon dioxide and carbon monoxide come from the decomposition of carboxyl-type groups and from carbonyl, hydroxyl and ether oxygen, respectively [2, 3]. Table D-3 summarises the evolved gases from different functional groups obtained by the TPD technique. The evolution of CO or CO₂ from surface oxidised carbons does not occur at fixed temperatures. It depends on the heating rate and can be shifted to lower temperatures by slower heating and vice versa [9].

Table D-3: Evolved gases, obtained by TPD technique, from functional groups present on carbon surfaces [9, 10].

Functional groups	Evolved gas (CO or CO ₂) and evolution peak temperatures (°C)
Carboxylic groups (strongly acidic)	CO ₂ @ 200-250
Lactones, lactoles and anhydrides	CO ₂ @ 350-400 CO ₂ @ 627
Peroxides	CO ₂ @ 550-600
Anhydrides	CO @ 400-450
Phenols and/or hydroquinones	CO @ 600-700
Carbonyls and/or quinones	CO @ 800-900
Carbonyl and/or ether	CO @ 700-800

The surface oxygen complexes formed on carbons with different methods are usually stable to about 250 °C. Outgassing around this temperature results in evolution of gases mostly consist of carbon dioxide and water vapour. There is very little carbon monoxide at this temperature. Around 500 °C, however, the evolution of carbon monoxide also commences and with increasing temperature the ratio of CO₂/CO continuously decreases. Above 600°C, the evolved gas is largely carbon monoxide [11].

The TGA instrument used in this project was a Setsys 16/18 TG-DTA.

References

1. Papirer, E., Dentzer, J., Li, S., and Donnet, J.B., Surface groups on nitric acid oxidized carbon black samples determined by chemical and thermodesorption analyses. *Carbon*, 1991. 29(1): p. 69-72.
2. Boehm, H.P., Surface oxides on carbon and their analysis: a critical assessment. *Carbon*, 2002. 40(2): p. 145-149.
3. Marsh, H. and Rodriguez-Reinoso, F., *Activated carbon*, 2006. Elsevier: Oxford. p. 185-187.
4. Griffiths, P.R. and De Haseth, J.A., *Fourier transform infrared spectrometry*, 2007. John Wiley & Sons: New Jersey. p. 1-3.
5. Sellitti, C., Koenig, J.L., and Ishida, H., Surface characterization of graphitized carbon fibers by attenuated total reflection fourier transform infrared spectroscopy. *Carbon*, 1990. 28(1): p. 221-228.
6. Fanning, P.E. and Vannice, M.A., A DRIFTS study of the formation of surface groups on carbon by oxidation. *Carbon*, 1993. 31(5): p. 721-730.
7. Zhuang, Q.L., Kyotani, T., and Tomita, A., DRIFT and TK/TPD analyses of surface oxygen complexes formed during carbon gasification. *Energy and Fuels*, 1994. 8(3): p. 714-718.
8. Figueiredo, J.L., Pereira, M.F.R., Freitas, M.M.A., and Orfao, J.J.M., Modification of the surface chemistry of activated carbons. *Carbon*, 1999. 37(9): p. 1379-1389.
9. Zielke, U., Huttinger, K.J., and Hoffman, W.P., Surface-oxidized carbon fibers: I. Surface structure and chemistry. *Carbon*, 1996. 34(8): p. 983-998.
10. Zhuang, Q.L., Kyotani, T., and Tomita, A., DRIFT and TK/TPD analyses of surface oxygen complexes formed during carbon gasification. *Energy and Fuels* 1994. 8(3): p. 714-718.
11. Philip, L. and Walker, J., *Chemistry and physics of carbon*, 1970. Marcel Dekker: New York. p. 191-281.

Appendix E: Other Instruments and Materials Used in this Project

1) Tube furnace: A horizontal vacuum tube furnace (Lenton, Model VTF 15/75/450) was used for all the heat treatments, curing and carbonisations performed in the experiments (Fig. E-1). The maximum temperature that the furnace could reach was 1500 °C.



Fig. E-1: Lenton vacuum tube furnace.

2) Spark plasma sintering (SPS): is a method for rapid sintering, where the sintering cycle can be completed in minutes. In SPS process, powders are sintered under the simultaneous effect of current and pressure (Fig. E-2). The SPS process uses pulsed high DC current along with uniaxial pressure to sinter powders with a high heating rate. Some of the benefits of using the SPS process compared to the conventional consolidation methods include; achieving a higher density, improved mechanical and electrical properties of the materials [1, 2].

Sintering of the carbon foam preforms accomplished using a Model HPD-25/1 FCT spark plasma sintering system (Rauenstein, Germany). For all the samples, the applied heating rate was 100 °C min⁻¹ and using a die no pressure was applied during the SPS experiments.

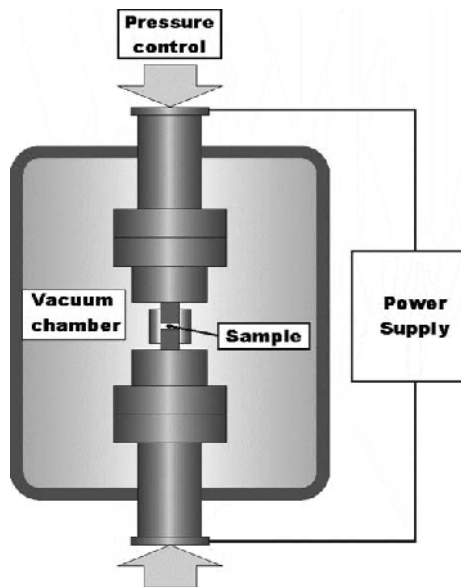


Fig. E-2: Schematic of spark plasma sintering (SPS) process [1].

3) Viscometer: A Viscometer Model B (Tokimec, Tokyo) was used for measuring the viscosity of the polyfurfuryl alcohol used in the experiments. The viscometer measures a viscous resistance torque of liquid caused by a disc or cylinder rotated in the liquid. In the viscometer, the dial rotates at a constant speed by synchronous motor and the rotor rotates at the same speed of dial by a coupling spring (see Fig. E-3). If the viscous resistance of liquid affects on the rotor, the spring will be given some torsion and will go to an extent to balance the torque by viscous resistance of the liquid and the restoring torque of the spring itself. Afterwards, the dial and rotor rotate at the same speed as the twisted spring, and with the indicator needle attached to the rotor, the torsional angle of the spring on the dial can be read. Torsion of the spring is proportional to the liquid viscosity when the rotation of the rotor is constant, thus, viscosity can be obtained by measuring the torsional angle [3]. A wide range of viscosity can be measured by Viscometer Model B as the viscous resistance torque, which is the source of giving torsion to the spring, is related to shape and dimension of the rotors and rotation speed as well as liquid viscosity. For example, low viscosity can be measured by using a large rotor and fast rotation speed and high viscosity can be measured by using a small rotor and low rotation speed.

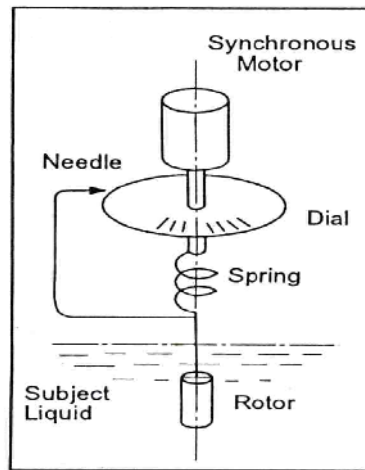


Fig. E-3: Schematic drawing of Viscometer Model B [3].

4) Particle size analyser: A Zetasizer Nano (Malvern) was used for determining the colloidal polystyrene and silica particle size distributions (Chapter 4). The Zetasizer system determines particle sizes by measuring the Brownian motion of particles in a sample using dynamic light scattering [4]. Brownian motion is the random movement of the particles suspended in a liquid due to the collision with the molecules of the liquid that surrounds the particles. The particles are illuminated with a laser and the intensity fluctuations of the scattered light is analysed and is related to the size of particles.

In the Brownian motion of the particles, small particles move rapidly and large particles move more slowly. The relation between the size of a particle and its speed due to the Brownian motion is defined by the Stokes-Einstein equation [5]:

$$D = \frac{KT}{6\pi\eta r} \quad (\text{E-1})$$

where, K is a constant and T is the absolute temperature, η is the viscosity of the liquid, r is the radius of the particles and D is the diffusion coefficient of the particles. The colloidal polystyrene samples were diluted with deionised water eight times and three tests were run for each sample.

5) Electrochemical measuring system: Cyclic voltammetry measurements were performed using a PGSTAT Autolab. In this technique, a potential applies to an

electrode and increases according to the scan rate and the current is measured at the end of each potential step. All the carbon samples produced for electrochemical tests were prepared as electrodes by connecting a copper wire to the samples using a silver paste and gluing around the connection for insulation.

6) Hydraulic press: A 15 ton manual hydraulic press (Specac), Fig. E-4, was used to press the silica particles into mesoporous and macroporous templates inside a cylindrical die in Chapter 4, and a bigger hydraulic press (Clarke Strong-Arm, Model AHP 25) was used to press the mixture of polyfurfuryl alcohol and polyethylene powder prepared in Chapter 5.



Fig. E-4: 15 ton manual hydraulic press (Specac) [6].

7) List of materials used in the experiments and their specifications:

- Graphite powder, general purpose grade (> 99%, Fisher Scientific)
- Carbon powder, charcoal decolorizing powder activated, BDH # 330324E (BDH Laboratory Supplies, Poole, England)
- Polyurethane, two-part foam (Grade GP1058A and GP1059A, Scott Bader, Wellingborough, UK)
- Potassium ferricyanide (Fisher Scientific)
- Oxalic acid, anhydrous ($\geq 99\%$, Fluka)
- Furfuryl alcohol (98%, Aldrich)

- Sulphuric acid (98%, Aldrich)
- Hydrofluoric acid (40%, Fluka)
- Calcium carbonate (grade: Ph Eur, Fluka)
- Polyethylene powder, ultrahigh molecular weight-surface modified (180 μm particle size, Aldrich)
- Ethanol (96% GPR, VWR)
- Nickel (II) nitrate hexahydrate ($\text{Ni}(\text{NO}_3)_2 \cdot 6\text{H}_2\text{O}$), ($\geq 98\%$, Fluka)
- Hydrochloric acid, analytical reagent grade ($\sim 36\%$, Fisher Scientific)
- Styrene (99%, Aldrich)
- Potassium persulphate, A.C.S. reagent ($\geq 99\%$, Sigma-Aldrich)
- Colloidal silica, Snowtex-ZL, particle sizes: 70-100 nm (Nissan Chemicals Industries)
- Colloidal silica, Ludox AS-40, average particle size: 22 nm (Sigma Aldrich)

References

1. Munir, Z., Anselmi-Tamburini, U., and Ohyanagi, M., The effect of electric field and pressure on the synthesis and consolidation of materials: A review of the spark plasma sintering method. *Journal of Materials Science*, 2006. 41(3): p. 763-777.
2. Chen, X.J., Khor, K.A., Chan, S.H., and Yu, L.G., Overcoming the effect of contaminant in solid oxide fuel cell (SOFC) electrolyte: spark plasma sintering (SPS) of 0.5 wt.% silica-doped yttria-stabilized zirconia (YSZ). *Materials Science and Engineering A*, 2004. 374(1-2): p. 64-71.
3. *Viscometer Model B User's Manual*. 1996: Tokyo. p. 31.
4. *Zetasizer Nano Series User Manual*. 2004: Worcestershire. p. 14.1-14.8.
5. Kuhn, H., Forsterling, H.-D., and Waldeck, D.H., *Principles of physical chemistry*, 2009. John Wiley & Sons: New Jersey. p. 429.
6. 15 and 25 Ton manual hydraulic presses, Specac Ltd. 2010 <<http://www.selectscience.net/products/15-and-25-ton-manual-hydraulic-presses/?prodID=10495>>.

Appendix F: Supplementary Results

1) Structures of the carbon foams after catalytic graphitisation: X-ray diffraction (XRD) patterns of the samples prepared in Section 3.3.1 of Chapter 3 are presented in Figs. F-1 and F-2. Addition of various concentrations of nickel salt and different methods of addition to the amorphous carbon foams resulted in graphitic carbon T- and G-components.

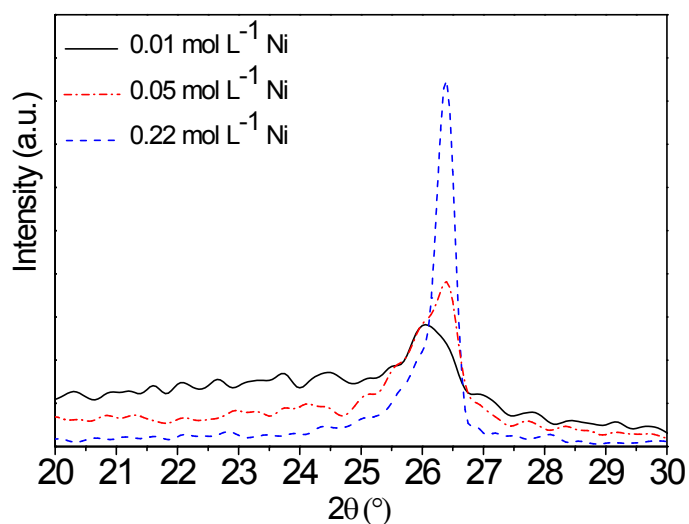


Fig. F-1: XRD patterns of the carbon foams after addition of 0.01, 0.05 and 0.22 mol L⁻¹ nickel salt by Method 1 that produced graphitic carbons T- and G-components.

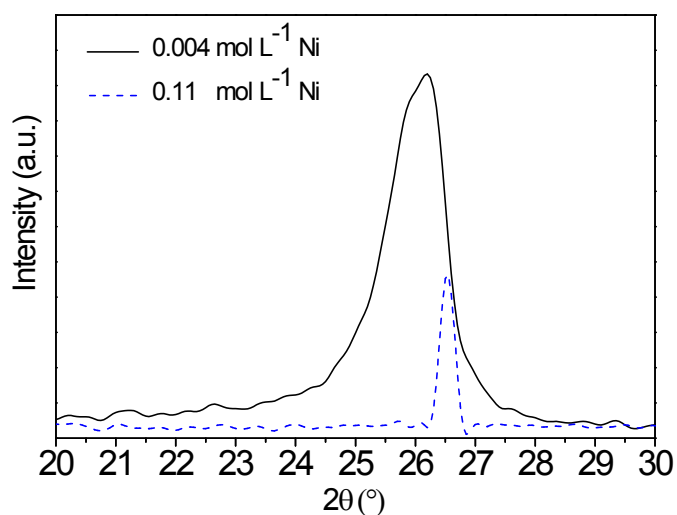


Fig. F-2: XRD patterns of the carbon foams after addition of 0.004 and 0.11 mol L⁻¹ nickel salt by Method 2 that produced graphitic carbons T- and G-components, respectively.

2) Graphitisation degree of the carbon foams: Raman spectra of the graphitised carbons T- and G-components prepared in Section 3.3.1 of Chapter 3 by Method 2 are shown in Figs. F-3 and F-4. Raman spectrum of at least three points on the samples was taken and the figures below show the spectra of two points for each sample.

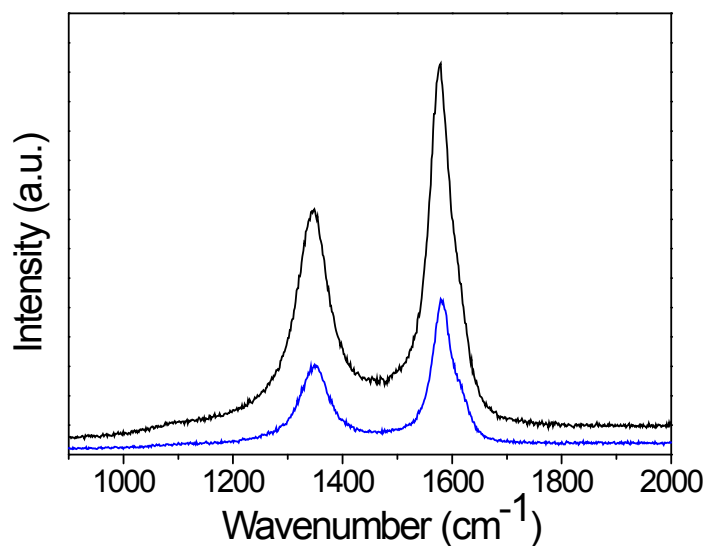


Fig. F-3: Raman spectra of graphitised carbon T-component produced by Method 2.

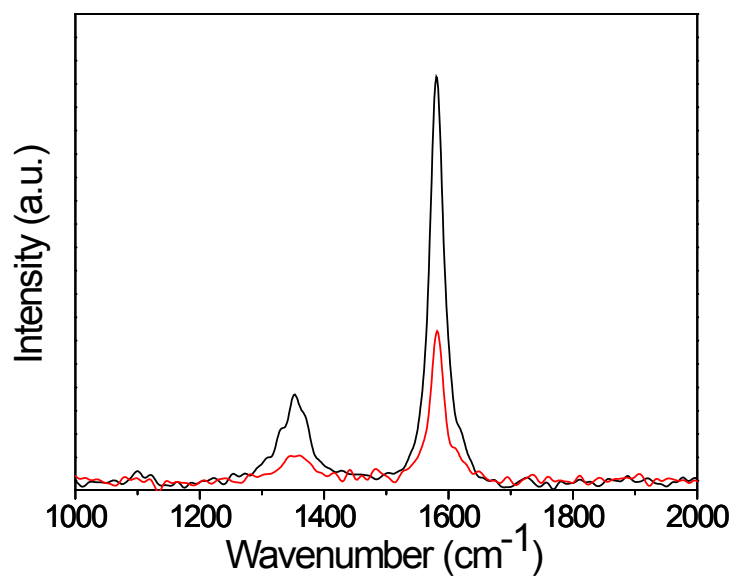


Fig. F-4: Raman spectra of graphitised carbon G-component produced by Method 2.

3) Pictures of the machined porous carbon: Fig. F-5 shows pictures of the machined porous carbon electrode produced by the polymer blend technique in Chapter 5.

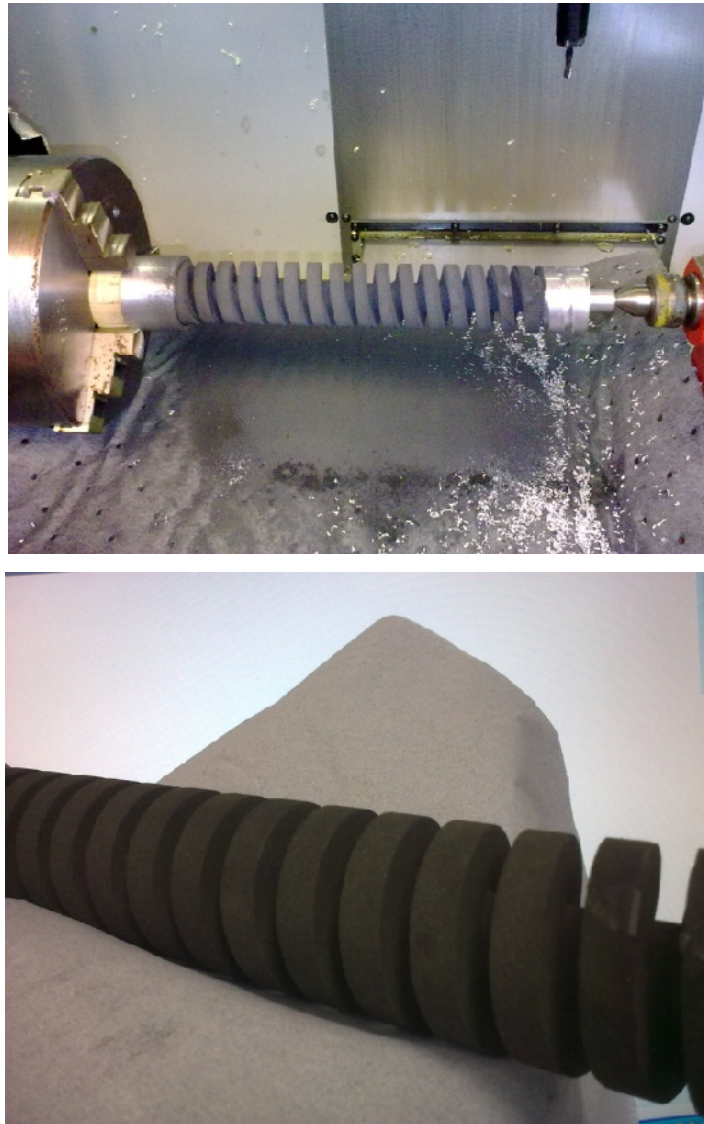


Fig. F-5: Pictures of the machined porous carbon electrode produced by the polymer blend technique [provided by Dr. G. C. Premier from Department of Engineering, University of Glamorgan].

Appendix G: Presentations and Publications

- N. Amini, K. F. Aguey-Zinsou, Z. X. Guo, “Carbon Electrodes in Large Scales”, *Oral Presentation*, Biofuel Cells Consortium Meeting, St Johns College, Oxford, 12-13 Jan 2009.
- N. Amini, K. F. Aguey-Zinsou, Z. X. Guo, “Porous Carbon Electrodes for Biofuel Cells”, *Oral Presentation*, Workshop on Biological Fuel Cells, University of Surrey, Guildford, 23-25 July 2008.
- D. Sun, N. Amini, H. Lei, K. F. Aguey-Zinsou, B. Kerkeni, and Z. X. Guo, “Towards [NiFe]-hydrogenase immobilization on functionalized porous carbon for biofuel cells”, *Poster Presentation*, Sustainable Energy UK: Meeting the science and engineering challenge, St Anne’s College, Oxford, 13-14 May 2008.
- N. Amini, K. F. Aguey-Zinsou, Z. X. Guo, “Design and Fabrication of Porous Carbon Electrodes”, *Oral Presentation*, Biofuel Cells Consortium Meeting, University of Glamorgan, Glamorgan, 7-8 Jan 2008.
- N. Amini, K. F. Aguey-Zinsou, Z. X. Guo, “Processing of porous carbon monoliths as electrode materials”, intend to submit to Journal of Materials Science, 2010.
- X. Lu, L. Chen, N. Amini, S. Yang, J. R. G. Evans, Z. X. Guo, “New methods for fabrication of 3D porous carbon structures with surface mesopores”, intend to submit to Carbon, 2010.